Sub-grid models for Large Eddy Simulation of non-conventional combustion regimes

Am Fachbereich Maschinenbau
an der Technischen Universität Darmstadt
zur
Erlangung des Grades eines Doktor-Ingenieurs (Dr.-Ing.)
eingereichte

Dissertation

vorgelegt von

Zhiyi Li, M. Sc.

aus Shandong, China

Berichterstatter:	Prof. Dr.-Ing. C. Hasse
Mitberichterstatter:	Prof. Dr.-Ing. A. Parente
	Prof. Dr.-Ing. A. Sadiki
Tag der Einreichung:	16. April 2019
Tag der mündlichen Prüfung:	8. August 2019

Darmstadt 2019

D17

Li, Zhiyi: Sub-grid models for Large Eddy Simulation of non-conventional combustion regimes

Darmstadt, Technische Universität Darmstadt,

Year thesis published in TUprints 2019

URN: urn:nbn:de:tuda-tuprints-90086

Date of the viva voce 08.08.19

Declaration

This thesis is submitted to the Technische Universität Darmstadt for the degree of philosophy doctor. This doctoral work has been performed at the Department of Aero-Thermo Mechanics, Université libre de Bruxelles, Brussels, Belgium with Professor Alessandro Parente and at the Department of Energy and Power Plant Technology, Technische Universität Darmstadt, Darmstadt, Germany with Professor Amsini Sadiki.

Zhiyi Li
August 2019

Acknowledgements

I would like to express my very great appreciation to my supervisor Prof. Alessandro Parente for his valuable and constructive suggestions during the planning and development of this research work.

Thanks are also due to my co-supervisor, Prof. Amsini Sadiki, for his valuable support. Special thanks to Prof. Alberto Cuoci and Prof. Francesco Contino for the useful advises regarding model implementation.

I would also like to thank all the co-workers. My gratitude goes out to all these colleagues. At last but not the least, I wish to thank my family for their support and encouragement throughout my study.

This project has received funding from the European Union′s Horizon 2020 research and innovation program under the Marie Skłodowska-Curie grant agreement No. 643134. The research is also sponsored by the European Research Council, Starting Grant No. 714605.

Abstract

Novel combustion technologies ensuring low emissions, high efficiency and fuel flexibility are essential to meet the future challenges associated to air pollution, climate change and energy source shortage, as well as to cope with the increasingly stricter environmental regulation. Among them, Moderate or Intense Low oxygen Dilution (MILD) combustion has recently drawn increasing attention. MILD combustion is achieved through the recirculation of flue gases within the reaction region, with the effect of diluting the reactant streams. As a result, the reactivity of the system is reduced, a more uniform reaction zone is obtained, thus leading to decreased NO_x and soot emissions. As a consequence of the dilution and enhanced mixing, the ratio between the mixing and chemical time scale is strongly reduced in MILD combustion, indicating the existence of very strong interactions between chemistry and fluid dynamics. In such a context, the use of combustion models that can accurately account for turbulent mixing and detailed chemical kinetics becomes mandatory.

Combustion models for conventional flames usually rely on the assumption of time-scale separation (i.e., flamelets and related models), which constrain the thermochemical space accessible in the numerical simulation. Whilst the use of transported PDF methods appears still computationally prohibitive, especially for practical combustion systems, there are a number of closures showing promise for the inclusion of detailed kinetic mechanisms with affordable computational cost. They include the Partially Stirred Reactor (PaSR) approach and the Eddy Dissipation Concept (EDC) model.

In order to assess these models under non-conventional MILD combustion conditions, several prototype burners were selected. They include the Adelaide and Delft jet-in-hot-coflow (JHC) burners, and the Cabra lifted flames in vitiated coflow. Both Reynolds Averaged Navier Stokes (RANS) and Large Eddy Simulations (LES) were carried out on these burners under various operating conditions and with different fuels. The results indicate the need to explicitly account for both the mixing and chemical time scales in the combustion model formulation. The generalised models developed currently show excellent predictive capabilities when compared with the available, high-fidelity experimental data, especially in their LES formulations. The advanced approaches for the evaluation of the mixing and chemical time scale were compared to several conventional estimation methods, showing their superior

performances and wider range of applications. Moreover, the PaSR approach was compared with the steady Flamelet Progress Variable (FPV) model on predicting the lifted Cabra flame, proving that the unsteady behaviours associated to flame extinction and re-ignition should be appropriately considered for such kind of flame.

Because of the distributed reaction area, the reacting structures in MILD combustion can be potentially resolved on a Large Eddy Simulation (LES) grid. To investigate that, a comparative study benchmarking the LES predictions for the JHC burner obtained with the PaSR closure and two implicit combustion models was carried out, with the implicit models having filtered source terms coming directly from the Arrhenius expression. The results showed that the implicit models are very similar with the conventional PaSR model on predicting the flame properties, for what concerns the mean and root-mean-square of the temperature and species mass fraction fields.

To alleviate the cost associated to the use of large kinetic mechanisms, chemistry reduction and tabulation methods to dynamically reduce their size were tested and benchmarked, allowing to allocate the computational resources only where needed. Finally, advanced post-processing tools based on the theory of Computational Singular Perturbation (CSP) were employed to improve the current understanding of flame-turbulence interactions under MILD conditions, confirming the important role of both autoignition and self propagation in these flames.

List of publications

International journals

- **Zhiyi Li**, Riccardo M. Galassi, Pietro P. Ciottoli, Mauro Valorani and Alessandro Parente, Computational Singular Perturbation analysis on Large Eddy Simulation of MILD combustion, *Combustion and Flame* 208, 281-298 (2019).
- **Zhiyi Li**, Alberto Cuoci and Alessandro Parente, Large Eddy Simulation of MILD combustion using finite rate chemistry: effect of combustion sub-grid closure, *Proceedings of the Combustion Institute* 37 (4), 4519-4529 (2019).
- **Zhiyi Li**, Michał T. Lewandowski, Francesco Contino and Alessandro Parente, Numerical investigation of MILD combustion with EDC model employing on-the-fly chemistry reduction and tabulation in OpenFOAM, *Energy & Fuels* 32 (10), 10121-10131 (2018).
- **Zhiyi Li**, Marco Ferrarotti, Alberto Cuoci and Alessandro Parente, Finite-rate chemistry modelling of non-conventional combustion regimes using a Partially-Stirred Reactor closure: combustion model formulation and implementation details, *Applied Energy* 225, 637-655 (2018).
- **Zhiyi Li**, Alberto Cuoci, Amsini Sadiki and Alessandro Parente, Comprehensive numerical study of the Adelaide Jet in Hot-Coflow burner by means of RANS and detailed chemistry, *Energy* 139, 555-570 (2017).
- **Zhiyi Li**, Alberto Cuoci, Amsini Sadiki and Alessandro Parente, Finite-rate chemistry modelling of non-conventional combustion regimes, *Energy Procedia* 142, 1570-1576.
- Marco Ferrarotti, **Zhiyi Li** and Alessandro Parente, On the role of mixing models in the simulation of MILD combustion using finite-rate chemistry combustion models, *Proceedings of the Combustion Institute* 37 (4), 4531-4538 (2019).

- Gianmarco Aversano, Aurelie Bellemans, **Zhiyi Li**, Axel Coussement, Olivier Gicquel and Alessandro Parente, Application of Reduced-Order Models based on PCA & Kriging for the development of digital twins of reacting flow applications, *Computers & Chemical Engineering* 121, 422-441 (2019).

In reparation for international journals

- **Zhiyi Li**, Michael J. Evans, Jingjing Ye, Paul Medwell and Alessandro Parente, Numerical investigation of turbulent n-heptane Jet in Hot Co-flow flames, *Combustion and Flame*, submitted.
- **Zhiyi Li**, Alberto Cuoci and Alessandro Parente, Large Eddy Simulation of MILD combustion with dynamic PaSR model.

International conferences

- **Zhiyi Li**, Rihab Mahmoud, Amsini Sadiki and Alessandro Parente, Numerical investigation of lifted turbulent flame with PaSR and FPV models, *12th International ERCOFTAC Symposium on Engineering Turbulence Modelling and Measurements*, 26-28 September, 2018, Montpellier, France.
- Michał T. Lewandowski, **Zhiyi Li**, Alessandro Parente, Ivar S. Ertesvåg and Jacek Pozorski, Comparison of the Eddy Dissipation Concept modifications in the modelling of MILD combustion, *XXIII International Symposium on Combustion Processes*, 3-6 September, 2017, Rynia, Poland.
- Mohammad Rafi Malik, **Zhiyi Li**, Alberto Cuoci and Alessandro Parente, edcSMOKE: A new combustion solver based on OpenFOAM, *10th Mediterranean Combustion Symposium Conference Proceedings*, 17-21 September, 2017, Naples, Italy.
- **Zhiyi Li**, Mohammad Rafi Malik, Alberto Cuoci and Alessandro Parente, edcSMOKE: A new combustion solver for stiff chemistrybased on OpenFOAM, *American Institute of Physics Conference Procedings* 1863, 180004 (2017).

Table of contents

List of figures

List of tables

Nomenclature

Roman Symbols

$\boldsymbol{a}_i$	modes in CSP analysis
$\boldsymbol{b}^i$	dual basis vector
C	progress variable
C_1	constant in transport equation for the mixture fraction dissipation rate
C_2	constant in transport equation for the mixture fraction dissipation rate
C_3	constant in transport equation for the mixture fraction dissipation rate
C_4	constant in transport equation for the mixture fraction dissipation rate
$C_{\varepsilon 1}$	model constant in turbulent kinetic energy dissipation rate transport equation
$C_{\varepsilon 2}$	model constant in turbulent kinetic energy dissipation rate transport equation
$C_{\varepsilon 3}$	model constant for Pope correction
C_γ	EDC model constant
C_τ	EDC model constant
C_A	consumption of species A
C_{dis}	model constant for the evaluation of dynamic mixing time scale in LES
C_k	model constant for sub-grid scale viscosity
C_{prd}	model constant for the evaluation of dynamic mixing time scale in LES
C_{var}	model constant for the evaluation of dynamic mixing time scale in LES

$cTot^*$ total concentration obtained from the ideal gas law in the reactive structures

D_f mixture fraction diffusivity

$D_{m,s}$ species molecular diffusivity in the mixture

D_t turbulent diffusivity

$\widetilde{f''^2}$ Favre-averaged or Favre-filtered mixture fraction variance

$\widetilde{f''^2_{sfs}}$ mixture fraction sub-filter variance

f mixture fraction

$f^i(\boldsymbol{g})$ the amplitude of the i-th mode based on only chemical source

$\boldsymbol{g}(\boldsymbol{z})$ chemical source term of the system

H number of exhausted modes

h enthalpy

$h^i(\boldsymbol{z})$ the amplitude of the i-th mode based on both chemical source and transport (convection and/or diffusion)

$\mathbf{J}$ Jacobian matrix of the chemical source terms

k turbulence kinetic energy

k_{sgs} sub-grid scale kinetic energy

S_{ij} mean flow strain rate

$\boldsymbol{L}(\boldsymbol{z})$ spatial differential operator for convection and/or diffusion

$\hat{R}_{s,r}$ Arrhenius rate of creation/destruction of species s in reaction r

M number of fast modes

M_s molecular weight of species

N number of species

n_p number of species on a certain path

n_r number of reactions

p pressure

$P_{\text{mode}_i}^{\omega_{\tilde{\tau}}}$ product of the participation index of the i-th mode to the TSR

P_A production of species A

Pr_t turbulent Prandtl number

$\mathbf{q}_r$ radiative heat loss

$\mathbf{R}(\psi^q)$ reduced reaction mapping

$\mathbf{R}(\psi_a^q)$ full reaction mapping

$\mathbf{R}^l(\psi^q)$ retrieved reaction mapping from ISAT

$\overline{r}^k$ averaged reaction rate of the remaining reactions after reaction k is removed

R_τ mechanical to scale time scale ratio

$r_{AB,p}$ interaction coefficient representing the contribution of species B to the production rate of species A on a certain path

r_{AB} interaction coefficient representing the contribution of species B to the production rate of species A

r_r individual reaction rates before removing a reaction k from the network

r_r^k individual reaction rates after removing a reaction k from the network

$\overline{S}_{ij}$ resolved scale strain rate

s^k variance after reaction k has been removed

S_{ij} rate of strain tensor

S_s species in TDAC

Sc_t turbulent Schmidt number

$\mathbf{u}$ velocity

$v^{'}$ sub-grid fluctuation

$\widetilde{y}_i$ Favre-averaged species mass fraction in each cell for FPV model

$\widetilde{Y}_s$ mean species mass fraction in the cell

Y_s species mass fraction

Y_s^* species mass fraction in the fine structures

Y_s^0 species mass fraction in the surrounding fluid

z (N+1)-dimensional state vector including the mass fractions of N species and the temperature

Greek Symbols

α thermal diffusivity

Δ filter width

$\widetilde{\chi}$ Favre-averaged or Favre-filtered mixture fraction dissipation rate

δ_{ij} Kronecker symbol

ε_{ISAT} user defined tolerance for ISAT

ε_{RED} error evaluated for chemistry reduction in TDAC

ε turbulence dissipation rate

$\widetilde{\varepsilon_\phi}$ Favre-averaged or Favre-filtered scalar dissipation rate

γ_λ mass fraction of the fine structures in EDC model

λ thermal conductivity

κ mass fraction of the reactive structures in PaSR model

λ_s Eigenvalues of the Jacobian matrix

μ molecular viscosity

μ_{Eff} effective viscosity

μ_t turbulent viscosity

$\nu_{A,r}$ stoichiometric coefficient of species A in reaction r

ν_{sgs} sub-grid viscosity

$\nu_{n_r,sum}$ the sum of the product stoichiometric coefficients

∇f gradient of mixture fraction

$\dot{\omega}_s$ instantaneous reaction rate in the fine structures

$\dot{\omega}_s^*$ species formation rate in the fine structures

$\omega_{\tilde{\boldsymbol{\tau}}}$ TSR time scales

ω_{ij} rotation tensor

ω_r reaction rate in each reaction r

$\omega_{\boldsymbol{g}+\boldsymbol{L}}$ extended TSR time scales

$\omega_{\boldsymbol{g}}$ chemical TSR time scales

$\overline{\dot{\omega}}_s$ mean species formation rate from combustion model

$\widetilde{\omega}_C$ Favre-averaged source term for progress variable

n_R total number of reactions

ψ vortex-stretching invariant

ψ^q species composition space

ψ_a^q reduced set of species compositions

$\widetilde{\phi''^2}$ Favre-averaged or Favre-filtered scalar variance

ρ density

σ_ε model constant in turbulent kinetic energy dissipation rate transport equation

σ_k model constant in turbulent kinetic energy transport equation

τ^* residence time within fine structures

τ_{ii}^{sgs} isotropic sub-grid Reynolds stresses

τ_c characteristic chemical time scale

$\tau_{mix_{DynamicLES}}$ dynamic mixing time scale in LES

τ_{mix} characteristic mixing time scale

$\tau_{c,s}$ characteristic time scale of a single species

T_{ij} unresolved Reynolds stresses

$\tau_{mix_{Dynamic}}$ dynamic mixing time scale

τ_{mix_I} integral mixing time scale

τ_{mix_K} Kolmogorov mixing time scale

$\tau_{mix_{LES}}$ mixing time scale in LES

$\tau_{mix_{Mean}}$ geometric mean mixing time scale

Superscripts

$''$ fluctuations

Subscripts

i direction i in space, or index in the chemical composition space for CSP analysis

j direction j in space, or index in the chemical composition space for CSP analysis

k reaction removed in reduction network in TDAC, or index in the chemical composition space for CSP analysis

r reaction r

s species s

Acronyms / Abbreviations

CFD Computational Fluid Dynamics

CSP Computational Singular Perturbation

DAC Dynamic Adaptive Chemistry

DNS Direct Numerical Simulation

DRG Directed Relation Graph

DRGEP DRG with Error Propagation

EDC Eddy Dissipation Concept

EFA Element Flux Analysis

EOA ellipsoid of accuracy

FEM Finite Volume Method

FPV Flamelet Progress Variable

HCCI Homogeneous Charge Compression Ignition

ISAT-RCCE *In situ* Adaptive Tabulation-Rate-Controlled Constrained Equilibrium

JHC jet-in-hot-coflow

LES Large Eddy Simulation

LFR Laminar Finite Rate

MILD Moderate or Intense Low oxygen Dilution

ODE Ordinary Differential Equation

PDF Probability Density Function

PFA Path Flux Analysis

PFR Plug Flow Reactor

PLIF planar laser-induced fluorescence

PSR Perfectly Stirred Reactor

QLFR Quasi-Laminar Finite Rate

RANS Reynolds Averaged Navier-Stokes

SIM slow invariant manifold

TSR Tangential Stretch Rate

Chapter 1

Introduction

1.1 Background

The present study is part of Marie Skłodowska-Curie CLEAN-Gas "European Joint Doctorate" programme. It is funded by the European Community through the Horizon 2020 Actions. The acronym CLEAN-Gas is the abbreviation for "Combustion for Low Emission Applications of Natural Gas".

Due to the availability and environmental and technological benefits of natural gas, it covers a significant proportion of the world energy landscape. However, as one of the fossil fuels, the energy conversion of natural gas is mainly achieved by combustion. The conventional combustion process induces two main side effects: the production of greenhouse gases (CO_2) and the emission of pollutant species such as nitrogen oxides (NO_x) and soot particles. Moreover, the availability of fossil fuel on the earth is limited. Facing the challenges of energy shortage and limited fossil fuel resources, as well as the increasing air pollution problems, the development of fuel flexible, efficient and environmentally friendly combustion technologies has become urgent. Novel combustion technologies with low emissions, high efficiency and fuel flexibility have become essential under the current challenges. One of the promising technology in energy production, transportation and manufacturing is Moderate or Intense Low oxygen Dilution (MILD) combustion which has gained increasing attention for the past few decades [4–6].

1.2 Non-conventional combustion regime

In industrial applications, MILD combustion is often achieved through strong flue gas recirculation by utilising high velocity fuel jets [7]. The resultant pre-heated mixture helps to

stabilize the flame and consequently, reduces combustion noise [4]. The chemistry reactivity is reduced because of dilution. As a result, a more uniform temperature field is obtained and thermal NO_x production is highly inhibited [4, 5]. Furthermore, more complete combustion can be achieved and the formation of pollutants such as CO [8, 9] and soot are strongly reduced [10, 11] as well.

MILD combustion technology has been demonstrated for many industrial applications. It was first introduced in industrial furnaces for methane combustion [12] and later extensively investigated for other gaseous fuels like hydrogen [13] and ethanol [14]. Cho et al. [15, 16] executed experiments and simulations on MILD oxidation burner, showing the effects of burner configuration and firing mode on efficiency and emissions. Sánchez et al. [17] evaluated an oxygen enhanced regenerative burner operated in MILD combustion mode. An energy recovery ratio above 80% and NO_x emissions below 5 ppm were achieved. Ye et al. [18] studied pre-vaporised liquid fuels burning in a reverse-flow MILD combustor under elevated pressures. They concluded that combustion stability is largely dependent on fuel type and NO_x emissions are highly influenced by the operating pressure, jet velocity and carrier gas. MILD technology can be utilized in gas turbines as well. Kruse et al. [19] conducted experimental and numerical studies on gas turbine under MILD condition, using gaseous fuels. The effect of pressure, mixing on combustion stability was analysed, indicating that mixing is the key parameter to control and stabilize MILD combustion. Recently, Xing et al. [14] evaluated the possibility of using liquid bio-fuels, diesel and kerosene fuels under MILD condition for gas turbine applications. They stated that MILD combustion can potentially substitute conventional gas turbine combustors. Furthermore, Adamczyk et al. [20] analysed the potential of oxy-MILD combustion for large scale pulverized coal boilers. Preliminary simulations showed the possibility of efficiency increase of more than 3%. There are also some other investigations focused on the applicability of MILD combustion under oxy-fuel conditions [21, 22], in order to further reduce the pollutants. The MILD combustion concept was extended to hybrid solar thermal devices, which combine concentrated solar radiation with combustion as well. According to Chinnici et al. [23], the integration of MILD combustion in a hybrid solar receiver can lead to increased thermal performances with respect to conventional combustion systems.

As a result of the reduced reactivity under MILD combustion conditions, the chemical time scale increases and the strong interaction between chemistry reaction and mixing makes the study of such flames more challenging than conventional combustion regimes. In order to decrease the influence of geometric complexity encountered in practical devices, simplified lab-scale axis-symmetric jet burners are generally used to emulate MILD conditions—for

example, the jet-in-hot-coflow (JHC) burner [24–27] and the lifted flame (Cabra flame) with vitiated coflow burner [28].

There are numerous studies on the JHC burners, both experimental and numerical [25, 29, 28, 30, 31, 24, 32, 33, 7, 34]. The JHC burner features a central jet and a secondary burner providing hot exhaust products as a coflow, reproducing the flue gas recirculation. Dally et al. [25] carried out experiments with planar laser-induced fluorescence (PLIF) and Rayleigh scattering techniques on this burner. The central jet fuel of CH_4/H_2 with molar fraction of 0.5/0.5 was used and the oxygen levels in the hot coflow were adjusted to 9%, 6% and 3% by mass. They concluded that the peak temperature increase in the reaction zone can get as low as 100 K, by reducing the oxygen level in the hot coflow; and the production of CO, NO and OH is suppressed with respect to conventional conditions. At the same time, they provided high fidelity mean and rms (root-mean-square) experimental data of temperature and various chemical species for numerical validation. Later, Medwell et al. [35, 30] revealed the distribution of hydroxyl radical (OH), formaldehyde (CH_2O), and temperature under the influences of hydrogen addition with PLIF and Rayleigh scattering. They stated that the independence of the reaction zone structure with hydrogen addition provides a possible evidence of using a wide variety of fuels in MILD combustion. They also observed a "lift-off" height based on the weak-to-strong transition of OH and pre-ignition is found in the apparent lifted region of these flames.

Up to now, experimental investigations on the lab-scale MILD combustion burners have been mostly concentrated on gaseous, simple hydrocarbon fuels. However, there are also a few studies [36, 37, 27, 38, 39] focusing on oxygenated fuels and long-chain alkanes. Even though there is high flexibility on the choice of fuel in MILD combustion [40], systems with more complex fuel types could lead to distinct behaviours, which influence the combustion stability [41–43]. Therefore, recently, Ye et al. [27] performed experimental investigations on n-heptane fuel with conventional photography and PLIF. They found that the n-heptane flame "lift-off" height (flame weak-to-strong transition height) changes monotonically with decreasing coflow oxygen level, which does not occur for other simple hydrocarbon fuels. Furthermore, the n-heptane flame transitional flame structure occurs with a much lower coflow oxygen content. After comparing the fuel pyrolysis process and heat release region with ethanol, they concluded that it is more difficult for n-heptane than ethanol to reach MILD combustion conditions.

Numerical investigations on burners with a hot coflow stabilizing the flame were carried out using Reynolds Averaged Navier-Stokes (RANS) [44–48, 7, 31, 49–52, 34, 53] simulation, Large Eddy Simulation (LES) [33, 54–56] and Direct Numerical Simulation (DNS) [57]; simple fuels such as methane, hydrogen and ethylene were the main focus. The

experimental and numerical studies on MILD combustion with simple fuels revealed some common signatures, such as the absence of the negative heat release region, the broadening of the heat production profile with a single peak in mixture fraction space and the suppression of pyrolytic reactions [58, 6]. However, using complex fuels such as oxygenated hydrocarbons and long-chain alkanes under MILD conditions has shown distinct features, like the appearance of visible flames and increased pollutant emissions, as indicated by previous studies [42, 59, 18].

1.3 Turbulence-chemistry interaction models

The distinguishing feature of MILD combustion is the very strong interactions between the fluid mixing and chemical kinetics, so that models based on the separation between turbulence and chemistry scales are not suitable to describe the complex interactions occurring in such a regime [60]. Therefore, models that account for finite-rate chemistry effects must be considered.

Different combustion models were evaluated by Shabanian et al. [48], Christo et al. [44], Parente el al. [13, 61], Fortunato et al. [62] and Galletti et al. [12] employing RANS simulation. In these approaches, the authors showed that the Eddy Dissipation Concept (EDC) [63–65] model can better handle the strong interactions between turbulence and chemistry with respect to the classic flamelet approach. The EDC model splits each computational cell into two regions: the fine structures, where reactions take place, and the surrounding fluid. In the original EDC formulation, the fine structures are modelled as Perfectly Stirred Reactors (PSRs). However, they are also modelled as Plug Flow Reactors (PFRs) in some software packages for numerical reasons [34, 66]. Beside the EDC model, the Partially Stirred Reactor (PaSR) [67] model, also based on the concept of cell splitting, is very promising for predicting MILD condition. In PaSR, the interaction between turbulence and chemistry is represented with a factor κ, which is defined as the ratio between the chemical time scale and the sum of mixing and chemical scales. In EDC model, a similar parameter is adopted: γ, whose definition depends solely on a mixing scale and an empirical constant C_γ [63–65]. In PaSR, both the chemical and mixing time scales are included in the model explicitly, allowing a more accurate description on turbulence/chemistry interactions. However, its performances strongly depend on the estimation of mixing and chemical time scales.

Regarding the evaluation of chemical and mixing time scales, Chomiak [68] estimated the chemical time scale using the fuel and oxidiser formation rates, and the mixing time from the geometric mean of integral and komogorov mixing time scales. Golovitchev et al. [69] proposed an approach in which the chemical time scale is estimated from forward

reaction rates only. Kärrholm [70] and Nordin [71] estimated the mixing time scale as a certain fraction of the integral one, using a mixing constant C_{mix} ranging from 0.001 to 0.3 [71]. Ferraroti and Li et al. [72, 53] proposed a dynamic (adaptive) estimation of the mixing time scale in PaSR using the ratio of the variance of mixture fraction and mixture fraction dissipation rate from the solution of three extra transport equations. Improvements on the predictions of species mass fractions and temperature were achieved with the dynamic method [72, 53] for Reynolds Averaged Navier-Stokes (RANS) simulations.

Despite high computational efficiency of RANS simulation, steady-state assumptions are not able to capture non-equilibrium phenomena, such as local extinction and re-ignition. To this end, LES can provide superior results with respect to RANS. Ihme et al. [54, 55] carried out LES on the JHC burner using a three-stream Flamelet Progress Variable (FPV) formulation. Good agreement with the experimental measurements was observed for the mean temperature and specie mass fraction profiles. The advanced flamelet based FPV model handles the interactions of turbulence and chemical reaction in JHC burner by introducing a progress variable (PV) and two mixture fractions. Afarin et al. [73] used PaSR to investigate the reaction zone structure as well as the distribution of temperature and minor species mass fractions, showing acceptable accuracy.

In MILD combustion, reaction can occur over a wide range of turbulent scales instead of the smallest scale in conventional combustion [74]. The system evolves towards a distributed reaction regime and low temperatures, because of the high dilution level and the intense mixing between fuel and hot-diluted oxidiser. This leads to characteristic Damköhler number of order $\sim$1 [4, 5]. Recently, it was shown that the κ in PaSR model approaches 1 in MILD combustion, suggesting that reacting structures can be resolved on the LES grid by using implicit LES combustion models [75]. Two implicit formulations were investigated in this thesis and compared with PaSR model, the Laminar Finite Rate (LFR) and the Quasi-Laminar Finite Rate (QLFR) formulations. In the LFR model, the mean source term is directly retrieved from the Arrhenius expression, while in the QLFR model, a time-splitting approach is used, solving an Ordinary Differential Equation (ODE) to describe the evolution of species mass fractions within the LES residence time [76].

1.4 Kinetics reduction and tabulation for finite-rate chemistry

In the finite-rate approach, the number of of species and reactions in a chemical mechanism grows with the number of carbon atoms in the fuel component. As a consequence, the CPU

time associated to chemistry resolution can be very significant, for industrial applications involving realistic fuels. In this framework, the use of pre-reduced or pre-tabulated chemical mechanisms may not be able to capture the dynamic phenomena like extinction and re-ignition accurately. Therefore, on-the-fly/dynamic chemistry reduction/tabulation methods are essential to alleviate the calculation burden for finite rate chemistry approaches. Various investigations based on the use of on-the-fly chemistry reduction techniques are reported in the literature. Tosatto [77] used a transport-flux-based Directed Relation Graph (DRG) model in a two-dimensional simulation of axisymmetric co-flow flames. A speed-up factor of about 5 was reported for a steady case, while a factor ranging from 10 to 20 was obtained for a time-dependent oscillating flame. Zhang et al. [78] and He et al. [79] conducted Homogeneous Charge Compression Ignition (HCCI) engine simulations with the Element Flux Analysis (EFA) approach. The size of kinetic scheme was significantly reduced, while maintaining reliable accuracy.

Dynamic reduction methods allow significant CPU savings; however, the cost associated to the direct ODE integration can be still significant, if the number of species in the reduced chemical mechanisms is non-negligible. Coupling with dynamic tabulation approach provides a solution to this issue. Tang et al.[80] combined chemistry dimension reduction and tabulation with a methodology called *In situ* Adaptive Tabulation-Rate-Controlled Constrained Equilibrium (ISAT-RCCE). The ISAT-RCCE calculations show good agreement with the accurate solution, and a significant speed-up factor of about 500 is obtained compared to the direct integration approach. Ren et al.[81] and Contino et al.[1] coupled Dynamic Adaptive Chemistry (DAC) approach with ISAT in engine simulations, achieving speed-up factors of the order of 100. The chemistry reduction model expedites the reaction sub-step in the operator-splitting scheme through local skeletal reduction, whereas ISAT expedites the calculations by reducing the number of direct ODE integrations through tabulating and re-using the solutions, thus making the use of detailed chemistry in Computational Fluid Dynamics (CFD) simulations more feasible [1].

1.5 Advanced post-processing tools

In MILD combustion, the relations between auto-ignition and flame propagation, local extinction and re-ignition are not well observed. To this end, the application of advanced post-processing tools on detailed CFD simulations are of great importance.

The computational singular perturbation (CSP) enables the definition of rigorous mathematical tools capable of extracting local information from chemically reactive flow fields. It takes advantage of an eigenmode decomposition of the chemical source term to determine

the intrinsic chemical time scales, a proper distinction between fast and slow scales, and the dimension of the slow invariant manifold (SIM), which is an attractive low-dimensional subspace where the system evolves according to the slow scales. The dimension of the SIM is related to the number of fast/exhausted chemical modes, being those giving a negligible net contribution to the dynamics, and it is a fair indicator of the actual local degrees of freedom of the chemical system under study.

The slow subspace, which is spanned by the slow modes, contains the active chemical scales, which can be either dissipative or explosive, characterizing an attractive dynamics towards the SIM and in turn equilibration, or a departing dynamics that drives the system away from equilibrium. The tangential stretching rate (TSR) is able to select, among the slow modes, those where the actual energy propagation takes place. The TSR approach, already employed for the characterization of laminar [82] and turbulent flames [83–85], is a representative of the driving chemical timescale, being either explosive or dissipative. In turn, proper indices are able to select the chemical reactions mostly participating to the dominant chemical eigenmodes, giving the opportunity to further characterize the underlying physics.

Chapter 2

Mathematical models

2.1 Turbulent combustion modeling using Computational Fluid Dynamics

In this section, the fundamental governing equations for reacting compressible flows for the Reynolds Averaged Navier-Stokes (RANS) simulation and Large Eddy Simulation (LES) are presented. The OpenFOAM® [86] Finite Volume Method (FVM) based, open-source CFD software is used for all simulations. The external OpenFOAM® based edcSMOKE combustion toolkit with the robust OpenSMOKE ODE chemistry solver for finite rate chemistry was adopted as well. The model equations solved by the code are shown in the following subsections.

2.1.1 RANS for turbulent combustion modeling

In RANS simulations, the density-based Favre-averaged (denoted with ˜) governing equations of mass, momentum and energy for low Mach number flow are solved [87] :

$$\frac{\partial \bar{\rho}}{\partial t} + \frac{\partial}{\partial x_j}\left(\bar{\rho}\tilde{u}_j\right) = 0, \tag{2.1}$$

$$\frac{\partial}{\partial t}\left(\bar{\rho}\tilde{u}_i\right) + \frac{\partial}{\partial x_j}\left(\bar{\rho}\tilde{u}_i\tilde{u}_j\right) = -\frac{\partial \bar{p}}{\partial x_i} + \frac{\partial}{\partial x_j}\left(\bar{\tau}_{ij} - \bar{\rho}\widetilde{u_i'' u_j''}\right), \tag{2.2}$$

$$\frac{\partial}{\partial t}\left(\bar{\rho}\tilde{h}\right) + \frac{\partial}{\partial x_i}\left(\bar{\rho}\tilde{h}\tilde{u}_i\right) - \overline{\frac{Dp}{Dt}} = \bar{\dot{\omega}}_T + \frac{\partial}{\partial x_i}\left[\overline{\lambda\frac{\partial T}{\partial x_i}} - \bar{\rho}\widetilde{u_i'' h''}\right] + \overline{\tau_{ij}\frac{\partial u_i}{\partial x_j}} - \frac{\partial}{\partial x_i}\left(\overline{\rho\sum_{s=1}^{N} V_{s,i} Y_s h_s}\right). \tag{2.3}$$

In Eqn. 2.1 - 2.3, ρ, $\mathbf{u}$, p represent the density, velocity and pressure respectively; h is the enthalpy; λ is the thermal conductivity. The term $\bar{\dot{\omega}}_T$ is the source term coming from combustion process. The turbulent Prandtl number Pr_t is introduced to close the enthalpy turbulent fluxes:

$$-\bar{\rho}\widetilde{u_i''h''} \approx \frac{\mu_t}{Pr_t}\frac{\partial \tilde{h}}{\partial x_i}. \tag{2.4}$$

In combustion processes, multiple species are involved. The Favre averaged transport equation of species Y_s reads:

$$\frac{\partial}{\partial t}\left(\bar{\rho}\widetilde{Y_s}\right) + \frac{\partial}{\partial x_j}\left(\bar{\rho}\widetilde{Y_s}\tilde{u}_j\right) = \frac{\partial}{\partial x_j}\left(\left(\bar{\rho}D_{m,s} + \frac{\mu_t}{Sc_t}\right)\frac{\partial \tilde{Y}_s}{\partial x_j}\right) + \bar{\dot{\omega}}_s, \tag{2.5}$$

where Sc_t is the turbulent Schmidt number and $D_{m,s}$ is the molecular diffusion coefficient for species s in the mixture. Because $Sc_t = \mu_t/(\rho D_t)$ (D_t is the turbulent diffusivity), the molecular diffusion can also be written as $Sc = \mu/(\rho D_m)$ (D_m is the molecular diffusivity) and therefore, $\rho D_m = \mu/Sc$. In some CFD codes, Sc_t is approximated to 1.0 [88]. Therefore, Eqn. 2.5 can be re-arranged as:

$$\frac{\partial}{\partial t}\left(\bar{\rho}\widetilde{Y_s}\right) + \frac{\partial}{\partial x_j}\left(\bar{\rho}\widetilde{Y_s}\tilde{u}_j\right) = \frac{\partial}{\partial x_j}\left((\mu + \mu_t)\frac{\partial \widetilde{Y_s}}{\partial x_j}\right) + \bar{\dot{\omega}}_s. \tag{2.6}$$

In Eqn. 2.6, $\mu + \mu_t$ is expressed as μ_{Eff} (the effective viscosity) in some CFD codes. In the present research, the molecular diffusion coefficient $D_{m,s}$ is included when species (like H_2) with non-uniform Lewis number is considered.

The standard k-ε turbulence model is often used in RANS simulation for its robustness. In the standard k-ε model, the unresolved turbulence stresses $\bar{\rho}\widetilde{u_i''u_j''}$ are modelled with the product of the eddy viscosity μ_t and mean flow strain rate S_{ij}. Finally, the eddy viscosity is estimated as:

$$\mu_t = \rho C_\mu \frac{\tilde{k}^2}{\tilde{\varepsilon}}. \tag{2.7}$$

In Equation 2.7, the constant C_μ equals to 0.09. The Favre-averaged turbulence kinetic energy $\tilde{k}$ and the dissipation rate $\tilde{\varepsilon}$ of the turbulence kinetic energy are solved via two separate transport equations [87]:

$$\frac{\partial}{\partial t}\left(\bar{\rho}\tilde{k}\right) + \frac{\partial}{\partial x_j}\left(\bar{\rho}\tilde{k}\tilde{u}_j\right) = \frac{\partial}{\partial x_j}\left(\left(\mu + \frac{\mu_t}{\sigma_k}\right)\frac{\partial \tilde{k}}{\partial x_j}\right) + 2\mu_t S_{ij}S_{ij} - \bar{\rho}\tilde{\varepsilon}, \tag{2.8}$$

$$\frac{\partial}{\partial t}\left(\bar{\rho}\tilde{\varepsilon}\right)+\frac{\partial}{\partial x_j}\left(\bar{\rho}\tilde{\varepsilon}\tilde{u}_j\right)=\frac{\partial}{\partial x_j}\left(\left(\mu+\frac{\mu_t}{\sigma_\varepsilon}\right)\frac{\partial\tilde{\varepsilon}}{\partial x_j}\right)+C_{\varepsilon 1}\bar{\rho}\frac{\tilde{\varepsilon}}{\tilde{k}}2\mu_t S_{ij}S_{ij}-C_{\varepsilon 2}\bar{\rho}\frac{\tilde{\varepsilon}^2}{\tilde{k}}, \tag{2.9}$$

in which S_{ij} represents the components of rate of deformation; σ_k, σ_ε, $C_{\varepsilon 1}$ and $C_{\varepsilon 2}$ are constants that by default equal to 1.0, 1.30, 1.45 and 1.90, respectively [89]. The standard k-ε model is robust, computationally fast and has the potential advantage of generality since it requires no direct empirical input such as a mixing-length specification. However, it has the well-known disadvantage of over-estimating the jet spread rate for axisymmetric jets. In order to correct the over-estimated calculation of the round jet decay, some modifications have been proposed, such as increasing the constant of $C_{\varepsilon 1}$ from 1.45 to 1.60 [89, 46, 7]. However, there is a lack of generality using such approach. In 1978, Pope [89] suggested a correction on the standard k-ε model, by adding an additional term to the kinetic energy dissipation rate transport equation:

$$Corr_{Pope}=C_{\varepsilon 3}\frac{\tilde{\varepsilon}^2}{\tilde{k}}\psi, \tag{2.10}$$

with $\psi=\omega_{ij}\omega_{jk}S_{ki}$, measuring the vortex stretching with the rate of strain tensor S_{ij} and rotation tensor ω_{ij}:

$$S_{ij}=\frac{1}{2}\frac{\tilde{k}}{\tilde{\varepsilon}}\left(\frac{\partial U_i}{\partial x_j}+\frac{\partial U_j}{\partial x_i}\right), \tag{2.11}$$

$$\omega_{ij}=\frac{1}{2}\frac{\tilde{k}}{\tilde{\varepsilon}}\left(\frac{\partial U_i}{\partial x_j}-\frac{\partial U_j}{\partial x_i}\right). \tag{2.12}$$

2.1.2 LES for turbulent combustion modeling

In LES, the Favre-filtered (denoted with ˜) governing equations of continuity, momentum, species and energy are solved [90]:

$$\frac{\partial\bar{\rho}}{\partial t}+\frac{\partial}{\partial x_i}\left(\bar{\rho}\tilde{u}_i\right)=0, \tag{2.13}$$

$$\frac{\partial}{\partial t}\left(\bar{\rho}\tilde{u}_i\right)+\frac{\partial}{\partial x_i}\left(\bar{\rho}\tilde{u}_i\tilde{u}_j\right)=-\frac{\partial\bar{p}}{\partial x_j}+\frac{\partial}{\partial x_i}\left[\bar{\tau}_{ij}-\bar{\rho}\left(\widetilde{u_iu_j}-\tilde{u}_i\tilde{u}_j\right)\right]. \tag{2.14}$$

$$\frac{\partial}{\partial t}\left(\bar{\rho}\widetilde{Y_s}\right)+\frac{\partial}{\partial x_i}\left(\bar{\rho}\widetilde{Y_s}\tilde{u}_i\right)=\frac{\partial}{\partial x_i}\left[\overline{V_{s,i}Y_s}-\overline{\rho}\left(\widetilde{u_iY_s}-\tilde{u}_i\widetilde{Y_s}\right)\right]+\bar{\dot{\omega}}_s, \tag{2.15}$$

$$\frac{\partial}{\partial t}\left(\bar{\rho}\tilde{h}\right)+\frac{\partial}{\partial x_i}\left(\bar{\rho}\tilde{h}\tilde{u}_i\right)-\overline{\frac{Dp}{Dt}}=\frac{\partial}{\partial x_i}\left[\overline{\lambda\frac{\partial T}{\partial x_i}}-\overline{\rho}\left(\widetilde{u_i h}-\widetilde{u}_i\widetilde{h}\right)\right]+\overline{\tau_{ij}\frac{\partial u_i}{\partial x_j}}-\frac{\partial}{\partial x_i}\left(\overline{\rho\sum_{s=1}^{N}V_{s,i}Y_s h_s}\right)+\bar{\omega}_T. \tag{2.16}$$

In Eqn. 2.16, λ is the thermal conductivity. The terms $\overline{V_{s,i}Y_s}$ and $\overline{\lambda\frac{\partial T}{\partial x_i}}$ are filtered laminar diffusion fluxes for species and enthalpy, modelled through a simple gradient assumption.

The unresolved Reynolds stresses:

$$\overline{\mathrm{T}_{ij}}=\left(\widetilde{u_i u_j}-\widetilde{u}_i\widetilde{u}_j\right), \tag{2.17}$$

require a turbulence model. The one equation eddy-viscosity (`oneEqnEddy` in OpenFOAM) model was chosen in the present thesis as the sub-grid turbulence model [91]. In one equation eddy-viscosity model, $\overline{\mathrm{T}_{ij}}$ is estimated by an subgrid-scale eddy viscosity ν_{sgs} and a resolved scale strain rate $\overline{S}_{ij}$:

$$\overline{\mathrm{T}_{ij}}=-2\nu_{sgs}\overline{S}_{ij}+\frac{1}{3}\tau_{ii}^{sgs}\delta_{ij}. \tag{2.18}$$

The sub-grid scale viscosity is computed as:

$$\nu_{sgs}=C_k\sqrt{k_{sgs}}\Delta, \tag{2.19}$$

where $C_k=0.094$, Δ is the grid size and k_{sgs} is the sub-grid scale kinetic energy which is solved through a dedicated transport equation [92]:

$$\frac{\partial(\rho k_{sgs})}{\partial t}+\frac{\partial(\rho\overline{u}_j k_{sgs})}{\partial x_j}-\frac{\partial}{\partial x_j}\left[\rho\left(\nu+\nu_{sgs}\right)\frac{\partial k_{sgs}}{\partial x_j}\right] \tag{2.20}$$

$$=-\rho\,\tau_{ij}:\overline{S}_{ij}-C_\varepsilon\frac{\rho k_{sgs}^{3/2}}{\Delta}, \tag{2.21}$$

in which the operator : is a double inner product and C_ε is a constant which equals to 1.048.

2.2 Eddy Dissipation Concept model

In the species transport equations (Eqn. 2.5 and 2.15), the mean source term $\bar{\omega}_s$ of chemical species shall be modelled with a combustion model.

The Eddy Dissipation Concept (EDC) combustion model separates each computational cell into two zones. One zone is indicated as “fine structures” and another one “surrounding

fluid". It assumes that combustion takes place in the fine structures where the dissipation of the flow turbulence kinetic energy occurs. In the original model by Magnussen [63], the fine structures are modelled as Perfectly Stirred Reactors (PSR). However, some software packages (for example, ANSYS Fluent [66]) treat them as Plug Flow Reactors (PFR), mainly for numerical reasons. A conceptual drawing of the EDC model is presented in Figure 2.1.

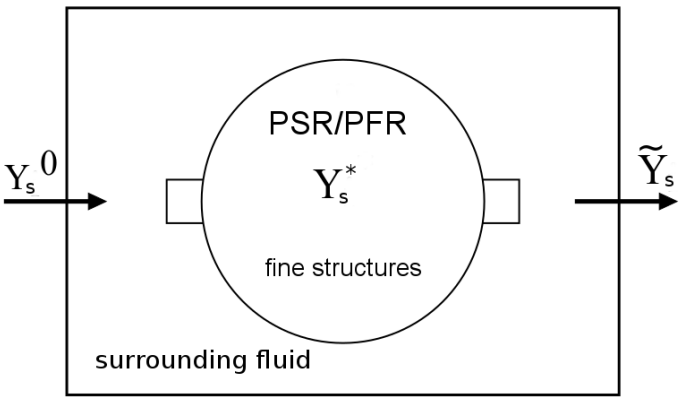

Fig. 2.1 Conceptual drawing of the EDC model.

EDC is based on a cascade model providing the mass fraction of the fine structures, γ_λ, and the mean residence time of the fluid within the fine structures τ^*, as a function of the flow characteristic scales:

$$\gamma_\lambda = C_\gamma \left(\frac{\nu \tilde{\varepsilon}}{\tilde{k}^2} \right)^{\frac{1}{4}}, \tag{2.22}$$

$$\tau^* = C_\tau \left(\frac{\nu}{\tilde{\varepsilon}} \right)^{\frac{1}{2}}. \tag{2.23}$$

In Eqn. 2.22 and Eqn. 2.23, ν is the kinematic viscosity, $C_\gamma = 2.1377$ and $C_\tau = 0.4083$ are constants in the EDC model [65]. The mean reaction rate (source term in the species transport equation) is expressed as [64]:

$$\overline{\dot{\omega}}_s = -\frac{\bar{\rho}\gamma_\lambda^2}{\tau^* \left(1 - \gamma_\lambda^3\right)} \left(\widetilde{Y}_s - Y_s^* \right). \tag{2.24}$$

The term $\widetilde{Y}_s$ in Eqn. 2.24 denotes the mean mass fraction of the species s between the fine structures and the surrounding fluid and Y_s^* is the mass fraction of species s in the fine

structures. The mean mass fraction $\widetilde{Y}_s$ can be expressed as a function of Y_s^* and Y_s^0 (mass fraction of species s in the surrounding fluid):

$$\widetilde{Y}_s = \gamma_\lambda^3 Y_s^* + (1-\gamma_\lambda^3) Y_s^0. \tag{2.25}$$

The expressions of the species mean reaction rate and mean mass fraction in Eqn. 2.24 and Eqn. 2.25 were proposed by Gran et al. in 1996 [64], thus it is denoted as "EDC1996".

In the earlier version of the EDC model, proposed originally by Magnussen in 1981 [63], the mean reaction rate of species s was given by

$$\overline{\dot{\omega}}_s = -\frac{\bar{\rho}\gamma_\lambda^3}{\tau^*\left(1-\gamma_\lambda^3\right)}\left(\widetilde{Y}_s - Y_s^*\right). \tag{2.26}$$

This formulation is referred as "EDC1981". Later in 2005, Magnussen modified the model [65], expressing $\overline{\dot{\omega}}_s$ as:

$$\overline{\dot{\omega}}_s = -\frac{\bar{\rho}\gamma_\lambda^2}{\tau^*\left(1-\gamma_\lambda^2\right)}\left(\widetilde{Y}_s - Y_s^*\right), \tag{2.27}$$

and mean mass fraction $\widetilde{Y}_s$ as:

$$\widetilde{Y}_s = \gamma_\lambda^2 Y_s^* + (1-\gamma_\lambda^2) Y_s^0. \tag{2.28}$$

This version of EDC model is denoted as "EDC2005".

In all three formulations, the mean mass fraction $\widetilde{Y}_s$ is obtained by solving the species transport equation. The mass fraction of each species inside the fine structure Y_s^* is computed with the finite-rate chemistry approach.

2.2.1 Finite-rate chemistry approach

The mass fraction Y_s^* of species s inside the fine structures is evaluated by modelling them to a Perfectly Stirred Reactor (PSR) [64]:

$$\frac{\dot{\omega}_s^*}{\rho^*} = \frac{1}{\tau^*}\left(Y_s{}^* - Y_0\right), \tag{2.29}$$

in which $\dot{\omega}_s^*$ is the formation rate of species s. Alternatively, the fine structures can be modelled as Plug Flow Reactors (PFR), evolving in a characteristic time equal to τ^*:

$$\frac{dY_s}{dt} = \frac{\dot{\omega}_s}{\rho}. \tag{2.30}$$

The final integration over $\frac{dY_s}{dt}$ is Y_s^*. The term $\dot{\omega}_s$ is the instantaneous formation rate of species s coming from a detailed kinetic mechanism. The initial condition for the species composition space provided to the PSR and PFR reactors are different. For PSR, the surrounding fluid value Y_0 is used. The term Y_0 can be obtained from Eqn. 2.28. While for PFR, the mean species mass fraction $\widetilde{Y}_s$ is directly used.

2.2.2 Limitation of fine structure fraction

In the EDC model, the chemical reaction process and mixing are interconnected. This mixing process time scale τ_{mix} should be larger or equal to the fine structures residence time scale τ^*. Defining R as the ratio [32]:

$$R = \frac{\tau^*}{\tau_{mix}} = \frac{\gamma_\lambda^2}{1-\gamma_\lambda^3}, \tag{2.31}$$

one can find the limit value for γ_λ. The ratio R and γ_λ limits for the various EDC formulations can be found in Table 2.1.

Table 2.1 Limitations of fine structure fraction

EDC version	time scale ratio	γ_λ limit
$'$EDC1981$'$	$\frac{\gamma_\lambda^3}{1-\gamma_\lambda^3}$	0.7937
$'$EDC1996$'$	$\frac{\gamma_\lambda^2}{1-\gamma_\lambda^3}$	0.7549
$'$EDC2005$'$	$\frac{\gamma_\lambda^2}{1-\gamma_\lambda^2}$	0.7071

2.3 Partially Stirred Reactor model

2.3.1 Conventional PaSR model

The theory behind PaSR model [67, 69] is actually very similar to the EDC model: each computational cell is split into two locally uniform zones: one where reactions take place, and another characterized by only mixing. The parameter κ is used to represent the mass fraction of the reaction zone in the computational cell. It can be estimated as [70]:

$$\kappa = \frac{\tau_c}{\tau_c + \tau_{mix}}, \tag{2.32}$$

where τ_c and τ_{mix} are the characteristic chemical and mixing time scales in each cell, respectively. They can be estimated following different approaches, as detailed later in this section.

The mean source term provided to the species transport equation can be expressed as:

$$\overline{\dot{\omega}}_s = \kappa \frac{\widetilde{\rho}\left(Y_s^* - Y_s^0\right)}{\tau^*}, \tag{2.33}$$

where τ^* represents the residence time in the reactive structure. In the present work, τ^* equals to the mixing time scale. In order to get the value of Y_s^*, a time-splitting approach is applied, as explained in Section 2.2.1.

Evaluation of chemical time scale

Chemical time scale estimation from Jacobian matrix eigenvalues For the evaluation of chemical time scale, Fox [93, 94] suggested using the eigenvalues of the Jacobian matrix **J** of the chemical source terms. The Jacobian matrix **J** has the dimension of $s \times s$, where s is the number of chemical species in the mechanism. After the decomposition of the Jacobian matrix, the chemical time scale is estimated with the inverse of the eigenvalues λ_s:

$$\tau_{c,s} = \frac{1}{|\lambda_s|}. \tag{2.34}$$

In Eqn. 2.34, $\tau_{c,s}$ is the characteristic time scale of species s. After removing the dormant species (characterised by infinite time scale values), the largest chemical time scale can be chosen as leading scale for the evaluation of the PaSR parameter κ.

Chemical time scale estimation from formation rates The decomposition of the source term Jacobian matrix is accurate but time consuming, especially when large chemical mechanisms are used. The formation rate based characteristic time scale evaluation is a simplified approach. Instead of getting the chemical time scale for each species from the Jacobian matrix decomposition, the ratio of species mass fraction and formation rate in the reactive structure is directly used [68, 34], approximating the Jacobian diagonal terms:

$$\tau_{c,s} = \frac{Y_s^*}{|dY_s^*/dt|}. \tag{2.35}$$

Chemical time scale estimation from reaction rates Another simplified method is based on the reaction rate. Here, the characteristic time scale for each species i is expressed as [69]:

$$\tau_{c,i} = \frac{n_r * cTot^*}{\sum_{n=1}^{n_r}((dc^*_{n_r,forward}/dt) * \nu_{n_r,sum})}, \tag{2.36}$$

where n_r is the number of reactions, and $cTot^*$ is the total concentration obtained from the ideal gas law. Only the forward reaction rate $dc^*_{n_r,forward}/dt$ is used here. The term $\nu_{n_r,sum}$ represents the sum of the product stoichiometric coefficients.

The three methods for evaluating chemical time scale can be both used in RANS and LES simulations.

Determination of mixing time scale

Kolmogorov time scale In conventional combustion systems, it is often assumed that reactions happen at the dissipation scales, of the order of the Kolmogorov one, $\tau_{mix_K} = \sqrt{\nu/\varepsilon}$ [7], where ν is the kinematic viscosity and ε is the turbulence kinetic energy dissipation rate. However, in MILD combustion, reactions can occur over a wide range of flow scales [5], and the use of the Kolmogorov mixing time scale could lead to inaccurate predictions of temperature and species mass fractions [95].

Integral time scale Another characteristic time scale in turbulent flow is the eddy break-up time leading from large-scale to Kolmogorov-scale non-uniformities [68], which is also referred to as integral time scale, $\tau_{mix_I} = \frac{k}{\varepsilon}$, where k is the turbulence kinetic energy.

Geometric mean of Kolmogorov and integral time scales To provide a more accurate evaluation of the mixing time, Borghi [96] proposed to consider the whole spectrum of time scales. A simple approach to achieve this is to take only the two most important time scales, via the geometrical mean of the Kolmogorov and integral time scales [68], that is:

$$\tau_{mix_{Mean}} = \sqrt{\tau_{mix_K}\tau_{mix_I}} = \sqrt{\frac{k}{\varepsilon}\left(\frac{\nu}{\varepsilon}\right)^{1/2}}. \tag{2.37}$$

Mixing time scale in LES The above mentioned ways for determining mixing time scale are generally used in RANS simulations. In LES, a mixing time scale is represented with the geometrical mean of the sub-grid velocity stretching time (Δ/v') and the Kolmogorov time scale ($(\nu/\varepsilon_{sgs})^{1/2}$) [97]:

$$\tau_{mix_{LES}} = \sqrt{\frac{\Delta}{v'}\frac{\nu}{(\varepsilon_{sgs})^{1/2}}}. \tag{2.38}$$

The four approaches for the evaluation of mixing time scale can be summarized as global methods. The choice of mixing time scale with global approaches vary from case to case,

there is no universal solution. A dynamic, or in another word, adaptive determination of the mixing time scale with the estimation of the scalar variance and dissipation rate can be more widely applied and it is introduced in Section 2.3.2. The PaSR model with such approach of obtaining the mixing time scale is also termed as dynamic PaSR model.

2.3.2 Dynamic PaSR model

The dynamic estimation of the mixing time scale is introduced in this subsection. It is based on the estimation of the scalar variance, $\widetilde{\phi''^2}$, to the scalar dissipation rate, $\widetilde{\varepsilon_\phi}$ [98] ratio:

$$\tau_{mix_{Dynamic}} = \frac{\widetilde{\phi''^2}}{\widetilde{\varepsilon_\phi}}. \tag{2.39}$$

The mixture fraction f is selected to describe the mixing process of a scalar. Therefore, the scalar variance and dissipation rate take the form of the mixture fraction variance ($\widetilde{f''^2}$) and mixture fraction dissipation rate ($\widetilde{\chi}$).

Dynamic PaSR model in RANS

In RANS, favre-averaged $\widetilde{f}$, $\widetilde{f''^2}$ and $\widetilde{\chi}$ are modelled with the following transport equations [3, 2, 72]:

$$\frac{\partial \bar{\rho}\widetilde{f}}{\partial t} + \frac{\partial \bar{\rho}\widetilde{u}_j\widetilde{f}}{\partial x_j} = \frac{\partial}{\partial x_j}\Big(\rho(D+D_t)\frac{\partial \widetilde{f}}{\partial x_j}\Big), \tag{2.40}$$

$$\frac{\partial \bar{\rho}\widetilde{f''^2}}{\partial t} + \frac{\partial \bar{\rho}\widetilde{u}_j\widetilde{f''^2}}{\partial x_j} = \frac{\partial}{\partial x_j}\Big(\rho(D+D_t)\frac{\partial \widetilde{f''^2}}{\partial x_j}\Big) + 2\rho D_t\Big(\frac{\partial \widetilde{f}}{\partial x_j}\Big)^2 - \bar{\rho}\widetilde{\chi}, \tag{2.41}$$

$$\begin{aligned}\frac{\partial \rho\widetilde{\chi}}{\partial t} + \frac{\partial \rho\widetilde{u}_j\widetilde{\chi}}{\partial x_j} &= \frac{\partial}{\partial x_j}\Big(\rho(D+D_t)\frac{\partial \widetilde{\chi}}{\partial x_j}\Big) - C_1\bar{\rho}\frac{\widetilde{\chi}^2}{\widetilde{f''^2}} \\ &-C_2\bar{\rho}^2\frac{C_\mu\widetilde{k}}{\mu_t}\widetilde{\chi} + C_3\frac{\bar{\rho}C_\mu\widetilde{k}}{Sc_t}\left(\frac{\partial \widetilde{f}}{\partial x_j}\right)^2 + C_4\mu_t\frac{\widetilde{\chi}}{\widetilde{k}}|\widetilde{S}|^2.\end{aligned} \tag{2.42}$$

In Eqn. 2.42, C_1, C_2, C_3 and C_4 are model constants. A comprehensive review about the scalar dissipation rate transport equation constants is reported in Table 2.2, in which $R_\tau = (k/\varepsilon)/(\widetilde{f''}/\chi)$ is the mechanical to scalar time scale ratio. Moreover, another four sets of values were proposed by Ye [3], as shown in Table 2.3.

Table 2.2 Coefficients of the scalar dissipation rate equation by various authors [2]

Author	C_1	C_2	C_3	C_4
Chen [99]	1.15	0.65	0.5	1.45
Jones and Musonge [100]	1.0	0.9	$1.7R_\tau^{-1}$	1.45
Sommer et al. [101]	1.1	0.8	0.9	0.72

Table 2.3 Model constants for the scalar dissipation rate transport equations [3].

Case	C_1	C_2	C_3	C_4
1	2.0	1.8	1.7	1.4
2	1.0	1.8	3.4	1.4
3	2.0	1.8	3.4	1.4
4	1.0	1.8	1.7	1.4

Dynamic PaSR model in LES

In LES of reacting flows, transport equation for scalar dissipation rate $\widetilde{\chi}$ requires additionally closures for the gradients of diffusivity and density [102]. To limit the appearance of unclosed terms, instead, $\widetilde{|\nabla f|^2}$ is solved, by using Eqn. 2.43 [102]:

$$\begin{aligned}
\frac{D}{D_t}\left(\overline{\rho}\widetilde{|\nabla f|^2}\right) = &\frac{\partial}{\partial x_j}\left(\overline{\rho}(\widetilde{D}_f + D_t)\frac{\partial}{\partial x_j}(\widetilde{|\nabla f|^2})\right) \\
&- 2\overline{\rho}\left(\frac{\partial \widetilde{u}_i}{\partial x_j}\frac{\partial \widetilde{f}}{\partial x_i}\frac{\partial \widetilde{f}}{\partial x_j}\right) \\
&- 2\overline{\rho}\widetilde{D}_f\left(\frac{\partial^2 \widetilde{f}}{\partial x_i \partial x_j}\right)^2 \\
&- \frac{2}{\overline{\rho}}\frac{\overline{\rho}}{\partial x_i}\frac{\widetilde{f}}{\partial x_i}\left(\frac{\partial}{\partial x_j}\left(\overline{\rho}\widetilde{D}_f\frac{\partial}{\partial x_j}(\widetilde{f})\right)\right) \\
&+ 2\frac{\partial(\overline{\rho}\widetilde{D}_f)}{\partial x_i}\frac{\partial \widetilde{f}}{\partial x_i}\left(\frac{\partial^2 \widetilde{f}}{\partial x_j \partial x_j}\right) \\
&+ 2\frac{\partial \widetilde{f}}{\partial x_i}\frac{\partial \widetilde{f}}{\partial x_j}\left(\frac{\partial^2(\overline{\rho}\widetilde{D}_f)}{\partial x_i \partial x_j}\right) \\
&+ C_{prd}\cdot\overline{\rho}\cdot\frac{32\cdot\nu_t}{\Delta^2}\cdot\left(\widetilde{|\nabla f|^2} - |\nabla\widetilde{f}|^2\right) \\
&- C_{dis}\cdot\overline{\rho}\cdot\frac{\widetilde{D}_f}{\widetilde{f''^2_{sfs}}}\left(\widetilde{|\nabla f|^2} - |\nabla\widetilde{f}|^2\right)^2,
\end{aligned} \tag{2.43}$$

in which D_f is the scalar diffusivity and $\widetilde{f''^2_{sfs}}$ denotes the sub-filter variance of mixture fraction. In Eq. 2.43, $C_{prd} = 1.0$ and C_{dis} is determined by the sub-filter scalar variance coefficient: $C_{dis} = 12C_{var}$. In the present approach, C_{var} is evaluated with [102]:

$$C_{var} = \widetilde{f''^2_{sfs}}/(\Delta^2|\nabla\widetilde{f}|^2). \tag{2.44}$$

The scalar dissipation rate is then calculated as $\widetilde{\chi} = 2D_f\widetilde{|\nabla f|^2}$. Again, because of numerical issues, the sub-filter mixture fraction variance $\widetilde{f''^2_{sfs}}$ is not directly solved with a transport equation as what is often done in RANS. Instead, Eqn. 2.45 is used:

$$\widetilde{f''^2_{sfs}} \equiv \widetilde{f^2} - (\widetilde{f})^2. \tag{2.45}$$

The term $\widetilde{f^2}$ is then obtained from solving a transport equation:

$$\frac{D}{D_t}\left(\overline{\rho}\widetilde{f^2}\right) = \frac{\partial}{\partial x_j}\left(\overline{\rho}(\widetilde{D}_f + D_t)\frac{\partial}{\partial x_j}(\widetilde{f^2})\right) - \rho\widetilde{\chi}, \tag{2.46}$$

and the filtered mixture fraction transport equation shall be solved to get $\widetilde{f}$:

$$\frac{\partial\bar{\rho}\widetilde{f}}{\partial t} + \frac{\partial\bar{\rho}\widetilde{u}_j\widetilde{f}}{\partial x_j} = \frac{\partial}{\partial x_j}\left(\rho(D_f + D_t)\frac{\partial\widetilde{f}}{\partial x_j}\right). \tag{2.47}$$

In the end, the dynamic mixing time scale in LES has form of:

$$\tau_{mix_{DynamicLES}} = \frac{\widetilde{f''^2}}{\widetilde{\chi}} = \frac{\widetilde{f^2} - (\widetilde{f})^2}{2D_f\widetilde{|\nabla f|^2}}. \tag{2.48}$$

2.4 Implicit combustion closures for LES

To investigate the influence of turbulence combustion closures in MILD combustion regime, two implicit closures were developed, the later gets the filtered source term directly from the chemical term, without inclusion of the turbulent effect. The implicit closures were benchmarked to the PaSR approach.

2.4.1 Quasi-Laminar Finite Rate model

Based on the PaSR model, the QLFR model is formulated merely by forcing $\kappa = 1.0$ [103], under the hypothesis that the mixing time scale is much smaller than the chemical time scale. Therefore, the turbulent eddies are assumed to be able to penetrate into the flame structures and the whole cell is treated as a Perfectly Stirred Reactor (PSR) [75]. The mean source term is then expressed as:

$$\overline{\dot{\omega}}_s = \frac{\widetilde{\rho}\left(Y_s^* - Y_s^0\right)}{\tau^*}. \tag{2.49}$$

As far as the CPU requirements are concerned, the QLFR model allows saving additional time compared to PaSR model, as it does not need any chemical time scale estimation for the evaluation of κ.

2.4.2 Laminar Finite Rate model

For the LFR model, the mean formation rates are determined by Arrhenius expressions [104]:

$$\overline{\dot{\omega}}_s = M_s \sum_{r=1}^{N_r} \hat{R}_{s,r}. \tag{2.50}$$

In Equation 2.50, M_s is the molecular weight of species s and $\hat{R}_{s,r}$ is the Arrhenius rate of creation/destruction of species s in reaction r. The LFR model is generally used for laminar reacting flows [105] or in the context of Direct Numerical Simulation (DNS). In LES applications, the LFR model is valid when the grid size is sufficiently small and the flame structure is thick enough (low Damköhler number system). It is worth mentioning that the direct coupling of source terms without a time splitting scheme imposes to use smaller time steps with respect to the one required from the PaSR and QLFR models, to ensure simulation stability. Nevertheless, this approach might be preferred when very large chemical mechanisms are used, as ODE integration will then require much more CPU hour.

2.5 Flamelet Progress Variable model in RANS

Based on the assumption of the flamelet model [106], which considers a turbulent diffusion flame as an ensemble of laminar flamelets, the steady FPV model obtains the composition space from solving scalar transport equations of mixture fraction f and progress variable C [107]:

$$\frac{\partial \bar{\rho}\widetilde{f}}{\partial t} + \nabla \cdot \bar{\rho}\widetilde{\mathbf{u}}\widetilde{f} = \nabla \cdot \left[\bar{\rho}(\widetilde{D}_f + D_t)\nabla\widetilde{f}\right], \tag{2.51}$$

$$\frac{\partial \bar{\rho}\widetilde{C}}{\partial t} + \nabla \cdot \bar{\rho}\widetilde{\mathbf{u}}\widetilde{C} = \nabla \cdot \left[\bar{\rho}(\widetilde{D}_C + D_t)\nabla\widetilde{C}\right] + \bar{\rho}\,\widetilde{\omega}_C, \tag{2.52}$$

where D_t is the turbulent diffusivity and the $\widetilde{}$ denotes the favre averaged values. The favre averaged specie mass fraction $\widetilde{y}_i$ and chemical source term $\widetilde{\omega}_C$ are calculated by integrating laminar composition state from flamelet library over the joint PDF of f and C:

$$\widetilde{y}_i = \int y_i(f,C)\,\widetilde{P}(f,C)\,df dC, \tag{2.53}$$

$$\widetilde{\omega}_C = \int \omega_C(f,C)\,\widetilde{P}(f,C)\,df dC. \tag{2.54}$$

The joint Probability Density Function (PDF) $\widetilde{P}(f,C)$ is modelled by:

$$\widetilde{P}(f,C) = \widetilde{P}(C|f)\,\widetilde{P}(f), \tag{2.55}$$

where $\widetilde{P}(f)$ is described by a beta PDF and $\widetilde{P}(C|f)$ is determined by a delta function:

$$\widetilde{P}(C|f) = \delta(C - \widetilde{C|f}). \tag{2.56}$$

The definition of Progress Variable (PV) C is defined using the mass fraction of CO, CO_2 and H_2O in the current research.

2.6 Chemistry reduction methods

A number of dynamic chemistry reduction/tabulation methods were investigated and benchmarked in the present thesis. The reduction and tabulation approach Tabulated Dynamic Adaptive Chemistry (TDAC), which couples a modified *In-situ* Adaptive Tabulation (ISAT) [108] algorithm and chemical mechanism reduction methods [109, 1, 110–113], including Directed Relation Graph (DRG) [114], DRG with Error Propagation (DRGEP) [115], Dynamic Adaptive Chemistry (DAC) [116], Elementary Flux Analysis (EFA) [117] and Path Flux Analysis (PFA) [118], was used. The TDAC process is visualised in Figure 2.2. ISAT stores the initial composition and the solution of the ODE integration with so-called "leafs" and retrieves them with a linear approximation when the composition space is within an ellipsoid of accuracy (EOA), avoiding the need for a direct integration. When ISAT needs growth or addition instead of retrieve, it provides first the composition ψ^q to the mechanism reduction method, which simplifies the mechanism and provides a reduced set of species compositions ψ_a^q to the ODE solver. The solver computes the reaction mapping $\mathbf{R}(\psi_a^q)$, and then ISAT builds the full reaction mapping $\mathbf{R}(\psi^q)$ from $\mathbf{R}(\psi_a^q)$ [1]. If the differences between the existing

and newly build reaction mappings are within the user-defined tolerance of ε_{ISAT}, the EOA will grow to include the new mapping. Otherwise, a new "leaf" will be added to include the newly computed mappings. Furthermore, a time-step specific scale factor is defined, to give more control on the time-step variations [119].

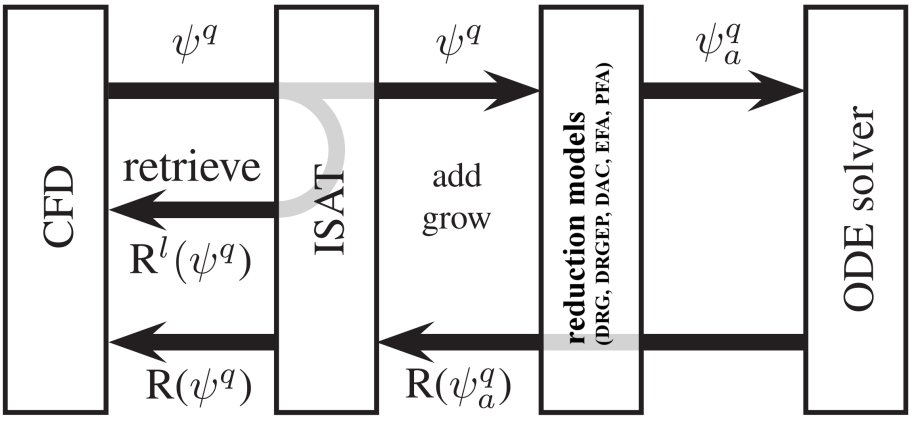

Fig. 2.2 Tabulation of Dynamic Adaptive Chemistry (TDAC) method flow chart. Adjusted from Contino et al. [1].

The five different reduction approaches (DRG, DRGEP, DAC, PFA and EFA) implemented in the TDAC code are all based on a network graph assumption, in which the relationship between various species or reactions are linked with weights. A reduction error ε_{RED} is evaluated when a species or reaction is removed and it is compared with the maximum acceptable value ε_{REDmax}, pre-defined by the user. If ε_{RED} is larger than the maximum error ε_{REDmax}, this means that the species/reaction is important for the network graph and cannot be removed. The DRG, DRGEP and PFA methods that were initially developed for mechanism pre-processing, have been adapted for dynamic reduction in TDAC method [1, 110–112].

In DRG [114] , the error ε_{RED} is expressed via an interaction coefficient r_{AB} representing the contribution of species B to the production rate of species A:

$$\varepsilon_{RED} = r_{AB} = \frac{\sum_{r=1,n_R} \mid \nu_{A,r}\omega_r\delta_{Br} \mid}{\sum_{r=1,n_R} \mid \nu_{A,r}\omega_r \mid}, \tag{2.57}$$

where $\nu_{A,r}$ is the stoichiometric coefficient of species A, ω_r represents reaction rate in each reaction, n_R is the number of reactions and δ_{Br} is defined as:

$$\delta_{Br} = \begin{cases} 1, & \text{if the } r\text{th elementary reaction involves species B,} \\ 0, & \text{otherwise.} \end{cases} \tag{2.58}$$

Later, Pepiot-Desjardins and Pitsch [115] proposed the DRG with Error Propagation (DRGEP) model. They argued that a more accurate way to consider the contribution of species B to species A is to use the net contribution instead of evaluating production and consumption individually. Therefore, a new definition of the direct interaction coefficient is introduced:

$$r_{AB} = \frac{|\sum_{r=1,n_R} \nu_{A,r}\omega_r\delta_{Br}|}{max(P_A, C_A)}, \tag{2.59}$$

in which P_A and C_A denote the production and consumption of species A, respectively. They are expressed with:

$$P_A = \sum_{r=1,n_R} max(0, \nu_{A,r}\omega_r), \tag{2.60}$$

and

$$C_A = \sum_{r=1,n_R} max(0, -\nu_{A,r}\omega_r). \tag{2.61}$$

Furthermore, the effect of removing a group of species (previously plus the present removed species) is also included. Most importantly, the notion of error propagation is brought up in the DRGEP approach. If the error r_{AB} is going to be evaluated, the longer the path of such error propagates to reach A, the smaller the effect will be. Therefore, from B to A, the length of the path that the error has to propagate is considered:

$$r_{AB,p} = \prod_{s=1}^{n_p-1} r_{S_sS_{s+1}}. \tag{2.62}$$

Instead, only the weakest contribution is taken in DRG:

$$r_{AB,p} = \min_{s=1}^{n_p-1} r_{S_sS_{s+1}}. \tag{2.63}$$

In Eqn. 2.62 and Eqn. 2.63, $S_1 = A$, $S_n = B$ and p denotes a certain path that links two species A and B. Finally,

$$\varepsilon_{RED} = r_{AB} = \max_{\text{all paths p}} r_{AB,p}. \tag{2.64}$$

The DAC method implemented in TDAC code is very similar to the DRGEP approach discussed above, except that the contribution of removing a group of species is neglected [116, 109]. Regarding the PFA model, based on the DRG and DRGEP methods, both the directly linked (first generation) and in-directly linked (higher generation) species contributions are evaluated [118], resulting in an interaction coefficient r_{AB} with information from multiple generations. For the EFA approach, the error evaluation is focused on removing individual reactions, expressed as [117]:

$$\varepsilon_{RED} = \frac{\sum_{r=1,n_R}(r_r - r_r^k)^2}{s^k}, \tag{2.65}$$

where r_r and r_r^k are the individual reaction rates before and after removing a reaction k from the network. The variance s^k is defined as:

$$s^k = \frac{\sum_{r=1,n_R}(r_r^k - \overline{r}^k)^2}{n_R - 1}, \tag{2.66}$$

where $\overline{r}^k$ is the averaged reaction rate of the remaining reactions after reaction k is removed:

$$\overline{r}^k = \frac{\sum_{r=1,n_R} r_r^k}{n_R}. \tag{2.67}$$

Table. 2.4 shows the differences and similarities of the five reduction models explained:

Table 2.4 Differences and similarities of the reduction models in TDAC.

Reduction model	DRG	DRGEP	DAC	PFA	EFA
Graph network	Yes	Yes	Yes	Yes	Yes
Species group effect	No	Yes	No	-	-
Error propagation	No	Yes	Yes	-	-
Error evaluation based on	Species	Species	Species	Species	Reaction

2.7 Advanced post-processing tool

2.7.1 Computational Singular Perturbation fundamentals

The species and energy equations that govern the evolution of a reactive-transport system can be cast in the general form of:

$$\frac{\partial \boldsymbol{z}}{\partial t} = \boldsymbol{L}(\boldsymbol{z}) + \boldsymbol{g}(\boldsymbol{z}), \tag{2.68}$$

where $\boldsymbol{g}(\boldsymbol{z})$ is the chemical source term of the system, $\boldsymbol{L}(\boldsymbol{z})$ is a spatial differential operator (convection and/or diffusion), $\boldsymbol{z}$ is the (N+1)-dimensional state vector including the mass fractions of N species and the temperature. The RHS of Eq.(2.68) can always be written with

respect to a new basis, spanned by a set of basis vectors, or modes, $\boldsymbol{a}_i$ (i=1, N+1), to yield:

$$\frac{\partial \boldsymbol{z}}{\partial t} = \sum_{i=1,N+1} \boldsymbol{a}_i(\boldsymbol{z}) h^i(\boldsymbol{z}), \tag{2.69}$$

where $h^i(\boldsymbol{z}) = h^i(\boldsymbol{L},\boldsymbol{g}) := \boldsymbol{b}^i \cdot (\boldsymbol{L}(\boldsymbol{z}) + \boldsymbol{g}(\boldsymbol{z}))$ is the amplitude of the i-th mode and $\boldsymbol{b}^i$ denotes the dual basis vector, such that $\boldsymbol{b}^i \cdot \boldsymbol{a}_j = \delta^j_i$ and $\sum_i \boldsymbol{a}_i \boldsymbol{b}^i = \mathbf{I}$, with $i = 1, N+1$. The bi-orthonormality condition allows to recover the original representation of system. Based on CSP, the basis vectors $\boldsymbol{a}_i$ and covectors $\boldsymbol{b}^i$ can be approximated to leading order, by the right and left eigenvectors of the Jacobian $J_{\boldsymbol{g}}$ of $\boldsymbol{g}(\boldsymbol{z})$, respectively. This set of basis vectors is traditionally employed in CSP to decouple the chemical modes time-evolution, i.e., each mode amplitude $f^i(\boldsymbol{g}) := \boldsymbol{b}^i \cdot \boldsymbol{g}(\boldsymbol{z})$ evolves in time independently, enabling in turn to define a spectrum of intrinsic local time scales of the reactive system based on $\boldsymbol{g}(\boldsymbol{z})$, which are defined as the reciprocal of the eigenvalues λ_i of $J_{\boldsymbol{g}}$.

It is well established that dissipative fast time scales develop, which are associated to the largest negative eigenvalues of $J_{\boldsymbol{g}}$. In purely reactive systems, the CSP modal decomposition enables a fast/slow subspaces partitioning of the original N+1-dimensional tangent space. Ordering the modes based on their associated time scale, from the fastest to the slowest, so that the first ($i = 1$) mode refers to the fastest chemical time scale (largest eigenvalue), the number M of fast modes is defined as the number of modes whose amplitude f^i gives a zero net contribution ($f^i \approx 0$) to the state evolution over a scale of the order τ^{M+1}. Hence, the first M time scales are considered exhausted, allowing for the definition of an attractive local subspace - the slow invariant manifold (SIM) - where the system evolves according to the slow scales. The slow time scales can be either dissipative or explosive, characterizing an attractive dynamics towards the SIM and in turn equilibration, or a departing dynamics that drives the system away from equilibrium.

The species most affected by the constraints $f^i \approx 0$ are those whose axis in phase space is the most parallel to the direction along which the fast time scales act, i.e., the directions of the fast modes. Therefore, when a fast time scale becomes exhausted, the concentration of that species will, in essence, not change along this direction, i.e., it has achieved a “directional steady-state” status. The terminology used in the CSP literature [120] refers to these species as “CSP radicals” or "fast species". The remaining species are considered "slow species", which evolve on the low dimensional, attractive subspace, i.e. the SIM. It is worth noting that $f^i \approx 0$ occurs because of cancellations of balancing reactions at equilibrium. Among the fast modes, there might be a subset of modes whose $f^i \approx 0$ occurs because of absence of contributions. These modes are frozen modes.

The extension to reactive-transport system is pursued with a local approach by keeping the purely reactive system's eigen-structure and by projecting the full right-hand-side onto the CSP chemical modes $\boldsymbol{a}_i$, as per Eq. (2.69). According to this approach, transport affects the mode amplitudes, i.e., not their directions, within the hypothesis that transport time scales are much slower than the fastest reactive time scales that are associated to the emergence of the low dimensional manifold. In this case, transport only perturbs the system off the chemical manifold, while the fast chemical processes rapidly relax the system back onto it.

Consistently with Eq. (2.69), the effect of transport on the mode amplitudes reveals itself in a different partition of the tangent space, determining the number H of exhausted modes/time scales as the number of modes whose amplitude h^i gives a zero net contribution to the state evolution over a scale of the order of τ^{H+1}. All the considerations that followed the definition of M are naturally extended to a reactive-transport system, e.g. fast/slow species and frozen modes, according to the behavior of h^i.

2.7.2 Tangential Stretching Rate

The important question then becomes how to sort out the most relevant time scales among the $N-M$ intrinsic slow time scales of the system: in fact, it might happen that no or little energy is associated to a specific time scale. In other words, although there might exist a *potential* channel to propagate energy through a mode (at the associated time scale), it might well happen that the system does not select that mode for the *actual* energy propagation. The TSR is a measure of how much the dynamics stretches/contracts in the direction of the vector field and it is employed to characterize the most energetic scale developing in the system. Based on the TSR approach [121, 82], the local stretching rate of the system dynamics in the direction tangential to the vector field $\boldsymbol{L}(\boldsymbol{z})+\boldsymbol{g}(\boldsymbol{z})$, is given by

$$\omega_{\tilde{\boldsymbol{\tau}}}(\boldsymbol{L},\boldsymbol{g}) := \sum_{i=1}^{N} W_i(\boldsymbol{L},\boldsymbol{g})\ \lambda_i, \tag{2.70}$$

with λ_i being the eigenvalue of the i-th mode, and the weight, W_i, of each chemical eigenvalue defined as:

$$W_i(\boldsymbol{L},\boldsymbol{g}) := \frac{h^i(\boldsymbol{L},\boldsymbol{g})}{|\boldsymbol{L}+\boldsymbol{g}|} \sum_{k=1}^{N} \frac{h^k(\boldsymbol{L},\boldsymbol{g})}{|\boldsymbol{L}+\boldsymbol{g}|}\,(\boldsymbol{a}_k\cdot\boldsymbol{a}_i)\,, \tag{2.71}$$

where $|\boldsymbol{L}+\boldsymbol{g}|$ is the norm of the RHS of Eq. (2.68). It follows that the tangential stretching rate $\omega_{\tilde{\boldsymbol{\tau}}}$ is a linear combination of all the time scales[1] of the chemical system and represents the

[1] The contribution to $\omega_{\tilde{\boldsymbol{\tau}}}$ of an eigenvalue λ_i is of the order $|(h^i)^2\ \lambda_i|$; the mode amplitude of a fast mode, by definition, should be negligibly small, $h^i \sim 0$; however, it can happen that because of numerical inaccuracies

stretching rate along the unit vector aligned with the state evolution direction. The magnitude of the TSR represents the reciprocal of the most energy containing time scale of the system, while its positive or negative sign indicates an explosive or non-explosive/dissipative nature of the dynamics.

The purely reactive TSR is referred as $\omega_{\boldsymbol{g}} := \omega_{\tilde{\boldsymbol{\tau}}}(\boldsymbol{L} = 0, \boldsymbol{g})$ and the reactive-transport TSR as $\omega_{\boldsymbol{g}+\boldsymbol{L}} := \omega_{\tilde{\boldsymbol{\tau}}}(\boldsymbol{L} \neq 0, \boldsymbol{g})$. When transport is absent, $\omega_{\boldsymbol{g}}$ provides the stretching rate along the unit vector oriented in the direction of the chemical source term. While in a purely reactive system, only $\omega_{\boldsymbol{g}}$ is defined, in a reactive-transport system both quantities are defined and meaningful, $\omega_{\boldsymbol{g}+\boldsymbol{L}}$ being the stretching along the reactive-transport (extended TSR) vector field and $\omega_{\boldsymbol{g}}$ the stretching along the chemical source term (chemical TSR) direction, i.e., the direction the system would follow if transport were abruptly removed. The latter is useful in the characterization of the chemistry budget in a reactive-transport system, i.e. to gain insights into the chemical dynamics that competes against transport.

The TSR is contributed by the most energy containing modes, which can be identified by resorting to a participation index of the i-th mode to the TSR, defined as

$$P^{\omega_{\tilde{\boldsymbol{\tau}}}}_{\text{mode}_i}(\boldsymbol{L}, \boldsymbol{g}) := \frac{\bar{W}_i(\boldsymbol{L}, \boldsymbol{g})\ |\lambda_i|}{\sum_{j'=1}^{N} \left|\bar{W}_{j'}(\boldsymbol{L}, \boldsymbol{g})\ \left|\lambda_{j'}\right|\right|} \qquad \text{no sum on i.} \tag{2.72}$$

It is of interest to quantify the relative contribution of each physical process most contributing to the development of $\omega_{\tilde{\boldsymbol{\tau}}}$, either a chemical reaction or a transport process. Hence, an index is introduced that relates the k–th process to $\omega_{\tilde{\boldsymbol{\tau}}}$, $P^{\omega_{\tilde{\boldsymbol{\tau}}}}_{\text{process}_k}$, as the product of the participation index of the i-th mode to the TSR, $P^{\omega_{\tilde{\boldsymbol{\tau}}}}_{\text{mode}_i}$, times the CSP participation index [122, 123] of the k–th process to the i–th mode, $P^{\text{mode}_i}_{\text{process}_k}$, that is:

$$P^{\omega_{\tilde{\boldsymbol{\tau}}}}_{\text{process}_k}(\boldsymbol{L}, \boldsymbol{g}) := \sum_{\text{mode}_i=1}^{N+1} P^{\omega_{\tilde{\boldsymbol{\tau}}}}_{\text{mode}_i}(\boldsymbol{L}, \boldsymbol{g})\ P^{\text{mode}_i}_{\text{process}_k}(\boldsymbol{L}, \boldsymbol{g}). \tag{2.73}$$

h^i is small but finite, say $h^i \sim O(10^{-12})$; this implies that $|(h^i)^2\ \lambda_i| > O(1)$ for $|\lambda_i| > O((h^i)^{-2})$, instead of remaining negligibly small. To prevent this source of contamination, it is safer to restrict the summation in Eqs. (2.70) and (2.71) over the slow subspace only.

Since the CSP participation indices to each mode $P^{\text{mode}_i}_{\text{process}_k}$ and the indices $P^{\omega_{\tilde{\boldsymbol{\tau}}}}_{\text{mode}_i}$ sum to 1 by construction, it follows that $\sum_{k=1}^{N_{proc}} P^{\omega_{\tilde{\boldsymbol{\tau}}}}_{\text{process}_k} = 1$ as well, in virtue of the following:

$$\sum_{\text{process}_k=1}^{N_{proc}} P^{\omega_{\tilde{\boldsymbol{\tau}}}}_{process_k} = \sum_{\text{process}_k=1}^{N_{proc}} \left(\sum_{\text{mode}_i=1}^{N+1} P^{\omega_{\tilde{\boldsymbol{\tau}}}}_{\text{mode}_i} P^{\text{mode}_i}_{\text{process}_k} \right) = \left(\sum_{\text{mode}_i=1}^{N+1} P^{\omega_{\tilde{\boldsymbol{\tau}}}}_{\text{mode}_i} \right) \left(\sum_{\text{process}_k=1}^{N_{proc}} P^{\text{mode}_i}_{\text{process}_k} \right) = 1. \tag{2.74}$$

There exist other metrics that allow to identify the processes most contributing to a time scale. On this regard, it is necessary to stress that - by construction - the indices $P^{\omega_{\tilde{\boldsymbol{\tau}}}}_{\text{process}_k}$ select the processes that are associated with (i) the time scale provided by $\omega_{\tilde{\boldsymbol{\tau}}}$, and (ii) all and only the (active) modes that contribute the most to the "energy" of the system during both the explosive and contractive phases of its dynamics. This way, it is not requested to make any a-priori assumptions about the specific system of interest.

Chapter 3

Paper contributions

The thesis has lead to the publication and preparation of seven journal articles and one conference paper with peer-review. In this section, a brief summary of each paper is given.

3.1 Numerical study of the Adelaide Jet in Hot-Coflow burner by means of RANS and detailed chemistry

This paper showed an in-depth numerical characterisation of the Jet in Hot Co-flow (JHC) configuration using the Reynolds Averaged Navier-Stokes (RANS) modelling with detailed chemistry. The JHC burner emulates the MILD combustion by means of a hot and diluted co-flow and high speed injection. The investigation focused on the effect of turbulent combustion models, turbulence model parameters, boundary conditions, multi-component molecular diffusion and kinetic mechanisms on the results. The obtained results showed that the approaches used to model the reaction fine structures, namely as Perfectly Stirred Reactors (PSR) or Plug Flow Reactors (PFR), do not have a major impact on the results. Similarly, increasing the complexity of the kinetic mechanism does not lead to major improvements on the numerical predictions. On the other hand, the inclusion of multi-component molecular diffusion and the appropriate choice of turbulent Schmidt and Prandtl numbers helps increasing the prediction accuracy. Three different Eddy Dissipation Concept (EDC) model formulations were compared, showing their interaction with the choice of the $C_{1\varepsilon}$ constant in the $k-\varepsilon$ turbulence model. Finally, two approaches were benchmarked for turbulence-chemistry interactions, the EDC model and the Partially Stirred Reactor (PaSR) model.

3.2 Finite-rate chemistry modelling of non-conventional combustion regimes using a Partially-Stirred Reactor closure: combustion model formulation and implementation details

In the paper above, the EDC and PaSR were compared but the PaSR approach was only briefly introduced. In the present paper, a more detailed investigation of the PaSR model was presented.

This work focused on the numerical simulation of Moderate or Intense Low oxygen Dilution combustion condition, using the Partially-Stirred Reactor model for turbulence-chemistry interactions. The Partially-Stirred Reactor model assumes that reactions are confined in a specific region of the computational cell, whose mass fraction depends both on the mixing and the chemical time scales. Therefore, the appropriate choice of mixing and chemical time scales becomes crucial to ensure the accuracy of the numerical simulation prediction. Results showed that the most appropriate choice for mixing time scale in Moderate or Intense Low oxygen Dilution combustion regime was to use a dynamic evaluation, in which the ratio between the variance of mixture fraction and its dissipation rate is adopted, rather than global estimations based on Kolmogorov or integral mixing scales. This was supported by the validation of the numerical results against experimental profiles of temperature and species mass fractions, available from measurements on the Adelaide Jet in Hot Co-flow burner. Different approaches for chemical time scale evaluation were also compared, using the species formation rates, the reaction rates and the eigenvalues of the formation rate Jacobian matrix. Different co-flow oxygen dilution levels and Reynolds numbers were considered in the validation work, to evaluate the applicability of Partially-Stirred Reactor approach over a wide range of operating conditions. Moreover, the influence of specifying uniform and non-uniform boundary conditions for the chemical scalars was assessed. This work shed light on the key mechanisms of turbulence-chemistry interactions in advanced combustion regimes. At the same time, it provided essential information to advance the predictive nature of computational tools used by scientists and engineers, to support the development of new technologies.

3.3 Assessment of on-the-fly chemistry reduction and tabulation approaches for the simulation of MILD combustion

Both EDC and PaSR model considers finite-rate chemistry, in which large number of species and reactions are generally involved. In order to increase the efficiency for numerical simulations, tabulation and chemistry reduction are necessary. In this paper, a comprehensive study on this topic was carried out.

This article focused on the numerical simulation of the Delft Jet-in-Hot-Coflow (DJHC) burner, fed with natural gas and biogas, using the Eddy Dissipation Concept (EDC) model with dynamic chemistry reduction and tabulation, i.e. Tabulated Dynamic Adaptive Chemistry (TDAC). The CPU time saving provided by TDAC was evaluated for various EDC model constants and chemical mechanisms of increasing complexity, using a number of chemistry reduction approaches. Results showed that the TDAC method provides speed-up factors of 1.5-2.0 and more than 10, when using a skeletal (DRM19) and a comprehensive kinetic mechanism (POLIMIC1C3HT), respectively. The Directed Relation Graph with Error Propagation (DRGEP), Dynamic Adaptive Chemistry (DAC) and Elementary Flux Analysis (EFA) reduction models show superior performances when compared to other approaches as Directed Relation Graph (DRG) and Path Flux Analysis (PFA). All the reduction models were adapted for run-time reduction. Furthermore, the contribution of tabulation is more important with small mechanisms, while reduction plays a major role with large mechanisms.

3.4 Numerical and experimental investigation of turbulent n-heptane jet-in-hot-coflow flames

The research work in the previous 3 journal papers focused mainly on the simple hydrocarbon fuels under MILD condition, in which these fuels reveal some common signatures. However, when a long chain alkane is considered, some distinction features are observed, both experimentally and numerically. The paper “Numerical and experimental investigation of turbulent n-heptane jet-in-hot-coflow flames” focused on this topic.

A jet-in-hot-coflow flame with *n*-heptane as fuel was numerically and experimentally investigated in the present article, revealing the distinct features of this fuel under MILD conditions. The RANS k-ε turbulence model in combination with a dynamic Partially Stirred Reactor combustion model was adopted. The simulation results were validated against newly-obtained experimental data on mean temperature, OH number density and normalised

CH_2O-PLIF signal values at several axial locations. The simulations captured the transitional phenomenon observed experimentally for the low coflow oxygen concentration case, and this behaviour is associated to the two chemical pathways which exist in *n*-heptane pyrolysis process. The predicted flame weak-to-strong transition heights showed distinct behaviour when the threshold OH number density value was varied. Furthermore, the investigation on negative heat release region showed that the absolute value of negative heat release increased with reduced coflow oxygen content.

3.5 Large Eddy Simulation of MILD combustion using finite rate chemistry: effect of combustion sub-grid closure

All previous papers were based on RANS simulations. In this paper, Large Eddy Simulation in MILD combustion was carried out.

In this work, we presented a detailed comparison between the conventional Partially Stirred Reactor (PaSR) combustion model and two implicit combustion models named Quasi Laminar Finite Rate (QLFR) model and Laminar Finite Rate (LFR) model, respectively. Large Eddy Simulation (LES) was employed and the Adelaide Jet in Hot Co-flow (AJHC) burner was chosen as validation case. In the implicit combustion models, the filtered source term comes directly from the chemical term, without inclusion of the turbulent effect. Results demonstrated that the two implicit models have very similar behaviour compared with the conventional PaSR model concerning the mean and root-mean-square of the temperature and species mass fraction fields and they all give satisfactory predictions, especially the mean values. This justifies the usage of implicit combustion models in low Damköhler number (Da $\leqslant$ 1.0) systems. The QLFR model was able to save $\sim$3 times computational time compared with the LFR model. Moreover, the comparison between two 4-step global mechanisms and a reduced 17 species 58 reactions skeletal mechanism proved the importance of using finite rate chemistry approach in MILD combustion regime.

3.6 Large Eddy Simulation of MILD combustion with dynamic PaSR model

The study carried out in the paper above was extended for various oxygen levels and Reynolds numbers, together with the inclusion of a dynamic model for the estimation of PaSR mixing time scale in LES.

This paper presented the LES results of a jet-in-hot-coflow burner under several operation conditions with varied coflow oxygen levels and jet Reynolds numbers. The conventional Partially Stirred Reactor combustion model was compared with two implicit models and one dynamic model which evaluates the mixing time scale in PaSR with the ratio of mixture fraction sub-grid fluctuation and mixture fraction dissipation rate. Results from cases with different oxygen levels (3%/6%/9% by mass, Reynolds number = 10 k) demonstrated that the two implicit models provide predictions of the mean and root-mean-square of the temperature and species mass fraction fields very similar to the conventional PaSR model. Moreover, they all give satisfactory predictions compared to experimental data, especially for the mean values. When the jet Reynolds number was increased from 10 k to 20 k, extinction was observed at low oxygen level (3%) with the conventional estimation of mixing time scale. The dynamic mixing model helps to capture the flame instabilities and improves the prediction with higher accuracy.

3.7 Computational Singular Perturbation analysis on Large Eddy Simulation of MILD combustion

In order to study the turbulence-chemistry interactions and the relationship between flame autoignition and propagation under MILD condition, advanced post-processing tools are required. Using datasets from the Large Eddy Simulation of the JHC burner, an analysis based on the Computational Singular Perturbation theory was carried out and makes the object of a paper submitted for publication.

This article presented a numerical study of the jet-in-hot-coflow (JHC) burner. Some fundamental mechanisms in MILD combustion are yet not well understood. For instance, the relation between auto-ignition and flame propagation, local extinction and re-ignition. The advanced post-processing tools based on the theory of Computational Singular Perturbation (CSP) can be used to improve our physical understanding. To this purpose, they were applied on the datasets obtained from the Large Eddy Simulation (LES) of JHC burner with different coflow oxygen levels. The analysis revealed low number of fast mode in the layer with

high heat release rate (HRR), while high number was found in the coflow area as it reaches equilibrium very fast. Observations on the reactive layer with the help of Tangential Stretch Rate (TSR) indicated the relevant role of auto-ignition; The ignited flame kernels were observed to be transported further downstream by propagation. Moreover, the analysis of the participation indices (PIs) of TSR marked the extinction and re-ignition zone for the low oxygen level case, indicating that the lack of oxygen in the coflow suppresses the path to produce final combustion products and heat—thus reducing the reactivity of the whole system.

3.8 Numerical investigation of lifted turbulent flame with PaSR and FPV models

The consideration of flame extinction and re-ignition is of great importance for flames with strong interactions between chemistry reaction and turbulence. From the previous journal papers, it can be concluded that the PaSR model handles such interactions with satisfaction. In conference paper “Numerical investigation of lifted turbulent flame with PaSR and FPV models”, the PaSR model was compared with steady Flamelet Progress Variable model.

This study focused on the Unsteady Reynolds Averaged Navier-Stokes (URANS) simulation of a lifted methane flame with vitiated co-flow. The Partially Stirred Reactor (PaSR) and steady Flamelet Progress Variable (FPV) models were adopted and compared. Three kinetic mechanisms (KEE58, GRI3.0 and San-Diego) with increasing number of species and reactions were used with PaSR model. Results indicated that using San-Diego mechanism improved the simulation results of mean temperature and species mass fraction, revealing the importance of chemical kinetics on the lifted flame. The PaSR model is able to predict the current flame with satisfaction. However, on the other hand, the steady FPV models was not able to capture the ignition process correctly.

Chapter 4

Concluding remarks

The present Chapter provides a brief discussion of the main accomplishments and original contributions of the present Thesis. A modelling framework for predicting and advancing the understanding of turbulence-chemistry interactions in Moderate or Intense Low oxygen Dilution (MILD) combustion has been proposed.

Successful predictions of lab-scale MILD systems with finite rate models are reported, with both Reynolds Average Navier-Stokes (RANS) simulation and Large Eddy Simulation (LES). The Eddy Dissipation Concept (EDC) model was first considered for the prediction of a jet-in-hot-coflow (JHC) burner with RANS simulation. A comprehensive sensitivity analysis focused on the effect of various parameters on the simulation results was carried out. Moreover, the EDC models was compared with the Partially Stirred Reactor (PaSR) model, showing that both models were suitable for modelling of MILD systems.

In PaSR, the turbulence-chemistry interaction factor is based on a more general definition which requires the estimation of chemical and mixing time scales. The choice of such scales has a crucial impact on the models predictions. Different approaches for the estimation of PaSR mixing and chemical time scales were assessed and benchmarked in the context of RANS modelling. They were compared on a variety of cases, varying the oxygen content in the co-flow and the fuel jet Reynolds number. Most importantly, a dynamic evaluation of mixing time scale in PaSR was proposed, presenting superior performance than the other globally defined mixing models under a wide range of operating conditions. In both EDC and PaSR models, each computational cell is separated into two zones, a reacting and a non-reacting one, with a factor defining the mass fraction of the reacting zone. In EDC, such factor is found to be proportional to the Kolmogorov mixing time, based on a turbulence cascade model, thus limiting the application of the model (in its base formulation). In PaSR, the choice of appropriate mixing and chemical time scales makes it applicable under wider range of conditions, with higher accuracy.

When working with finite-rate models, a large number of species and reactions are generally involved. It is computationally expensive. The use of pre-reduced or pre-tabulated mechanisms can fail to capture non-equilibrium phenomena like extinction and re-ignition in flames with strong turbulence-chemistry interactions. Therefore, a coupled dynamic chemistry reduction and tabulation approach, named Tabulated Dynamic Adaptive Chemistry (TDAC), was applied and tested in the context of RANS simulation of the JHC burner. Remarkable speed-up of the simulation was achieved with TDAC, especially when large mechanisms, such as POLIMIC1C3HT (107 species, 2642 reactions), were used. In this case, speed-up factor up to roughly 10 were observed.

The investigation of MILD combustion systems was extended to higher molecular weight fuels. Indeed, the experimental and numerical investigation of the MILD combustion with simple fuels revealed (CH_4, H_2 and C_2H_4) some common signatures, such as the absence of the negative heat release region, the broadening of the heat production profile with a single peak in mixture fraction space and the suppression of pyrolytic reactions. However, using complex fuels such as oxygenated hydrocarbons and long-chain alkanes under MILD condition has shown experimentally distinct features, like the appearance of visible flames and increased pollutant emissions. To shed light on this, the RANS simulations of *n*-heptane combustion in the JHC burner were carried out. A transitional flame structure was observed for the low oxygen level (3 % O_2) case, based on the distribution of OH, and the negative heat release region did not disappear as the coflow oxygen level was reduced to extreme low level of 1 %. Because of the existence of two pyrolysis chemical pathways, the appearance of the transitional structure for *n*-heptane flames happens at lower coflow oxygen level compared to simple fuels. The numerical results confirmed that it is more challenging for n-heptane flames to reach MILD condition, compared to simple fuels like methane, hydrogen and ethylene.

Despite the high computational efficiency of RANS simulation, more sophisticated modelling approaches such as Large Eddy Simulations are needed to decode complex phenomena taking place under MILD conditions. To this end, LES with two implicit combustion models were benchmarked against the conventional PaSR approach on the JHC burner with various coflow oxygen levels and Reynolds numbers. Both implicit models were found to provide very similar results compared with the conventional PaSR model, for the mean and root-mean-square of the temperature and species mass fraction fields. This justifies the usage of implicit combustion models in low Damköhler number ($Da \leqslant 1.0$) systems. The comparison between two 4-step global mechanisms and a reduced 17 species 58 reactions skeletal mechanism proved the importance of using finite rate chemistry approach in MILD combustion regime. Moreover, a dynamic estimation of PaSR mixing time under

LES framework was proposed. When the jet Reynolds number was increased from 10 k to 20 k, extinction was observed at low oxygen level (3%) with the conventional estimation of PaSR mixing time scale, while the dynamic mixing model was able to capture the flame re-ignition, thus improving prediction accuracy.

Thanks to the availability of a number of LES datasets at different operating conditions, a detailed investigation based on Computational Singular Perturbation (CSP) was applied. The Tangential Stretch Rate (TSR) was calculated to reveal the explosive and contractive nature of the flame. Local flame extinction and re-ignition were found for the instantaneous snapshot of the 3 % case, because of the low availability of oxygen in the coflow and the entrainment of air. The extended TSR with diffusive term showed the importance of both autoignition and flame propagation under MILD condition. The observations substantiated findings from previous research works stating that the initiated ignition kernels from autoignition are transported further downstream by flame propagation. More importantly, results showed that at the location close to the flame ignition point, the 3 % case is driven by chemical reactions while the 9 % case is mainly transport driven. Such observation confirmed the regime difference between the 3 % and 9 % cases, operating in MILD combustion regime and as a conventional diffusion flame, respectively.

Chapter 5

Selected papers

5.1 Journal paper 1

This paper was published in Energy:

Zhiyi Li, Alberto Cuoci, Amsini Sadiki and Alessandro Parente, Comprehensive numerical study of the Adelaide Jet in Hot-Coflow burner by means of RANS and detailed chemistry, Energy 139, 555-570 (2017).

Comprehensive numerical study of the Adelaide Jet in Hot-Coflow burner by means of RANS and detailed chemistry

Zhiyi Li[a,*], Alberto Cuoci[b], Amsini Sadiki[c], Alessandro Parente[a,**]

[a] *Université Libre de Bruxelles, Aero-Thermo-Mechanics Department, Belgium*
[b] *Politecnico di Milano, Department of Chemistry, Materials, and Chemical Engineering "G. Natta", Italy*
[c] *Technische Universität Darmstadt, Institute of Energy and Powerplant technology, Germany*

Abstract

The present paper shows an in-depth numerical characterisation of the Jet in Hot Co-flow (JHC) configuration using the Reynolds Averaged Navier-Stokes (RANS) modelling with detailed chemistry. The JHC burner emulates the MILD combustion by means of a hot and diluted co-flow and high speed injection. The current investigation focuses on the effect of turbulent combustion models, turbulence model parameters, boundary conditions, multi-component molecular diffusion and kinetic mechanisms on the results. Results show that the approaches used to model the reaction fine structures, namely as Perfectly Stirred Reactors (PSR) or Plug Flow Reactors (PFR), do not have a major impact on the results. Similarly, increasing the complexity of the kinetic mechanism does not lead to major improvements on the numerical predictions. On the other hand, the inclusion of multi-component molecular diffusion and the appropriate choice of turbulent Schmidt and Prandtl numbers helps increasing the prediction accuracy. Three different Eddy Dissipation Concept (EDC) model formulations are compared, showing their interaction with the choice of the $C_{1\epsilon}$ constant in the $k-\epsilon$ turbulence model. Finally, two approaches are benchmarked for turbulence-chemistry interactions, the EDC model and the Partially Stirred Reactor (PaSR) model.

Keywords: `Eddy Dissipation Concept, Jet in Hot Co-flow burner, MILD combustion, Partially Stirred Reactor, RANS simulation`

1. Introduction

Facing the challenges of energy shortage and limited fossil fuel resources, as well as the increasing air pollution problems, the development of fuel flexible, efficient and environ-

*Zhiyi.Li@ulb.ac.be
**Alessandro.Parente@ulb.ac.be

mentally friendly combustion technologies has become urgent. Some new combustion technologies appeared during the last few decades. Among those, the Moderate or Intense Low oxygen Dilution (MILD) combustion [1, 2] has drawn increasing attention recently. MILD combustion is characterised by diluted reactants, non-visible or audible flames and uniform distributed temperatures [3, 4, 5]. As a result, complete combustion can be assured and the formation of pollutants such as CO, NO_x [6, 7] and soot are strongly reduced [8, 9]. More recently, there are also some investigations focused on the applicability of MILD combustion to oxy-fuel conditions [10, 11], in order to further reduce the pollutants.

According to Li et al.[12], high temperature pre-heating of combustion air and the high-speed injection of fuel are the main requirements to achieve MILD combustion condition. Based on these requirements, model flames like the Adelaide Jet in Hot Co-flow (JHC) burner [13] and Delft JHC burner [14, 15] were built to emulate MILD condition. The Adelaide JHC burner has a central high speed jet and secondary burners providing hot exhaust products mixing with air. Dally et al. [13] have carried out experiments on this burner with central jet fuel of CH_4 and H_2, in equal proportions on a molar basis. Different oxygen levels (9%, 6% and 3%) are fixed in the hot co-flow. Medwell et al. [16] used laser diagnostic to reveal the distribution of hydroxyl radical (OH), formaldehyde (H_2CO), and temperature under the influences of hydrogen addition. They also found out that the weak to strong transition of OH and the appearance of H_2CO are the evidences for the occurrence of pre-ignition in the apparent lifted region of ethylene flames [17].

In addition to experimental investigations, increasing attention has been paid to the numerical modelling of MILD combustion. Most of the numerical investigations were carried out using Reynolds Averaged Navier-Stokes (RANS) simulation or Large Eddy Simulation (LES). The LES approach is able to capture more details of the flame, while RANS is still important in the industrial context or for the early stage academic research because of its reduced computational cost. Due to the strong mixing and the reduced temperature levels in MILD combustion, a stronger competition between chemistry reaction and fluid dynamics exists in this regime. This leads to a system characterised by a relatively low Damköhler number ($Da = turbulence\_time\_scale/chemical\_time\_scale$). As a result, the interactions between the fluid dynamics and chemical reaction become more important. Thus, they need to be carefully considered in the modelling process. In terms of chemical kinetics, global mechanisms are not sufficient to capture the main features of MILD combustion [18]. Using a turbulent combustion model with the possibility of implementing detailed mechanism plays a vital role therefore. Different approaches were evaluated by Shabanian et al. [19], Christo et al. [20], Parente el al. [21, 22], Fortunato et al. [23] and Galletti et al. [24] employing Reynolds Averaged Navier-Stokes (RANS) simulation. In these approaches, the authors

showed that the Eddy Dissipation Concept (EDC) [25] model can better handle the strong interactions between turbulence and chemistry with respect to the classic flamelet approaches. The EDC model splits every computational cell into two regions: the fine structures, where reactions take place, and the surrounding fluid mixture. In the original EDC formulation, the fine structures are modelled as Perfectly Stirred Reactors (PSR). However, they are also modelled as Plug Flow Reactors (PFR) in some software packages for numerical reasons. To the author's knowledge, up to now there is no study showing the impact of such a choice on the results. Beside chemistry, turbulence model also influences the accuracy of prediction. Frassoldati et al. [26] compared the performances of several RANS models, the standard $k-\epsilon$ model, modified $k-\epsilon$ model ($C_{1\epsilon}$ adjusted from 1.44 to 1.60), and Reynolds Stress Model (RSM). The modified $k-\epsilon$ model was found to better reproduce experimental data, as also indicated by Christo et al. [20]. Moreover, there exist different formulations of the EDC model [27, 28, 25]. The combination of the $k-\epsilon$ parameters with different EDC formulations has not been studied yet. This will be discussed in the present paper. Beside the EDC model, other combustion models such as the Partially Stirred Reactor (PaSR) [29] combustion model and closures based on the Perfectly Stirred Reactor (PSR) [30] have been proposed to simulate MILD combustion. In the present paper, the PaSR model is compared to the EDC model.

Apart from the turbulence and chemistry models, there are other modelling aspects that require careful evaluation. The strong mixing and uniform temperature field result in a lower reaction rate in MILD combustion. Therefore, molecular diffusion effects are enhanced [20], especially when H_2 is present in the fuel, due to its significant molecular diffusion coefficient. Christo et al. [20] and Mardani et al.[31] showed that the numerical predictions for the JHC burner could be improved by including laminar diffusion in the solver. Besides, the EDC model was found to perform reasonably well for an oxygen content in the co-flow of 9% and 6%, while an over-prediction of the temperature level downstream of the jet outlet was observed for the 3% case [20]. According to Parente et al. [32], the over-prediction can be alleviated by adjusting the EDC parameters of C_γ and C_τ. They derived the dependence of the C_γ and C_τ parameters on the Kolmogorov Damköhler number, Da_η and turbulent Reynolds Number, Re_T. With the proposed formulations for Da_η and Re_T in MILD combustion, C_γ and C_τ were adjusted accordingly [32].

Up to now, quite a few sensitivity analyses have been conducted on the JHC burner, to investigate the effect of different modelling choices, including the turbulent and chemistry models, model parameters, co-flow oxygen levels and molecular diffusion. However, a comprehensive sensitivity study of the JHC burner has not been yet carried out. In the current paper, the influences of turbulence model parameters, combustion models (closures based on PSR and PFR, as in EDC or PaSR), molecular diffusion, turbulent Schmidt Number, turbu-

Table 1: Physical properties of the jet

Profiles	Central jet	Annulus	Tunnel
Velocity	58.74 m/s	3.2 m/s	3.3 m/s
Temperature	294 K	1300 K	294 K

lent Prandtl Number, uniform and non-uniform boundary conditions as well as the kinetic mechanisms will all be presented and discussed. The purpose of this paper is to provide a deep and comprehensive study on the sensitivity of model predictions in MILD combustion regime and to extend it to a wider range of modelling choices.

2. Experimental Basis

The validation test case used in the present work is taken from the Adelaide JHC burner[13]. They include different fuel types, various jet Reynolds numbers and co-flow oxygen levels. The Adelaide JHC burner has an insulated and cooled central jet with the inner diameter of 4.25 *mm*. The central fuel jet provides an equi-molar mixture of CH_4 and H_2. A secondary burner mounted upstream of the exit plane has the inner diameter of 82 *mm*. It provides the hot combustion products. The combustion products are mixed with air and nitrogen, thus oxygen level can be controlled with the amount of nitrogen added. The oxygen level is adjusted to 3%, 6% and 9%. The wind tunnel on which the burner is mounted has the cross section of 254 $mm \times 254$ *mm*. In Fig. 1, a 2D sketch of the domain investigated in the numerical simulation is presented. The gas temperature and velocity profiles of the central jet, annulus and wind tunnel can be found in Table 1. In the present study, the condition corresponding to a Reynolds number of 10000 and and co-flow oxygen content of 3% is investigated.

The single-point Raman-Rayleigh-laser-induced fluorescence technique was applied in the experimental measurement. The mean and variance profiles of temperature and mass fractions of species (CH_4, H_2, H_2O, CO_2, N_2, O_2, NO, CO, and OH) along the centerline as well as on the radial position of 30/60/120/200 *mm* are available. More details about the Adelaide JHC burner experiment carried out by Dally et al. can be found in [13].

3. Mathematical Models

The Reynolds Average Navier-Stokes (RANS) based simulations are carried out on the Adelaide JHC MILD burner. Turbulence chemistry interactions are handled with EDC (Eddy Dissipation Concept) and with PaSR (Partially Stirred Reactor) models. Detailed chemistry can be applied with both models. The OpenFOAM®[33] Finite Volume Method (FVM)

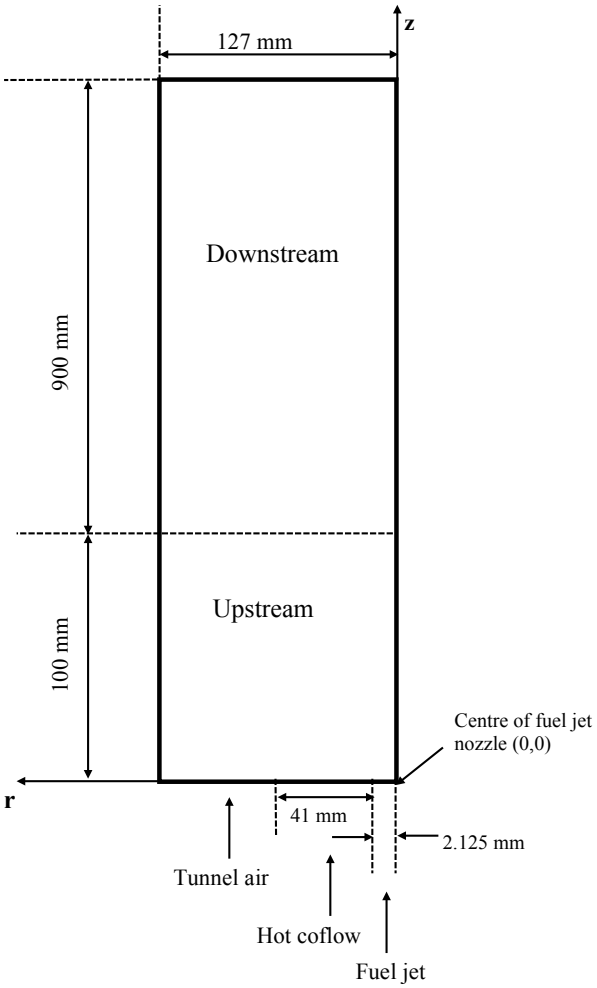

Figure 1: 2D sketch of the Adelaide Jet in Hot Co-flow burner (adapted from Ferrarotti et al. [7]).

based, open-source CFD software is used for all simulations. The model equations solved by the code are shown in the following sections.

3.1. Turbulence Model

In RANS simulations, the density-based Favre-averaged (denoted with ˜) governing equations of mass, momentum and energy are solved [34] :

$$\frac{\partial \bar{\rho}}{\partial t} + \frac{\partial}{\partial x_j}\left(\bar{\rho}\tilde{u}_j\right) = 0, \tag{1}$$

$$\frac{\partial}{\partial t}\left(\bar{\rho}\tilde{u}_i\right) + \frac{\partial}{\partial x_j}\left(\bar{\rho}\tilde{u}_i\tilde{u}_j\right) = -\frac{\partial \bar{p}}{\partial x_i} + \frac{\partial}{\partial x_j}\left(\bar{\tau}_{ij} - \bar{\rho}\widetilde{u_i'' u_j''}\right), \tag{2}$$

$$\frac{\partial}{\partial t}\left(\bar{\rho}\tilde{h}\right) + \frac{\partial}{\partial x_j}\left(\bar{\rho}\tilde{h}\tilde{u}_j\right) = \frac{\partial}{\partial x_j}\left(\bar{\rho}\alpha\frac{\partial \tilde{h}}{\partial x_j} - \bar{\rho}\widetilde{u_j'' h''}\right) - \frac{\partial}{\partial x_j}\left(\bar{q}_{rj}\right) + \bar{S}_{hc}. \tag{3}$$

In Eqn. 1 - 3, ρ, $\mathbf{u}$, p represent the density, velocity and pressure respectively; h is the enthalpy; α is the thermal diffusivity. The term $\mathbf{q}_r$ denotes the radiative heat loss and S_{hc} is the source term coming from combustion process. The turbulent Prandtl number Pr_t has an impact on the turbulent heat flux:

$$-\bar{\rho}\widetilde{u_j'' h''} \approx \frac{\mu_t}{Pr_t}\frac{\partial \tilde{h}}{x_j}. \tag{4}$$

In combustion processes, multiple species are involved. The Favre averaged transport equation of species Y_s reads:

$$\frac{\partial}{\partial t}\left(\bar{\rho}\widetilde{Y}_s\right) + \frac{\partial}{\partial x_j}\left(\bar{\rho}\widetilde{Y}_s\tilde{u}_j\right) = \frac{\partial}{\partial x_j}\left(\left(\bar{\rho}D_{m,s} + \frac{\mu_t}{Sc_t}\right)\frac{\partial \tilde{Y}_s}{\partial x_j}\right) + \bar{\dot{\omega}}_s, \tag{5}$$

where Sc_t is the turbulent Schmidt number and $D_{m,s}$ is the molecular diffusion coefficient for species s in the mixture. Because $Sc_t = \mu_t/(\rho D_t)$ (D_t is the turbulent diffusivity), the molecular diffusion can also be written as $Sc = \mu/(\rho D_m)$ (D_m is the molecular diffusivity) and therefore, $\rho D_m = \mu/Sc$. Assuming ideal gas conditions [35], $Sc = 1$; moreover, according to Yimer et al. [36], $Sc_t \approx 1$. Therefore, Eqn. 5 can be re-arranged as:

$$\frac{\partial}{\partial t}\left(\bar{\rho}\widetilde{Y}_s\right) + \frac{\partial}{\partial x_j}\left(\bar{\rho}\widetilde{Y}_s\tilde{u}_j\right) = \frac{\partial}{\partial x_j}\left(\left(\mu + \mu_t\right)\frac{\partial \widetilde{Y}_s}{\partial x_j}\right) + \bar{\dot{\omega}}_s. \tag{6}$$

In Eqn. 6, $\mu + \mu_t$ can be expressed as μ_{Eff} (the effective viscosity). The comparison between the formulations in Eqn. 5 and Eqn. 6 will be shown in Section 4.4.

Previous works on the JHC burner ([20, 26]) have shown that the modified $k - \epsilon$ model, based on the adjustment of the $C_{1\epsilon}$ constant in the turbulent dissipation transport equation, is

well suited for this configuration. The $k-\epsilon$ model is based on solving the transport equations of turbulence kinetic energy $\tilde{k}$ and the dissipation rate $\tilde{\epsilon}$ of the turbulence kinetic energy [34]:

$$\frac{\partial}{\partial t}\left(\bar{\rho}\tilde{k}\right)+\frac{\partial}{\partial x_j}\left(\bar{\rho}\tilde{k}\tilde{u}_j\right)=\frac{\partial}{\partial x_j}\left(\left(\mu+\frac{\mu_t}{\sigma_k}\right)\frac{\partial\tilde{k}}{\partial x_j}\right)+G_k-\bar{\rho}\tilde{\epsilon}, \tag{7}$$

$$\frac{\partial}{\partial t}\left(\bar{\rho}\tilde{\epsilon}\right)+\frac{\partial}{\partial x_j}\left(\bar{\rho}\tilde{\epsilon}\tilde{u}_j\right)=\frac{\partial}{\partial x_j}\left(\left(\mu+\frac{\mu_t}{\sigma_\epsilon}\right)\frac{\partial\tilde{\epsilon}}{\partial x_j}\right)+C_{1\epsilon}\bar{\rho}\frac{\tilde{\epsilon}}{\tilde{k}}G_k-C_{\epsilon 2}\bar{\rho}\frac{\tilde{\epsilon}^2}{\tilde{k}}, \tag{8}$$

in which G_k is the turbulence kinetic energy production rate. The model constants in Eqn. 7 and Eqn. 8 are C_μ, $C_{1\epsilon}$, $C_{\epsilon 2}$, σ_k and σ_ϵ. The $C_{1\epsilon}$ constant is increased from 1.44 to 1.60 in the modified $k-\epsilon$ model. The other constants do not change [37].

3.2. Combustion Models

3.2.1. EDC Model

The Eddy Dissipation Concept (EDC) combustion model assumes that combustion takes place in the fine structures where the dissipation of the flow turbulence kinetic energy occurs. In the original model by Magnussen [27], the fine structures are modelled as Perfectly Stirred Reactors (PSR). However, some software packages (for example, ANSYS Fluent [38]) treat them as Plug Flow Reactors (PFR), mainly for numerical reasons. EDC is based on a cascade model providing the mass fraction of the fine structures, γ_λ, and the mean residence time of the fluid within the fine structures τ^*, as a function of the flow characteristic scales:

$$\gamma_\lambda=C_\gamma\left(\frac{\nu\tilde{\epsilon}}{\tilde{k}^2}\right)^{\frac{1}{4}}, \tag{9}$$

$$\tau^*=C_\tau\left(\frac{\nu}{\tilde{\epsilon}}\right)^{\frac{1}{2}}. \tag{10}$$

In Eqn. 9 and Eqn. 10, ν is the kinematic viscosity, $C_\gamma=2.1377$ and $C_\tau=0.4083$ are model constants in the EDC model [25]. The mean reaction rate (source term in the species transport equation) is expressed as [28]:

$$\overline{\dot{\omega}}_s=-\frac{\bar{\rho}\gamma_\lambda^2}{\tau^*\left(1-\gamma_\lambda^3\right)}\left(\widetilde{Y}_s-Y_s^*\right). \tag{11}$$

The term $\widetilde{Y}_s$ in Eqn. 11 denotes the mean mass fraction of the species s between the fine structures and the surrounding fluid and Y_s^* is the mass fraction of species s in the fine structures. The mean mass fraction $\widetilde{Y}_s$ can be expressed as a function of Y_s^* and Y_s^0 (mass fraction of species s in the surrounding fluids):

$$\widetilde{Y}_s=\gamma_\lambda^3Y_s^*+(1-\gamma_\lambda^3)Y_s^0. \tag{12}$$

The expressions of the species mean reaction rate and mean mass fraction in Eqn. 11 and Eqn. 12 were proposed by Gran et al. in 1996 [28], thus it will be referenced as ′EDC1996′ in the rest of the paper.

In the earlier version of the EDC model, proposed originally by Magnussen in 1981 [27], the mean reaction rate of species s is given by

$$\overline{\dot{\omega}}_s = -\frac{\bar{\rho}\gamma_\lambda^3}{\tau^*\left(1-\gamma_\lambda^3\right)}\left(\widetilde{Y}_s - Y_s^*\right). \tag{13}$$

This formulation will be referred as ′EDC1981′. Later in 2005, Magnussen modified the model [25], expressing $\overline{\dot{\omega}}_s$ as:

$$\overline{\dot{\omega}}_s = -\frac{\bar{\rho}\gamma_\lambda^2}{\tau^*\left(1-\gamma_\lambda^2\right)}\left(\widetilde{Y}_s - Y_s^*\right), \tag{14}$$

and mean mass fraction $\widetilde{Y}_s$ as

$$\widetilde{Y}_s = \gamma_\lambda^2 Y_s^* + (1-\gamma_\lambda^2)Y_s^0. \tag{15}$$

This version of EDC model will be denoted as ′EDC2005′.

In all three formulations, the mean mass fraction $\widetilde{Y}_s$ is obtained by solving the species transport equation. The mass fraction of each species inside the fine structure Y_s^* is computed with the finite-rate chemistry approach.

Finite-rate Chemistry Approach

The mass fraction Y_s^* of species s inside the fine structures is evaluated by modelling them to a Perfectly Stirred Reactor (PSR) [28]:

$$\frac{\dot{\omega}_s^*}{\rho^*} = \frac{1}{\tau^*}\left(Y_s^* - Y_0\right), \tag{16}$$

in which $\dot{\omega}_s^*$ is the formation rate of species s. Alternatively, the fine structures can be modelled as Plug Flow Reactors (PFR), evolving in a characteristic time equal to τ^*:

$$\frac{dY_s}{dt} = \frac{\dot{\omega}_s}{\rho}. \tag{17}$$

The final integration over $\frac{dY_s}{dt}$ is Y_s^*. The term $\dot{\omega}_s$ is the instantaneous formation rate of species s coming from a detailed kinetic mechanism. In the present study, the KEE (17 species, 58 reactions) [39], GRI3.0 (53 species, 325 reactions) [40], San-Diego (50 species, 247 reactions) [41] and POLIMI_C1C3HT (107 species, 2642 reactions) [42] mechanisms are used.

Table 2: Limitations of fine structure fraction

EDC version	time scale ratio	γ_λ limit
'EDC1981'	$\frac{\gamma_\lambda^3}{1-\gamma_\lambda^3}$	0.7937
'EDC1996'	$\frac{\gamma_\lambda^2}{1-\gamma_\lambda^3}$	0.7549
'EDC2005'	$\frac{\gamma_\lambda^2}{1-\gamma_\lambda^2}$	0.7071

N-containing species are only included in the mechanisms for a selected number of simulations, as they do not effect the main combustion process.

Limitation of Fine Structure Fraction

In the EDC model, the chemical reaction process and mixing are interconnected. This mixing process time scale τ_{mix} should be larger or equal to the fine structures residence time scale τ^*. Defining R as the ratio [43]:

$$R = \frac{\tau^*}{\tau_{mix}} = \frac{\gamma_\lambda^2}{1-\gamma_\lambda^3}, \tag{18}$$

one can find the limit value for γ_λ. The ratio R and γ_λ limits for the various EDC formulations can be found in Table 2.

3.2.2. The Partially Stirred Reactor model

The Partially Stirred Reactor (PaSR) concept, originally proposed by Chomiak [29], assumes that every computational cell can be separated into two zones. All the reactions take place in one zone, while no reactions occur in the other zone [44]. Thus, the chemical reaction rate for the species s can be expressed with:

$$\overline{\dot{\omega}}_s = \kappa \dot{\omega}_s^*(\widetilde{\boldsymbol{Y}}, \widetilde{T}). \tag{19}$$

In the equation above, $\dot{\omega}_s^*(\widetilde{\boldsymbol{Y}}, \widetilde{T})$ is the formation rate of species s based on the mean species concentration in the cell. The term κ is the factor that provides the *partially stirred* condition. It is formulated as:

$$\kappa = \frac{\tau_c}{\tau_c + \tau_{mix}}, \tag{20}$$

where τ_c is the chemical time scale, estimated by rate of formation of each species and taking the highest limiting value as the characteristic one. The term τ_{mix} is the mixing time scale.

Table 3: Grid Convergence Index (GCI) for different grids

Mesh resolution	coarse	medium	fine	superfine
Number of cells	15900	34830	79110	179186
GCI (%)	0.93	1.52	1.87	1.92

Table 4: Discretization schemes

Field	Discretization scheme
Velocity (U)	Total Variance Diminishing (TVD)
Pressure (p)	Total Variance Diminishing (TVD)
Species mass fraction (Y)	bounded ([0,1]) TVD

In the present work, the mixing time scale is taken as the geometric mean of the integral and Kolmogorov mixing time scales:

$$\tau_{mix} = \left(\frac{\tilde{k}}{\tilde{\epsilon}} \cdot \sqrt{\frac{\nu}{\tilde{\epsilon}}} \right)^{\frac{1}{2}} . \tag{21}$$

The inherent idea behind PaSR model has similarities with the EDC model. But the mathematical formulations are different. This makes it interesting to compare the simulation results from these two combustion models.

3.3. Numerical Settings

In this section, the numerical settings for the JHC simulations are presented in detail.

A 2-dimensional axis-symmetric mesh is used in the simulations. A grid convergence study was carried out to optimise the number of cells. The Grid Convergence Index (GCI) [45] was calculated for different mesh resolutions, as indicated in Table 3 for four mesh resolutions. The medium mesh resolution was chosen, because it provides a reasonable compromise between CPU time requirements and numerical accuracy. The selected mesh has 30150 hexahedral cells and 450 prisms. The burner walls are ignored in the domain. The computation domain starts from the burner exit and extends 1000 *mm* downstream.

The second order discretization schemes are applied for the governing equations. An overview of selected numerical schemes can be found in Table 4.

Both uniform and non-uniform boundary conditions are used in the simulation for the species mass fractions and temperature. The uniform boundary conditions are obtained from the theoretical data provided by Dally et al. [13], as they are shown in Table 5. The non-uniform ones are obtained from the mean sampled experimental value 4 *mm* downstream of

Table 5: Uniform boundary condition values for the JHC burner

Boundaries	Inlet fuel	Inlet co-flow	Inlet air
Temperature (K)	305	1300	294
Velocity (m/s)	58.74	3.2	3.3
CH4 mass fraction (-)	0.888	0	0
H2 mass fraction (-)	0.112	0	0
O2 mass fraction (-)	0	0.03	0.232

Table 6: Numerical Settings of the Reference Case

Turbulent Schmidt Number	0.7
Turbulent Prandtl Number	0.85
$k-\epsilon$ model constant $C_{1\epsilon}$	1.60
Combustion Model	Eddy Dissipation Concept
EDC model version	'EDC1996'
EDC model constant	standard
Canonical reactor	PFR
Kinetic mechanism	KEE
Boundary conditions	uniform
Radiation model	none
Multi-component molecular diffusion	on

the jet exit. Since no velocity profiles are provided in the experimental data base, uniform inlet velocity is specified based on the Reynolds number.

The transient solver edcPimpleSMOKE based on the open source software OpenFOAM® is used. The solver and EDC model implementation come from edcSMOKE [46, 47].

A reference case is defined to have a clear understanding of the discrepancies between the different cases in the sensitivity analysis. The numerical settings of the reference case are listed in Table 6. The multi-component molecular diffusion is included because of the existence of Hydrogen in the fuel. Radiation effects are neglected, because preliminary simulations with both OpenFOAM® and ANSYS Fluent 14.5 [38] solvers have shown that they have a very minor impact on the results.

4. Results and Discussion

In this section, the simulation results compared with the experimental measurements are presented and discussed. Based on the reference case in Table 6, one parameter at time is investigated. The impact of the various parameters on the temperature and species mass fraction profiles represents the focus of this section.

4.1. Turbulence Model Parameters

We first discuss the impact of various $k-\epsilon$ model parameters on the results. They include the turbulent Schmidt number (Eqn. 5), the turbulent Prandtl number (Eqn. 4) and the $k-\epsilon$ model constant $C_{1\epsilon}$ (Eqn. 8).

4.1.1. Effect of the turbulent Schmidt and Prandtl numbers

The turbulent Schmidt number (Sc_t) in Eqn. 5 affects the turbulent mass diffusivity of the species. It is generally set to unity in the OpenFOAM® solvers as in Eqn. 6 to simplify the problem. According to Tominaga et al. [48], the values are widely spread from 0.2 to 1.3 depending on the geometry and flow properties. Tominaga et al. [48] also demonstrated that in axi-symmetric jets, $Sc_t = 0.7$ is recommend. Here, the results obtained with Sc_t numbers of 0.6, 0.7 and 1.0 are compared with experimental profiles. On the other hand, the turbulent Prandtl number (Pr_t) in Eqn. 4 impacts the turbulent heat flux in energy equation (see Eqn. 3). When the simplest Reynolds analogy [49] is used, it yields $Pr_t = 1.0$. But according to experimental data, Pr_t has an average value of 0.85 [50].

As far as the turbulent Schmidt number is concerned, the mean temperature profiles with varying Sc_t are presented in Fig. 2. It can be observed that with higher Sc_t, turbulent mass diffusivity is decreased, thus the over-prediction of the peak temperature at axial positions of 60 *mm* and 120 *mm* can be alleviated. On the centerline, for $Sc_t = 1.0$, there is an obvious under-prediction of the temperature profile, especially starting from 120 *mm* onward. With $Sc_t = 0.7$, the centerline temperature profile is well predicted. As a result, it is concluded that using $Sc_t = 0.7$ is the most appropriate choice for the current study.

Figure 3 shows the comparison between the temperature profiles obtained using $Pr_t = 1.0$ and $Pr_t = 0.85$, respectively. In general, small differences can be observed, although a value of $Pr_t = 0.85$ results in better agreement with the experimental data. Moreover, the temperature peak at 120 *mm* is slightly suppressed when $Pr_t = 0.85$.

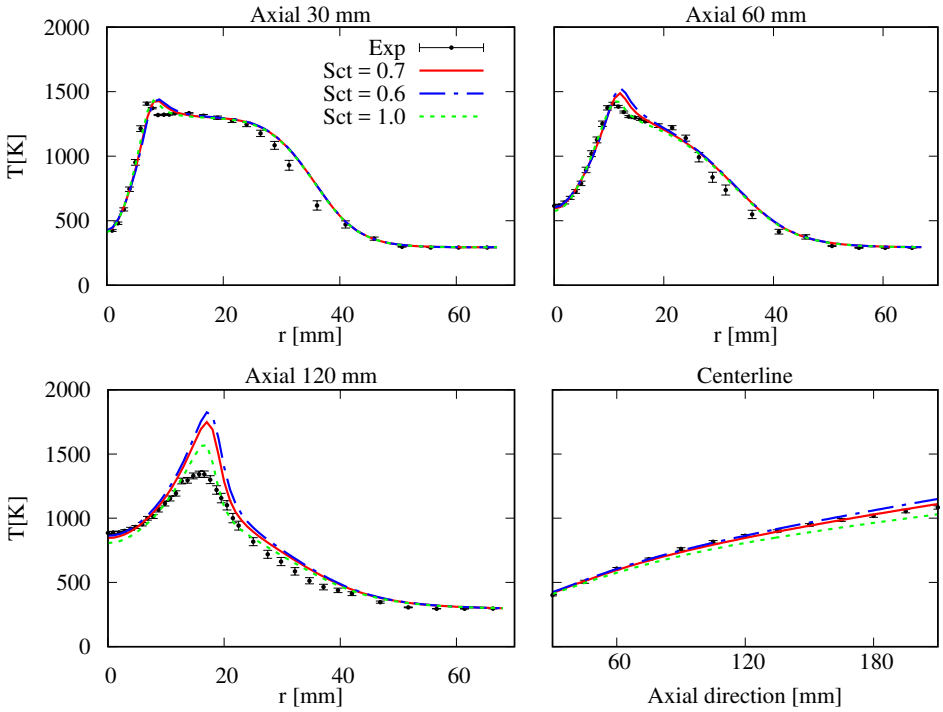

Figure 2: Effects of turbulent Schmidt number on predicted mean temperature profiles at several axial locations in radial direction and along the centerline.

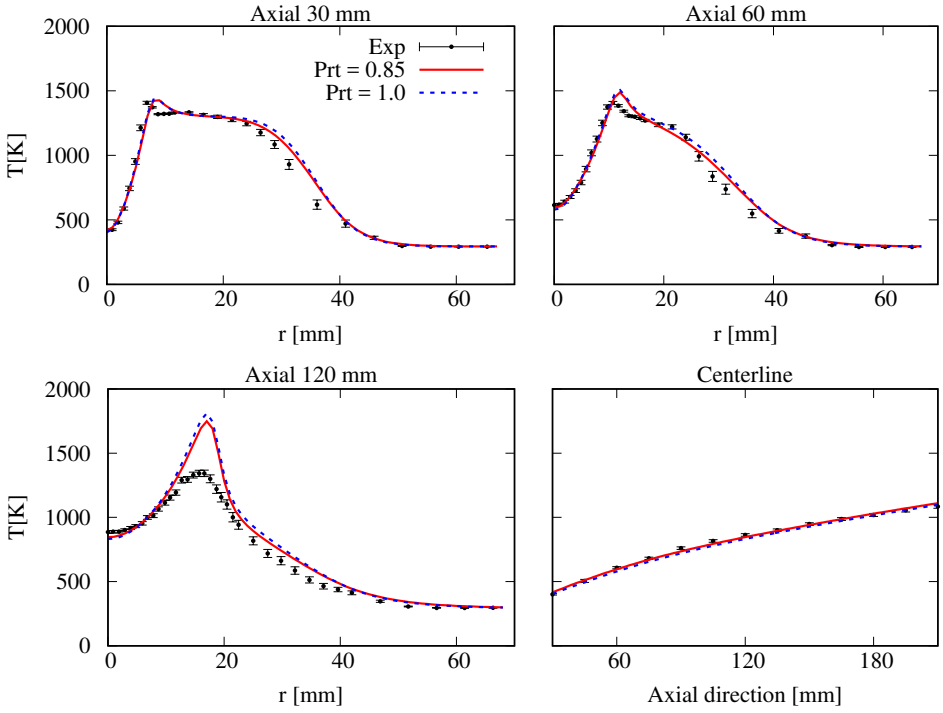

Figure 3: Effects of turbulent Prandtl number on predicted mean temperature profiles at several axial locations in radial direction and along the centerline.

In conclusion, the values of $Sc_t = 0.7$ and $Pr_t = 0.85$ are considered more suitable for the present case and used for all subsequent simulations.

4.1.2. k-ϵ model constant

In a round jet flow, Dally et al. [51] confirmed that there is an over-prediction of decay rate and the spreading rate when the standard $C_{1\epsilon}$ constant value [37] is applied in the k-ϵ model. The authors concluded that $C_{1\epsilon} = 1.60$ helped to improve the prediction of the flow and mixing field. This was confirmed by the other authors ([20, 26]) as well. In this paper, the same conclusion can be made under the condition that the 'EDC1996' version (in Eqn. 11) of the combustion model is used. In Fig. 4, the advantages of setting $C_{1\epsilon} = 1.60$ over $C_{1\epsilon} = 1.44$ are very clear. For the model versions 'EDC1981' and 'EDC2005', the results are discussed in the following subsection.

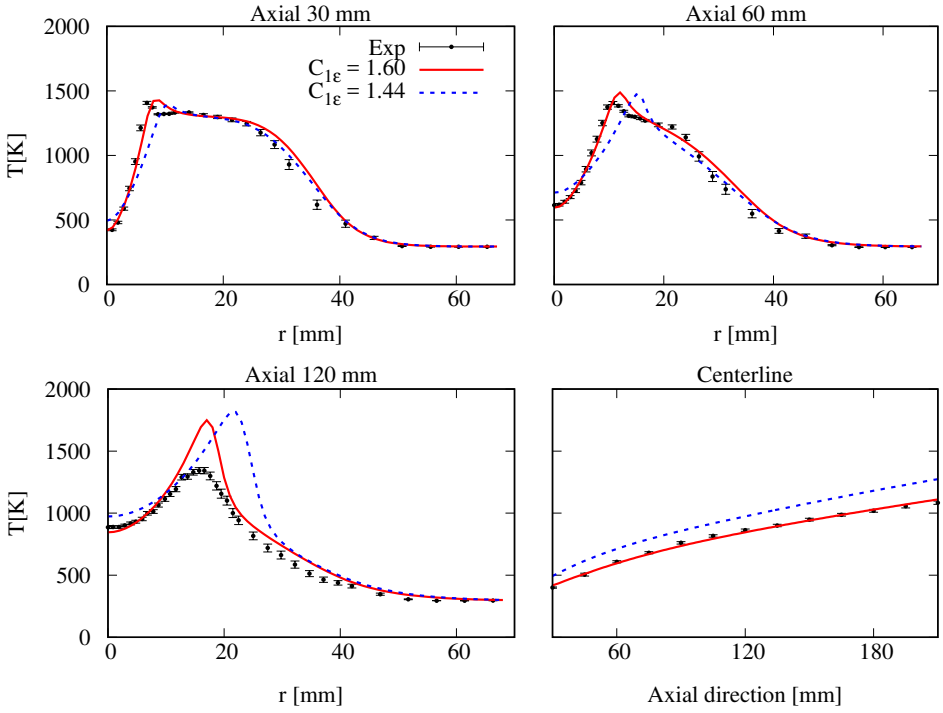

Figure 4: Effects of k-ϵ model parameter $C_{1\epsilon}$ on predicted mean temperature profiles at several axial locations in radial direction and along the centerline (EDC model version: 'EDC1996').

4.2. Combustion Model Parameters

In this subsection, the effects of the combination of EDC formulations and $C_{1\epsilon}$ value mentioned in Section 4.1.2 will be further discussed, along with the effect of the EDC model constants and canonical reactors simulating the fine structures.

4.2.1. EDC model formulation

The earliest 'EDC1981' formulation was indicated in Eqn. 13. When it is combined with two different $C_{1\epsilon}$ value, the results shown in Fig. 5 are obtained. Here, the adjusted $C_{1\epsilon}$ constant has the advantages of better predicting the experimental values.

However, the 'EDC2005' model formulation shows different features. In Fig. 6, the case with $C_{1\epsilon} = 1.44$ better predicts the experimental values than that with $C_{1\epsilon} = 1.60$. This indicates the existence of a strong interplay between turbulence and combustion model formulations. In particular, the evaluation of the mean mass fraction using Eqns. 12 and 15 has the strongest impact on the results. If it is assumed that the fine structures are localised in nearly constant energy regions (Eqn. 15), then the most appropriate choice is the use of the standard formulation of the k-ϵ model, as the over-estimation of the jet spread [52] is compensated by a reduced mass exchange between the fine structures and the surroundings. When the round-jet analogy is corrected by a modified $C_{1\epsilon}$ constant, it is clear that the most appropriate assumption for the EDC model is that the mass exchange between the fine structures is volumetric (Eqn. 12).

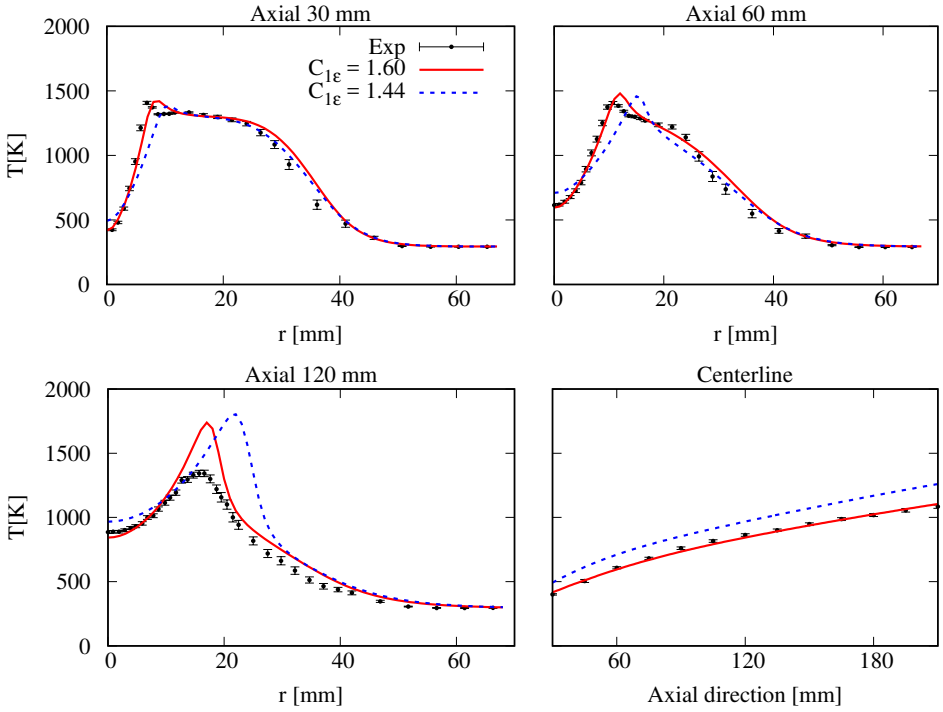

Figure 5: Effects of k-ϵ model parameter $C_{1\epsilon}$ on predicted mean temperature profiles at several axial locations in radial direction and along the centerline (EDC model version: 'EDC1981').

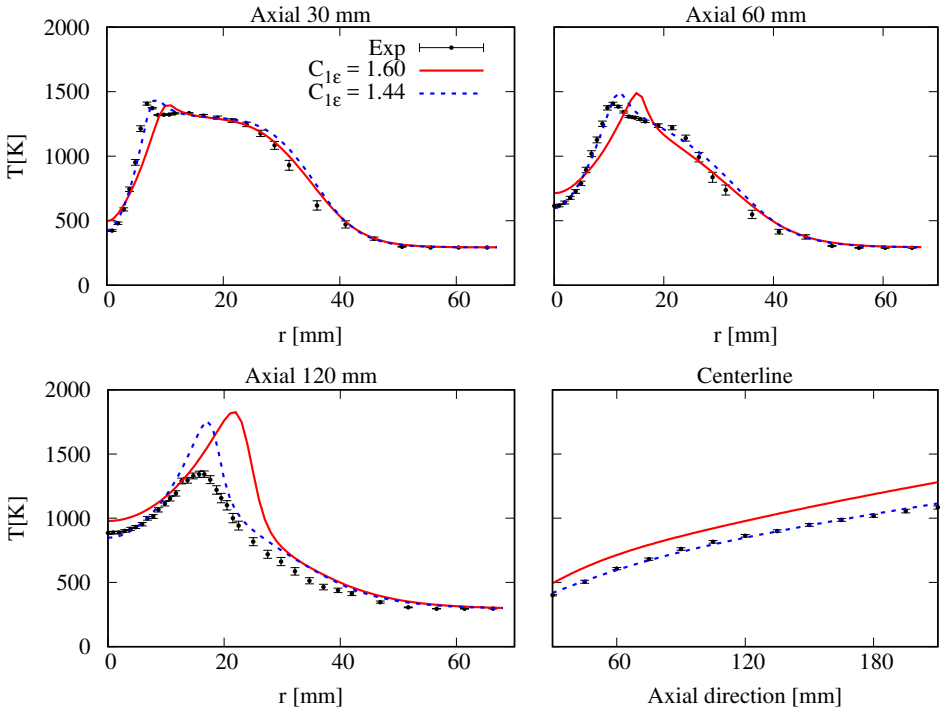

Figure 6: Effects of k-ϵ model parameter $C_{1\epsilon}$ on predicted mean temperature profiles at several axial locations in radial direction and along the centerline (EDC model version: 'EDC2005').

4.2.2. EDC model constants

From the former results (Fig. 2 - Fig. 6), it is not hard to find out that there is an obvious over-prediction of the peak temperature downstream of the jet, especially at the position of 120 *mm*. This agrees with the outcome from Christo et al. [20]. There are different authors [53, 19, 54, 32] who used the approach of adjusted EDC constants to alleviate the over-predicted temperature peak. Among them, the adjustment proposed by Parente et al. [32] is not simply based on a fitting procedure, but it arises from a phenomenological analysis on the chemical and fluid dynamics scales in MILD combustion.

Therefore, the adjustment of the EDC constants from Parente et al. [32] is adopted here in order to reduce the peak temperature. The model constant C_γ is decreased from 2.1377 to 1.9 and C_τ is increased from 0.4083 to 1.47. This setting is denoted as 'Adjusted-1'. It results in a decreased fine structures mass fraction and increased residence time. The results of the mean temperature values can be found in Fig. 7. The temperature peaks are successfully suppressed by 6.5% and 10.8% at axial positions of 60 and 120 *mm* respectively. However, temperature peak at axial position of 120 *mm* is still over-predicted by 17.9%. In order to further investigate the effect of the model constants , a second set of adjusted values is used,

with $C_\gamma = 1.5$ and $C_\tau = 1.47$. It is indicated as ′Adjusted-2′. Compared with the standard values of the parameters, the ′Adjusted-2′ constants reduce the temperature peak at 120 *mm* axial location by 17.1%. This has however an effect on the centerline temperature, which is reduced slightly with respect to the experimental values.

The effect of the adjusted EDC parameters on the flow field is also investigated. Because the lack of experimental velocity profile, the mixture fraction profile constructed from the Bilger's definition [39] is shown in Fig. 8. The profiles from three set of parameters (Standard, Adjusted-1 and Adjusted-2) are virtually identical, with very minor differences visible only on the centerline starting from 120 *mm* axial position. This indicates that the modification of the model constants only impacts the species and temperature profile, with a negligible effect on the turbulent mixing field.

Overall, the proposed EDC constants by Parente et al. [32] (′Adjusted-1′) help to alleviate the temperature over-prediction at axial locations above 60 *mm* from the burner exit. However, the observed reduction of the temperature peak in the present work is less significant to the one shown by Parente et al. [32], and comparable results can be obtained only using the ′Adjusted-2′ settings. This discrepancies can be likely attributed to the different discretization schemes used. Indeed, the present investigation is based on the half second order discretization schemes of Total Variation Diminishing (TVD) on the divergence terms, while the results by Parente et al. [32] were obtained using the fully second order schemes of Linear Upwind (LUD) or Central Differencing Scheme (CDS) on the divergence term.

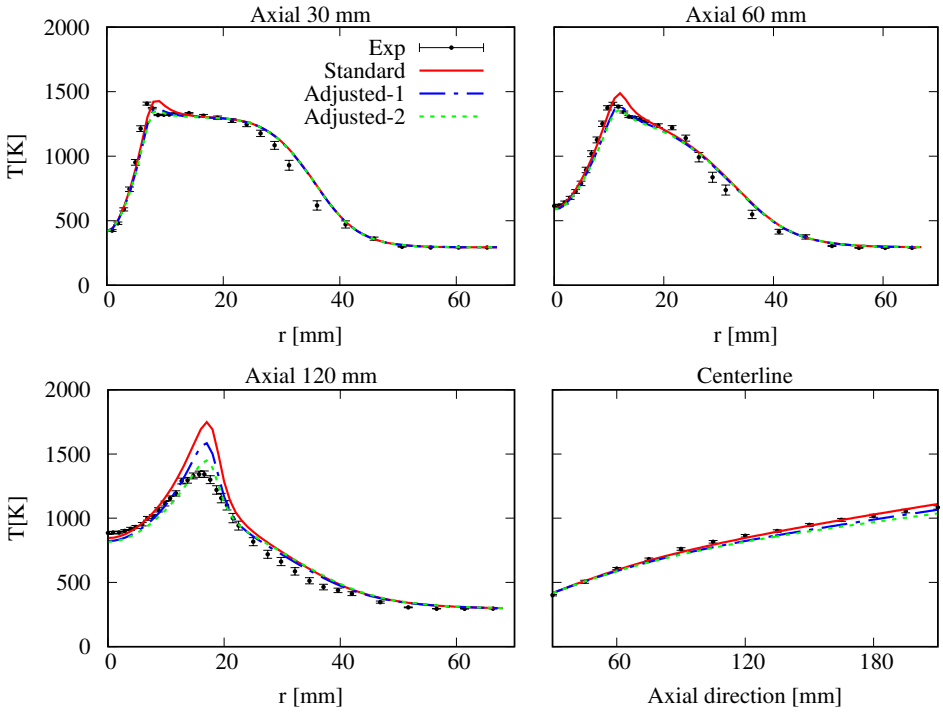

Figure 7: Effects of the adjusted EDC constants on predicted mean temperature profiles at several axial locations in radial direction and along the centerline.

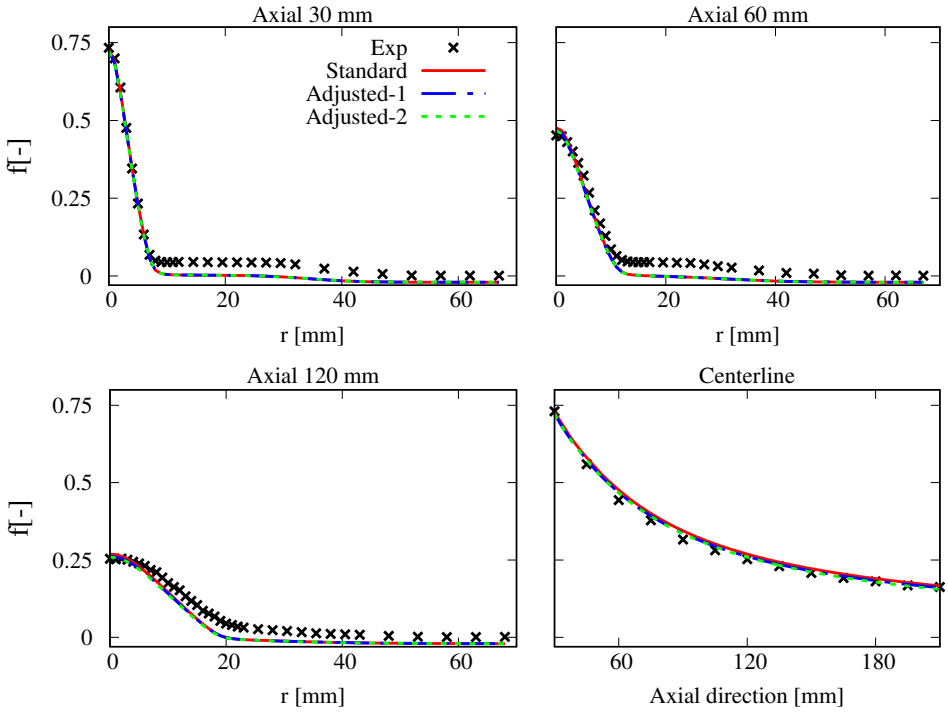

Figure 8: Effects of the adjusted EDC constants on mixture fraction profiles at several axial locations in radial direction and along the centerline.

4.2.3. PSR vs. PFR closures for the fine structures

The Perfectly Stirred Reactor (PSR) is generally used as the canonical reactor to simulate the fine structures in EDC model. Numerically speaking, the use of Plug Flow Reactor (PFR) can help improving the robustness. That's because PFR is described by a set of Ordinary Differential Equations (ODEs) with initial conditions, while a PSR is described by a set of algebraic non-linear equations, whose solution requires an iterative procedure. Moreover, even though the solution of a ODE system is generally more expensive than an algebraic non-linear system, the PFR can be more easily combined with tabulation method like In-situ Adapted Tabulation (ISAT) to increase computational efficiency. The purpose of this subsection is to determine whether PFR can be used instead of PSR without loss of accuracy. The comparison of the results obtained with the two approaches is shown in Fig. 9, Fig. 10 and Fig. 11, for the temperature, H_2O, OH and CO mass fraction profiles, respectively. The mean temperature profiles as well as the mean H_2O mass fraction from the cases with PFR and PFR are very close to each other and virtually identical. The same conclusion holds for other major species. For the minor species, the profiles of CO and OH at axial positions of 30 *mm* and 60 *mm* show close results with PSR and PFR in Fig. 11. Therefore, PFR can be

used instead of PSR in EDC model, to simulate the fine structures.

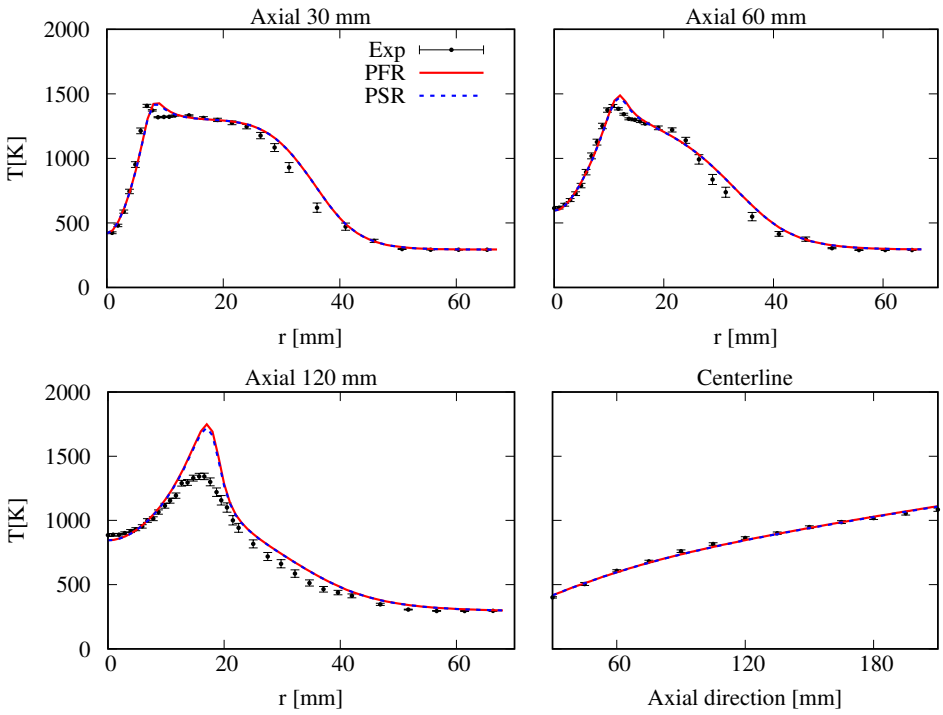

Figure 9: Effects of the canonical reactor (PFR vs. PSR) on predicted mean temperature profiles at several axial locations in radial direction and along the centerline.

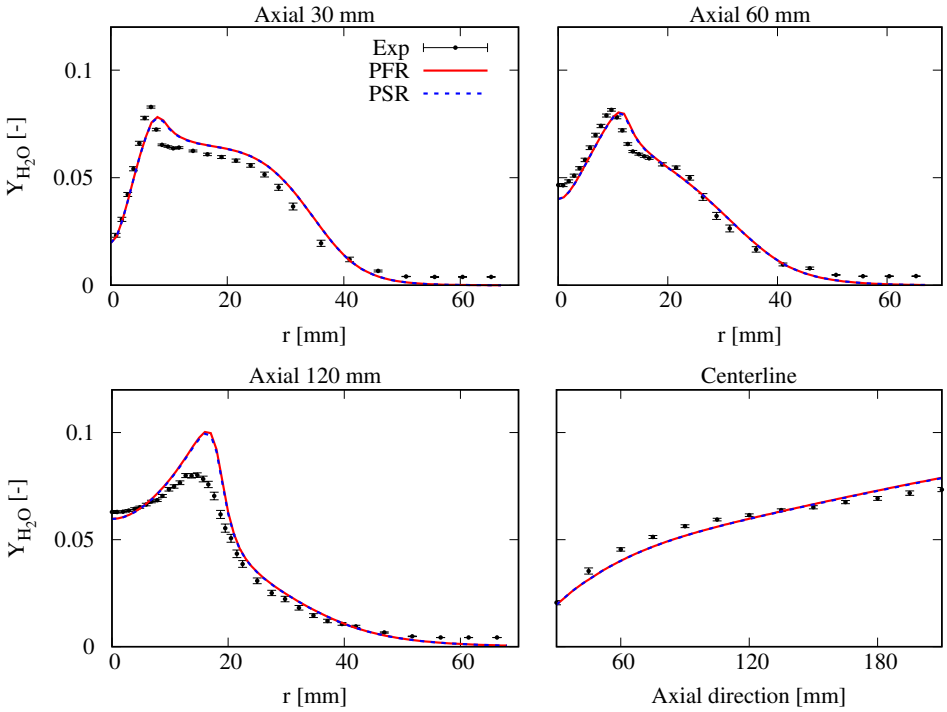

Figure 10: Effects of the canonical reactor (PFR vs. PSR) on predicted mean H_2O mass fraction profiles at several axial locations in radial direction and along the centerline.

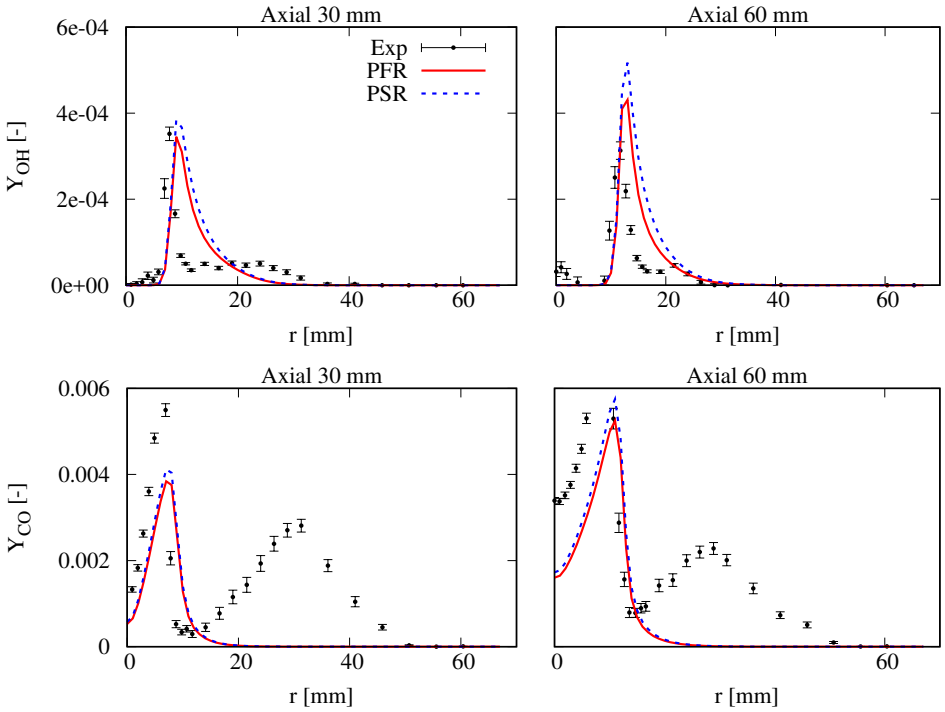

Figure 11: Effects of the canonical reactor (PFR vs. PSR) on predicted mean OH and CO mass fraction profiles at 30 *mm* and 60 *mm* axial locations in radial direction.

4.2.4. EDC VS. PaSR

In this part, the results from EDC model and the newly implemented PaSR model are benchmarked.

Fig. 12 shows the experimental profiles of temperature as well as the computed ones using EDC and PaSR models at different axial locations and along the centerline. It can be observed that the PaSR model reduced the temperature over-prediction at axial position 60 *mm*. Most importantly, the highly over-predicted 120 *mm* temperature peak is alleviated to a large extent. The similar conclusion can be drawn looking at the CO_2 mass fraction profiles, shown in Fig. 13. In particular, NO emissions are largely over-predicted (more then two times) using EDC model, as a result of the temperature over-prediction. Conversely, predictions based on the PaSR model are quite accurate, at both 120 *mm* and 200 *mm* axial locations.

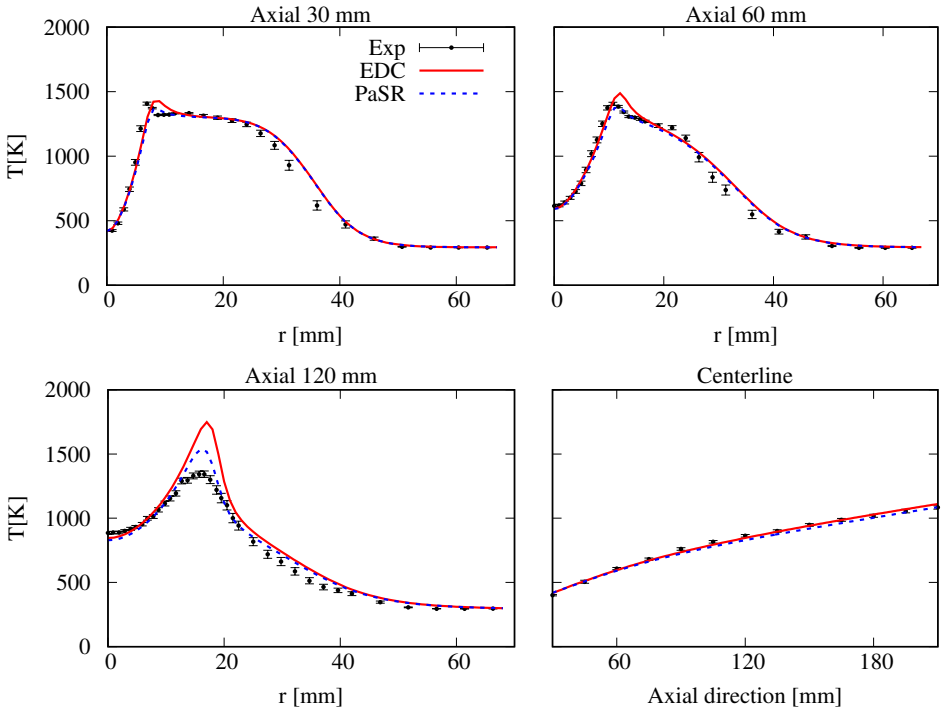

Figure 12: Comparison between the experimental and numerical mean temperature profiles at several axial locations in radial direction and along the centerline. Combustion models: EDC and PaSR.

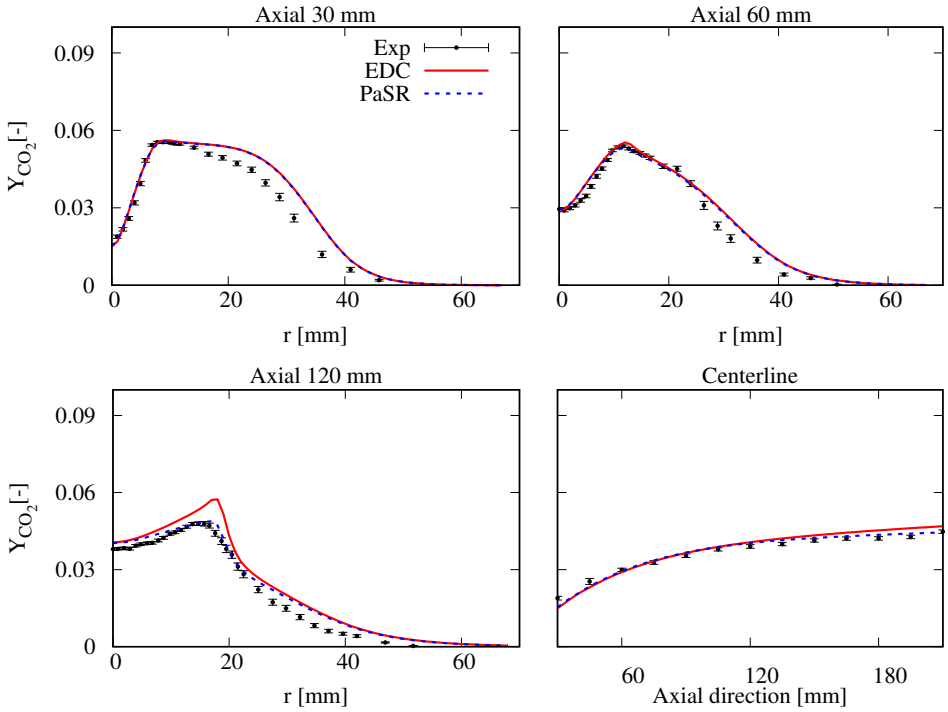

Figure 13: Comparison between the experimental and numerical mean CO_2 mass fraction profiles at several axial locations in radial direction and along the centerline. Combustion models: EDC and PaSR.

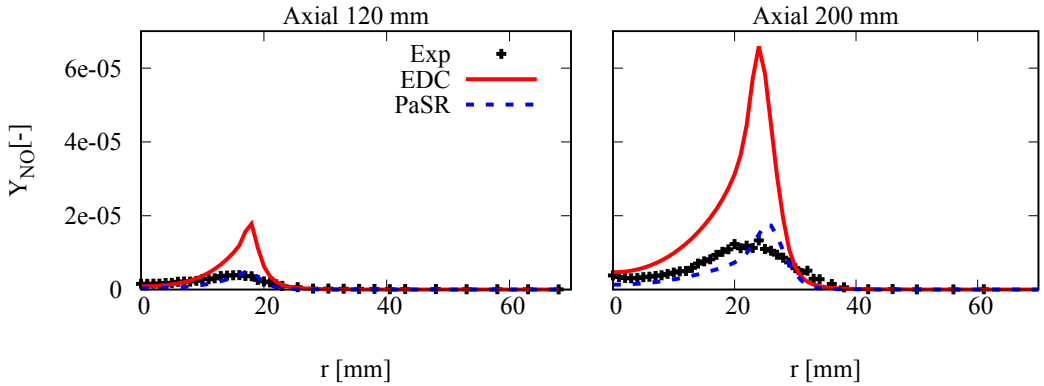

Figure 14: Comparison of the mean NO mass fraction radial profiles using the EDC and PaSR models at 120 *mm* and 200 *mm* axial locations.

4.3. Boundary Conditions

In RANS simulation, uniform inlet boundary values of the species, velocity and temperature are generally used. In the current work, the profiles of species mass fractions and temperature accessible from the experimental data at 4 *mm* from the burner exit are used to

simulate non-uniform boundary conditions. Thus, the simulation results with the uniform and non-uniform boundary conditions are compared in Fig. 15, Fig. 16 and Fig. 17, where the mean profiles of temperature, H_2O mass fraction and CO mass fraction are presented, respectively.

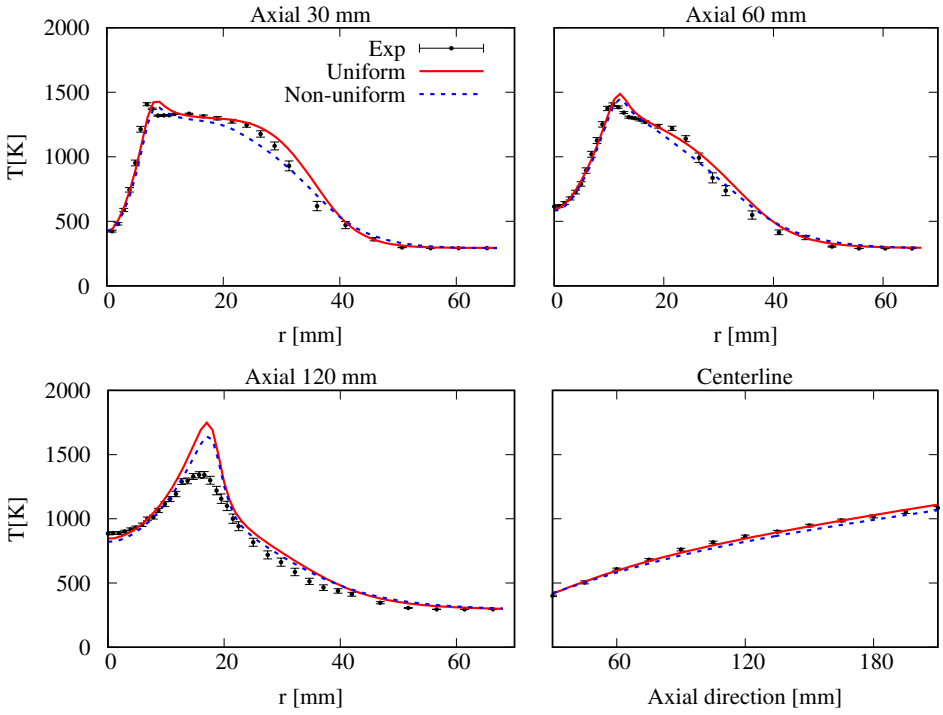

Figure 15: Comparison of the mean temperature profiles from the cases with uniform boundary conditions and non-uniform boundary conditions at several axial locations in radial direction and along the centerline.

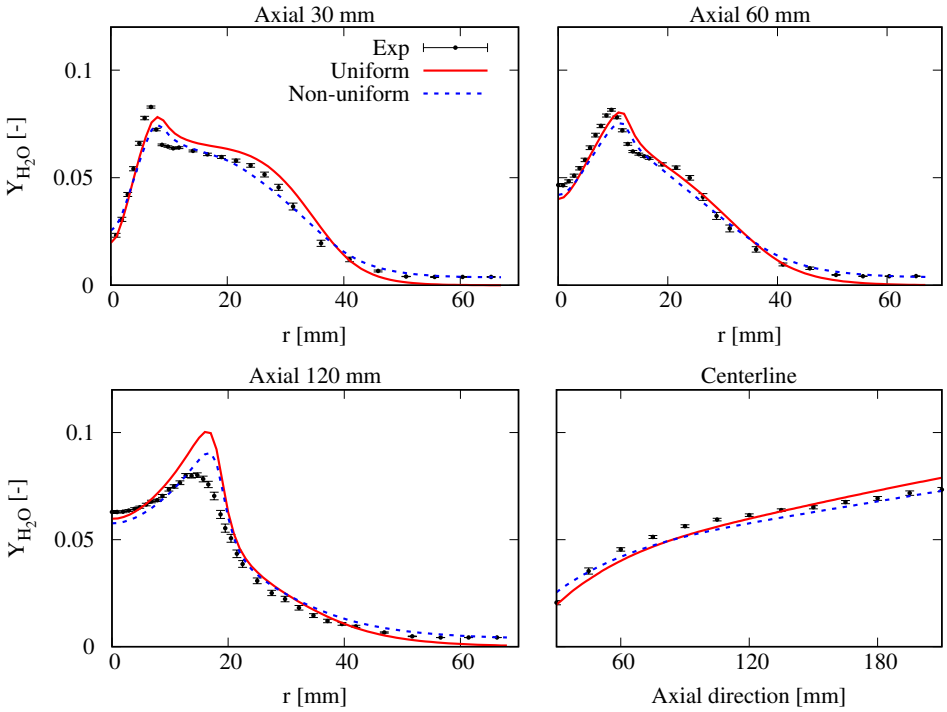

Figure 16: Comparison of the mean H_2O mass fraction profiles from the cases with uniform boundary conditions and non-uniform boundary conditions at several axial locations in radial direction and along the centerline.

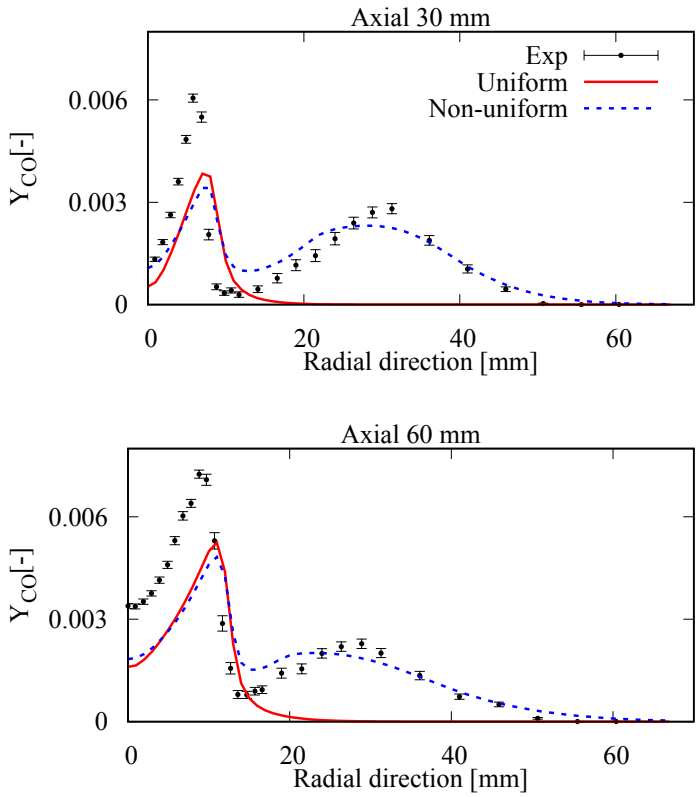

Figure 17: Comparison of the mean CO mass fraction profiles from the cases with uniform boundary conditions and non-uniform boundary conditions at 30 *mm* and 60 *mm* axial locations in radial direction.

In Fig. 15, it can be observed that the non-uniform boundary conditions help to reduce the peak temperature at the different axial positions, and the centerline temperature is also slightly decreased. The differences between using the uniform and non-uniform boundary conditions can be better identified in Fig. 16. In the near centerline regions, the H_2O mass fraction values are not well predicted by the non-uniform boundary conditions, while the values far from the centerline are well predicted. In particular, the use of non-uniform boundary conditions allows to recover the non-zero values of H_2O mass fractions at axial positions corresponding to 30 and 60 *mm*. The over prediction of H_2O mass fraction values at axial position of 120 *mm* and along the centerline is alleviated with non-uniform boundary conditions. However, at 30 and 60 *mm* axial positions, the peak mass fraction is not well predicted, and a general under-prediction can be observed. The obvious advantage of using the non-uniform boundary conditions is revealed by the analysis of CO profiles in Fig. 17. The experimental data show two peaks for the mean CO mass fraction at different radial positions. When uniform boundary conditions are applied, only one peak appears in the CO mass fraction profiles. The second peak can be recovered by providing non-uniform boundary conditions.

In conclusion, the non-uniform boundary conditions help to better predict the jet surrounding regions. Nevertheless, it shows some deficiencies in predicting the major species H_2O in the jet core region.

4.4. Multi-component Molecular Diffusion

Because of the presence of H_2 in the fuel stream, it is necessary to consider the effect of molecular diffusivity of the calculated profiles. The inclusion of multi-component molecular diffusion is carried out following Eqn. 5. Moreover, the transport of enthalpy due to species diffusion is included in the energy equation. The mean temperature profiles with and without multi-component molecular diffusion are shown in Fig. 18. It can be observed that, without molecular diffusion, it is not possible to capture the correct temperature peak at 30 *mm* axial position and along the centerline. The temperature peak without molecular diffusion is 5% lower than the experimental one at axial position of 30 *mm*. A slight temperature over-prediction can be observed using molecular diffusion at 60 and 120 *mm* axial positions. However, this can be suppressed using the adjusted EDC constants C_γ and C_τ, as indicated in Section 4.2.2. Furthermore, as shown in Fig. 19, the inclusion of the multi-component molecular diffusion term helps increasing the accuracy of H_2O predictions near centerline regions. The peak values of H_2O at axial positions of 30 and 60 *mm* are increased by about 13-15% with the inclusion of molecular diffusion.

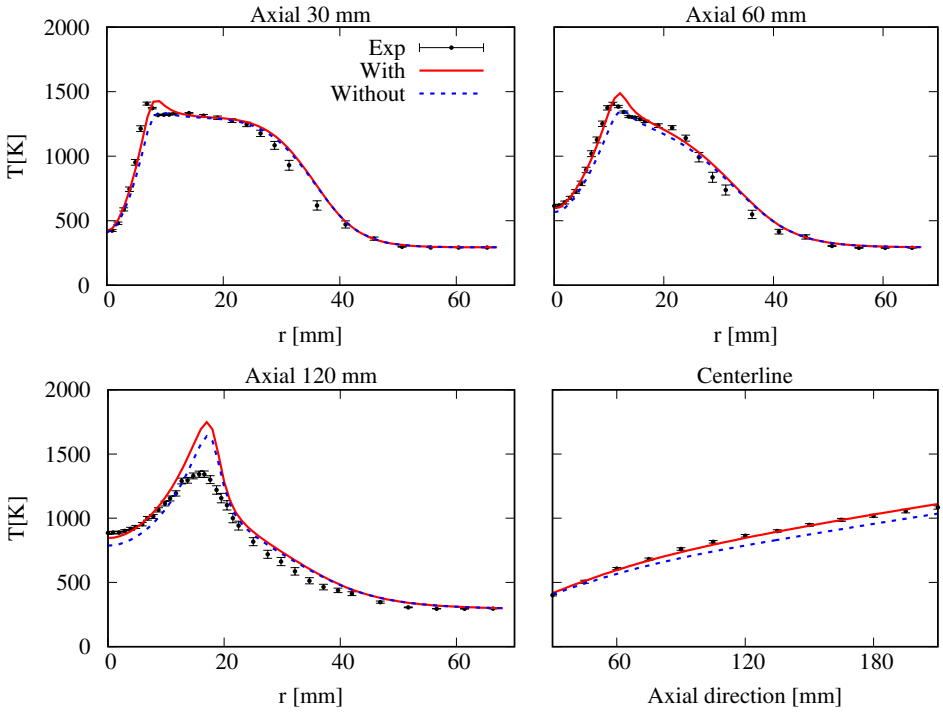

Figure 18: Comparison of the mean temperature profiles from the cases with and without multi-component molecuar diffusion at several axial locations in radial direction and along the centerline.

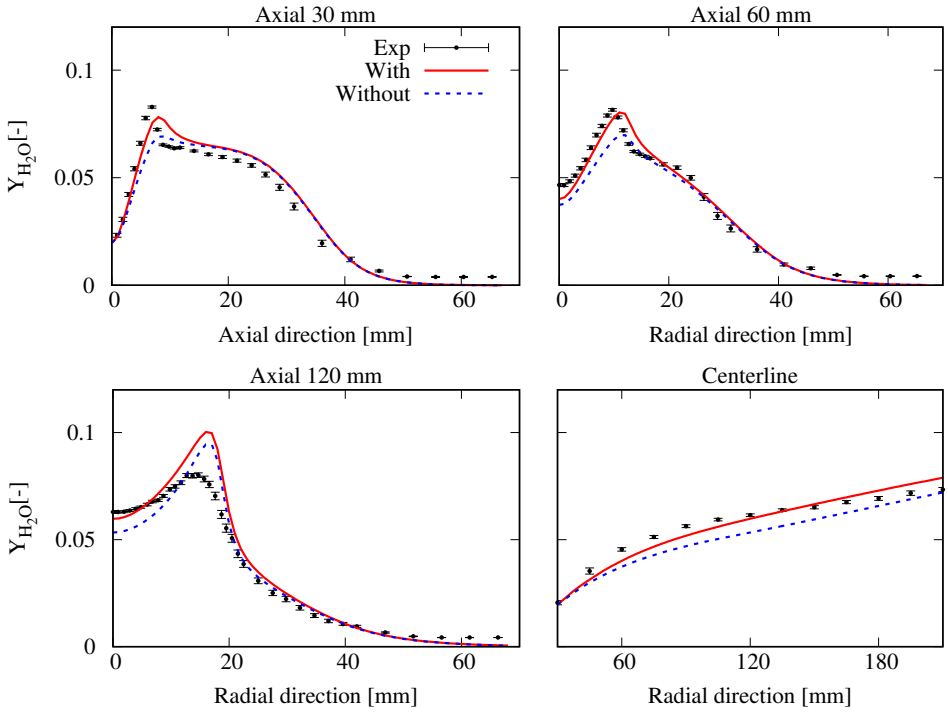

Figure 19: Comparison of the mean H_2O mass fraction profiles from the cases with and without multi-component molecuar diffusion at several axial locations in radial direction and along the centerline.

4.5. Kinetic Mechanisms

In MILD combustion, the use of detailed mechanisms is essential to capture finite rate chemistry effects. The EDC model closure allows to account for detailed chemistry via the canonical reactors used to model the fine structures. In the present work, the KEE, GRI3.0, San-Diego and POLIMI_C1C3HT mechanisms were chosen, as mentioned in Section 3.2.1, with the objective of determining the degree of complexity required to correctly capture the main features of the combustion regime. The sampled numerical profiles obtained with the mechanisms are compared with experimental data in Fig. 20 and Fig. 21 . The main observation is that the results provided by the different mechanisms do not show major differences. The GRI3.0, San-Diego and POLIMI_C1C3HT mechanisms correct the slightly over-predicted centerline mean temperature, with respect to the predictions of the KEE mechanism. The same trend can be observed for the major species mass fractions. For other species, minor differences are observed for the OH radical (Fig. 21 top), while the KEE mechanism better captures the CO peak value. On the other hand, the simulation cost of GRI3.0, San-Diego and POLIMI_C1C3HT is 3.7, 4.8 times and 14.3 times the cost of KEE, respectively. This makes the usage of large mechanisms not strictly necessary in the current

case.

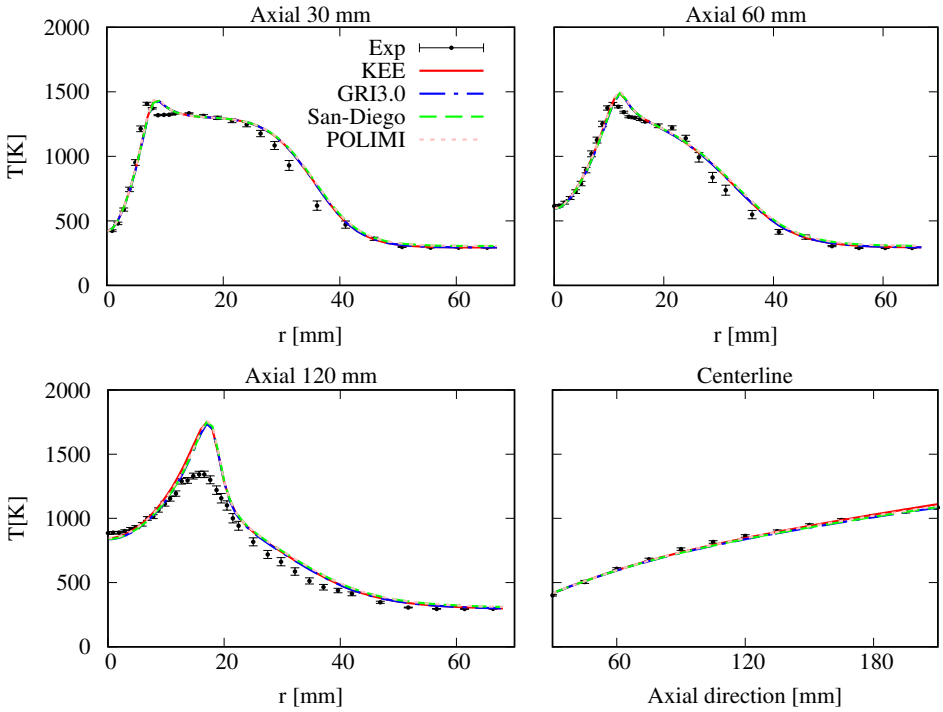

Figure 20: Comparison of the mean temperaturehe profiles from the cases with different kinetic mechanisms at several axial locations in radial direction and along the centerline.

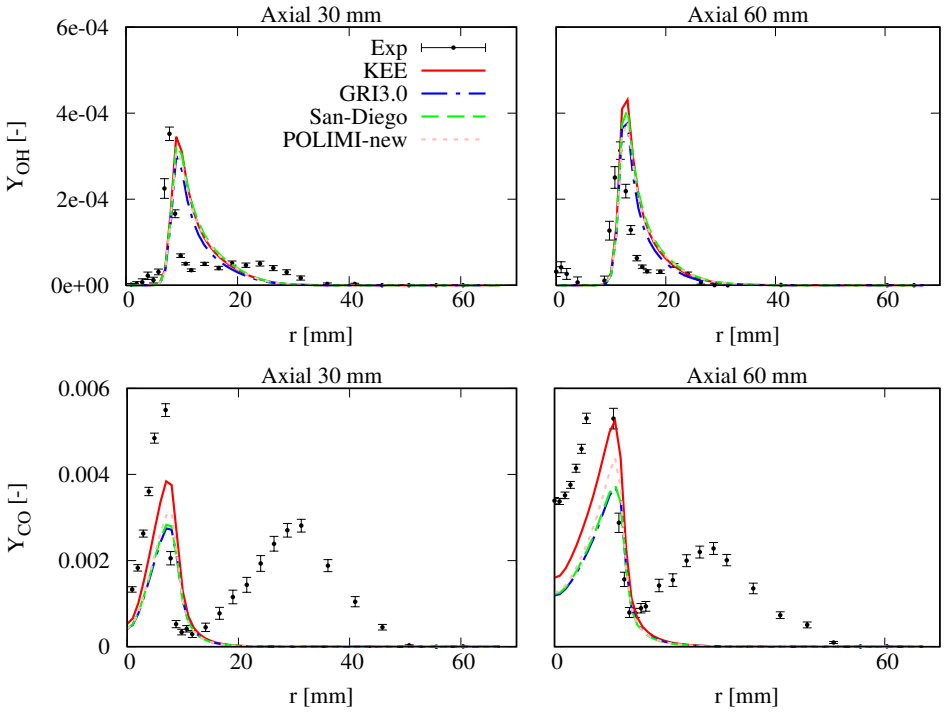

Figure 21: Comparison of the OH and CO mass fraction profiles from the cases with different kinetic mechanisms at 30 *mm* and 60 *mm* axial locations in radial direction.

5. Conclusion

In the present work, the Adelaide Jet in Hot Co-flow burner was numerically investigated by means of RANS simulations with detailed kinetic mechanisms. The study focuses on the effect of various parameters on the results, including turbulence model parameters (the turbulent Schmidt number, turbulent Prandtl number, $k-\epsilon$ model constant), the combustion model formulation (formulation of EDC and PaSR, combustion model constants and choice of the canonical reactors simulating the fine structures), boundary conditions definition, multi-component molecular diffusion and degree of complexity of the kinetic mechanisms.

The main results can be summarised as follows:

– The combination of $Sc_t = 0.7$ and $Pr_t = 0.85$ helps increasing the prediction accuracy.

– A strong interplay between combustion and turbulence model formulation is found. In particular, the EDC formulations 'EDC1981' and 'EDC1996' result in a better agreement with the experimental data when the $k-\epsilon$ model constant $C_{1\epsilon} = 1.60$. When $C_{1\epsilon} = 1.44$, the 'EDC2005' formulation provides the best results.

– The fine structures can be modelled using PFR equations without loss of accuracy. This helps increasing the robustness of calculation and offers the potential of a more straightforward coupling with tabulation method like In-situ Adaptive Tabulation (ISAT).

– The use of non-uniform boundary conditions allows improving species predictions, especially away from centerline region.

– Multi-component molecular diffusion is found to play an important role, due to the presence of H_2 in the fuel. This is in agreement with the work carried out by Christo et al. [20] and Mardani et al. [31].

– Minor differences in the predictions are observed between using KEE mechanism and kinetic mechanisms with increasing complexity (GRI3.0, San-Diego and POLIMI_C1C3HT). The use of a more comprehensive mechanism nevertheless improves the prediction of the centerline temperature.

– The over-prediction of the temperature peak at 120 *mm* axial position with EDC model can be alleviated by using modified constants.

– The benchmark between EDC and PaSR models shows that both models are suitable for simulating MILD regimes. Further investigations are needed for the PaSR model, in order to clarify the effect of turbulent and chemical time scale calculations on the predictions.

The developed model is characterised by sufficient complexity to allow its application in presence of gaseous mixtures with various components, including hydrogen. This is a very attractive feature of the approach towards its application to model modern combustion technologies designed to deal with multiple fuels and non-conventional combustion regimes.

6. Acknowledgement

This project has received funding from the European Union′s Horizon 2020 research and innovation program under the Marie Skłodowska-Curie grant agreement No 643134, and from the Fédération Wallonie-Bruxelles, via ′Les Actions de Recherche Concertée (ARC)′ call for 2014 - 2019, to support fundamental research.

References

[1] J. A. Wünning and J. G. Wünning. Flameless oxidation to reduce thermal NO-formation. *Progress in Energy and Combustion Science*, 23:81–94, 1997.

[2] A. Cavaliere and M. de Joannon. MILD combustion. *Progress in Energy and Combustion Science*, 30:329–366, 2004.

[3] B. B. Dally, E. Riesmeier, and N. Peters. Effect of fuel mixture on moderate and intense low oxygen dilution combustion. *Combustion and Flame*, 137:418–431, 2004.

[4] M. de Joannon, G. Sorrentino, and A. Cavaliere. MILD combustion in diffusion-controlled regimes of hot diluted fuel. *Combustion and Flame*, 159:1832–1839, 2012.

[5] Xuan Gao, Fei Duan, Seng Chuan Lim, and Mee Sin Yip. NOx formation in hydrogen-emethane turbulent diffusion flame under the moderate or intense low-oxygen dilution conditions. *Energy*, 59:559–569, 2013.

[6] Yizhuo He, Chun Zou, Yu Song, Yang Liu, and Chuguang Zheng. Numerical study of characteristics on NO formation in methane MILD combustion with simultaneously hot and diluted oxidant and fuel (HDO/HDF). *Energy*, 112:1024–1035, 2016.

[7] Marco Ferrarotti, Chiara Galletti, Alessandro Parente, and Leonardo Tognotti. Development of reduced NOx models for flameless combustion. In *18th IFRF Members Conference*, 2015.

[8] G. G. Szegö, B. B. Dally, and G. J. Nathan. Scaling of NOx emissions from a laboratory-scale MILD combustion furnace. *Combustion and Flame*, 154:281–295, 2008.

[9] Amir Mardani, Sadegh Tabejamaat, and Shahla Hassanpour. Numerical study of CO and CO2 formation in CH4/H2 blended flame under MILD condition. *Combustion and Flame*, 160:1636–1649, 2013.

[10] Yaming Liu, Sheng Chen, Shi Liu, Yongxin Feng, Kai Xu, and Chuguang Zheng. Methane combustion in various regimes: First and second thermodynamic-law comparison between air-firing and oxyfuel condition. *Energy*, 115:26–37, 2016.

[11] A. Mardani and A. Fazlollahi Ghomshi. Numerical study of oxy-fuel MILD (Moderate or intense Low-oxygen Dilution combustion) combustion for CH4/H2 fueli. *Energy*, 99:136–151, 2016.

[12] Pengfei Li and Jianchun Mi. Influence of inlet dilution of reactants on premixed combustion in a recuperative furnace. *Flow Turbulence and Combustion*, 87:617–638, 2011.

[13] B. B. Dally, A. N. Karpetis, and R. S. Barlow. Structure of turbulent non-premixed jet flames in a diluted hot coflow. *Proceedings of the Combustion Institute*, 29:1147–1154, 2002.

[14] E. Oldenhof, Mark J. Tummers, E.H. van Veen, and D.J.E.M. Roekaerts. Ignition kernel formation and lift-off behaviour of Jet-in-Hot-Coflow flames. *Combustion and Flame*, 157:1167–1178, 2010.

[15] E. Oldenhof, Mark J. Tummers, E. H. van Veen, and D. J. E. M. Roekaerts. Role of entrainment in the stabilisation region of Jet-in-Hot-Coflow flames. *Combustion and Flame*, 158(8):1553–1563, 2011.

[16] Paul R. Medwell and Bassam B. Dally. Effect of fuel composition on jet flames in a heated and diluted oxidant stream. *Combustion and Flame*, 159:3138–3145, 2012.

[17] Paul R. Medwell, Peter A.M. Kalt, and Bassam B. Dally. Imaging of diluted turbulent ethylene flames stabilized on a Jet in Hot Coflow (JHC) burner. *Combustion and Flame*, 152:100–113, 2007.

[18] A. Parente, J. Sutherland, B. Dally, L. Tognotti, and P. Smith. Investigation of the MILD combustion regime via principal component analysis. *Proceedings of the Combustion Institute*, 33:3333–3341, 2011.

[19] Seyed Reza Shabanian, Paul Ross Medwell, Masoud Rahimi, Alessio Frassoldati, and Alberto Cuoci. Kinetic and fluid dynamic modeling of ethylene jet flames in diluted and heated oxidant stream combustion conditions. *Applied Thermal Engineering*, 52:538–554, 2012.

[20] F. C. Christo and B. B. Dally. Modelling turbulent reacting jets issuing into a hot and diluted coflow. *Combustion and Flame*, 142:117–129, 2005.

[21] A. Parente, C. Galletti, and L. Tognotti. Effect of the combustion model and kinetic mechanism on the MILD combustion in an industrial burner fed with hydrogen enriched fuels. *international journal of hydrogen energy*, 33:7553–7564, 2008.

[22] A. Parente, C. Galletti, and L. Tognotti. A simplified approach for predicting NO formatio in MILD combustion of CH4/H2 mixtures. *Proceeding of the Combustion Institute*, 33:3343–3350, 2011.

[23] Valentina Fortunato, Chiara Galletti, Leonardo Tognotti, and Alessandro Parente. Influence of modelling and scenario uncertainties on the numerical simulation of a semi-industrial flameless furnace. *Applied Thermal Engineering*, 76:324–334, 2014.

[24] Chiara Galletti, Alessandro Parente, and Leonardo Tognotti. Numerical and experimental investigation of a mild combustion burner. *Combustion and Flame*, 151:649–664, 2007.

[25] Bj/orn F. Magnussen. The eddy dissipation concept a bridge between science and technology. In *ECCOMAS Thematic Conference on Computational Combustion*, Lisbon, Portugal, 2005.

[26] Alessio Frassoldati, Pratyush Sharma, Alberto Cuoci, Tiziano Faravelli, and Eliseo Ranzi. Kinetic and fluid dynamics modeling of methane/hydrogen jet flames in diluted coflow. *Applied Thermal Engineering*, 30:376–383, 2009.

[27] Bjørn F. Magnussen. On the structure of turbulence and a generalized eddy dissipation concept for chemical reaction in turbulent flow. In *19th AIAA Aerospace Science Meeting*, St. Louis, Missouri, USA, January 1981.

[28] I.R. Gran and B. F. Magnussen. A numerical study of a bluff-body stabilized diffusion flame, part 2: Influence of combustion modelling and finite-rate chemistry. *Combustion Science and Technology*, 119(1-6):191–217, 1996.

[29] J. Chomiak. *Combustion: A Study in Theory, Fact and Application*. Abacus Press/Gorden and Breach Science Publishers, 1990.

[30] Feifei Wang, Pengfei Li, Zhenfeng Mei, and Jianpeng Zhang andJianchun Mi. Combustion of CH4 /O2 /N2 in a well stirred reactor. *Energy*, 72:242–253, 2014.

[31] Amir Mardani, Sadegh Tabejamaat, and Mohsen Ghamari. Numerical study of influence of molecular diffusion in the MILD combustion regime. *Combustion Theory and Modelling*, 14(5):747–774, 2010.

[32] Alessandro Parente, Mohammad Rafi Malik, Francesco Contino, Alberto Cuoci, and Bassam B. Dally. Extension of the eddy dissipation concept for turbulence/chemistry interactions to MILD combustion. *Fuel*, 163:98–111, 2015.

[33] H. G. Weller, G. Tabor, H. Jasak, and C. Fureby. A tensorial approach to computational continuum mechanics using object-oriented techniques. *COMPUTERS IN PHYSICS*, 12(6), 1998.

[34] Dmitry A. Lysenko, Ivar S. Ertesvåg, and Kjell Erik Rian. Numerical simulation of non-premixed turbulent combustion using the eddy dissipation concept and comparing with the steady laminar flamelet model. *Flow, Turbulence and Combustion*, 53:577–605, 2014.

[35] Markus Winterer. *Nanocrystalline Ceramics: Synthesis and Structure*. Number 43. Springer, 2002.

[36] I. Yimer, I. Campbell, and L. Y. Jiang. Estimation of the turbulent schmidt number from experimental profiles of axial velocity and concentration for high-reynolds-number jet flows. *Canadian Aeronautics and Space Journa*, 48(3):195–200, 2002.

[37] B. E. Launder and D. B. Spalding. The numerical computations of turbulent flows. *Computer Methods in Applied Mechanics and Engineering*, 1973.

[38] *ANSYS® Academic Research, Release 14.5*.

[39] R. W. Bilger, S. H. Stårner, and R. J. KEE. On reduced mechanisms for methane-air combustion in nonpremixed flames. *Combustion and Flame*, 80(2):135–149, 1990.

[40] Gregory P. Smith, David M. Golden, Michael Frenklach, Nigel W. Moriarty, Boris Eiteneer, Mikhail Goldenberg, C. Thomas Bowman, Ronald K. Hanson, Soonho Song, William C. Gardiner, Jr., Vitali V. Lissianski, and Zhiwei Qin.

[41] Chemical-kinetic mechanisms for combustion applications.

[42] E. Ranzi, A. Frassoldati, R. Grana, A. Cuoci, T. Faravelli, A.P. Kelley, and C.K. Law. Hierarchical and comparative kinetic modeling of laminar flame speeds of hydrocarbon and oxygenated fuels. *Progress in Energy and Combustion Science*, 38(4):468–501, 2012.

[43] Ashoke De, Ernst Oldenhof, Pratap Sathiah, and Dirk Roekaerts. Numerical simulation of Delft-Jet-in-Hot-Coflow (DJHC) flames using the eddy dissipation concept model for turbulencechemistry interaction. *Flow Turbulence Combustion*, 87:537–567, 2011.

[44] Fabian Peng Kärrholm. *Numerical Modelling of Diesel Spray Injection, Turbulence Interaction and Combustion*. PhD thesis, Chalmers University of Technology, 2008.

[45] P.J. Roache. *Fundamentals of Computational Fluid Dynamics*. Hermosa Publishers, 1998.

[46]

[47] M. R. Malik, Z. Li, A. Cuoci, and A. Parente. Edcsmoke: A new combustion solver based on openfoam. In *Tenth Mediterranean Combustion Symposium*, 2017.

[48] Yoshihide Tominaga and Ted Stathopoulos. Turbulent schmidt numbers for CFD analysis with various types of flowfield. *Atmospheric Environment*, 41:8091–8099, 2007.

[49] Christie John Geankoplis. *Transport processes and separation process principles*. Prentice Hall, 4th edition, 2003.

[50] S. Vodret, D. Vitale, Di Maio, and G. Caruso. Numerical simulation of turbulent forced convection in liquid metals. *Journal of Physics: Conference Series*, 547, 2014.

[51] B. B. Dally, D. F. Fletcher, and A. R. Masri. Flow and mixing fields of turbulent bluff-body jets and flames. *Combustion Theory and Modelling*, 2:193–219, 1998.

[52] S.B. Pope. *Turbulent Flows*. Cambridge University Press, 2011.

[53] Javad Aminian, Chiara Galletti, Shahrokh Shahhosseini, and Leonardo Tognotti. Numerical investigation of a MILD combustion burner: Analysis of mixing field, chemical kinetics and turbulence-chemistry interaction. *Flow, Turbulence and Combustion*, 88(4):597–623, 2012.

[54] Michael John Evans, Paul Ross Medwell, and Zhao Feng Tian. Modelling lifted jet flames in a heated coflow using an optimised eddy dissipation concept model. *Combustion Science and Technology*, 187(7):1093–1109, 2015.

5.2 Journal paper 2

This paper was published in Applied Energy:

Zhiyi Li, Marco Ferrarotti, Alberto Cuoci and Alessandro Parente, Finite-rate chemistry modelling of nonconventional combustion regimes using a Partially-Stirred Reactor closure: combustion model formulation and implementation details, Applied Energy 225, 637-655 (2018).

Finite-rate chemistry modelling of non-conventional combustion regimes using a Partially-Stirred Reactor closure: combustion model formulation and implementation details ☆

Zhiyi Li[a,b], Marco Ferrarotti[a,b,c], Alberto Cuoci[d], Alessandro Parente[a,b,*]

[a] *Université Libre de Bruxelles, Ecole Polytechnique de Bruxelles, Aero-Thermo-Mechanics Laboratory, Bruxelles, Belgium*
[b] *Université Libre de Bruxelles and Vrije Universiteit Brussel, Combustion and Robust Optimization Group (BURN), Bruxelles, Belgium*
[c] *Service de Thermique et Combustion, Université de Mons, Mons, Belgium*
[d] *Department of Chemistry, Materials, and Chemical Engineering, Politecnico di Milano, Piazza Leonardo da Vinci, 20133 Milano, Italy*

Abstract

The present work focuses on the numerical simulation of Moderate or Intense Low oxygen Dilution combustion condition, using the Partially-Stirred Reactor model for turbulence-chemistry interactions. The Partially-Stirred Reactor model assumes that reactions are confined in a specific region of the computational cell, whose mass fraction depends both on the mixing and the chemical time scales. Therefore, the appropriate choice of mixing and chemical time scales becomes crucial to ensure the accuracy of the numerical simulation prediction. Results show that the most appropriate choice for mixing time scale in Moderate or Intense Low oxygen Dilution combustion regime is to use a dynamic evaluation, in which the ratio between the variance of mixture fraction and its dissipation rate is adopted, rather than global estimations based on Kolmogorov or integral mixing scales. This is supported by the validation of the numerical results against experimental profiles of temperature and species mass fractions, available from measurements on the Adelaide Jet in Hot Co-flow burner. Different approaches for chemical time scale evaluation are also compared, using the species formation rates, the reaction rates and the eigenvalues of the formation rate Jacobian matrix. Different co-flow oxygen dilution levels and Reynolds numbers are considered in the validation work, to evaluate the applicability of Partially-Stirred Reactor approach over a wide range of operating conditions. Moreover, the influence of specifying uniform and non-uniform boundary conditions for the chemical scalars is assessed. The present work sheds light on the key mechanisms of turbulence-chemistry interactions in advanced combustion regimes. At the same time, it provides essential information to advance the predictive nature of computational tools used by scientists and engineers, to support the development of new

technologies.

Keywords: Characteristic time scales, Chemical time scale, Finite-rate chemistry, MILD combustion, Mixing time scale, Partially-Stirred Reactor

1. Introduction

Recently, the reduction of fossil fuel availability and the increasing environmental concerns associated to their utilization in conventional systems have pushed the development of new combustion technologies that feature high fuel flexibility, increased efficiency and low pollution emissions. Among them, Moderate or Intense Low oxygen Dilution (MILD) combustion [1, 2] has recently drawn increasing attention. MILD combustion is characterized by elevated reactant temperature and low temperature increase [1, 3], intensive reactant and product mixing, as well as no audible or visible flame, under ideal conditions. Moreover, MILD combustion delivers very low NO_x and CO emissions and high efficiency, with a large flexibility of fuel types [2, 4].

MILD combustion technology has been demonstrated for many industrial applications. It was first introduced in industrial furnaces for methane combustion [5] and later extensively investigated for other gaseous fuels like hydrogen [6] and ethanol [7]. Cho et al. [8, 9] executed experiments and simulations on MILD oxidation burner, showing the effects of burner configuration and firing mode on efficiency and emissions. Sánchez et al. [10] evaluated an oxygen enhanced regenerative burner operated in MILD combustion mode. An energy recovery ratio above 80% and NO_x emissions below 5 ppm were achieved. Ye et al. [11] studied prevaporised liquid fuels burning in a reverse-flow MILD combustor under elevated pressures. They concluded that combustion stability is largely dependent on fuel type and the NO_x emission is highly influenced by the operating conditions of pressure, jet velocity and carrier gas. MILD technology can be utilized in gas turbines as well. Kruse et al. [12] conducted experimental and numerical studies on gas turbine under MILD condition, using gaseous fuel. The effect of pressure, mixing on combustion stability was analysed, indicating that mixing is the key parameter to control and stabilize MILD combustion. Recently, Xing et al. [7] evaluated the possibility of using liquid bio-fuels, diesel and kerosene fuels under MILD condition for gas turbine applications. They stated that MILD combustion can potentially substitute conventional gas turbines. Furthermore, Adamczyk et al. [13] analysed the

☆The short version of the paper was presented at ICAE2017, Aug 21-24, Cardiff, UK. This paper is a substantial extension of the short version of the conference paper.

*Corresponding author: Alessandro.Parente@ulb.ac.be

potential of oxy-MILD combustion for large scale pulverized coal boilers. Preliminary simulations showed the possibility of efficiency increase of more than 3%. The MILD combustion concept was also extended to hybrid solar thermal devices, which combine concentrated solar radiation with combustion. According to Chinnici et al. [14], the integration of MILD combustion in a hybrid solar receiver can lead to increased thermal performances with respect to conventional flames.

The distinguishing feature of MILD combustion is the very strong interactions between the fluid mixing and chemical kinetics, so that models based on the separation between turbulence and chemistry are not suitable to describe the complex interactions occurring in such a regime [15]. Therefore, models that account for finite-rate chemistry effects must be considered. The present study focuses on Unsteady Reynolds Averaged Navier-Stokes (URANS) simulations in combination with finite-rate chemistry. The Partially-Stirred Reactor (PaSR) model [16] is chosen for turbulence/chemistry interactions. In PaSR, the interaction between turbulence and chemistry is represented with a factor κ, which is defined as the ratio between the chemical time scale and the sum of mixing and chemical scales. PaSR models the combustion process as a sequence of reaction and mixing processes in locally uniform regions. Both the chemical and mixing time scales are included in the model explicitly, allowing more comprehensive descriptions on turbulence/chemistry interactions. Therefore, its performances strongly depend on the accurate estimation of mixing and chemical time scales.

Regarding the evaluation of chemical and mixing time scales, Chomiak [17] estimated the chemical time scale using the fuel and oxidiser formation rates, and the mixing time from the geometric mean of integral and komogorov mixing time scales. Golovitchev et al. [18] proposed an approach in which the chemical time scale is estimated from forward reaction rates only. Kärrholm [19] and Nordin [20] estimated the mixing time scale as a certain fraction of the integral one, using a mixing constant C_{mix} ranging from 0.001 to 0.3 [20]. To the best of the authors' knowledge, no study was carried out to compare the available approaches for mixing and chemical time scale evaluation.

The objective of the present article is to provide a comprehensive analysis on existing and novel approaches for the evaluation of chemical and mixing time scales and boundary conditions in the framework of finite-rate chemistry approach for turbulent reacting flows. The available models are benchmarked in the context of MILD combustion simulations under a wide range of operation conditions. A cross-comparison between an open-source CFD software OpenFOAM and a commercial one, ANSYS Fluent 17.0 [21], is also carried out, to show the applicability of the proposed methodology on different computing platforms.

Numerical simulations are validated against high-fidelity experimental results available from the Adelaide Jet in Hot Co-flow (AJHC) burner [22]. The AJHC burner emulates MILD

conditions via the injection of a heated and vitiated co-flow. Measurement data for different co-flow oxygen levels (3%, 6% and 9%) and fuel jet Reynolds numbers (5 k, 10 k and 20 k) are available. The AJHC burner with 3% co-flow oxygen content and Re = 10 k is chosen first for the evaluation of various mixing time scale and chemical time scale formulations. The best combination of mixing and chemical scales is then used for the other co-flow oxygen levels and Reynolds numbers. Finally, the influence of uniform and non-uniform boundary conditions on the model prediction is assessed, paying particular attention to carbon monoxide prediction.

2. Methodology

The Finite Volume Method (FVM) based URANS simulations are carried out with PaSR combustion model.

2.1. Turbulence Model

In the context of compressible URANS simulations, the Favre-averaged (denoted with ˜) governing equations are solved [23]:

$$\frac{\partial \bar{\rho}}{\partial t} + \frac{\partial}{\partial x_j}\left(\bar{\rho}\tilde{u}_j\right) = 0, \tag{1}$$

$$\frac{\partial}{\partial t}\left(\bar{\rho}\tilde{u}_i\right) + \frac{\partial}{\partial x_j}\left(\bar{\rho}\tilde{u}_i\tilde{u}_j\right) = -\frac{\partial \bar{p}}{\partial x_i} + \frac{\partial}{\partial x_j}\left[\bar{\tau}_{ij} - \bar{\rho}\left(\widetilde{u_i u_j} - \tilde{u}_i\tilde{u}_j\right)\right]. \tag{2}$$

$$\frac{\partial}{\partial t}\left(\bar{\rho}\tilde{h}\right) + \frac{\partial}{\partial x_j}\left(\bar{\rho}\tilde{h}\tilde{u}_j\right) = \frac{\partial}{\partial x_j}\left(\bar{\rho}\alpha\frac{\partial \tilde{h}}{\partial x_j} - \bar{\rho}\widetilde{u_j'' h''}\right) - \frac{\partial}{\partial x_j}\left(\bar{q}_{rj}\right) + \bar{S}_{hc}, \tag{3}$$

$$\frac{\partial}{\partial t}\left(\bar{\rho}\widetilde{Y}_i\right) + \frac{\partial}{\partial x_j}\left(\bar{\rho}\widetilde{Y}_i\tilde{u}_j\right) = \frac{\partial}{\partial x_j}\left(\left(\bar{\rho}D_{m,i} + \frac{\mu_t}{S\,c_t}\right)\frac{\partial \tilde{Y}_i}{\partial x_j}\right) + \overline{\dot{\omega}}_i. \tag{4}$$

In Eqn. 1 - 4, ρ, $\mathbf{u}$, p are the density, velocity and pressure, respectively; h and α represent the enthalpy and thermal diffusivity; $S\,c_t$ and $D_{m,i}$ denote the turbulent Schmidt number and molecular diffusion coefficient for species i in the mixture. The standard $k-\epsilon$ model is chosen as turbulence model. It is based on the eddy viscosity assumption. The unresolved turbulence stresses $\bar{\rho}\widetilde{u_i'' u_j''}$ are modelled with the product of an eddy viscosity μ_t and mean flow strain rate S^*_{ij}. The eddy viscosity μ_t in standard $k-\epsilon$ model is estimated as:

$$\mu_t = \rho C_\mu \frac{\tilde{k}^2}{\tilde{\epsilon}}. \tag{5}$$

The turbulence kinetic energy $\tilde{k}$ and the dissipation rate $\tilde{\epsilon}$ of the turbulence kinetic energy [23] are solved via two separate transport equations.

2.2. Partially-Stirred Reactor

In the PaSR model [16, 18], the computational cell is split into two locally uniform zones: one where reactions take place, and another characterized by only mixing. The final species concentration of the cell is determined from the mass exchange between the two zones, driven by the turbulence. A conceptual drawing of the PaSR model is shown in Fig. 1.

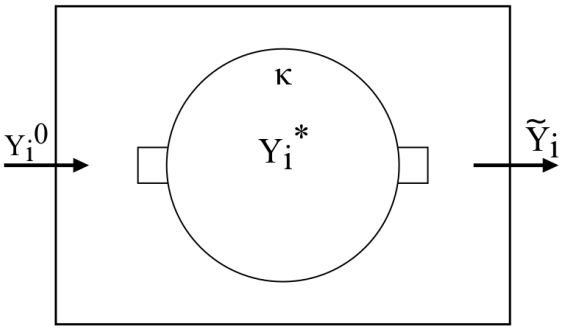

Figure 1: Conceptual drawing of the PaSR model.

The drawing in Fig. 1 refers to one computational cell, in which Y_i^0 is the initial i_{th} species mass fraction in the non-reactive region, $\widetilde{Y}_i$ is the final averaged i_{th} species mass fraction in the cell and Y_i^* is the i_{th} species mass fraction in the reactive zone. κ is the mass fraction of the reaction zone in the computational cell, which can be estimated as [19]:

$$\kappa = \frac{\tau_c}{\tau_c + \tau_{mix}}, \tag{6}$$

where τ_c and τ_{mix} are the characteristic chemical and mixing time scales in each cell, respectively. They can be estimated following different approaches, as detailed in Section 2.3 and 2.4. The mean source term provided to the species transport equation can be expressed as:

$$\overline{\dot{\omega}}_i = \kappa \frac{\widetilde{\rho}\left(Y_i^* - Y_i^0\right)}{\tau^*}, \tag{7}$$

where τ^* represents the residence time in the reactive structure. In the present work, τ^* equals to the mixing time scale. In order to get the value of Y_i^*, a time-splitting approach is applied. The reactive zone is modelled as an ideal reactor evolving from Y_i^0, during a residence time τ^*:

$$\frac{dY_i^*}{dt} = \frac{\dot{\omega}_i}{\rho}. \tag{8}$$

The term $\dot{\omega}_i$ is the instantaneous formation rate of species i. The final integration of $\frac{dY_i^*}{dt}$ over the residence time τ^* in the reactor is Y_i^*.

2.3. Mixing time scale in PaSR

Kolmogorov time scale. In conventional combustion systems, it is often assumed that reactions happen at the dissipation scales, of the order of the Kolmogorov one, $\tau_{mix_K} = \sqrt{\nu/\epsilon}$ [24], where ν is the kinematic viscosity and ϵ is the turbulence kinetic energy dissipation rate. However, in MILD combustion, reactions can occur over a wide range of flow scales [2], and the use of the Kolmogorov mixing time scale could lead to inaccurate predictions of temperature and species mass fractions [25].

Integral time scale. Another characteristic time scale in turbulent flow is the eddy break-up time leading from large-scale to Kolmogorov-scale non-uniformities [17], which is also referred to as integral time scale, $\tau_{mix_I} = \frac{k}{\epsilon}$, where k is the turbulence kinetic energy.

Geometric mean of Kolmogorov and integral time scales. To provide a more accurate evaluation of the mixing time, Borghi [26] proposed to consider the whole spectrum of time scales. A simple approach to achieve this is to take only the two most important time scales, via the geometrical mean of the Kolmogorov and integral time scales [17], that is:

$$\tau_{mix_{Mean}} = \sqrt{\tau_{mix_K}\tau_{mix_I}} = \sqrt{\frac{k}{\epsilon}\left(\frac{\nu}{\epsilon}\right)^{1/2}}. \tag{9}$$

Dynamic time scale. The three ways of estimating mixing scales introduced above can be regarded as global approaches. A more comprehensive approach consists in using a dynamic approach. The dynamic estimation of mixing time scale is based on the ratio of the scalar variance, $\widetilde{\phi''^2}$, to the scalar dissipation rate, $\widetilde{\epsilon_\phi}$ [27]:

$$\tau_{mix_{Dynamic}} = \frac{\widetilde{\phi''^2}}{\widetilde{\epsilon_\phi}}. \tag{10}$$

The mixture fraction f is selected to describe the mixing process of a scalar. Therefore, the scalar variance and dissipation rate take the form of the mixture fraction variance ($\widetilde{f''^2}$) and mixture fraction dissipation rate ($\widetilde{\chi}$). They are modelled with the following transport equations [28, 29]:

$$\frac{\partial\bar{\rho}\widetilde{f}}{\partial t} + \frac{\partial\bar{\rho}\widetilde{u}_j\widetilde{f}}{\partial x_j} = \frac{\partial}{\partial x_j}\Big(\rho(D+D_t)\frac{\partial\widetilde{f}}{\partial x_j}\Big), \tag{11}$$

$$\frac{\partial\bar{\rho}\widetilde{f''^2}}{\partial t} + \frac{\partial\bar{\rho}\widetilde{u}_j\widetilde{f''^2}}{\partial x_j} = \frac{\partial}{\partial x_j}\Big(\rho(D+D_t)\frac{\partial\widetilde{f''^2}}{\partial x_j}\Big) + 2\rho D_t\Big(\frac{\partial\widetilde{f}}{\partial x_j}\Big)^2 - \bar{\rho}\widetilde{\chi}, \tag{12}$$

$$\frac{\partial \rho \widetilde{\chi}}{\partial t} + \frac{\partial \rho \widetilde{u}_j \widetilde{\chi}}{\partial x_j} = \frac{\partial}{\partial x_j}\Big(\rho(D + D_t)\frac{\partial \widetilde{\chi}}{\partial x_j}\Big) - C_1 \bar{\rho}\frac{\widetilde{\chi}^2}{\widetilde{f''^2}} - C_2 \bar{\rho}^2 \frac{C_\mu \widetilde{k}}{\mu_t}\widetilde{\chi} + C_3 \frac{\bar{\rho} C_\mu \widetilde{k}}{S\, c_t}\left(\frac{\partial \widetilde{f}}{\partial x_j}\right)^2 + C_4 \mu_t \frac{\widetilde{\chi}}{\widetilde{k}}|\widetilde{S}|^2. \tag{13}$$

In Eqn. 13, C_1, C_2, C_3 and C_4 are model constants. Four different set of values were proposed in [28], as shown in Table 1. Based on a sensitivity study, the present work focuses on the results obtained with set 2 and set 4.

Table 1: Model constants for the scalar dissipation rate transport equations [28].

Case	C_1	C_2	C_3	C_4
1	2.0	1.8	1.7	1.4
2	1.0	1.8	3.4	1.4
3	2.0	1.8	3.4	1.4
4	1.0	1.8	1.7	1.4

2.4. Chemical time scale evaluation in PaSR

Chemical time scale estimation from Jacobian matrix eigenvalues. For the evaluation of chemical time scale, Fox [30, 31] suggested using the eigenvalues of the Jacobian matrix $\mathbf{J}$ of the chemical source terms. The Jacobian matrix $\mathbf{J}$ has the dimension of $i \times i$, where i is the number of chemical species in the mechanism. Each element J_{jk} of the matrix is expressed as:

$$J_{jk} = \frac{\partial R_j^*}{\partial Y_k^*}, \tag{14}$$

where the superscript $*$ denotes reactive structures values. After the decomposition of the Jacobian matrix, the chemical time scale is estimated with the inverse of the eigenvalues λ_i:

$$\tau_{c,i} = \frac{1}{|\lambda_i|}. \tag{15}$$

In Eqn. 15, $\tau_{c,i}$ is the characteristic time scale of a single species. After removing the dormant species (characterised by infinite time scale values), the slowest chemical time scale is chosen as leading scale for the evaluation of the PaSR parameter κ.

Chemical time scale estimation from formation rates. The decomposition of the source term Jacobian matrix is accurate but time consuming, especially when large scale simulations with much detailed mechanism is used. The formation rate based characteristic time scale

evaluation is a simplified approach. Instead of getting the chemical time scale for each species from the Jacobian matrix decomposition, the ratio of species mass fraction and formation rate in the reactive structure is directly used [17, 32], approximating the Jacobian diagonal terms:

$$\tau_{c,i} = \frac{Y_i^*}{|dY_i^*/dt|}. \tag{16}$$

Chemical time scale estimation from reaction rates. Another simplified method is based on the reaction rate. Similar to the two approaches above, the characteristic time scale for each species i is expressed as [18]:

$$\tau_{c,i} = \frac{n_r * cTot^*}{\sum_{n=1}^{n_r}((dc^*_{n_r,forward}/dt) * \nu_{n_r,sum})}, \tag{17}$$

where n_r is the number of reactions, and $cTot^*$ is the total concentration obtained from the ideal gas law. Only the forward reaction rate $dc^*_{n_r,forward}/dt$ is used here. The term $\nu_{n_r,sum}$ represents the sum of the product stoichiometric coefficients.

3. Model validation

3.1. Experimental data

The AJHC burner emulates MILD combustion with a simple geometry. It has an insulated and cooled central jet with the inner diameter of 4.2 mm, providing an equi-molar mixture of CH_4 and H_2. There is an annulus pipe with a secondary burner mounted upstream. The burner provides hot combustion products, which are further mixed with air and nitrogen in order to control the oxygen levels to 3%, 6% and 9% in mass fraction. The annulus inner diameter is 82 mm. The wind tunnel, on which the burner is mounted, has the cross section of 254 mm $\times$ 254 mm. In Fig. 2, a 2D simple sketch of the investigated area in the numerical modelling is presented. The central jet, annulus and wind tunnel gas temperatures and velocities (for the Re = 10 k case) are presented in Table 2. In the current study, 5 cases with the combination of different co-flow oxygen contents and fuel jet Reynolds numbers are investigated, as highlighted in Table 3. The other conditions are not investigated since no experimental data is provided for them.

Table 2: Physical properties of the jet (Central jet velocity is for the Re = 10 k case.)

Profiles	Central jet	Annulus	Tunnel
Velocity	58.74 m/s	3.2 m/s	3.3 m/s
Temperature	294 K	1300 K	294 K

Table 3: Investigated cases

Co-flow oxygen level:	3%	6%	9%
Re = 5,000	✓		
Re = 10,000	✓	✓	✓
Re = 20,000	✓		

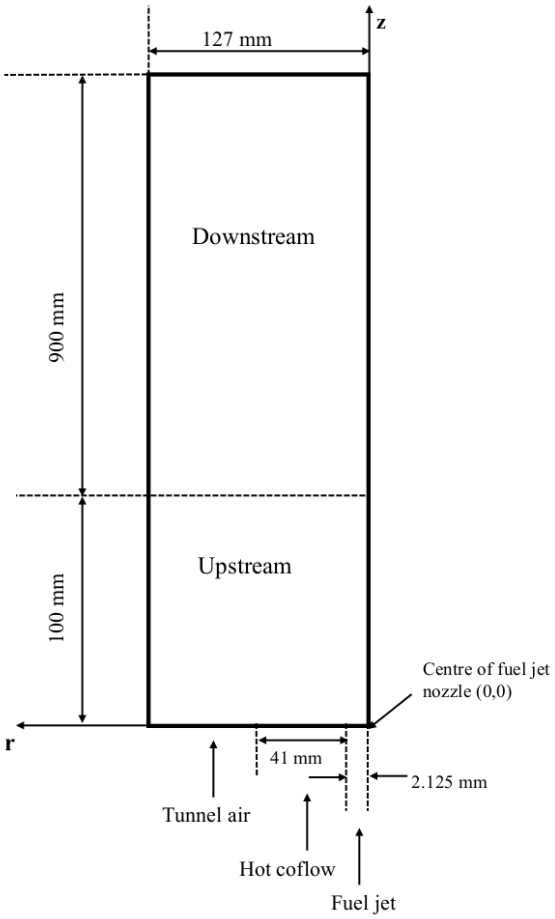

Figure 2: 2D sketch of the Adelaide Jet in Hot Co-flow burner (adapted from Ferrarotti et al. [33]).

The mean, variance and scattered data of temperature and various species mass fractions (CH_4, H_2, H_2O, CO_2, N_2, O_2, NO, CO, and OH), along the centerline as well as on the different axial locations of 30/60/120/200 mm (z = 30/60/120/200 mm), are available for validation. The experimental profiles used for comparison include both the mean values and the error bar with 99.99% confidence interval associated with a Student′s distribution for the true mean value [34].

3.2. Numerical set-up

Based on a Grid Convergence Index (GCI) study [32], a 2-dimensional structured axis-symmetric mesh with ~31500 cells was used in the simulations. The computational domain starts from the burner exit and extends 1000 mm further downstream. Second order discretization schemes for space and time are applied. Both non-uniform and uniform boundary conditions are used in the simulation for the species mass fractions and temperature. The non-uniform boundary conditions are based on the profiles of O_2, CO, CO_2, H_2O mass fractions and temperature, obtained from the experimental data at 4 mm downstream of the burner exit. The uniform boundary conditions are set according to Dally et al. [22]. Additional details about the numerical settings can be found in [32].

Unsteady simulations were carried out using two solvers, the PaSRPimpleSMOKE [24, 35] solver, based on OpenFOAM®, and ANSYS Fluent 17.0 unsteady solver. The PaSR model and different formulations of mixing and chemical time scale estimation were implemented in ANSYS Fluent 17.0 via a bespoke user-defined function. Multi-component molecular diffusion was included, because of the presence of hydrogen in the fuel. Since preliminary simulations with ANSYS Fluent 17.0 showed (see supplementary material) that radiation does not impact significantly the temperature and species profiles at the locations of interest, it was not included in the present study. A reduced skeletal mechanism KEE58 [36], with 17 species and 58 reactions, was chosen for finite rate chemistry approach. The turbulent Schmidt and Prandtl numbers are set to 0.7 and 0.85, respectively. Previous work on the AJHC burner ([37, 38]) showed improved prediction with the modified $C_{1\epsilon}$ constant in the standard $k-\epsilon$ model. In the current study, the $C_{1\epsilon}$ constant was increased from 1.44 to 1.60 [39], to correct the well-known round-jet anomaly.

4. Results and discussion

In this section, the influence of different choices of mixing and chemical time scales in the context of the PaSR model is shown. The case corresponding to 3% O_2 in the co-flow and Re = 10,000 is used for validation in Section 4.1 and 4.2. In Section 4.3, the influence of co-flow oxygen levels (6% and 9%) and Reynolds numbers (Re = 5,000 and Re = 20,000) is shown. Modelling results obtained with OpenFOAM and ANSYS Fluent 17.0 are benchmarked, for all the five cases in Table 3. In Section 4.4, the effect of specifying non-uniform boundary conditions for the thermo-chemical scalars is discussed, with special focus on CO prediction.

4.1. Influence of mixing time scale estimation

The mean temperature profiles obtained with mixing time scale estimated with the Kolmogorov scale, the integral scale and the geometric mean of the two are compared and val-

idated against experimental data in Fig. 3 at several sampling locations. The chemical time scale is estimated from the formation rates and uniform boundary conditions are used.

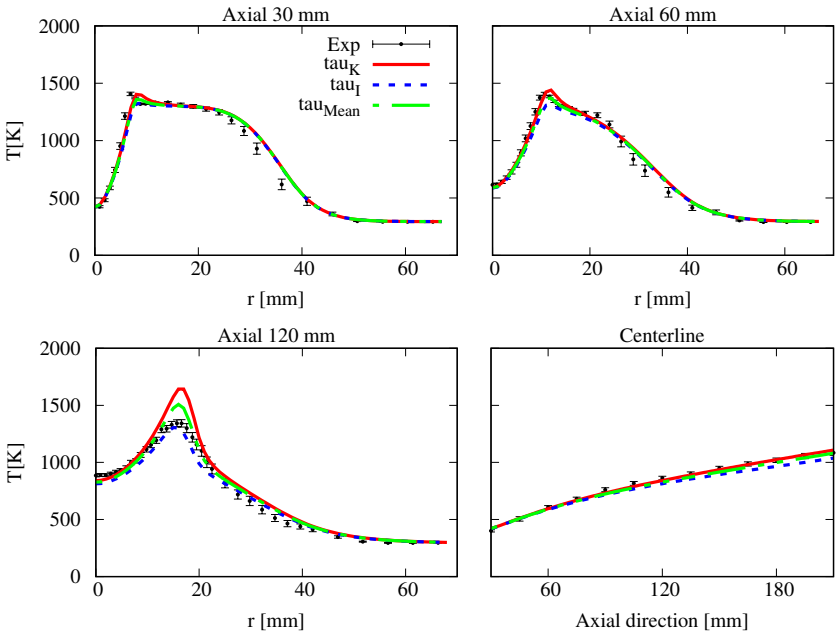

Figure 3: Mean temperature profiles obtained with mixing time scale evaluated from the Kolmogorov scale (tau_K), the integral scale (tau_I) and the geometric mean of the two (tau_{Mean}).

Fig. 3 shows that the use of a mixing scale based on the Kolmogorov one results in temperature over-prediction at z = 60 mm and, more significantly, at z = 120 mm. Using the integral mixing time scale, the temperature profiles are under-predicted at z = 30 mm and 60 mm downstream of the burner exit, and along the centerline. On the other hand, the temperature peak at 120 mm axial location is well predicted. However, the use of the integral mixing time scale strongly under-predicts the H_2O profile at 120 mm axial location, as indicated in Fig. 4. When the geometric mean of the two scales is used, the z = 30 mm/60 mm and centerline temperature profiles agree well with the experimental ones. A slight over-prediction of the temperature profile at 120 mm can be observed. However, the H_2O mass fraction profiles at z = 30 mm and 60 mm are significantly under-predicted. The use of the Kolmogorov mixing time scale improves H_2O prediction upstream ($z \leqslant 100$ mm).

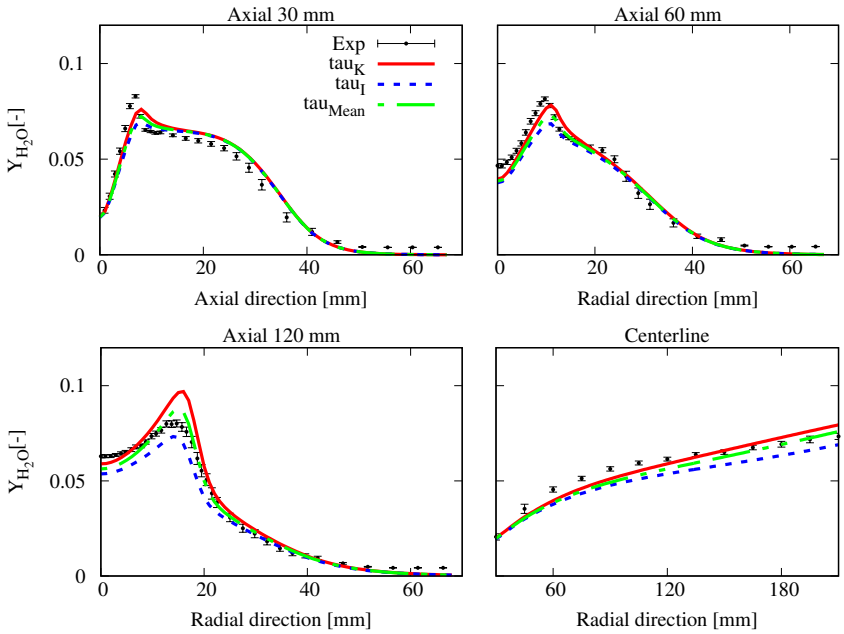

Figure 4: Mean H_2O mass fraction profile obtained with mixing time scale evaluated from the Kolmogorov scale (tau_K), the integral scale (tau_I) and the geometric mean of the two (tau_{Mean}).

From the results above, one can conclude that the global defined mixing time scale is not suitable for the whole flow field condition. The use of a dynamic mixing model potentially offers a solution to this, by providing locally an optimal mixing scale. The dynamic model is compared with the global approaches in Fig. 5. No major differences can be observed at z = 30 mm/60 mm and along the centerline for the temperature value. At 120 mm axial location, the temperature over-prediction is corrected using the dynamic model with coefficient set 4 (Table 1), indicated as dyn4 in short. The same can be observed for the H_2O mass fraction profiles in Fig. 6, whose prediction is strongly improved using the dyn4 model. At z = 30 mm, better prediction of the H_2O peak value using the dyn2 model can be also observed.

The scaled CPU time associated to the various mixing models are estimated taking the Kolmogorov mixing scale as reference in Table 4. Even though using the kolmogorov time scale reduces the CPU time, this would lead to non-negligible over-prediction of mean temperature and species mass fraction at z = 120 mm (see Fig. 3 and Fig. 4). On the other hand, the dynamic model requires medium CPU time, while showing superior results compared to all the other models.

Table 4: CPU time consumption of various mixing models.

Mixing model	kolmogorov	geometric mean	dynamic	integral
CPU time	1.0	1.4	1.53	1.85

To summarize, the use of a dynamic model (especially dyn4) can correctly fix the temperature over-prediction at 120 mm, without compromising the predictions at z = 30 mm and 60 mm (see the integral mixing scale profiles in Fig. 3). Furthermore, the dynamic model reproduces the species mass fraction profiles accurately, which is not the case with the globally defined time scales.

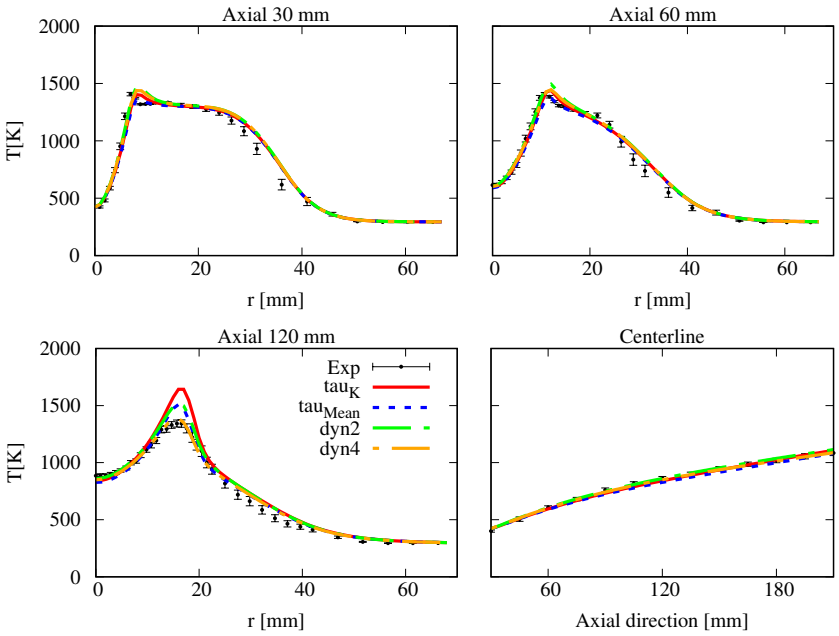

Figure 5: Mean temperature profiles obtained with a mixing time scale evaluated using the using the Kolmogorov scale (tau_K), the geometric mean of Kolmogorov and integral scale (tau_{Mean}), the second (dyn2) and fourth (dyn4) parameter sets of the dynamic model.

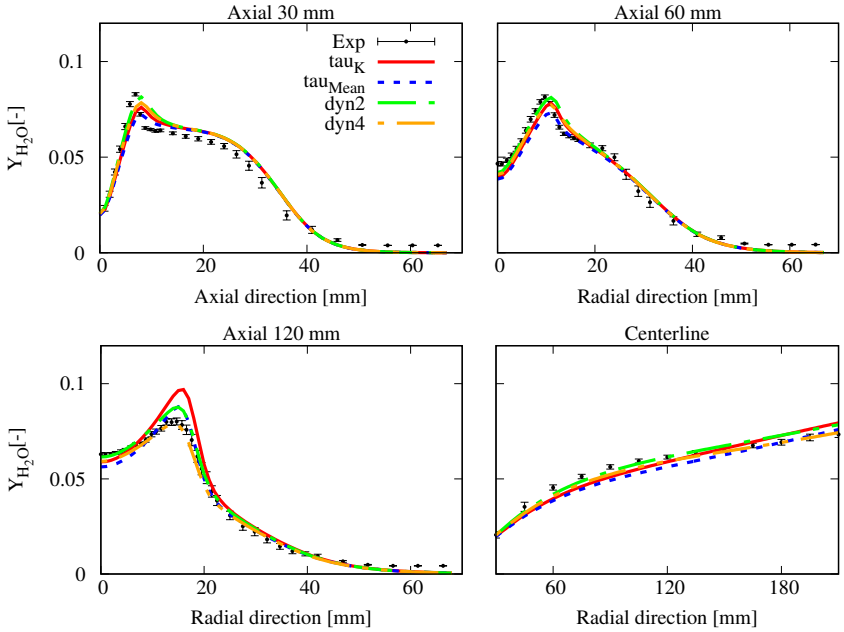

Figure 6: Mean H_2O mass fraction profile obtained with mixing time scale evaluated from the Kolmogorov scale (tau_K), the geometric mean of Kolmogorov and integral scale (tau_{Mean}), the second (dyn2) and fourth (dyn4) parameter sets of the dynamic model.

To highlight the differences between the global and dynamic scale definition, an equivalent C_{mix} value is defined as $C_{mix,eq} = \tau_{mix}/\tau_I$, where τ_{mix} is the mixing scale provided by the different approaches, i.e. global and dynamic. The equivalent C_{mix} values at several locations of interest are shown in Fig. 7. A first observation is that $C_{mix,eq}$ is bounded smaller than 1, indicating a time scale ranging from the Kolmogorov to the integral one. Looking at the radial profiles, there is a location where the $C_{mix,eq}$ profiles associated to the Kolmogorov (red solid line) and dyn2 (green dashed-dotted line) mixing scale models intersect. The same happens for the profiles provided by the geometric mean (blue dotted line) and dyn4 (orange dotted-dashed line) models, at almost the same location. The intersection occurs at radial locations of 7-8 mm, 11-12 mm and 19-20 mm for z = 30/60/120 mm positions, respectively. They are adjacent to the locations of maximum temperatures, i.e. 6.9 mm, 10.7 mm and 16.6 mm for z = 30/60/120 mm, respectively. All the mixing models in Fig. 7 are able to capture the interaction between the fuel and co-flow streams, but only the dynamic ones can account for the breakup of large eddies into smaller ones downstream of the jet, providing $C_{mix,eq}$ values decreasing from 1.0 to lower values. Among the dynamic model variants, the dyn4 always provides higher $C_{mix,eq}$ values, corresponding to lower κ in PaSR model. The effect of the different $C_{mix,eq}$ values provided by the two dynamic models can be appreciated

from the mean temperature and H_2O profiles in Fig. 5 and Fig. 6.

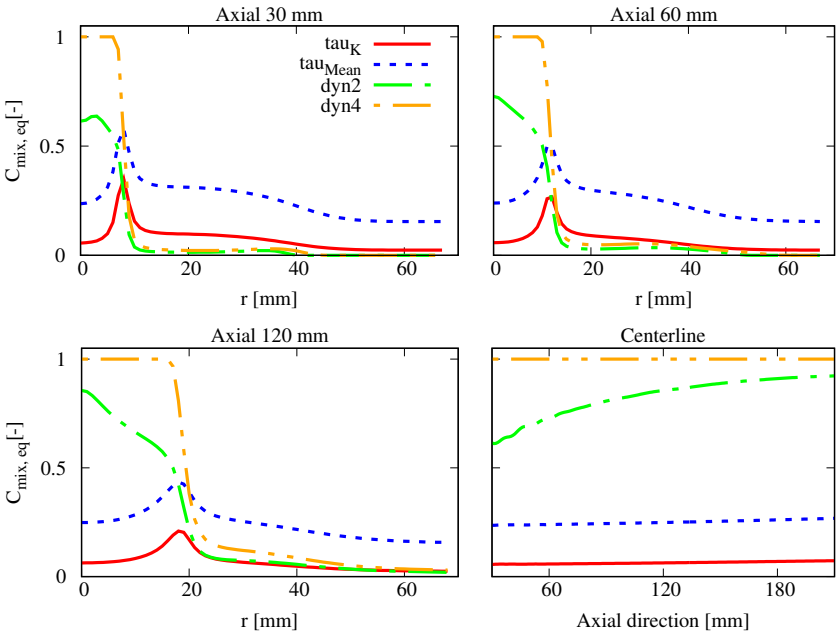

Figure 7: $C_{mix,eq}$ profiles obtained with mixing time scale evaluated from using the Kolmogorov scale (tau_K), the geometric mean of Kolmogorov and integral scale (tau_{Mean}), the second (dyn2) and fourth (dyn4) parameter sets of the dynamic model.

4.2. Influence of chemical time scale estimation

From Section 4.1, the dynamic mixing model has proven to be more superior to other approaches for mixing time scale evaluation and it is then set as a default for further investigation. Figure 8 shows the mean temperature profiles adopting different approaches to estimate the chemical time scales. The dyn2 mixing model is used and uniform boundary conditions are applied. As observed in Fig. 8, the dyn2 mixing model, in combination with the chemical time scale calculation based on the formation rate, over-predicts the mean temperatures. This is especially obvious at z = 120 mm, where the peak temperature is over-predicted by 123 K. The evaluation of the chemical time scale using the reaction rate based approach provides very similar results, with a temperature over-prediction at z = 120 mm of 172 K. On the other hand, estimating the time scale from the formation rate Jacobian, the mean temperature is correctly predicted, at all axial locations.

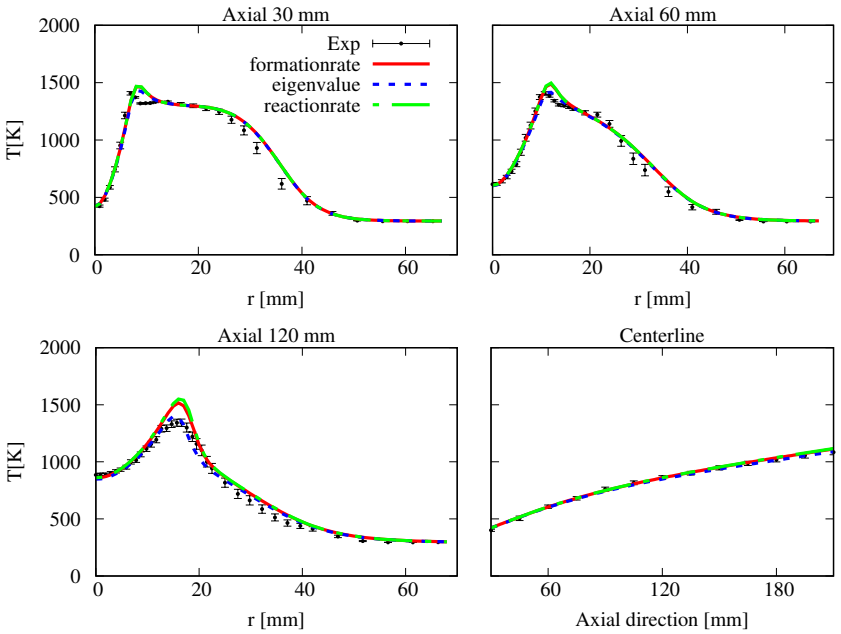

Figure 8: Mean temperature profiles obtained with chemical time scale evaluated from the formation rates, the Jacobian eigenvalues and the reaction rates.

As far as species predictions are concerned, the H_2O mass fraction profiles are shown in Fig. 9. It can be observed that the approaches based on the formation and reaction rates provide more accurate predictions upstream, while using the Jacobian eigenvalues improves the predictions downstream. At z = 120 mm, the use of formation and reaction rates for chemical time scale evaluation lead to over-prediction errors of 7% and 9.2%, respectively. As for CO_2 (Fig. 10), the eigenvalue approach slightly under-predicts the peak value (by 4.8%) at axial 120 mm, while the reaction rate approach over-predicts it by about 4%.

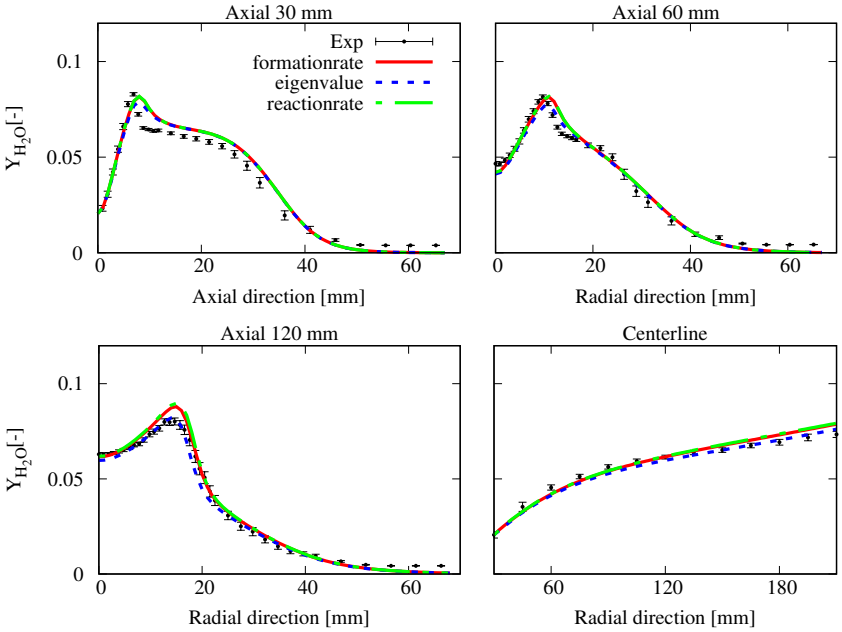

Figure 9: Mean H_2O mass fraction profiles obtained with chemical time scale evaluated from the formation rates, the Jacobian eigenvalues and the reaction rates.

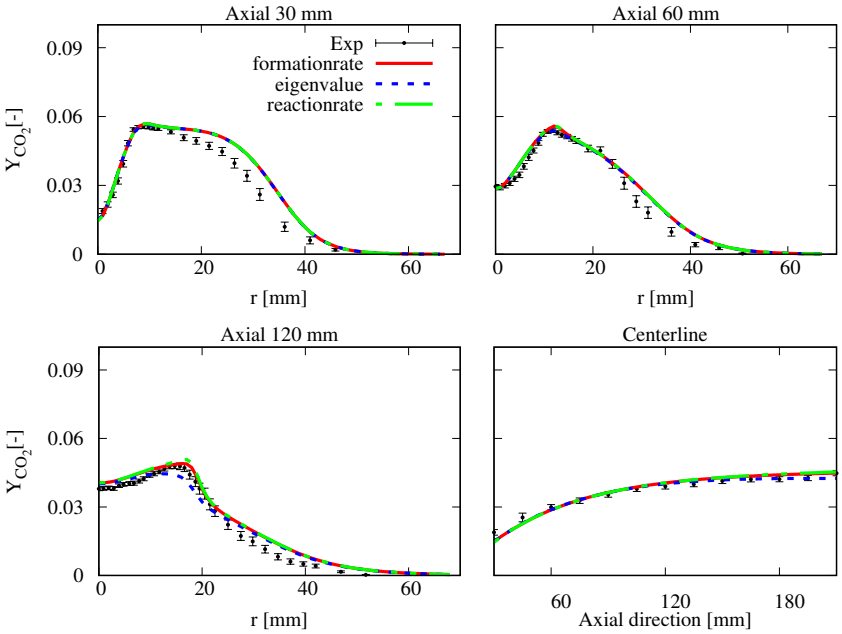

Figure 10: Mean CO_2 mass fraction profiles obtained with chemical time scale evaluated from the formation rates, the Jacobian eigenvalues and the reaction rates.

The results obtained using the dyn4 model are also shown in Fig. 11. Being different from Fig. 8, the various approaches used for the evaluation of the chemical time scale predict the mean temperatures accurately. This is expected, considering that the dyn4 model predicts larger C_{mix} and, thus, larger τ_{mix} values, making the PaSR approach less dependent on the chemical time scale (see the definition of κ in Eqn. 6).

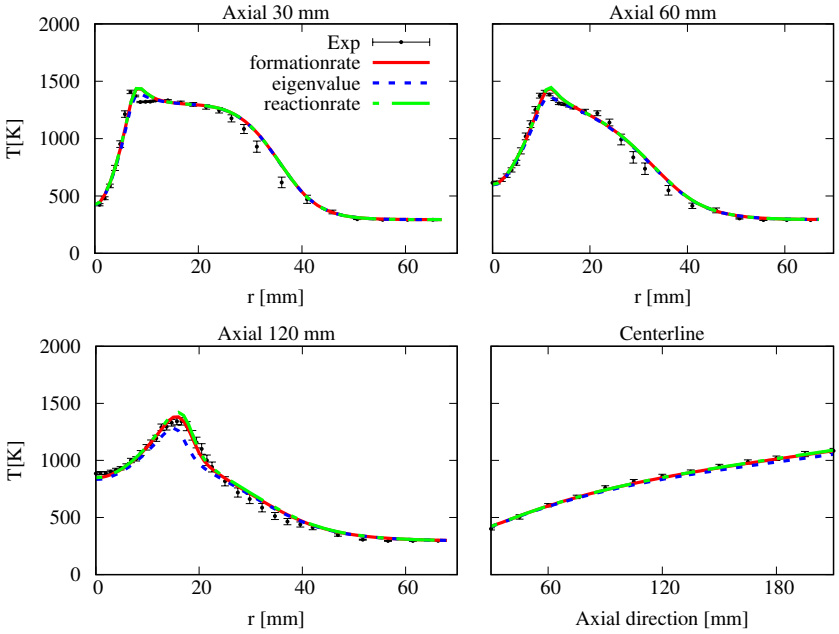

Figure 11: Mean temperature profiles obtained with chemical time scale evaluated from the formation rates, the Jacobian eigenvalues and the reaction rates.

Figure 12 shows contour plots of the local chemical time scales estimated with the three methods. The eigenvalue-based approach shows wider reaction region (the blue area with $tau_C \leqslant 0.02$ s), whereas the other two models estimate these regions to be dormant and set $tau_C = 0.1$ s, which is the maximum cut-off value for the chemical time scale. Comparing the formation and reaction rate based methods, the latter gives higher tau_C values in the combustion region, which implies higher κ, leading to the observed over-prediction of mean temperature and specie mass fractions, especially at downstream locations. In summary, the chemical time scale evaluation from reaction rates tends to over-estimate the κ values in the PaSR approach, while the formation rate and eigenvalue methods correct this, improving the thermo-chemical scalar predictions.

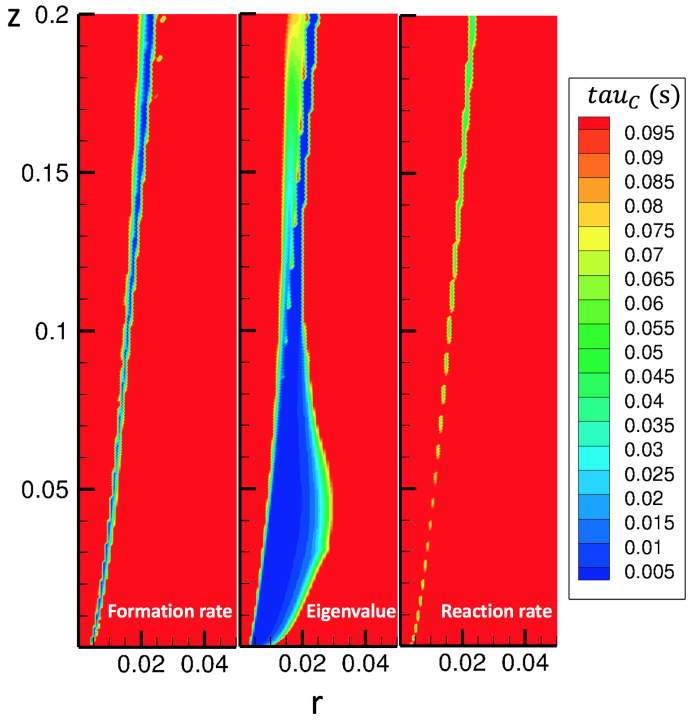

Figure 12: Chemical time scale (tau_C) distribution estimated from the formation rates, the Jacobian eigenvalues and the reaction rates. Only the area of interest of the simulation domain is shown. Legend unit: m. OpenFOAM solver.

4.3. Comparison with Fluent

The present section shows a throughout comparison between the OpenFOAM and ANSYS Fluent solvers, for the different cases in Table 3. Second-order temporal and spatial discretizations schemes are used for both OpenFOAM and ANSYS Fluent. Both solvers adopt the PIMPLE algorithm for a URANS simulation. Chemical and mixing time scales are evaluated using the formation rate based and dynamic model, respectively. Results from both the second and fourth sets of dynamic mixing time scale evaluation model parameters are shown. Uniform boundary conditions are used. The mean temperature profiles are first presented in Fig. 13. The 10,000 Reynolds number case is considered, adjusting the oxygen content in the co-flow to 3%, 6% and 9%. The abbreviation OF means that the data are obtained from OpenFOAM simulation, while FL denotes ANSYS Fluent.

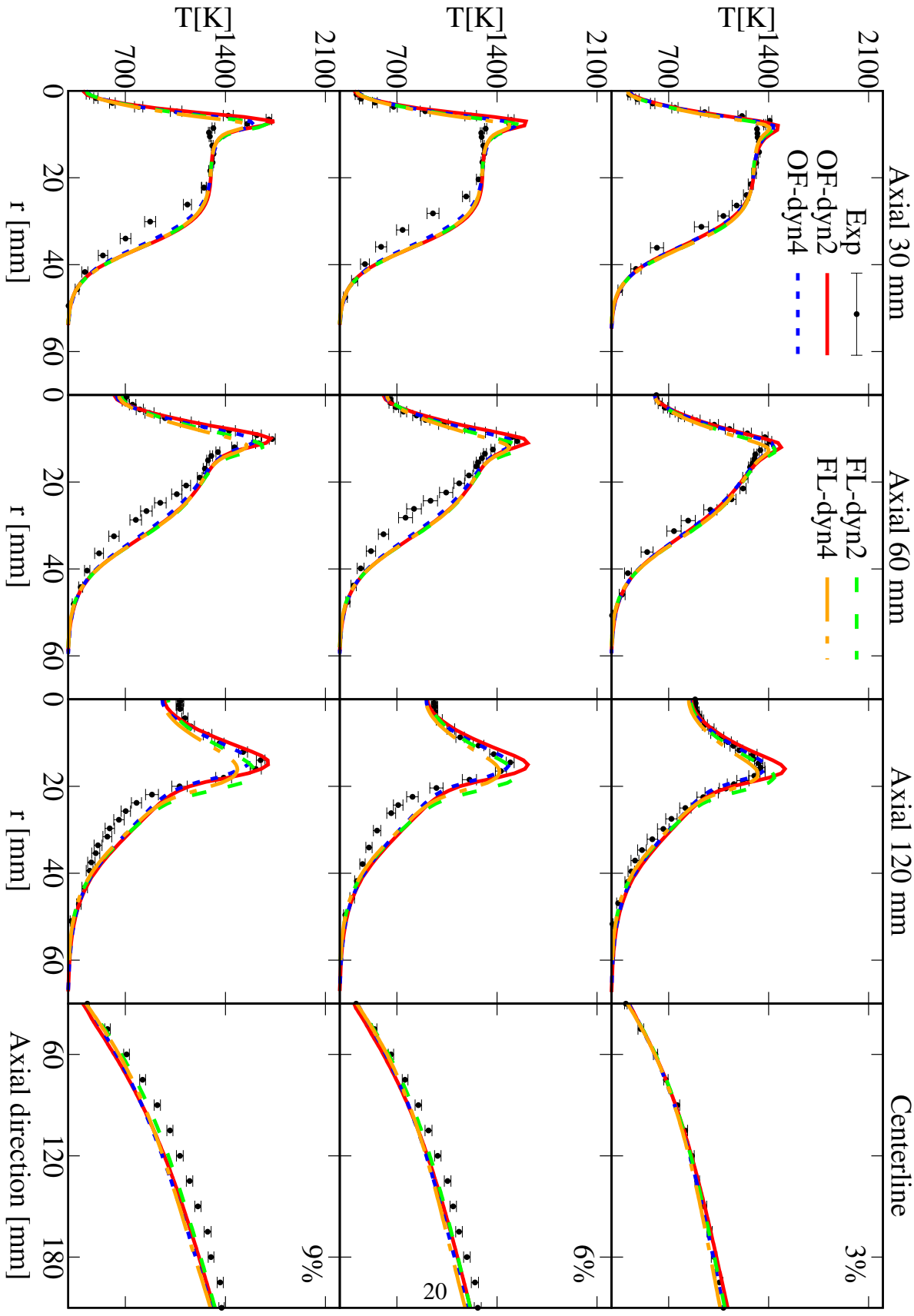

Figure 13: Mean temperature profiles obtained for different co-flow oxygen levels (3%, 6% and 9%), using two dynamic model formulations. OpenFOAM and Fluent solvers.

Both solvers are able to provide satisfactory predictions of mean temperatures, at different oxygen levels. Similarly to OF, the FL results obtained with the dyn2 model show higher temperature levels when compared to the dyn4 model. The dyn4 model provides better predictions with both solvers, for a co-flow oxygen level equal to 3%, especially at z = 120 mm. For 6% and 9% O_2 levels, the FL results with dyn4 cannot predict the peak temperature accurately, and the dyn2 model is found to perform better. The same is found using OpenFOAM. In general, FL results present slightly lower temperature values with respect to OF, and it provides radially shifted temperature peaks. The observed differences could be caused by the more dissipative nature of FL with respect to OF, as documented in [40]. The same conclusion can be drawn from the species mass fraction profiles in Fig. 14, 15 and 16.

Capturing the OH radical mass fraction distribution is very important, as it can be used as flame marker. In Fig. 14, the experimental and numerical profiles of OH mass fraction are shown, for different O_2 levels in the co-flow (3%, 6% and 9%). The results obtained with both solvers are very close to each other. The dyn2 mixing model shows excellent agreement with the experimental data for 3% co-flow O_2 level, while slight under-predictions are observed for 6% and 9%, at z = 60 mm and 120 mm. A more pronounced over-prediction of the OH peak can be detected at 30 mm axial location, for the 9% O_2 case. On the other hand, the FL and OF results obtained with dyn4 mixing model are able to reproduce the experimental peak values with satisfactory accuracy.

The analysis of the H_2O profiles in Fig. 15 reveals interesting information. Overall, satisfactory predictions of H_2O mass fraction profiles is obtained with both OF and FL, for the case of 3% O_2.

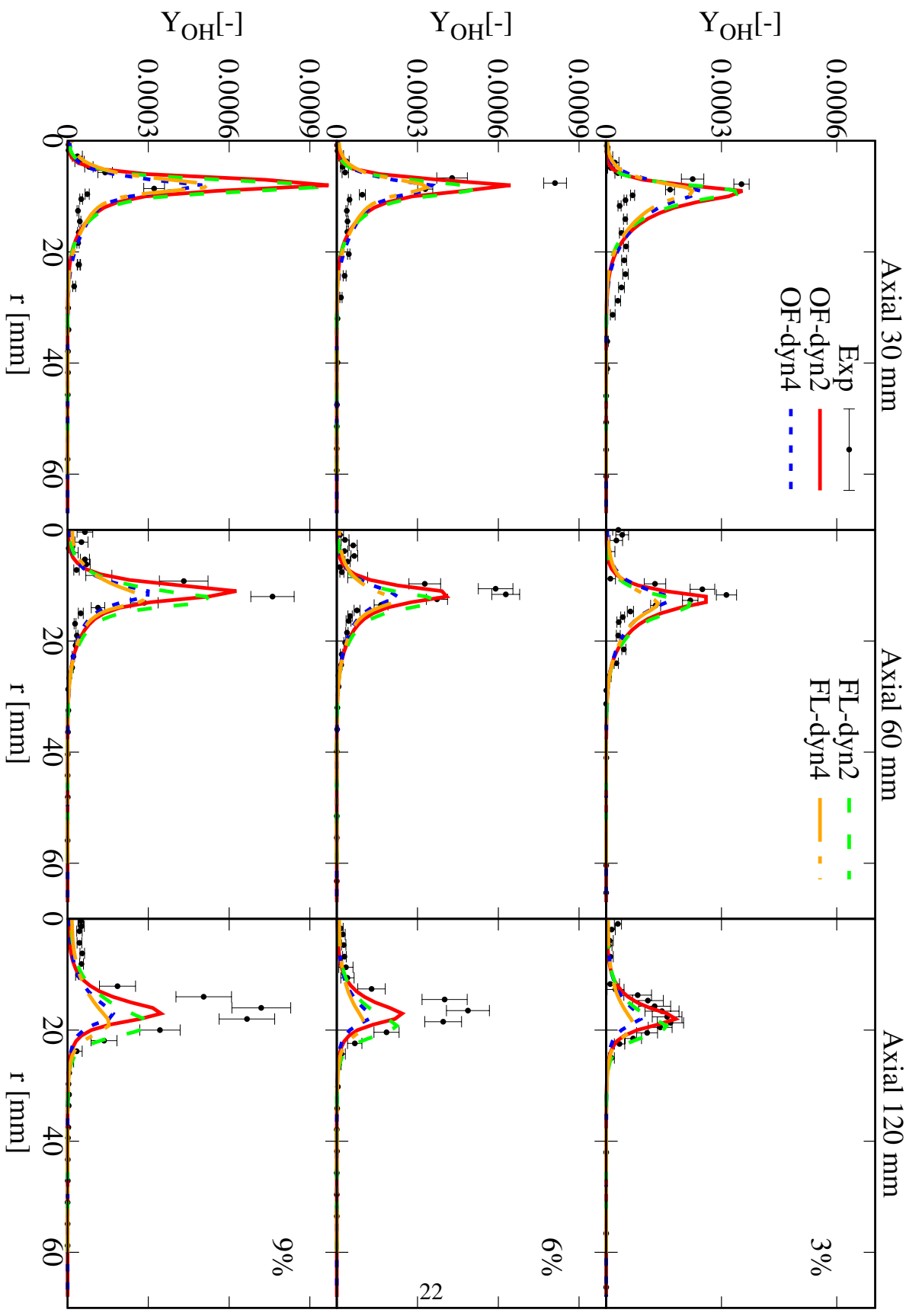

Figure 14: Mean OH mass fraction profile obtained for different co-flow oxygen levels (3%, 6% and 9%), using two dynamic model formulations. OpenFOAM and Fluent solvers.

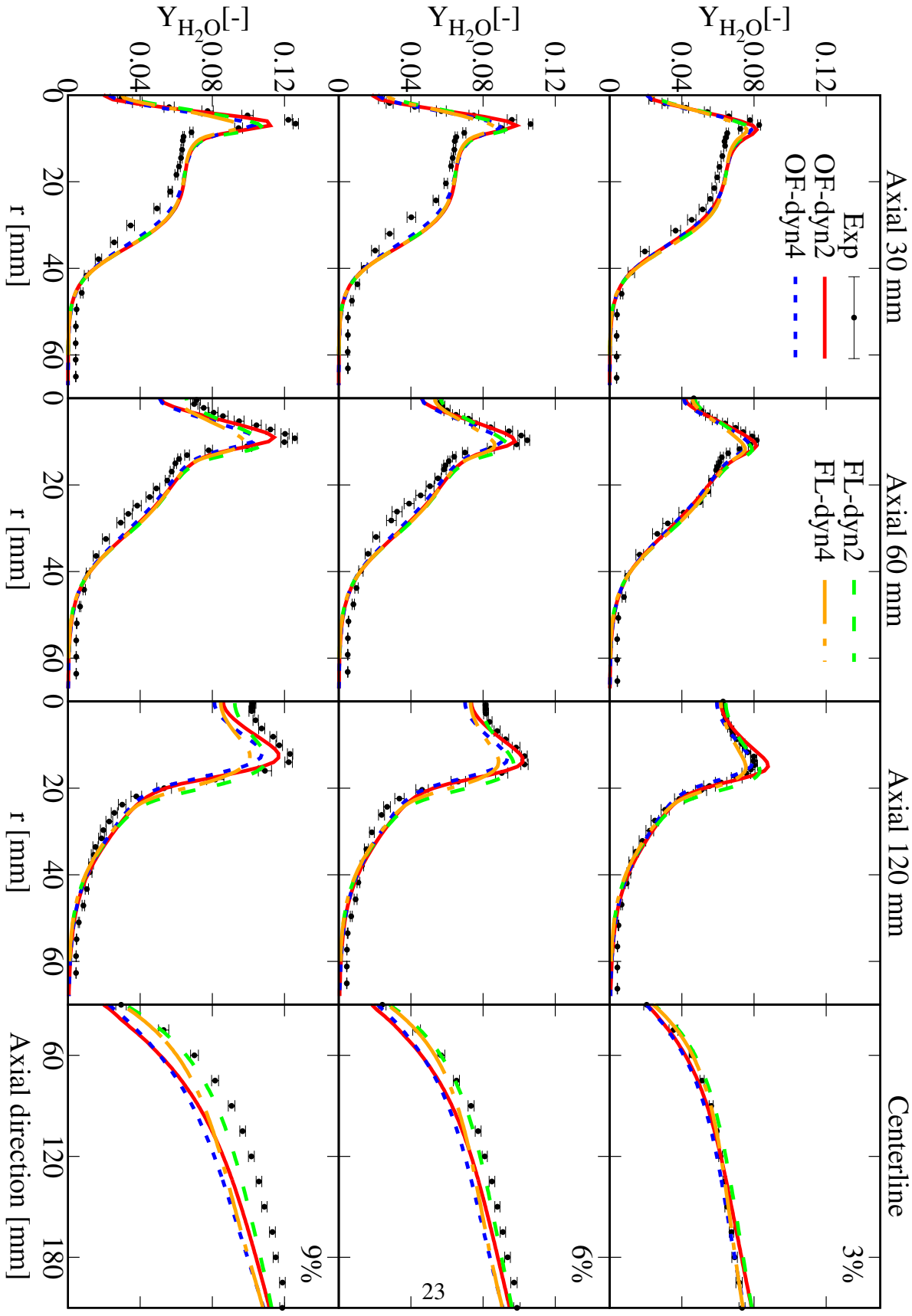

Figure 15: Mean H_2O mass fraction profile obtained for different co-flow oxygen levels (3%, 6% and 9%), using two dynamic model formulations. OpenFOAM and Fluent solvers.

For the 6% and 9% O_2 case, the centerline measurements are significantly under-predicted with OF solver, particularly at upstream locations. The under-prediction along the centerline could be detected, although less significant, also for the temperature profile in Fig. 13. As for the CO_2 mass fraction profiles (not-shown here), no under-prediction exists for upstream centerline values. Therefore, it can be concluded that the temperature under-prediction observed for the 6% and 9% O_2 cases, is associated to the under-prediction of H_2O production, which affects the heat release rate and the temperature levels. The FL solver with dyn2 model, however, provides better prediction on the centerline results for 6% and 9% O_2 cases. As far as the radial species profiles are concerned, the OF results with the dyn2 model show the highest accuracy, whereas all other combinations show obvious under-prediction, especially for the peak values. The FL solver shows in general a bit lower predicted profile than that with OF solver. A slightly shifted peak values can also be captured.

The OF solver with the dyn2 mixing model provides the best predictions of the CO mass fraction profiles, as indicated in Fig. 16 by the red solid line. The CO profiles for 3% O_2 and z = 120 mm are slightly over-predicted by the dyn2 model, while the OF results with dyn4 and FL with dyn2 provide better results. All solver and dynamic model combinations cannot accurately reproduce the centerline profile.

The analysis of the CO radial profiles in Fig. 16 shows the existence of a second peak, at $z \leqslant 60$ mm, in the measurement data. This is due to the non-zero CO concentration in the hot co-flow, that is convected downstream. Because uniform boundary conditions are adopted in the simulations, this second peak can not be captured. A discussion about the influence of boundary conditions on the prediction of CO is presented in Section 4.4.

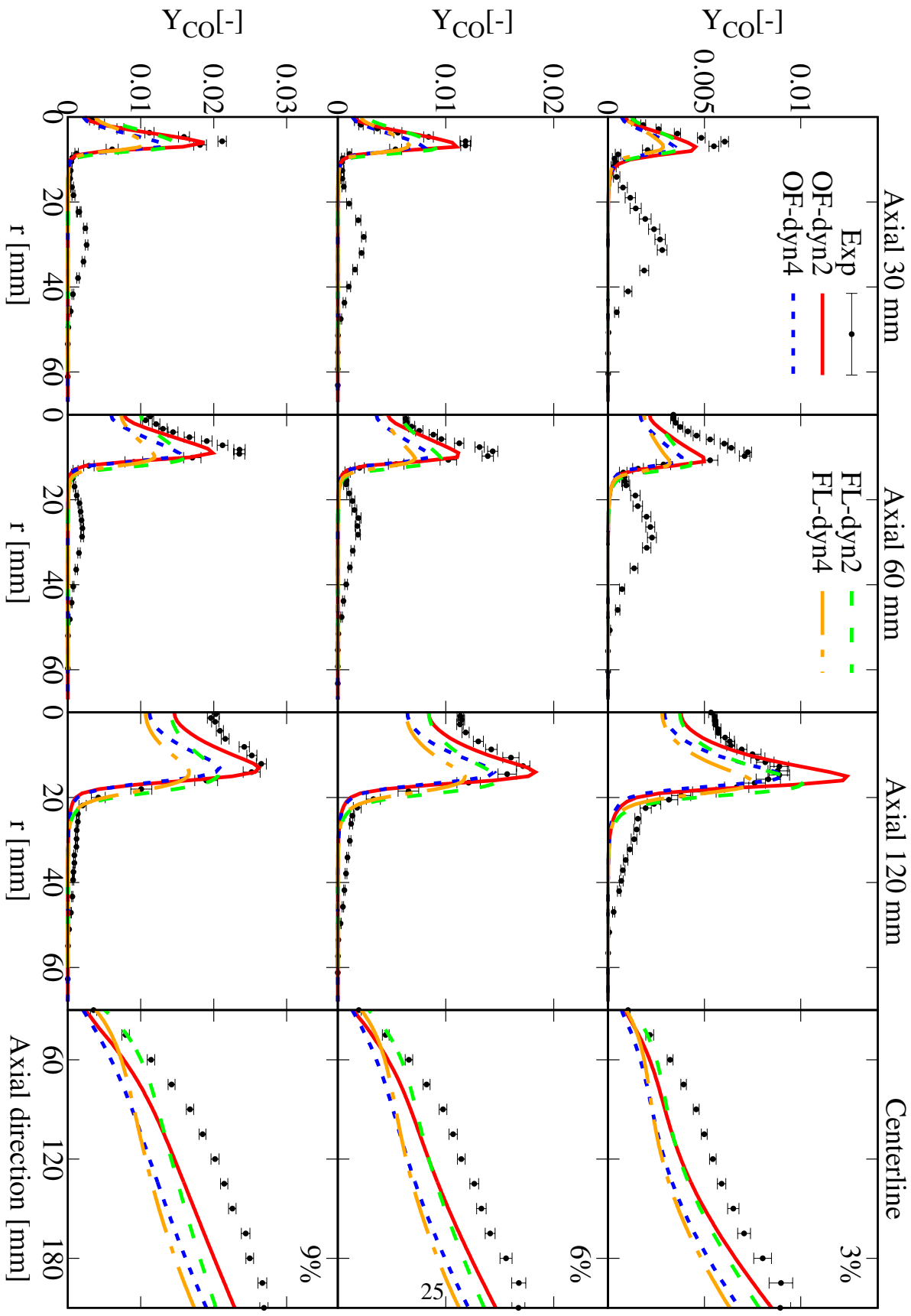

Figure 16: Mean CO mass fraction profile obtained for different co-flow oxygen levels (3%, 6% and 9%), using two dynamic model formulations. OpenFOAM and Fluent solvers.

The results shown above refer to cases with a fixed Reynolds number, varying the O_2 content in the co-flow. This means that the mixing time is not strongly affected, while the chemical time scale changes due to the change of the oxidizing atmosphere. The contour plots showing the chemical time scale distributions for the three O_2 level cases (3%, 6% and 9%) are compared in Fig. 17. With increasing oxygen content, more oxygen is available to mix with the fuel stream, and the reaction process is enhanced. This can be well indicated by the expansion of the reactive region in the flow, which is characterized by chemical time scales (tau_C) smaller than the fixed threshold value of 0.1 s.

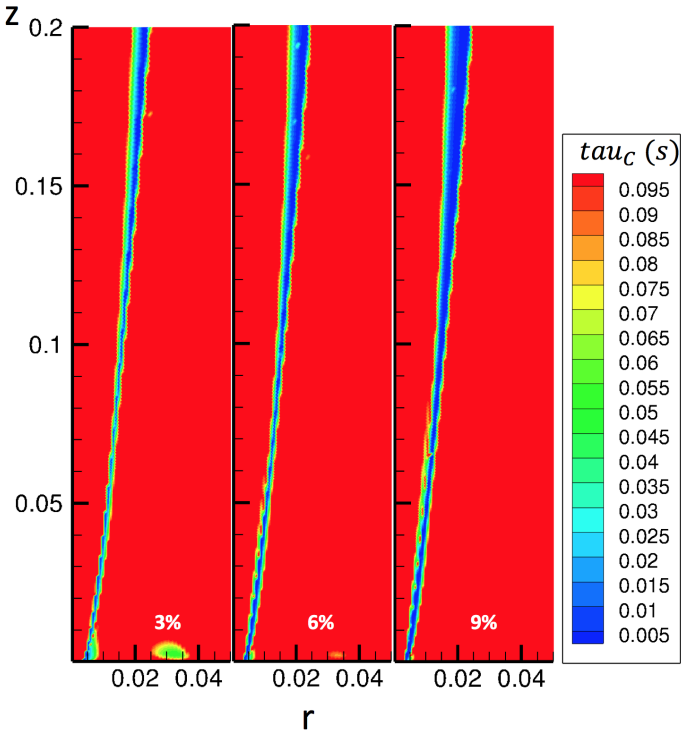

Figure 17: Chemical time scale (tau_C) distribution. Mixing time scale estimated from the dyn2 mixing model. Only the area of interest of the simulation domain is shown. Legend unit: m. OpenFOAM solver.

For the purpose of investigating how the model performs for varied flow field, cases with different fuel jet Reynolds numbers are simulated, fixing co-flow oxygen content to 3%. The mean temperature profiles and distribution of $C_{mix,eq}$ values are presented in Fig. 18 and Fig. 19, separately. The mean temperature profiles are mostly well predicted with both solvers and parameter sets. The dyn2 model with OpenFOAM solver gives some over-predictions at z = 120 mm. While the dyn2 model with FL solver alleviates the over-prediction, except for the case of Re = 20 k. As for the Re = 20 k at 120 mm axial location, the dyn2 model with OpenFOAM solver gives overall more satisfactory prediction. On the other hand, the

FL solver with the dyn2 model shows non-negligible over-prediction of temperature levels. Moreover, both dyn2 and dyn4 models with the FL solver show flame extinction for the 20 k case above z $\geqslant$ 150 mm.

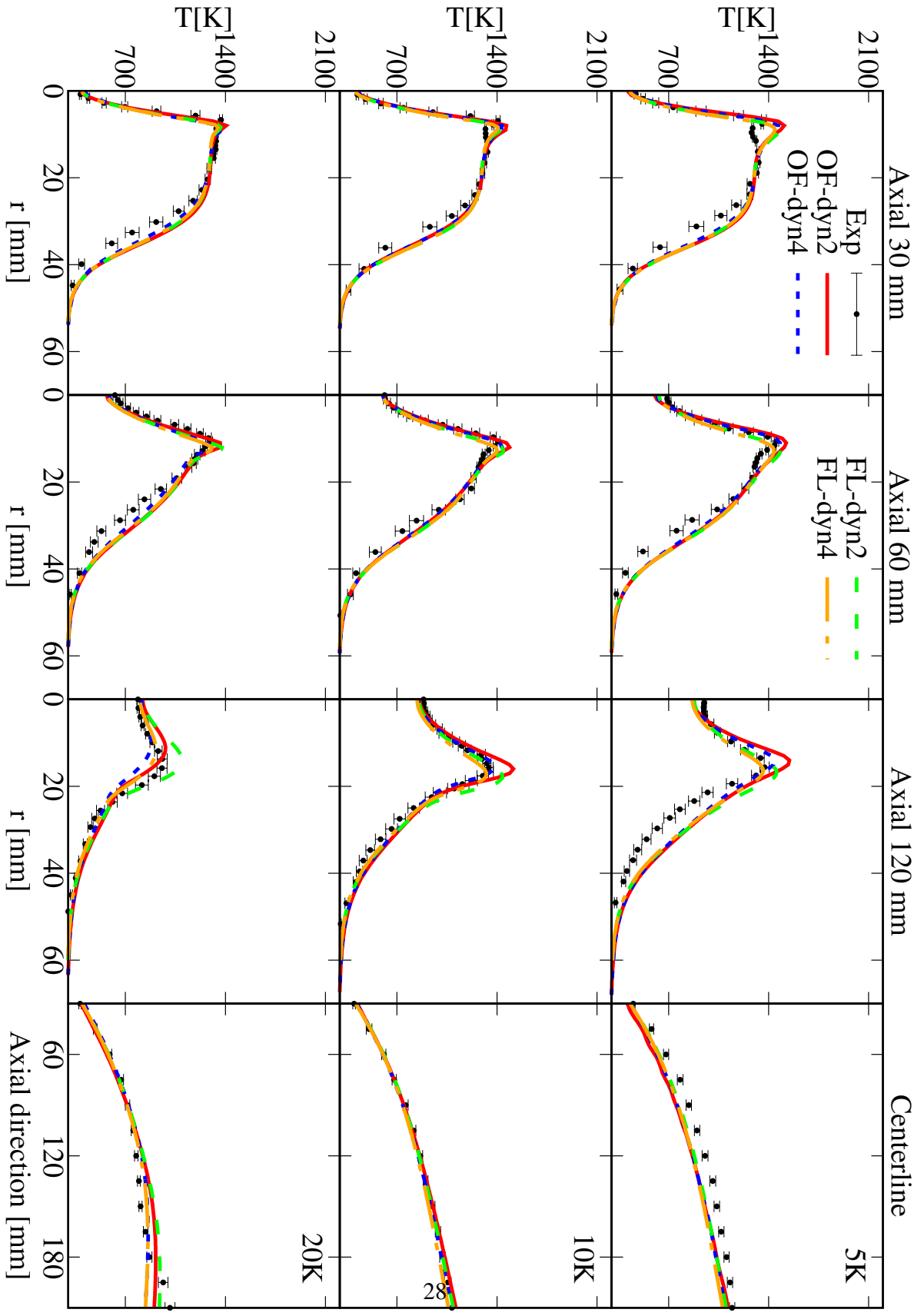

Figure 18: Mean temperature profiles obtained for different fuel jet Reynolds numbers (5 k, 10 k and 20 k), using two dynamic model formulations. OpenFOAM and Fluent solvers.

The $C_{mix,eq}$ distribution with various fuel jet Reynolds numbers can be appreciated in Fig. 19. The Re = 5 k case shows a pronounced shear layer between the co-flow and fuel jet. This layer is progressively reduced when increasing the Reynolds number to 10 k and 20 k. The reason is that the increased fuel jet velocity reduces the inter-facial area and diminishes mixing [41]. Furthermore, for Re = 20 k, there is a high $C_{mix,eq}$ region in the jet potential core and further downstream, the $C_{mix,eq}$ value close to centerline is increased with increased Reynolds number. For a fully developed turbulent pipe flow, the turbulent intensity has a negative correlation with the Reynolds number, meaning that higher Reynolds number jet breaks up later than the one with lower Reynolds number [42, 43]. Therefore, a larger mixing scale is found for the case with higher Reynolds number, thus resulting in higher τ_{mix} value and lower values of reacting fractions. This justifies the reduction of the temperature levels going from Re=5 k to Re=20 k, as seen in Fig. 18.

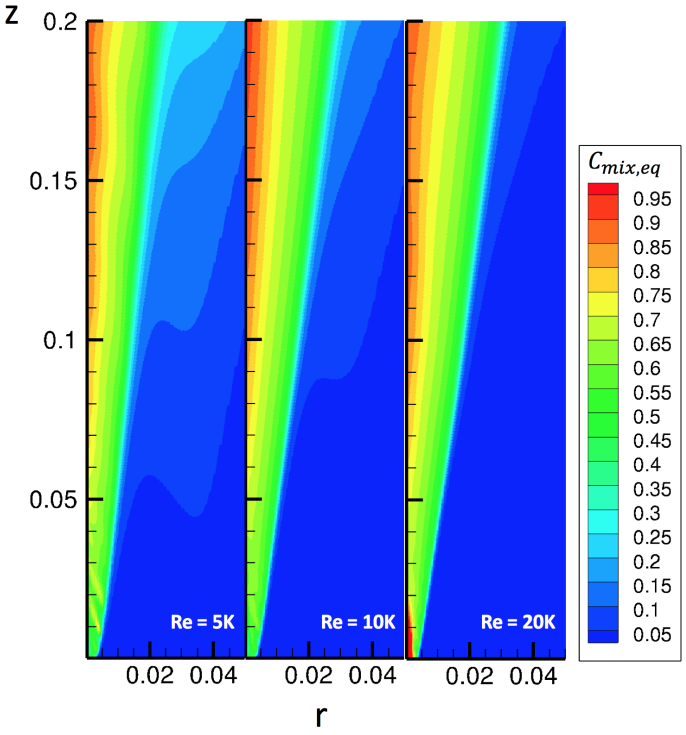

Figure 19: Mixing time constant C_{mix} distribution for the different fuel jet Reynolds number cases (5 k, 10 k and 20 k). Only the area of interest of the simulation domain is shown. Legend unit: m. OpenFOAM solver.

4.4. Influence of boundary conditions on CO prediction

The CO mass fraction profiles obtained with non-uniform and uniform boundary conditions are presented in Fig. 20 and Fig. 21. The mixing model dyn2 is used and the chemical time scale is calculated with the formation rate based approach. It is very clear that the use of

non-uniform boundary conditions helps to improve the CO predictions, as it allows capturing the second radial peak, without impairing the prediction of the first peak for 6% and 9% O_2 cases in Fig. 20. On the other hand, the use of non-uniform boundary conditions worsen the CO prediction at z = 30 mm and z = 60 mm, for the 3% O_2 case, and for all O_2 levels along the centerline. Regarding the temperature profile (not-shown here), using non-uniform boundary conditions corrects the temperature peak over-prediction by the dyn2 model, while the centerline value is under-estimated.

Fig. 21 shows the mean CO profiles obtained using the uniform and non-uniform boundary conditions, when varying the fuel jet Reynolds number. It can be observed that using the non-uniform boundary conditions allows capturing the second CO peak, but it significantly impacts the accuracy in the reconstruction of the first peak. Moreover, the use of non-uniform boundary conditions leads to the global extinction of the flame for the case of Re = 20 k, after z = 120 mm (from the burner exit).

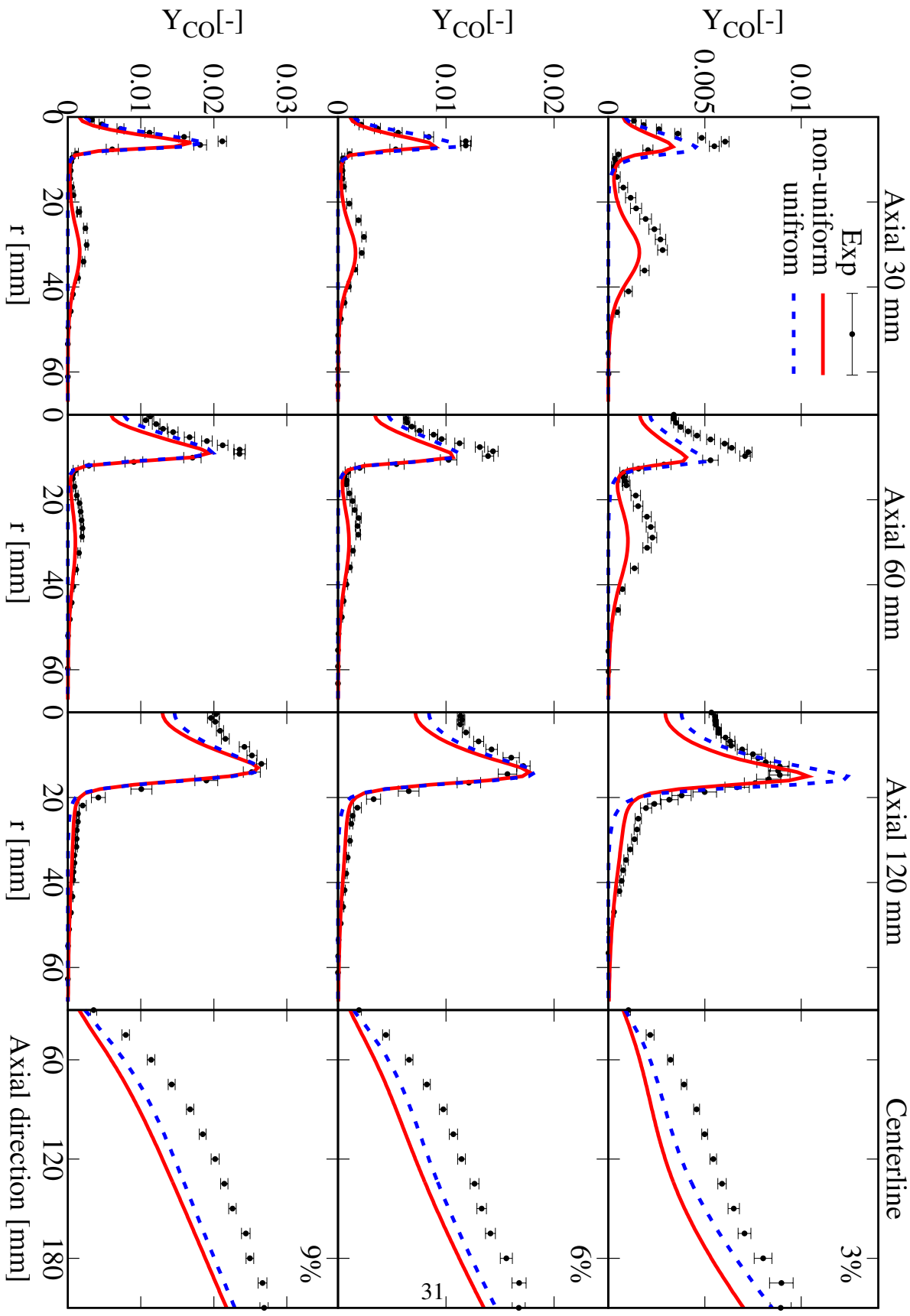

Figure 20: Mean CO mass fraction profiles obtained using non-uniform and uniform boundary conditions. O_2 mass fraction in the co-flow: 3%, 6% and 9%.

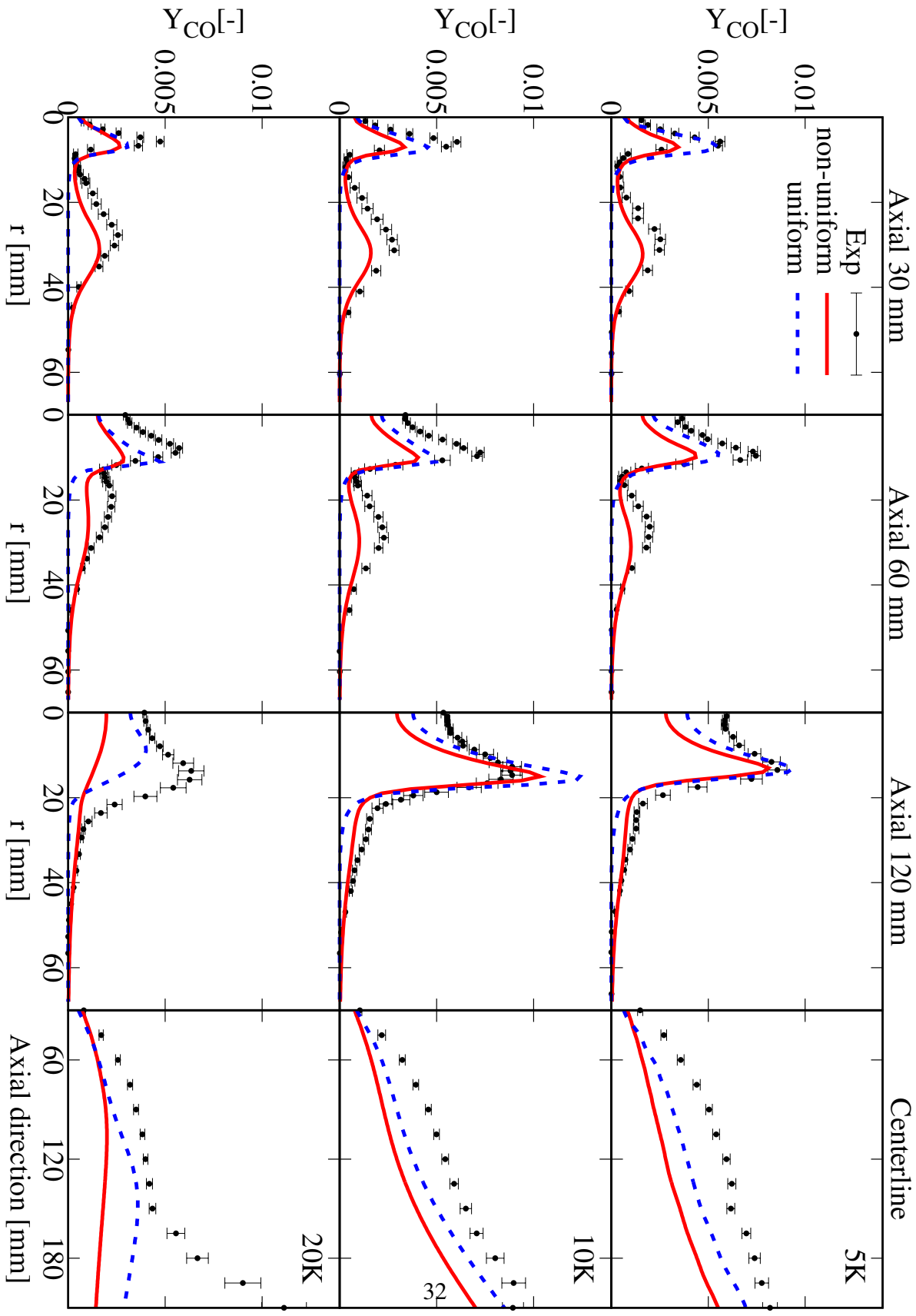

Figure 21: Mean CO mass fraction profile obtained using the non-uniform and uniform boundary conditions. Fuel jet Reynolds number: 5 k, 10 k and 20 k.

5. Conclusion

In the current article, different approaches for mixing time scale and chemical time scale estimation are assessed and benchmarked, for their use in the context of the Partially-Stirred Reactor closure. The OpenFOAM and ANSYS Fluent 17.0 [21] solvers are compared on a variety of cases, varying the oxygen content in the co-flow and the fuel jet Reynolds number. The influence of using non-uniform and uniform boundary conditions is also assessed. The following conclusions can be drawn:

- The dynamic mixing model can identify optimal local values of the mixing time scale when compared to global approaches based on the Kolmogorov and integral scales, or combination of the two. The mean temperature profile on axial 120 mm location is well predicted using a dynamic mixing model without compromising the prediction at z = 30 mm. Therefore, the appropriate mixing scale was found to improve the prediction of the temperature and species profiles (especially H_2O) in the whole domain significantly, and it is not only in specific regions, as reported in the literature with other ad-hoc approaches.

- The decomposition of the source term Jacobian matrix is the most accurate and time consuming method for the evaluation of the chemical time scale. The approach based on the formation rates provides the best compromise between accuracy and computational cost, while the approach based on reaction rates may lead to inaccurate results as it tends to over-predict the chemical time scales.

- The combination of the dynamic mixing model and the formation rate based chemical time scale estimation approach performs the best for applications under Moderate or Intense Low oxygen Dilution combustion condition, with a wide range of oxygen levels (3%, 6% and 9%) in the co-flow and fuel jet Reynolds numbers (Re = 5,000/10,000 and 20,000).

- OpenFOAM provides overall more accurate results with respect to Fluent for the current case. This might arise from the highly diffusive nature of the Fluent code. Cases characterized by a more complicated geometry will be analysed in the future.

- The use of non-uniform boundary conditions allows capturing the second radial CO peak, while worsening the CO level along the centerline and close to the axis.

The present study demonstrates the applicability of the Partially-Stirred Reactor model under Moderate or Intense Low oxygen Dilution combustion condition. Various approaches

on chemical and mixing time scales evaluation were compared and discussed comprehensively, giving references to the application of Partially-Stirred Reactor model within non-conventional regime. A dynamic model on the estimation of mixing time is evaluated, presenting superior performance than the global models under a wide range of operation conditions. The CPU time required by the dynamic model is comparable with the global ones.

In industrial burners, a wide range of operation conditions exist and the interactions between chemistry and turbulence are complicated because of complex geometry. In this framework, the availability of affordable and accurate numerical tools is the key to unlock the potential of new technologies which are able to deal with a variety of energy vectors, ensuring high efficiency and low pollutant emissions. The present work evaluates a novel implementation of the Partially-Stirred Reactor model, based on the accurate estimation of chemical and mixing time scales. Results show that it has great potentiality for the simulation and development of large scale industrial burners.

Acknowledgments

This project has received funding from the European Union′s Horizon 2020 research and innovation program under the Marie Skłodowska-Curie grant agreement No. 643134. The research of the second author has received funding from the Fonds de la Recherche Scientifique - FNRS Belgium. The research of the last author is sponsored by the European Research Council, Starting Grant No. 714605, and from the Fédération Wallonie-Bruxelles, via ′Les Actions de Recherche Concertée (ARC)′ call for 2014-2019.

References

[1] J. A. Wünning and J. G. Wünning. Flameless oxidation to reduce thermal NO-formation. *Progress in Energy and Combustion Science*, 23:81–94, 1997.

[2] A. Cavaliere and M. de Joannon. MILD combustion. *Progress in Energy and Combustion Science*, 30:329–366, 2004.

[3] M. de Joannon, G. Sorrentino, and A. Cavaliere. MILD combustion in diffusion-controlled regimes of hot diluted fuel. *Combustion and Flame*, 159:1832–1839, 2012.

[4] Paul R. Medwell and Bassam B. Dally. Effect of fuel composition on jet flames in a heated and diluted oxidant stream. *Combustion and Flame*, 159:3138–3145, 2012.

[5] Chiara Galletti, Alessandro Parente, and Leonardo Tognotti. Numerical and experimental investigation of a mild combustion burner. *Combustion and Flame*, 151:649–664, 2007.

[6] A. Parente, C. Galletti, and L. Tognotti. Effect of the combustion model and kinetic mechanism on the MILD combustion in an industrial burner fed with hydrogen enriched fuels. *International Journal of Hydrogen Energy*, 33:7553–7564, 2008.

[7] F. Xing, A. Kumar, Y. Huang, S. Chan, C. Ruan, S. Gu, and X. Fan. Flameless combustion with liquid fuel: A review focusing on fundamentals and gas turbine application. *Applied Energy*, 193:28–51, 2017.

[8] E.-S. Cho, B. Danon, W. de Jong, and D.J.E.M. Roekaerts. Behavior of a 300kwth regenerative multi-burner flameless oxidation furnace. *Applied Energy*, 88(12):4952–4959, 2011.

[9] E.-S. Cho, D. Shin, J. Lu, W. de Jong, and D.J.E.M. Roekaerts. Configuration effects of natural gas fired multi-pair regenerative burners in a flameless oxidation furnace on efficiency and emissions. *Applied Energy*, 107:25–32, 2013.

[10] Mario Sánchez, Francisco Cadavid, and Andrés Amell. Experimental evaluation of a 20kw oxygen enhanced self-regenerative burner operated in flameless combustion mode. *Applied Energy*, 111:240–246, 2013.

[11] Jingjing Ye, Paul R. Medwell, Emilien Varea, Stephan Kruse, Bassam B. Dally, and Heinz G. Pitsch. An experimental study on mild combustion of prevaporised liquid fuels. *Applied Energy*, 151:93–101, 2015.

[12] Stephan Kruse, Bruno Kerschgens, Lukas Berger, Emilien Varea, and Heinz Pitsch. Experimental and numerical study of mild combustion for gas turbine applications. *Applied Energy*, 148:456–465, 2015.

[13] W. P. Adamczyk, R. A. Bialecki, M. Ditaranto, P. Gladysz, N. E. L. Haugen, A. Katelbach-Wozniak, A. Klimanek, S. Sladek, A. Szlek, and G. Wecel. CFD modelling and thermodynamic analysis of a concept of a MILD-Oxy combustion large scale pulverized coal boiler. *Energy*, 140(1):1305–1315, 2017.

[14] A. Chinnici, Z. F. Tian, J. H. Lim, G. J. Nathan, and B. B. Dally. Comparison of system performance in a hybrid solar receiver combustor operating with MILD and conventional combustion. Part II: Effect of the combustion mode. *Solar Energy*, 147:478–488, 2017.

[15] Y. Minamoto and N. Swaminathan. Subgrid scale modelling for MILD combustio. *Proceedings of the Combustion Institute*, 35(3):3529–3536, 2015.

[16] J. Chomiak. *Combustion: A Study in Theory, Fact and Application*. Abacus Press/Gorden and Breach Science Publishers, 1990.

[17] J. Chomiak and A. Karlsson. Flame liftoff in diesel sprays. In *Twenty-Sixth Symposium (International) on Combustion*, pages 2557–2564. The Combustion Institute, 1996.

[18] V. Golovitchev and J. Chomiak. Numerical modeling of high temperature air flameless combustion. In *The 4th international symposium on high temperature air combustion and gasification*, 2001.

[19] Fabian Peng Kärrholm. *Numerical Modelling of Diesel Spray Injection, Turbulence Interaction and Combustion*. Phd thesis, Chalmers University of Technology, Chalmers, Sweden, 2008.

[20] P. A. Niklas Nordin. *Complex Chemistry Modeling of Diesel Spray Combustion*. Phd thesis, Chalmers University of Technology, Chalmers, Sweden, 2001.

[21] *ANSYS® Academic Research, Release 17.0.*

[22] B. B. Dally, A. N. Karpetis, and R. S. Barlow. Structure of turbulent non-premixed jet flames in a diluted hot coflow. *Proceedings of the Combustion Institute*, 29:1147–1154, 2002.

[23] Dmitry A. Lysenko, Ivar S. Ertesvåg, and Kjell Erik Rian. Numerical simulation of non-premixed turbulent combustion using the eddy dissipation concept and comparing with the steady laminar flamelet model. *Flow, Turbulence and Combustion*, 53:577–605, 2014.

[24] Alessandro Parente, Mohammad Rafi Malik, Francesco Contino, Alberto Cuoci, and Bassam B. Dally. Extension of the eddy dissipation concept for turbulence/chemistry interactions to MILD combustion. *Fuel*, 163:98–111, 2015.

[25] L. Kjäldman, A. Brink, and M. Hupa. Micro mixing time in the Eddy Dissipation Concept. *Combustion Science and Technology*, 154:207–227, 2007.

[26] M. Gonzales and R. Borghi. *Turbulent Shear Flows*. Number 293-311 in 7. Springer Verlag, Berlin, 1991.

[27] Venkatramanan Raman and Heinz Pitsch. A consistent LES/filtered-density function formulation for the simulation of turbulent flames with detailed chemistry. *Proceedings of the Combustion Institute*, 31(2):1711– 1719, 2007.

[28] I.K. Ye. *Investigation of the scalar variance and scalar dissipation rate in URANS and LES*. Phd thesis, University of Waterloo, Ontario, Canada, Waterloo, Ontario, Canada, 2011.

[29] J. P. H. Sanders and I. Gökalp. Scalar dissipation rate modelling in variable density turbulent axisymmetric jets and diffusion flames. *Physics of Fluids*, 10(4):938–948, 1998.

[30] Benjamin J. Isaac, Alessandro Parente, Chiara Galletti, Jeremy N. Thornock, Philip J. Smith, and Leonardo Tognotti. A novel methodology for chemical time scale evaluation with detailed chemical reaction kinetic. *Energy Fuels*, 27(4):2255–2265, 2013.

[31] R. O. Fox. *Computational Models for Turbulent Reacting Flows*. Cambridge University Press, Cambridge, UK, 2003.

[32] Zhiyi Li, Alberto Cuoci, Amsini Sadiki, and Alessandro Parente. Comprehensive numerical study of the Adelaide Jet in Hot-Coflow burner by means of RANS and detailed chemistry. *Energy*, 139:555–570, 2017.

[33] Marco Ferrarotti, Chiara Galletti, Alessandro Parente, and Leonardo Tognotti. Development of reduced NOx models for flameless combustion. In *18th IFRF Members Conference*, 2015.

[34] William L. Oberkampf and Matthew F. Barone. Measures of agreement between computation and experiment: Validation metrics. *Journal of Computational Physics*, 217(1):5–36, 2006.

[35] A. Cuoci, A. Frassoldati, T. Faravelli, and E. Ranzi. Opensmoke++: An object-oriented framework for the numerical modeling of reactive systems with detailed kinetic mechanisms. *Computer Physics Communications*, 192:237–264, 2015.

[36] R. W. Bilger, S. H. Stårner, and R. J. KEE. On reduced mechanisms for methane-air combustion in nonpremixed flames. *Combustion and Flame*, 80(2):135–149, 1990.

[37] F. C. Christo and B. B. Dally. Modelling turbulent reacting jets issuing into a hot and diluted coflow. *Combustion and Flame*, 142:117–129, 2005.

[38] Alessio Frassoldati, Pratyush Sharma, Alberto Cuoci, Tiziano Faravelli, and Eliseo Ranzi. Kinetic and fluid dynamics modeling of methane/hydrogen jet flames in diluted coflow. *Applied Thermal Engineering*, 30:376–383, 2009.

[39] B. E. Launder and D. B. Spalding. The numerical computations of turbulent flows. *Computer Methods in Applied Mechanics and Engineering*, 3(2):269–289, 1973.

[40] Valerio D'Alessandro, Lorenzo Binci, Sergio Montelpare, and Renato Ricci. On the development of openfoam solvers based on explicit and implicit high-order runge-kutta schemes for incompressible flows with heat transfer. *Computer Physics Communications*, 222(Supplement C):14–30, 2018.

[41] A. Ghasemi, V. Roussinova, Ram Balachandar, and R.M. Barron. Reynolds number effects in the near-field of a turbulent square jet. *Experimental Thermal and Fluid Science*, 61:249–258, 2015.

[42] F. Russo and N. T. Basse. Scaling of turbulence intensity for low-speed flow in smooth pipes. *Flow Measurement and Instrumentation*, 52:101–114, 2016.

[43] N. T. Basse. Turbulence intensity and the friction factor for smooth- and rough-wall pipe flow. *Fluids*, 2(30), 2017.

5.3 Journal paper 3

This paper was published in Energy and Fuels:

Zhiyi Li, Michał T. Lewandowski, Francesco Contino and Alessandro Parente, Assessment of on-the-fly chemistry reduction and tabulation approaches for the simulation of MILD combustion, Energy and Fuels 32(10), 10121-10131 (2018).

Assessment of on-the-fly chemistry reduction and tabulation approaches for the simulation of MILD combustion

Zhiyi Li[a,b,*], Michał T. Lewandowski[c], Francesco Contino[d], Alessandro Parente[a,b,**]

[a] *Université Libre de Bruxelles, Ecole Polytechnique de Bruxelles, Aero-Thermo-Mechanics Laboratory, Bruxelles, Belgium*
[b] *Université Libre de Bruxelles and Vrije Universiteit Brussel, Combustion and Robust Optimization Group (BURN), Bruxelles, Belgium*
[c] *Institute of Fluid Flow Machinery, Polish Academy of Sciences, Gdańsk, Poland*
[d] *Vrije Universiteit Brussel, Department of Mechanical Engineering, Brussels, Belgium*

Abstract

The current article focuses on the numerical simulation of the Delft Jet-in-Hot-Coflow (DJHC) burner, fed with natural gas and biogas, using the Eddy Dissipation Concept (EDC) model with dynamic chemistry reduction and tabulation, i.e. Tabulated Dynamic Adaptive Chemistry (TDAC). The CPU time saving provided by TDAC is evaluated for various EDC model constants and chemical mechanisms of increasing complexity, using a number of chemistry reduction approaches. Results show that the TDAC method provides speed-up factors of 1.5-2.0 and more than 10, when using a skeletal (DRM19) and a comprehensive kinetic mechanism (POLIMIC1C3HT), respectively. The Directed Relation Graph with Error Propagation (DRGEP), Dynamic Adaptive Chemistry (DAC) and Elementary Flux Analysis (EFA) reduction models show superior performances when compared to other approaches as Directed Relation Graph (DRG) and Path Flux Analysis (PFA). All the reduction models have been adapted for run-time reduction. Furthermore, the contribution of tabulation is more important with small mechanisms, while reduction plays a major role with large mechanisms.

1. Introduction

Moderate or Intense Low oxygen Dilution (MILD) combustion technology has gained increasing attention for the past few decades [1, 2, 3]. It is characterized by very strong mixing between the reactant and product. As a result, the fuel conversion rate is higher and the temperature field is more uniform than in conventional combustion, thereby reducing CO,

*Corresponding author: Zhiyi.Li@ulb.ac.be
**Corresponding author: Alessandro.Parente@ulb.ac.be

soot and NO_x emissions [1, 2]. Due to the intensive mixing and reduced temperature peak, reactivity in MILD combustion is reduced to the point that the overall oxidation process is controlled by chemical kinetics [4]. Thus, combustion models which can include detailed chemistry are required when modelling such a combustion regime. In the present work, the Eddy Dissipation Concept (EDC) combustion model [5] is used.

The number of of species and reactions in a reaction mechanism grows with the number of carbon atoms in the fuel component. As a consequence, the CPU time associated to chemistry resolution can be very significant, for industrial applications involving realistic fuels. In this framework, the use of pre-reduced or pre-tabulated mechanisms may not be able to capture the dynamic phenomena like extinction and re-ignition accurately. Therefore, on-the-fly/dynamic chemistry reduction/tabulation methods are essential to alleviate the calculation burden for finite rate chemistry approaches. Various investigations based on the use of on-the-fly chemistry reduction techniques are reported in the literature. Tosatto[6] used a transport-flux-based Directed Relation Graph (DRG) model in a two-dimensional simulation of axisymmetric co-flow flames. A speed-up factor of about 5 was reported for a steady case, while a factor ranging from 10 to 20 was obtained for a time-dependent oscillating flame. Zhang et al.[7] and He et al.[8] conducted Homogeneous Charge Compression Ignition (HCCI) engine simulations with the Element Flux Analysis (EFA) approach. The size of kinetic scheme was significantly reduced, while maintaining reliable accuracy. Dynamic reduction method allows significant CPU savings; however, the cost associated to the direct ODE integration can be still significant, if the number of species in the reduced mechanisms is non-negligible. The coupling with dynamic tabulation approach provides a solution to this issue. Tang et al.[9] combined chemistry dimension reduction and tabulation with a methodology called *In situ* Adaptive Tabulation-Rate-Controlled Constrained Equilibrium (ISAT-RCCE). The ISAT-RCCE calculations show good agreement with the accurate solution, and a significant speed-up factor of about 500 is obtained compared to the direct integration approach. Ren et al.[10] and Contino et al.[11] coupled Dynamic Adaptive Chemistry (DAC) approach with ISAT in engine simulations, achieving speed-up factors of the order of 100. The chemistry reduction model expedites the reaction sub-step in the operator-splitting scheme through local skeletal reduction, whereas ISAT expedites the calculations by reducing the number of direct ODE integrations through tabulating and re-using the solutions, thus making the use of detailed chemistry in CFD simulations more achievable[11].

The current investigation focuses on the application of Tabulated Dynamic Adaptive Chemistry (TDAC) [11] for the simulation of MILD combustion. The study is motivated by the specific features of such a combustion regime: indeed, there is a general consensus about the need of detailed kinetics in MILD combustion, but yet it is not clear to which extent

a chemical mechanism can be reduced without loss of accuracy. The Delft Jet in Hot Co-flow (DJHC) burner [12, 13] is chosen as the validation case. Two fuels, Dutch natural gas and biogas; and three chemical mechanisms, DRM19 [14], GRI 3.0 [15] and POLIMIC1C3HT [16] are chosen to assess the speed-up achievable with TDAC. The EDC constants are adjusted to optimize simulation results, following recent studies [17, 18, 19, 20, 21]. Several reduction approaches are benchmarked against DAC, and the contribution of reduction and tabulation in TDAC approach is assessed. The objective of the present work is to feature an overall assessment of TDAC method under MILD regime using EDC combustion model. All the numerical model are implemented in the OpenFOAM development version without external libraries.

2. Numerical models

In this section, the Eddy Dissipation Concept (EDC) combustion model and the Tabulation of Dynamic Adaptive Chemistry (TDAC) approach for chemistry reduction and tabulation are presented in detail.

2.1. Eddy Dissipation Concept

The EDC model, proposed by Magnussen[5], assumes that combustion happens in fine structures, where energy dissipation takes place. In the original model formulation, the fine structures are described as Perfectly Stirred Reactors (PSR). However, some software packages (for example, ANSYS Fluent) treat them as Plug Flow Reactors (PFR), for mainly numerical convenience. A previous work has shown that there are no distinguishable differences when using PSR and PFR reactors [22]. Therefore, the PFR treatment is selected in the current study. Each computational cell is separated into a fine structure region and surrounding fluid region. The mass fraction of the fine structures (γ_λ) and the mean residence time of the fluid inside the fine structures (τ^*) are described as:

$$\gamma_\lambda = C_\gamma \left(\frac{\nu\epsilon}{k^2}\right)^{\frac{1}{4}}, \tag{1}$$

and

$$\tau^* = C_\tau \left(\frac{\nu}{\epsilon}\right)^{\frac{1}{2}}, \tag{2}$$

where ν is the kinematic viscosity and ϵ is the dissipation rate of kinetic energy, k. C_γ and C_τ are two model parameters, set to 2.1377 and 0.4083, respectively. Finally, the mean reaction

rate of specie i is expresses as:

$$\overline{\dot{\omega}}_i = -\frac{\rho\gamma_\lambda^2}{\tau^*\left(1-\gamma_\lambda^2\right)}\left(\widetilde{Y}_i - Y_i^*\right). \tag{3}$$

This expression of the EDC model is proposed by Magnussen in 2005, therefore denoted as EDC2005 in the present work. The term $\widetilde{Y}_i$ in Eqn. 3 is the mean mass fraction of species i between the fine structures, Y_i^*, and the surrounding fluid, Y_i^0. The mean mass fraction $\widetilde{Y}_i$ is expressed as:

$$\widetilde{Y}_i = \gamma_\lambda^2 Y_i^* + (1-\gamma_\lambda^2)Y_i^0. \tag{4}$$

The mass fraction Y_i^* of species i inside the fine structures is estimated solving a Plug Flow Reactor (PFR) equation, considering the evolution within the fine structure residence time τ^*:

$$\frac{dY_i}{dt} = \frac{\dot{\omega}_i^*}{\rho^*}. \tag{5}$$

The integration over $\frac{dY_i}{dt}$ for a time period of τ^* is Y_i^*. The term $\dot{\omega}_i^*$ denotes the instantaneous formation rate of species i in PFR, which is evaluated from a detailed kinetic mechanism. In the present study, the DRM19 (19 species + N_2 and AR, 58 reactions) [14], GRI3.0 (53 species, 325 reactions) [15], and POLIMIC1C3HT (107 species, 2642 reactions) [16] mechanisms are used.

The EDC2005 model has been reported to over-predict peak temperatures in MILD combustion condition [19, 18]. Adjustments of the C_γ and C_τ constants have been proposed to correct this behaviour [17, 18, 19, 20, 21]. Among them, the adjustment proposed by De et al. [20] focused on the DJHC flame, for which C_τ was increased to 3.0 or C_γ decreased to 1.0.

2.2. Tabulation of Dynamic Adaptive Chemistry

TDAC couples a modified *In-situ* Adaptive Tabulation (ISAT) [23] algorithm and chemical mechanism reduction methods [24, 11, 25, 26, 27, 28], including Directed Relation Graph (DRG) [29], DRG with Error Propagation (DRGEP) [30], Dynamic Adaptive Chemistry (DAC) [31], Elementary Flux Analysis (EFA) [32] and Path Flux Analysis (PFA) [33]. The TDAC process is visualised in Figure 1. ISAT stores the initial composition and the solution of the ODE integration with so-called "leafs" and retrieves them with a linear approximation when the composition space is within an ellipsoid of accuracy (EOA), avoiding the need for a direct integration. When ISAT needs growth or addition instead of retrieve, it provides first the composition ψ^q to the mechanism reduction method, which simplifies the

mechanism and provides a reduced set of species compositions ψ_a^q to the ODE solver. The solver computes the reaction mapping $\mathbf{R}(\psi_a^q)$, and then ISAT builds the full reaction mapping $\mathbf{R}(\psi^q)$ from $\mathbf{R}(\psi_a^q)$ [11]. If the differences between the existing and newly build reaction mappings are within the user-defined tolerance of ϵ_{ISAT}, the EOA will grow to include the new mapping. Otherwise, a new "leaf" will be added to include the newly computed mappings. Furthermore, a time-step specific scale factor is defined, to give more control on the time-step variations.[34]

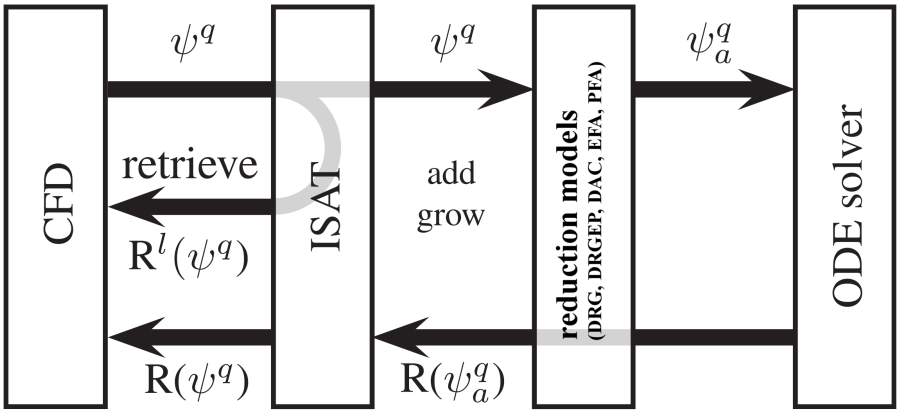

Figure 1: Tabulation of Dynamic Adaptive Chemistry (TDAC) method flow chart. Adjusted from Contino et al. [11].

The five different reduction approaches (DRG, DRGEP, DAC, PFA and EFA) implemented in the TDAC code are all based on a network graph assumption, in which the relationship between various species or reactions are linked with weights. An error ϵ is evaluated when a species or reaction is removed and it is compared with the maximum acceptable value ϵ_{max}, pre-defined by the user. If ϵ is larger than the maximum error ϵ_{max}, this means that the species/reaction is important for the network graph and can not be removed. The DRG, DRGEP and PFA methods that were initially developed for mechanism pre-processing, have been adapted for dynamic reduction in TDAC method [11, 25, 26, 27].

In DRG [29] , the error ϵ is expressed via an interaction coefficient r_{AB} representing the contribution of species B to the production rate of species A:

$$\epsilon = r_{AB} = \frac{\sum_{i=1,n_R} \mid \nu_{A,i}\omega_i\delta_{Bi} \mid}{\sum_{i=1,n_R} \mid \nu_{A,i}\omega_i \mid}, \tag{6}$$

where $\nu_{A,i}$ is the stoichiometric coefficient of species A, ω_i represents reaction rate in each reaction, n_R is the number of reactions and δ_{Bi} is defined as:

$$\delta_{Bi} = \begin{cases} 1, & \text{if the } i\text{th elementary reaction involves species B,} \\ 0, & \text{otherwise.} \end{cases} \tag{7}$$

Later, Pepiot-Desjardins and Pisch [30] proposed the DRG with Error Propagation (DRGEP) model. They argued that a more accurate way to consider the contribution of species B to species A is to use the net contribution instead of evaluating production and consumption individually. Therefore, a new definition of the direct interaction coefficient is introduced:

$$r_{AB} = \frac{|\sum_{i=1,n_R} \nu_{A,i}\omega_i\delta_{Bi}|}{max(P_A, C_A)}, \tag{8}$$

in which P_A and C_A denote the production and consumption of species A, respectively. They are expressed with:

$$P_A = \sum_{i=1,n_R} max(0, \nu_{A,i}\omega_i), \tag{9}$$

and

$$C_A = \sum_{i=1,n_R} max(0, -\nu_{A,i}\omega_i). \tag{10}$$

Furthermore, the effect of removing a group of species (previously plus the present removed species) is also included. Most importantly, the notion of error propagation is brought up in the DRGEP approach. If the error r_{AB} is going to be evaluated, the longer the path of such error propagates to reach A, the smaller the effect will be. Therefore, from B to A, the length of the path the error has to propagate is considered:

$$r_{AB,p} = \prod_{i=1}^{n-1} r_{S_iS_{i+1}}. \tag{11}$$

Instead, only the weakest contribution is taken in DRG:

$$r_{AB,p} = \min_{i=1}^{n-1} r_{S_iS_{i+1}}. \tag{12}$$

In Eqn. 11 and Eqn. 12, $S_1 = A$, $S_n = B$ and p denotes a certain path that links two species A and B. Finally,

$$\epsilon = r_{AB} = \max_{\text{all paths p}} r_{AB,p}. \tag{13}$$

The DAC method implemented in TDAC code is very similar to the DRGEP approach discussed above, except that the contribution of removing a group of species is neglected [31, 24]. Regarding the PFA model, based on the DRG and DRGEP methods, both the directly linked (first generation) and un-directly linked (higher generation) species contributions are

evaluated [33], resulting in an interaction coefficient r_{AB} with information from multiple generations. For the EFA approach, the error evaluation is focused on removing individual reactions, expressed as [32]:

$$\epsilon = \frac{\sum_{i=1,n_R}(r_i - r_i^k)^2}{s^k}, \tag{14}$$

where r_i and r_i^k are the individual reaction rates before and after removing a reaction k from the network. The variance s^k is defined as:

$$s^k = \frac{\sum_{i=1,n_R}(r_i^k - \overline{r}^k)^2}{n_R - 1}, \tag{15}$$

where $\overline{r}^k$ is the averaged reaction rate of the remaining reactions after reaction k is removed:

$$\overline{r}^k = \frac{\sum_{i=1,n_R} r_i^k}{n_R}. \tag{16}$$

Table. 1 shows the differences and similarities of the five reduction models explained:

Table 1: Differences and similarities of the reduction models in TDAC.

Reduction model	DRG	DRGEP	DAC	PFA	EFA
Graph network	Yes	Yes	Yes	Yes	Yes
Species group effect	No	Yes	No	-	-
Error propagation	No	Yes	Yes	-	-
Error evaluation based on	Species	Species	Species	Species	Reaction

3. Validation cases

The Delft Jet in Hot Co-flow (DJHC) burner [12, 13] is chosen as validation case, to test the EDC2005 model and the TDAC potential for CPU time saving. The DJHC burner has a central fuel jet with inner diameter of 4.5 mm. The hot co-flow is provided by a secondary burner mounted in an outer tube with the inner diameter of 82.8 mm. A schematic 2D drawing of DJHC burner is shown in Figure 2. Detailed description of the DJHC jet can be found in the publication of Oldenhof et al. [12] and Sarras et al. [13].

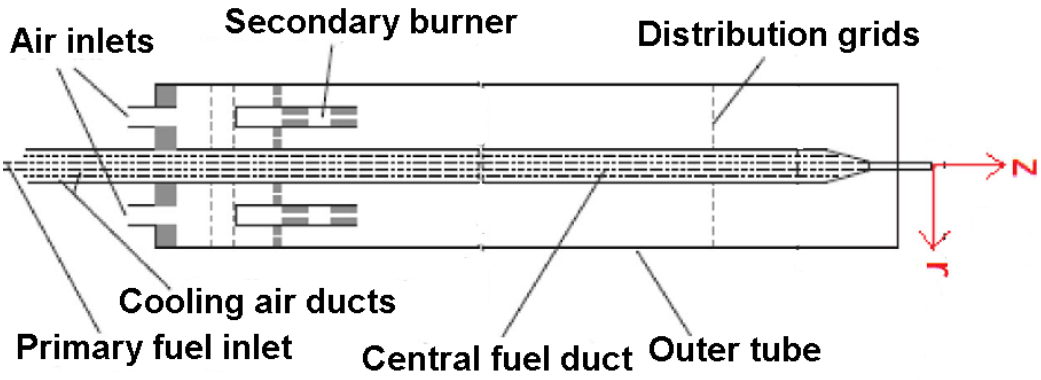

Figure 2: 2D schematic drawing of DJHC burner. Adjusted from Oldenhof et al. [12].

The mean and variance of the temperature and velocity experimental values are available for validation. Both Dutch natural gas [12] and biogas [13] are used as central jet fuel. The differences on the fuel component are listed in Table. 2.

Table 2: Central jet fuel content for the Dutch natural gas and biogas cases [12, 13].

Molar content (%)	CH_4	N_2	C_2H_6	CO_2
Dutch natural gas	81	15	4	-
Biogas	56.7	10.5	2.8	30

Further properties of the fuel and co-flow streams are presented in Table. 3.

Table 3: Physical properties of the natural gas and biogas flames. [12, 13]

Case	$U_{fuel,mean)}$	$T_{co-flow,max}$	$Y_{co-flow,O_2}$	Re_{fuel}
Dutch natural gas	16.1 nl/min	1540 K	0.076	4100
Biogas	15.3 nl/min	1436 K	0.095	4000

4. Numerical settings

Unsteady Reynolds Averaged Navier-Stokes (URANS) simulations with Local Time Stepping (LTS) were performed, using the standard $k-\epsilon$ turbulence model. The simulation domain is extended 225 mm axially (z) downstream of the burner exit and 80 mm towards radial direction (r). The whole domain is discretised with a structured 2D axi-symmetric mesh. After a grid independence study [35], the mesh with 14400 cells is chosen. The inlet boundary

conditions for temperature and velocity were taken from experimental values measured 3 mm downstream the jet exit, as proposed by De et al. [20]. The reactingFoam solver is used. The DRM19 [14], GRI3.0 [15] and POLIMIC1C3HT [16] mechanisms are selected, as they are characterised by an increasing complexity, i.e. number of species and reactions. TDAC is used with a tolerances for both reduction and tabulation of 1e-04. The seulex solver is used for ODE integration.

The standard EDC parameters are first used for the simulation of both natural gas and biogas cases. Looking at Eqn. 2, it is clear that increasing C_τ leads to an increased residence time in the fine structures. This results in higher CPU time required for the ODE integration. Preliminary simulations confirmed this, indicating that setting C_τ to 3.0 results in a simulation time 2.6 times higher than with standard constants. Therefore, we chose to adjust first the value of C_γ to 1.0, as alternatively suggested by De et al. [20], and then modify the constant C_τ [20, 19, 17], to improve the prediction of the validation cases. Since, in the present study we paid attention to the dynamic chemistry reduction and tabulation, approach of using adjusted EDC constants was found to be more straightforward. However, in general for MILD combustion simulations more advanced EDC extensions such as the use of functional expressions accounting for local flow conditions [19] or using variable reacting fraction of the fine structures [35] can be considered.

5. Results and discussion

In the present section, numerical simulations of the DJHC fed with natural gas and biogas are validated against experimental data. The CPU saving provided by TDAC is demonstrated. The influence of chemical mechanism and reduction methods on TDAC performances is also discussed. Finally, reduction and tabulation in TDAC are tested separately, to identify their contributions to speed-up.

5.1. Natural gas flame modelling

For the natural gas case, the mean radial and axial temperature and velocity profiles are used for validation. The axial locations for the radial profiles are z = 15/30/60/120/150 mm. The mean temperature profile is first presented in Figure 3. The corresponding values of C_τ and C_γ are listed in Table 4.

Table 4: Standard and adjusted EDC constants.

Constants	Standard	Adjust1	Adjust2	Adjust3
C_γ	2.1377	1.0	1.0	1.0
C_τ	0.4083	0.4083	1.47	3.0

In Figure 3, the effect of the EDC model parameters become clear at axial locations above 30 mm. At z = 60 mm, a pronounced temperature peak, more than 300 K higher than the experimental value, is obtained using the standard and Adjust1 constants. With the Adjust2 set of constants, this over-prediction is alleviated to 100 K. Further downstream, at z = 120 mm and 150 mm, a slightly shifted temperature peak is observed for all the cases, with the case using the Adjust2 set closer to the measured values. For the centerline profile, applying the Adjust2 constants helps correcting the over-prediction of temperature downstream (z $\geq$ 100 mm) of the jet. Overall, the Adjust2 parameters better capture the experimental temperatures, for the DJHC natural gas flame case. Using the Adjust3 constants leads to an extinguished flame. Thus, the corresponding profiles are not shown here.

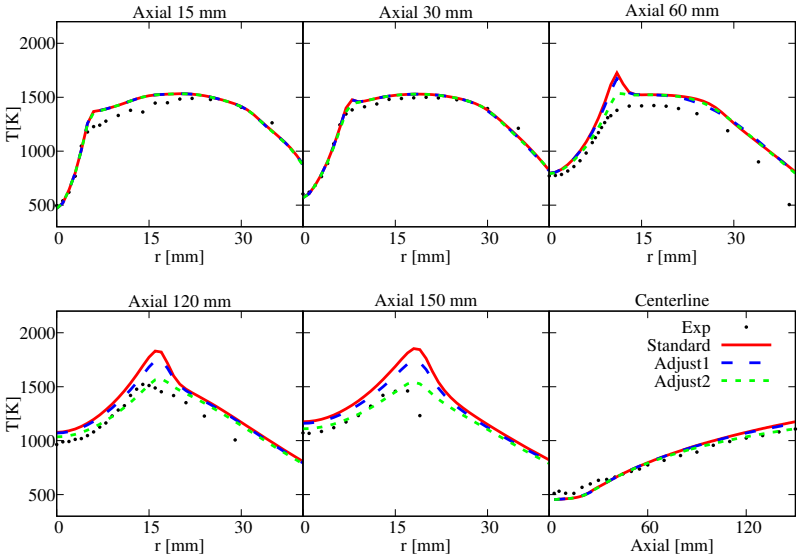

Figure 3: Mean temperature profiles obtained with the EDC2005 model, using standard and adjusted constants, compared to the experimental measurements. Kinetic mechanism: DRM19. TDAC with DAC reduction model. Fuel: Dutch natural gas.

The velocity profiles are presented in Figure 4. Using different parameter sets results in negligible differences at almost all locations. However, the case with standard constants shows earlier decay, as indicated by the centerline profile. Generally, the prediction of the

radial velocity profiles is quite accurate, at all axial locations. The centerline profile shows, however, an under-prediction of velocity after z = 30 mm, by 13.5% at z = 60 mm. This means that the jet decay rate is over-predicted by the model.

As far as the computational savings are concerned, the relative, normalized CPU time of the simulations, with and without TDAC, is shown in Table 5. The normalization is based on the CPU time consumption of the base case, defined as the simulation with standard EDC and TDAC. A speed-up of 1.5-2 times is obtained using the DRM19 mechanism, depending on the set of adjusted constants used, for the natural gas flame. The mean temperature and velocity profile obtained using TDAC are virtually identical to the results obtained without TDAC; therefore, they are not shown here.

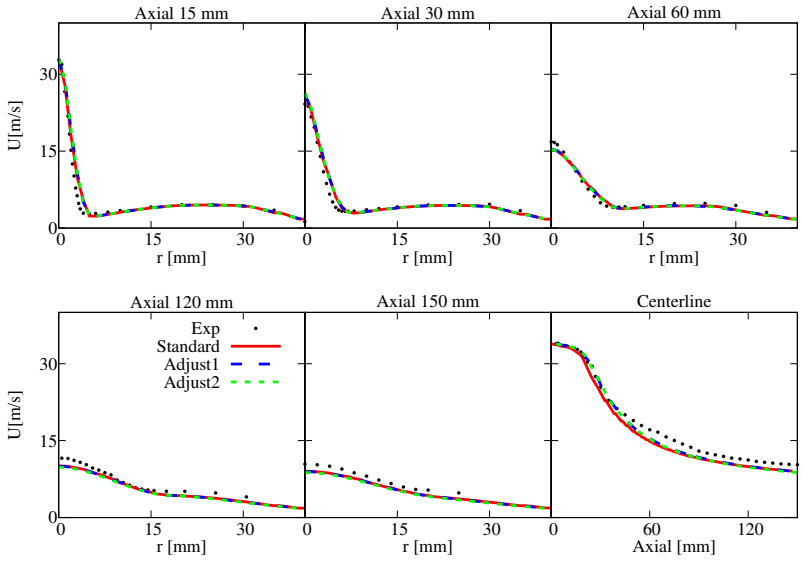

Figure 4: Mean velocity profiles obtained with the EDC2005 model using standard and adjusted constants, compared to the experimental measurements. Kinetic mechanism: DRM19. TDAC with DAC reduction model. Fuel: Dutch natural gas.

Table 5: Normalized time consumption with/without TDAC and using various EDC set of constants. TDAC with DAC reduction model applied. Fuel: Dutch natural gas.

Constants set	Standard	Adjust1	Adjust2	Adjust3
Without TDAC	1.98	1.42	3.85	-
With TDAC	1.0	0.99	2.49	-
Speed-up	1.98	1.43	1.55	-

5.2. *Biogas flame modelling*

For the biogas case, the radial profiles at axial locations z = 65/110/140/170 mm are used for temperature validation, while the experimental data at z = 30/60/90/120 mm are available to compare with computed velocities. In Figure 5, the mean numerical and experimental temperature profiles are compared, using several EDC2005 parameter settings. The trend is very similar to what is observed for the natural gas case. A clear over-prediction of temperature levels is obtained using the standard and Adjust1 sets of constants. The level of agreement is significantly improved using the Adjust2 and Adjust3 set of constants, although some over-predictions (10-20%) can still be observed at z = 140/170 mm with Adjust3 constants. Figure 6 shows the comparison between the measured and computed velocity profiles. The agreement is very satisfactory, with the maximum difference being always below 1.0 m/s, and no distinctive difference can be observed between the profiles provided by the different EDC constant sets.

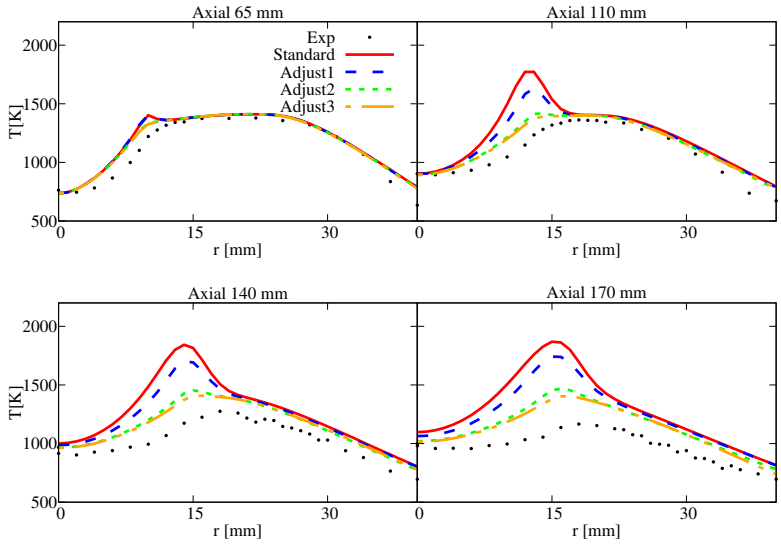

Figure 5: Mean temperature profiles obtained with the EDC2005 model, using standard and adjusted constants, compared to the experimental measurements. Kinetic mechanism: DRM19. TDAC with DAC reduction model. Fuel: biogas.

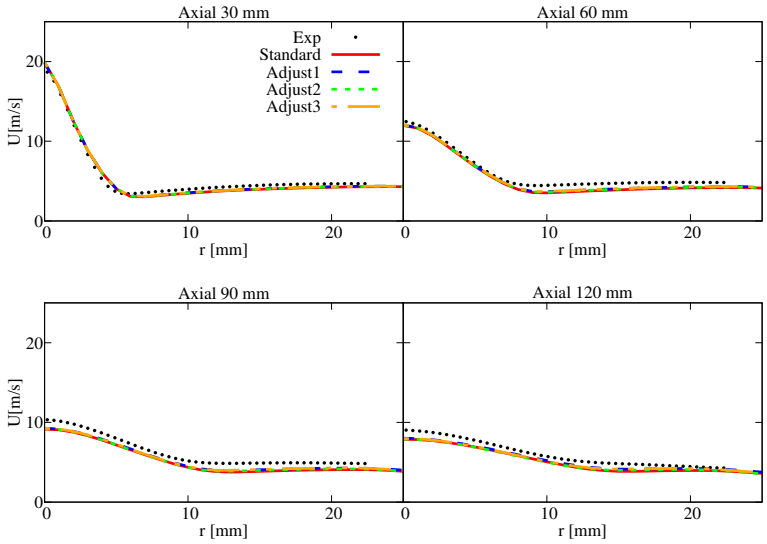

Figure 6: Mean velocity profiles obtained with the EDC2005 model using standard and adjusted constants, compared to the experimental measurements. Kinetic mechanism: DRM19. TDAC with DAC reduction model. Fuel: biogas.

The normalized time consumption factor with and without TDAC is shown in Table 6. Together with the data from natural gas case in Table 5, a conclusion can be drawn that the total CPU time is indeed increased with the increased C_τ value. Furthermore, the speed-up factor still lies in the range between 1.5 to 2.0. No appreciable difference can be observed between the results obtained with and without TDAC.

Table 6: Normalized time consumption with/without TDAC and using various EDC set of constants. TDAC with DAC reduction model applied. Fuel: biogas.

Constants set	Standard	Adjust1	Adjust2	Adjust3
Without TDAC	1.82	2.44	2.87	3.43
With TDAC	1.0	1.42	1.88	2.07
Speed-up	1.82	1.7	1.53	1.66

5.3. Influence of chemical mechanisms

The natural gas flame is chosen for the current and the following sections, to demonstrate the influence of chemical kinetics and reduction algorithm on the simulation spped-up, as well as to clarify the role of tabulation and reduction in TDAC. In the study of De et al. [20], the DRM19 mechanism was found to perform satisfactorily for the DJHC natural gas flame. However, to test the potential speed-up of the TDAC method, two additional mechanisms

of increasing size are chosen, namely the GRI3.0 and POLIMIC1C3HT. At the same time, the effect of the mechanism on the accuracy of the predictions is assessed as well. Figure 7 compares the temperature profiles provided by the different mechanisms, compared to the experimental data. The Adjust2 constant set is employed for all simulations. The profiles provided by the different mechanisms do not show major differences. Nevertheless, using a more detailed mechanism at downstream axial distances, z = 120 mm, helps reducing the temperature over-prediciton by 30 K to 40 K.

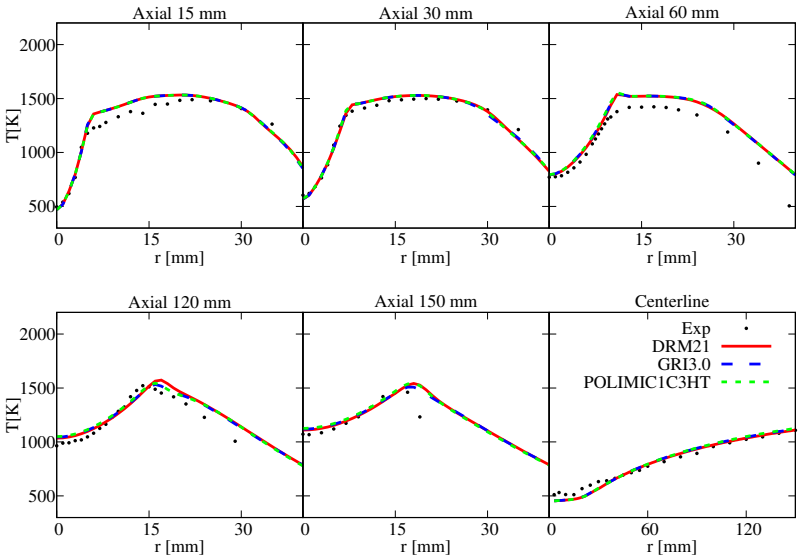

Figure 7: Mean temperature profiles obtained with EDC2005 model using the DRM19, GRI3.0 and POLIMIC1C3HT mechanisms, compared to the experimental measurements. EDC2005 constants: Adjust2. TDAC with DAC reduction model. Fuel: Dutch natural gas.

In Table 7, a trend of increasing speed-up is observed when more complicated mechanisms are chosen. The CPU time consumption normalization is based on the case with DRM19 mechanism and TDAC. Using the POLIMIC1C3HT mechanism requires 27.55 (42.51/1.53) times the CPU required for the DRM19 case, when neither reduction nor tabulation is applied. Using the TDAC method reduces the gap to 4.16 times, which corresponds to roughly 10 times speed-up. The use of a mechanism as complicated as the POLIMIC1C3HT might not be necessary for the present case. However, the significant CPU time saving achieved using TDAC is very promising for the application of the method to more complex cases and regimes, with no a-priori knowledge about the appropriateness of a pre-reduced mechanism (as the DRM19).

Table 7: Normalized time consumption with/without TDAC and various chemical mechanisms. TDAC with DAC reduction model. Fuel: Dutch natural gas.

Mechanisms	DRM19	GRI3.0	POLIMIC1C3HT
Without TDAC	1.55	6.22	42.51
With TDAC	1.0	3.26	4.16
Speed-up	1.55	1.91	10.22

Finally, the number of active species distribution for the various chemical mechanisms in the domain is presented in Figure 8. The number of active species indicates the species left after removing unimportant ones. We can observe that almost 100% of the species are used in both the reaction zone and the downstream ($z \geqslant 100$ mm) area of the simulation domain, when DRM19 mechanism is chosen. Away from these regions, the number of active species drops, thus saving computational resources. This effect is magnified with the two other chemical mechanisms. With GRI3.0, around 75% of them are necessary in the active zone close to the centerline. Upstream and far from centerline region, the number of active species is further reduced to around 20-30. With the POLIMIC1C3HT mechanism, approximately 56% of the species set is retained, leading to the observed speed-up factor of 10.22, as indicated in Table 7.

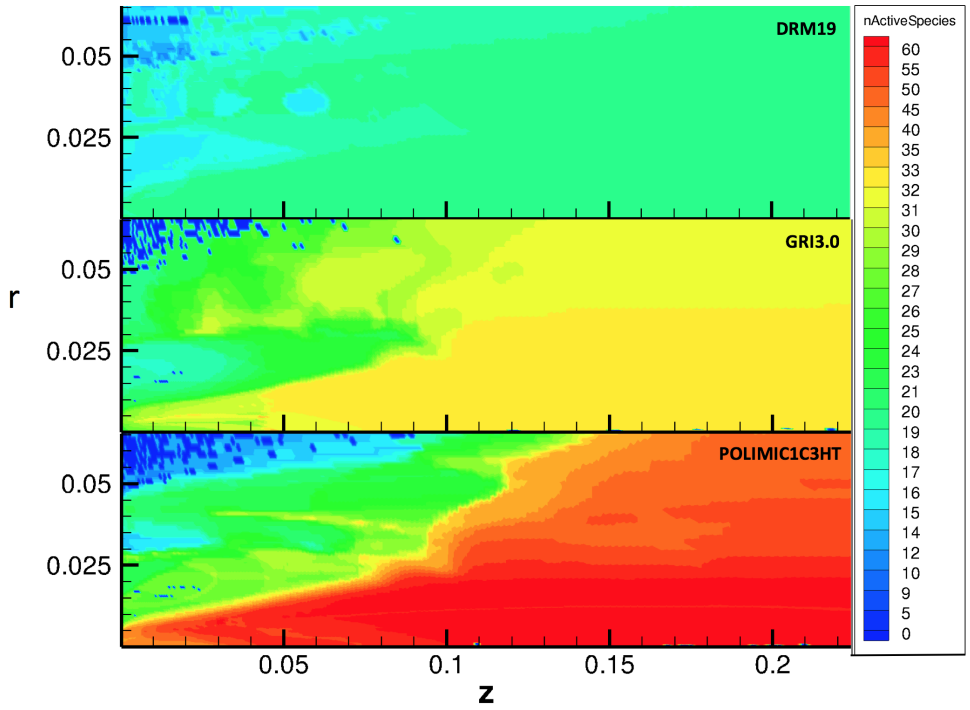

Figure 8: Contour plot of the number of active species (nActiveSpecies) obtained using the EDC2005 model with the DRM19, GRI3.0 and POLIMIC1C3HT mechanisms. EDC2005 constants: Adjust2. TDAC with DAC reduction model applied. Fuel: Dutch natural gas. Axis unit: m.

5.4. Influence of chemistry reduction approach

In the present section, the speed-up factor of various chemistry reduction models (DRG, DRGEP, DAC, PFA and EFA) are compared using both the skeletal and comprehensive mechanisms. The mean temperature and velocity profiles obtained from the 5 different reduction models show negligible differences, therefore they are not shown here. In Table 8, the speed-up factors are listed and compared. Minor differences are observed for the DRM19 case, using the different chemistry reduction approaches. This can be explained with the help of Figure 8. Indeed, the DRM19 mechanism is already a reduced mechanism and this implies that the margins for further reduction are tight. On the other hand, using the POLIMIC1C3HT mechanism, larger differences are identified between the five methods. The DRGEP, DAC and EFA models have speed-up factors around 3 times higher than those obtained using DRG and PFA models. Using a more complicated mechanism helps to better evaluate the efficiency of the various approaches.

Table 8: Simulation speed-up with various reduction methods. Tabulation turned on. Fuel: Dutch natural gas.

Reduction model	DRG	DRGEP	DAC	PFA	EFA
Speed-up with DRM19	1.57	1.55	1.55	1.58	1.55
Speed-up with POLIMIC1C3HT	3.9	10.90	10.22	3.2	9.6

In Figure 9, a contour plot of the number of active species in the simulation domain is again presented, when POLIMIC1C3HT mechanism is applied. The reduction ability of DRG, DRGEP, DAC, PFA and EFA models can thus be analysed. The DRG and PFA reduction models provide very weak reduction ability. Approximately only 10% of the whole species set are removed for the reaction area and regions nearby. Whereas the other three approaches, DRGEP, DAC and EFA, present a significantly reduced set of species, around 40% by estimation. Among them, the DRGEP model provides the most reduced set of species in the whole domain. Moreover, the reactive area is well identified with DRGEP, DAC and EFA models as well.

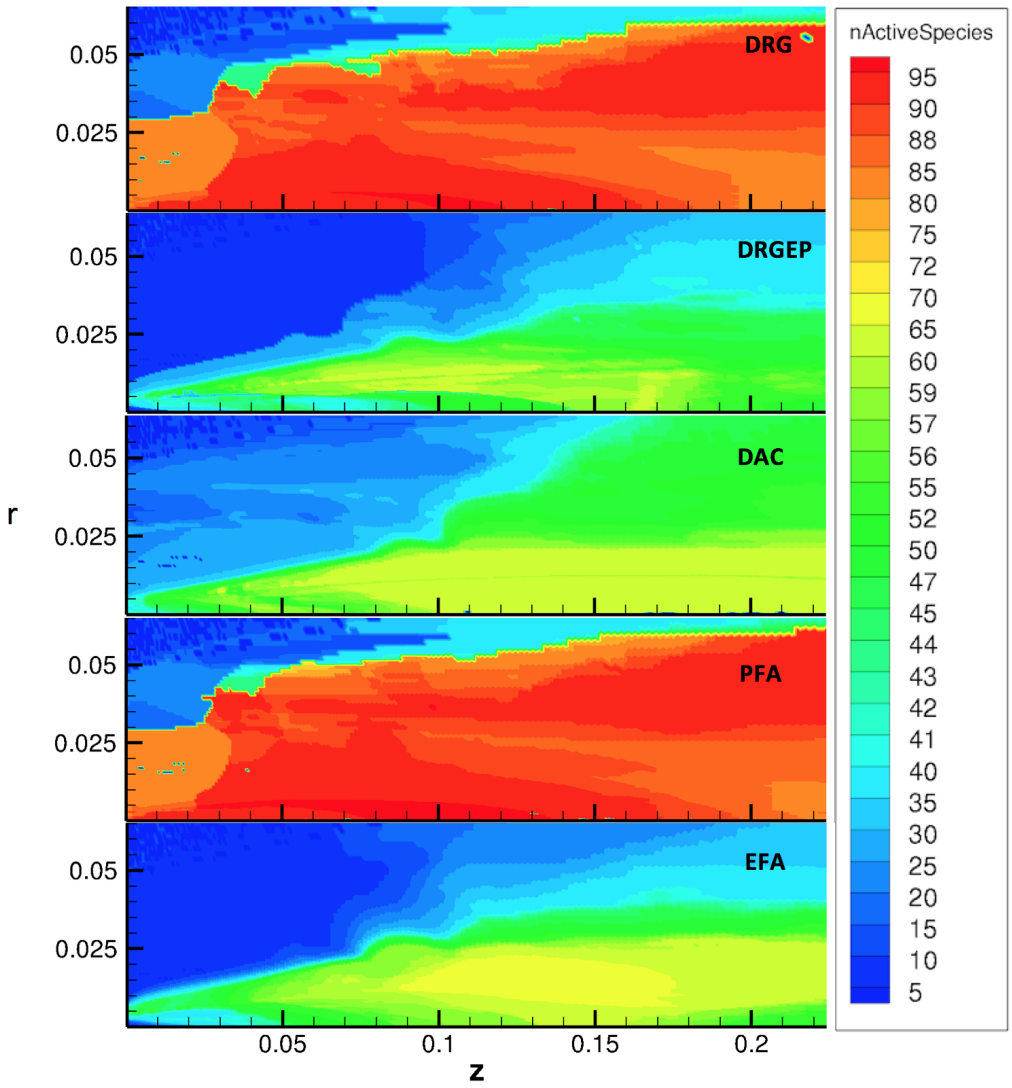

Figure 9: Contour plot of the number of active species (nActiveSpecies) obtained using the EDC2005 model with the DRM19, GRI3.0 and POLIMIC1C3HT mechanisms. EDC2005 constants: Adjust2. TDAC with DAC reduction model applied. Fuel: Dutch natural gas. Axis unit: m.

CH_2O is a key precursor in the initiation process of reaction, especially in MILD combustion [36, 37, 38, 39]. Therefore, it is adopted here in combination with temperature to identify the reactive region in the flame. The regions with high temperature and high CH_2O mass fraction are highlighted in Figure 10, When DRGEP, DAC or EFA methods are chosen, a larger number of active species is identified in these regions (Figure 9) which is not the case when the DRG or PFA methods are used. The latter identify a large number of active species far from the centerline, after z = 100 mm, where low temperature and CH_2O levels

are observed. This proves that the DRG and PFA models are not as efficient and accurate as the other reduction approaches in selecting the appropriate active species in the relevant regions of the flame.

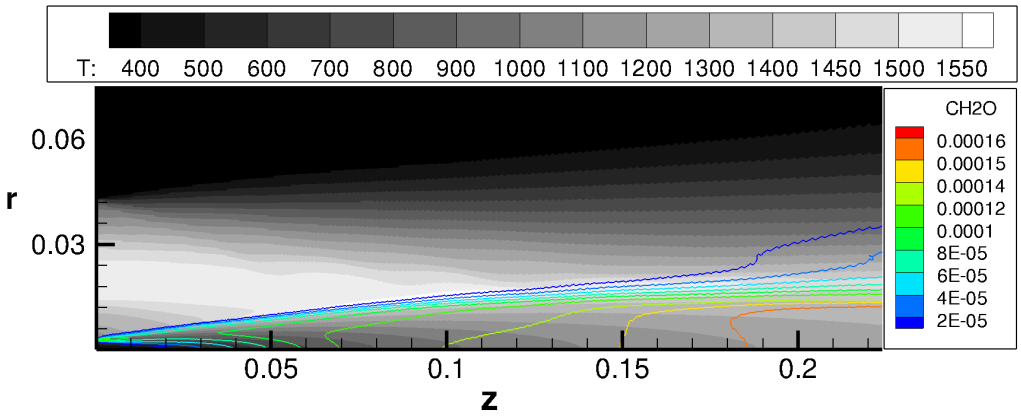

Figure 10: Contour plot of the mean CH_2O mass fraction and mean temperature obtained using the EDC2005 model. Kinetic mechanism: POLIMIC1C3HT. EDC2005 constants: Adjust2. Tabulation turned on. DAC reduction models. Fuel: Dutch natural gas. Axis unit: m.

5.5. Influence of reduction/tabulation

Since the TDAC method is a combination of chemistry tabulation and reduction, it is interesting to quantify how much they contribute to the speed-up separately. In Table 9, the normalized CPU time is listed considering both tabulation and reduction, only reduction, only tabulation and without reduction/tabulation. Both DRM19 and POLIMIC1C3HT mechanisms were used. The base case for normalization is the case with both tabulation and reduction, for a given mechanism used (vertical comparison is not possible). From Table 9, it can be observed that, using a small mechanism like DRM19, the tabulation contribution is more significant, whereas with a large mechanism as the POLIMIC1C3HT, the reduction step plays the major role. Such conclusion was somehow expected considering that for a detailed mechanism such as the POLIMIC1C3HT, the reduction of the number of species significantly speed-up the ODE integration step. When it comes to the DRM19 case, the mechanism is already very light and the reduction potential is much lower. Therefore, tabulation is the key step under such condition.

Table 9: Normalized time consumption with/without reduction & tabulation. DAC reduction model. Fuel: Dutch natural gas. Comparison between the normalized times is possible only horizontally.

Model	no TDAC	TDAC	only reduction	only tabulation
DRM19	1.55	1.0	1.41	1.03
POLIMIC1C3HT	10.22	1.0	2.38	6.33

A contour plot of the tabulation results is shown in Figure 11. The retrieve, grow and add in each computational cell are denoted with red, green and blue colours. Most regions are marked with grow and add in the upper figure, when DRM19 kinetics is chosen. A region of new ”leafs” is observed, in correspondence to the high temperature region in Figure 10. In the lower figure, the same region is characterised mostly by green (grow), indicating an expansion of the EOA. One can also appreciate that larger regions are characterised by retrieve when POLIMIC1C3HT mechanism is used. Using two mechanisms, the reaction system is described with different reactions and species. Therefore, the contributions of reactions and dominating phenomenon in local regions are different as well, showing inconsistency on the tabulation results.

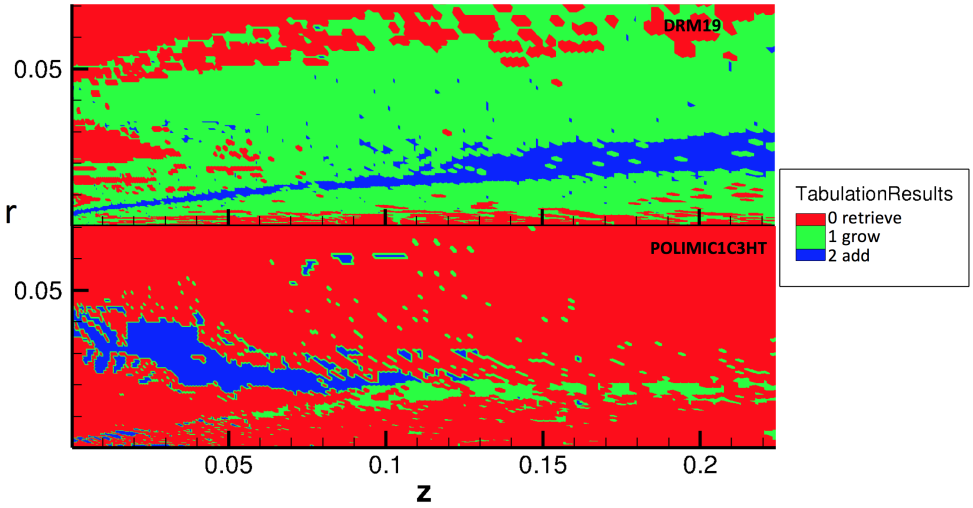

Figure 11: Contour plot of the tabulation results (TabulationResults) obtained using the EDC2005 model with DRM19 and POLIMIC1C3HT mechanisms. EDC2005 constants: Adjust2. Reduction model: DAC. Fuel: Dutcj natural gas. Axis unit: m.

6. Conclusion

In the current article, the Delft Jet in Hot Co-flow burner was numerically investigated by means of RANS-LTS simulations with detailed kinetic mechanisms and dynamic chemistry

reduction/tabulation. Two fuels, Dutch natural gas and biogas, were selected for the preliminary model validation. The speed-up potential of TDAC is assessed using three mechanisms (DRM19, GRI3.0 and POLIMIC1C3HT) and different chemistry reduction models (DRG, DRGEP, DAC, PFA and EFA). Moreover, the contributions of tabulation and reduction are investigated separately. The followings conclusions are summarised:

- The current EDC model implementation in OpenFOAM with a modified set of constants (Adjust2) provide satisfactory predictions on mean temperature profiles of natural gas flame, while the lower reactivity of the biogas flame make the Adjust3 set of constants more performing. The mean velocity distribution is well predicted for both flames with all the model settings. A speed-up factor of 1.5-2.0 is obtained using TDAC method with the DRM19 mechanism.

- Using more complicated chemical mechanism, such as the GRI3.0 or POLIMIC1C3HT, slightly improves temperature predictions, and leads to significantly increased CPU time with respect to the DRM19 case (27.4 times for POLIMIC1C3HT), when TDAC is turned off. However, with TDAC, a 10 times speed-up is obtained for the POLIMIC1C3HT mechanism, reducing the CPU time gap between POLIMIC1C3HT and DRM19 to 4.16 times.

- The DRGEP, DAC and EFA reduction approaches are more efficient and accurate compared the DRG and PFA models.

- When a small mechanism is used (DRM19), tabulation is the main contributor to computational saving. With more complex mechanisms (POLIMIC1C3HT), chemistry reduction plays the main role.

The current investigation validates the application of the EDC model in combination with TDAC method under MILD regime, using the open-source software OpenFOAM. The time saving using TDAC with complex chemistry is very promising, thus making it possible to extend it to industrial or semi-industrial applications.

Acknowledgments

This project has received funding from the European Union′s Horizon 2020 research and innovation program under the Marie Skłodowska-Curie grant agreement No. 643134. The research of the last author is sponsored by the European Research Council, Starting Grant No. 714605, and from the Fédération Wallonie-Bruxelles, via ′Les Actions de Recherche Concertée (ARC)′ call for 2014-2019. We are indepted to Professor Dirk Roekaerts at TU Delft for his courtesy to provide the experimental data of DJHC flames.

References

[1] J. A. Wünning and J. G. Wünning. Flameless oxidation to reduce thermal NO-formation. *Progress in Energy and Combustion Science*, 23:81–94, 1997.

[2] A. Cavaliere and M. de Joannon. MILD combustion. *Progress in Energy and Combustion Science*, 30:329–366, 2004.

[3] M. de Joannon, G. Sorrentino, and A. Cavaliere. MILD combustion in diffusion-controlled regimes of hot diluted fuel. *Combustion and Flame*, 159:1832–1839, 2012.

[4] Matthias Ihme, Jian Zhang, Guowei He, and Bassam Dally. Large-eddy simulation of a jet-in-hot-coflow burner operating in the oxygen-diluted combustion regime. *Flow, Turbulence and Combustion*, 89:449–464, 2012.

[5] Bj/orn F. Magnussen. The eddy dissipation concept: A bridge between science and technology. In *ECCOMAS Thematic Conference on Computational Combustion*, Lisbon, Portugal, 2005.

[6] L. Tosatto, B. A. V. Bennett, and M. D. Smooke. A transport-flux-based directed relation graph method for the spatially inhomogeneous instantaneous reduction of chemical kinetic mechanisms. *Combustion and Flame*, 158:820–835, 2011.

[7] Shuliang Zhang, Linda J. Broadbelt, Ioannis P. Androulakis, and Marianthi G. Ierapetritou. Comparison of biodiesel performance based on hcci engine simulation using detailed mechanism with on-the-fly reduction. *Energy & Fuels*, 26:976–983, 2012.

[8] Kaiyuan He, Ioannis P. Androulakis, and Marianthi G. Ierapetritou. Numerical investigation of homogeneous charge compression ignition (hcci) combustion with detailed chemical kinetics using on-the-fly reduction. *Energy & Fuels*, 25:3369–3376, 2011.

[9] Qing Tang and Stephen B. Pope. Implementation of combustion chemistry by in situ adaptive tabulation of rate-controlled constrained equilibrium manifolds. *Proceedings of the Combustion Institute*, 29:1411–1417, 2002.

[10] Zhuyin Ren, Yufeng Liu, Tianfeng Lu, Liuyan Lu, Oluwayemisi O. Oluwole, and Graham M. Goldin. The use of dynamic adaptive chemistry and tabulation in reactive flow simulations. *Combustion and Flame*, 161:127–137, 2014.

[11] Francesco Contino, Hervé Jeanmart, Tommaso Lucchini, and Gianluca D'Errico. Coupling of in situ adaptive tabulation and dynamic adaptive chemistry: An effective

method for solving combustion in engine simulations. *Proceedings of the Combustion Institute*, 33:3057–3064, 2011.

[12] E. Oldenhof, M. J. Tummers, E. H. van Veen, and D. J. E. M. Roekaerts. Role of entrainment in the stabilisation of jet-in-hot-coflow flames. *Combustion and Flame*, 158:1553–1563, 2011.

[13] G. Sarras, Y. Mahmoudi, L. D. Arteaga Mendez, E. H. van Veen, M. J. Tummers, and D. J. E. M. Roekaerts. Modeling of turbulent natural gas and biogas flames of the delft jet-in-hot-coflow burner: Effects of coflow temperature, fuel temperature and fuel composition on the flame lift-offff height. *Flow Turbulence Combustion*, 93:607–635, 2014.

[14] Andrei Kazakov and Michael Frenklach. Website.

[15] Gregory P. Smith, David M. Golden, Michael Frenklach, Nigel W. Moriarty, Boris Eiteneer, Mikhail Goldenberg, C. Thomas Bowman, Ronald K. Hanson, Soonho Song, William C. Gardiner Jr., Vitali V. Lissianski, and Zhiwei Qin. Website.

[16] A. Frassoldati, T. Faravelli, and E. Ranzi. Kinetic modeling of the interactions between no and hydrocarbons at high temperature. *Combust. Flame*, 135:97–112, 2003.

[17] Michael John Evans, Paul Ross Medwell, and Zhao Feng Tian. Modelling lifted jet flames in a heated coflow using an optimised eddy dissipation concept model. *Combustion Science and Technology*, 187(7):1093–1109, 2015.

[18] Seyed Reza Shabanian, Paul Ross Medwell, Masoud Rahimi, Alessio Frassoldati, and Alberto Cuoci. Kinetic and fluid dynamic modeling of ethylene jet flames in diluted and heated oxidant stream combustion conditions. *Applied Thermal Engineering*, 52:538–554, 2012.

[19] Alessandro Parente, Mohammad Rafi Malik, Francesco Contino, Alberto Cuoci, and Bassam B. Dally. Extension of the eddy dissipation concept for turbulence/chemistry interactions to MILD combustion. *Fuel*, 163:98–111, 2016.

[20] Ashoke De, Ernst Oldenhof, Pratap Sathiah, and Dirk Roekaerts. Numerical simulation of delft-jet-in-hot-coflow (djhc) flames using the eddy dissipation concept model for turbulence-chemistry unteraction. *Flow Turbulence and Combustion*, 87:537–567, 2011.

[21] Javad Aminian, Chiara Galletti, Shahrokh Shahhosseini, and Leonardo Tognotti. Numerical investigation of a MILD combustion burner: Analysis of mixing field, chemical kinetics and turbulence-chemistry interaction. *Flow, Turbulence and Combustion*, 88(4):597–623, 2012.

[22] Zhiyi Li, Alberto Cuoci, Amsini Sadiki, and Alessandro Parente. Comprehensive numerical study of the Adelaide Jet in Hot-Coflow burner by means of RANS and detailed chemistry. *Energy*, 139:555–570, 2017.

[23] S. B. Pope. Computationally efficient implementation of combustion chemistry using in situ adaptive tabulation. *Combustion Theory and Modelling*, 1:44–63, 1997.

[24] Francesco Contino. *Combustion in Homogeneous Charge Compression Ignition engines : experimental analysis using ethyl esters and development of a method to include detailed chemistry in numerical simulations.* PhD thesis, Université catholique de Louvain, 2011.

[25] F. Contino, T. Lucchini, G. D'Errico, C. Duynslaegher, V. Dias, and H. Jeanmart. Simulations of advanced combustion modes using detailed chemistry combined with tabulation and mechanism reduction techniques. *SAE International Journal of Engines*, 5(2):185–196, 2012.

[26] F. Contino, F. Foucher, P. Dagaut, T. Lucchini, G. D'Errico, and C. Mounaïm-Rousselle. Experimental and numerical analysis of nitric oxide effect on the ignition of iso-octane in a single cylinder hcci engine. *Combustion and Flame*, 160(8):1476–1483, 2013.

[27] F. Contino, J.-B. Masurier, F. Foucher, T. Lucchini, G. D'Errico, and P. Dagaut. Cfd simulations using the tdac method to model iso-octane combustion for a large range of ozone seeding and temperature conditions in a single cylinder hcci engine. *Fuel*, 137:179–184, 2014.

[28] N. Bourgeois, S. S. Goldsborough, G. Vanhove, M. Duponcheel, H. Jeanmart, and F. Contino. Cfd simulations of rapid compression machines using detailed chemistry: Impact of multi-dimensional effects on the auto-ignition of the iso-octane. *Proceedings of the Combustion Institute*, 36(1):383–391, 2017.

[29] T. Lu and C. K. Law. A directed relation graph method for mechanism reduction. *Proceedings of the Combustion Institute*, 30:1333–1341, 2005.

[30] P. Pepiot-Desjardins and H. Pitsch. An efficient error-propagation-based reduction method for large chemical kinetic mechanisms. *Combustion and Flame*, 154:67–81, 2008.

[31] L. Liang, J. G. Stevens, and J. T. Farrell. A dynamic adaptive chemistry scheme for reactive flow computations. *Proceedings of the Combustion Institute*, 32:527–534, 2009.

[32] Florian Karst, Matteo Maestri, Hannsjörg Freund, and Kai Sundmacher. Reduction of microkinetic reaction models for reactor optimization exemplified for hydrogen production from methane. *Chemical Engineering Journal*, 281:981–994, 2015.

[33] Wenting Sun, Zheng Chen, Xiaolong Gou, and Yiguang Ju. A path flux analysis method for the reduction of detailed chemical kinetic mechanisms. *Combustion and Flame*, 157:1298–1307, 2010.

[34] Nicolas Bourgeois. *Numerical study of multi-dimensional effects in Rapid Compression Machines*. PhD thesis, Université catholique de Louvain and Vrije Universiteit Brussel, 2017.

[35] M. T. Lewandowski and I. S. Ertesvåg. Analysis of the eddy dissipation concept formulation for mild combustion modeling. *Fuel*, 224:687–700, 2018.

[36] Robert L. Gordon, Assaad R. Masri, Stephen B. Pope, and Graham M. Goldin. Transport budgets in turbulent lifted flames of methane autoigniting in a vitiated co-flow. *Combustion and Flame*, 151:495–511, 2007.

[37] P. R. Medwell. *Laser diagnostics in MILD combustion*. PhD thesis, The University of Adelaide, 2007.

[38] C. Duwig, B. Li, and M. Aldén. High resolution imaging of flameless and distributed turbulent combustion. *Combustion and Flame*, 159:306–316, 2012.

[39] Yuki Minamoto. *Physical aspects and modelling of turbulent MILD combustion*. PhD thesis, University of Cambridge, 2013.

5.4 Journal paper 4

This paper has been submitted to Combustion and Flame.

Numerical and experimental investigation of turbulent *n*-heptane jet-in-hot-coflow flames

Zhiyi Li[a,b,*], Michael Evans[c], Jingjing Ye[c], Paul Medwell[c], Alessandro Parente[a,b,**]

[a] *Université Libre de Bruxelles, Ecole polytechnique de Bruxelles, Aero-Thermo-Mechanics Laboratory, Brussels, Belgium*
[b] *Université Libre de Bruxelles and Vrije Universiteit Brussel, Combustion and Robust Optimization Group (BURN), Brussels, Belgium*
[c] *The University of Adelaide, School of Mechanical Engineering, Adelaide, Australia*

Abstract

A turbulent *n*-heptane jet flame in a jet-in-hot-coflow burner is numerically and experimentally investigated, revealing distinct features of this fuel under MILD conditions. The RANS k-ε turbulence model is adopted in combination with a dynamic partially-stirred reactor (PaSR) combustion model. The simulation results are validated against newly-obtained experimental measurements of mean temperature, OH number density and normalised CH_2O-PLIF signal values at several axial locations. The simulations capture the transitional phenomenon observed experimentally for the low coflow oxygen concentration case, which is determined to be due to the two chemical pathways which exist for the *n*-heptane fuel. The predicted flame weak-to-strong transition heights show a transition from monotonic to non-monotonic behaviour when the threshold OH number density value is reduced. Furthermore, an investigation on negative heat release region shows that the absolute value of negative heat release increases with reduced coflow oxygen content, in contrast to the suppression phenomenon seen in laminar opposed-flow flames.

Keywords: `n-heptane, turbulent flames, partially-stirred reactor (PaSR), jet-in-hot-coflow (JHC) burner, MILD combustion, RANS simulation`

1. Introduction

Novel combustion technologies with low emissions, high efficiency and fuel flexibility have become essential to cope with the energy supply challenge the world will face in the near future. One such technology is termed Moderate or Intense Low-oxygen Dilution (MILD)

*Zhiyi.Li@ulb.ac.be
**Alessandro.Parente@ulb.ac.be

combustion [1–3]. In industrial applications, MILD combustion is often achieved by means of high velocity burners and flue gas recirculation [4]. The resultant pre-heated mixture helps to stabilize and homogenize the flame, thus reducing combustion noise [1]. Dilution also impacts the system reactivity, leading to a distributed oxidation process. As a result, a more uniform temperature field is obtained and thermal NO_x production is largely suppressed [1, 2].

For research purposes, jet-in-hot-coflow (JHC) burners [5–8] are often used to produce MILD conditions, to decrease the geometrical complexity and allow the use of sophisticated measurement techniques. Several investigations have focused on the JHC burners, both experimentally and numericallly [4–6, 9–14]. JHC burners feature a central jet and a secondary burner providing hot exhaust products as a coflow, thus emulating the effect of flue gas recirculation. Dally et al. [6] carried out experiments with an equimolar fuel jet of CH_4/H_2, at different oxygen levels (9%, 6% and 3% by mass) in the hot coflow. They concluded that the peak temperature increase in the reaction zone can be as low as 100 K, by reducing the oxygen level to 3%; and the production of CO, NO and OH is largely reduced when compared with conventional combustion conditions. At the same time, they provided high-fidelity mean and RMS (root-mean-square) experimental data of temperature and various chemical species for numerical validation. Medwell et al. [9, 15] used planar laser-induced fluorescence (PLIF) and Rayleigh scattering techniques to reveal the distribution of hydroxyl radical (OH), formaldehyde (CH_2O), and temperature under the influences of hydrogen addition. They indicated that the reaction zone was not very sensitive to hydrogen addition, indicating the potential of MILD combustion for fuel flexibility. They also observed a "lift-off" height based on the weak-to-strong transition of OH and the existence of a pre-ignition region in the apparent lifted region of these flames [15].

Experimental investigations on JHC burners have mostly focused on gaseous, simple hydrocarbon fuels. However, a few studies [8, 16–21] focused on the behaviour of pre-vaporized oxygenated fuels and long-chain alkanes. Despite the high flexibility about the fuel choice in MILD combustion [22], systems with more complex fuels could lead to distinct features [23–25]. Therefore, Ye et al. [8] performed experimental investigations with *n*-heptane fuel using conventional photography and PLIF, finding found that the "lift-off" height (weak-to-strong transition height) changes monotonically with decreasing coflow oxygen level—this does not occur for other simple hydrocarbon fuels. Furthermore, the *n*-heptane flame transitional flame structure is observed for a much lower coflow oxygen content [8]. Based on the analysis of fuel pyrolysis and heat release with *n*-heptane and ethanol, they concluded that it is more difficult to establish MILD conditions with *n*-heptane [8].

As a result of the reduced reactivity under MILD combustion conditions, the chemi-

cal timescales increase and the strong interaction between chemistry reaction and mixing makes the modelling of such flames more challenging than the conventional combustion regime. Numerical investigations of JHC-type burners have been carried out using Reynolds-Averaged Navier-Stokes (RANS) simulations [4, 10, 14, 26–35], Large Eddy Simulations (LES) [13, 36–39] and Direct Numerical Simulations (DNS) [40]. Simple fuels with well-studied combustion chemistry—such as methane, hydrogen and ethylene—have been the main focus. The experimental and numerical studies on MILD combustion with simple fuels reveal some common signatures, such as the absence of the negative heat release region, the broadening of the heat production profile with a single peak in mixture fraction space and the suppression of the pyrolytic reactions [3, 41]. However, using complex fuels such as oxygenated hydrocarbons and long-chain alkanes under MILD conditions has shown distinct features, like the appearance of visible flames and increased pollutant emissions [24, 42, 43].

The intense turbulence-chemistry interactions characterising MILD combustion make the use of models based on the principle of timescale separation unsuitable [44]. Therefore, models accounting for finite-rate chemistry should be considered. Among them, the eddy dissipation concept (EDC) model [45–47] and the partially stirred reactor (PaSR) [48] represent a viable choice, as they allow inclusion of detailed chemistry in an computationally-affordable way. Compared to the models based on scale separation like the flamelet model [49] and eddy dissipation model (EDM) [50], the finite-rate based models (EDC and PaSR) solve transport equations of each chemical species and integrate the ordinary differential equations (ODEs) of the chemical source terms. The EDC and PaSR model split each computational cell into two regions: the reactive structures, where reactions take place, and the surrounding fluid, where mixing happens. In PaSR, the interaction between turbulence and chemistry is represented with a factor κ [48], which is defined as the ratio between the chemical timescale and the sum of mixing and chemical scales. In EDC model, a similar parameter is adopted: γ [45–47], whose definition depends solely on turbulence parameters, through an energy cascade model [45–47]. In PaSR, both the chemical and mixing timescales are included in the estimation of the splitting fraction explicitly, allowing a more accurate description on turbulence/chemistry interactions. Recently, an extension of the PaSR model has been proposed, based on the dynamic estimation of the mixing timescale, showing improved predictions for the simulation of the JHC burner [51, 52]. Therefore, the dynamic PaSR model is adopted in the present paper.

The features of *n*-heptane under MILD conditions have been captured through experimental studies and laminar calculations [8]. The purpose of the current article is to investigate the role of turbulence-chemistry interactions through detailed CFD simulations. Unsteady Reynolds-averaged Navier-Stokes (RANS) simulations were carried out using the dynamic

PaSR combustion model. The influence of turbulence modelling on the results is first reported, to identify optimised settings for the subsequent simulations focusing on turbulence-chemistry interactions. The numerical results are validated against new experimental measurements, including the mean temperature and semi-quantitative species measurements, *viz.* OH number density values and normalized CH_2O-PLIF signals. An investigation of chemical timescale distribution, flame weak-to-strong transition heights and negative heat release are presented as well, to identify the key features of *n*-heptane flames.

2. Mathematical Models

2.1. Turbulence Model

The density-based Favre-averaged (marked with ˜) governing equations of mass, momentum and energy [53] are solved using the URANS approach:

$$\frac{\partial \bar{\rho}}{\partial t} + \frac{\partial}{\partial x_j}\left(\bar{\rho}\tilde{u}_j\right) = 0, \tag{1}$$

$$\frac{\partial}{\partial t}\left(\bar{\rho}\tilde{u}_i\right) + \frac{\partial}{\partial x_j}\left(\bar{\rho}\tilde{u}_i\tilde{u}_j\right) = -\frac{\partial \bar{p}}{\partial x_i} + \frac{\partial}{\partial x_j}\left(\bar{\tau}_{ij} - \bar{\rho}\widetilde{u_i'' u_j''}\right), \tag{2}$$

$$\frac{\partial}{\partial t}\left(\bar{\rho}\tilde{h}\right) + \frac{\partial}{\partial x_j}\left(\bar{\rho}\tilde{h}\tilde{u}_j\right) = \frac{\partial}{\partial x_j}\left(\bar{\rho}\alpha\frac{\partial \tilde{h}}{\partial x_j} - \bar{\rho}\widetilde{u_j'' h''}\right) - \frac{\partial}{\partial x_j}\left(\bar{q}_{r\,j}\right) + \bar{S}_{hc}, \tag{3}$$

where ρ, $\mathbf{u}$ and p represent the density, velocity and pressure respectively; the enthalpy is denoted with h; α is the thermal diffusivity. The term $\mathbf{q}_r$ denotes the radiative heat loss and S_{hc} represents the heat production from chemical reaction. The Favre-averaged transport equation of reactive scalar Y_s reads:

$$\frac{\partial}{\partial t}\left(\bar{\rho}\widetilde{Y}_s\right) + \frac{\partial}{\partial x_j}\left(\bar{\rho}\widetilde{Y}_s\tilde{u}_j\right) = \frac{\partial}{\partial x_j}\left(\left(D_s + \frac{\mu_t}{Sc_t}\right)\frac{\partial \tilde{Y}_s}{\partial x_j}\right) + \bar{\dot{\omega}}_s, \tag{4}$$

in which D_s is the molecular diffusivity and Sc_t denotes the turbulent Schmidt number, representing the ratio between turbulent viscosity μ_t and turbulent diffusivity, D_t; $\bar{\dot{\omega}}_s$ is the chemical source term. The choice of the turbulent Schmidt number strongly impacts the temperature and species distribution.

The standard k-ε turbulence model is used. The unresolved turbulence stresses $\bar{\rho}\widetilde{u_i'' u_j''}$ are modelled with the product of an eddy viscosity μ_t and mean flow strain rate S_{ij}^*. Finally, the eddy viscosity μ_t in standard k-ε model is estimated as:

$$\mu_t = \rho C_\mu \frac{\tilde{k}^2}{\tilde{\epsilon}}. \tag{5}$$

In Equation 5, the constant C_μ equals 0.09. The Favre-averaged turbulence kinetic energy $\tilde{k}$ and the dissipation rate $\tilde{\epsilon}$ of the turbulence kinetic energy are solved via two separate transport equations [53]:

$$\frac{\partial}{\partial t}\left(\bar{\rho}\tilde{k}\right) + \frac{\partial}{\partial x_j}\left(\bar{\rho}\tilde{k}\tilde{u}_j\right) = \frac{\partial}{\partial x_j}\left(\left(\mu + \frac{\mu_t}{\sigma_k}\right)\frac{\partial \tilde{k}}{\partial x_j}\right) + 2\mu_t E_{ij}E_{ij} - \bar{\rho}\tilde{\epsilon}, \tag{6}$$

$$\frac{\partial}{\partial t}\left(\bar{\rho}\tilde{\epsilon}\right) + \frac{\partial}{\partial x_j}\left(\bar{\rho}\tilde{\epsilon}\tilde{u}_j\right) = \frac{\partial}{\partial x_j}\left(\left(\mu + \frac{\mu_t}{\sigma_\epsilon}\right)\frac{\partial \tilde{\epsilon}}{\partial x_j}\right) + C_{\epsilon 1}\bar{\rho}\frac{\tilde{\epsilon}}{\tilde{k}}2\mu_t E_{ij}E_{ij} - C_{\epsilon 2}\bar{\rho}\frac{\tilde{\epsilon}^2}{\tilde{k}}, \tag{7}$$

in which E_{ij} represents the component of rate of deformation; σ_k, σ_ϵ, $C_{\epsilon 1}$ and $C_{\epsilon 2}$ are model constants, set by default to 1.0, 1.30, 1.45 and 1.90, respectively [54]. The standard k-ε model is robust, computationally fast and has the potential advantage of generality since it requires no direct empirical input such as a mixing-length specification. However, it has the well-known disadvantage of over-estimating the jet spread rate for axisymmetric jets [54].To correct that, some model modifications have been proposed. Whilst changing the $C_{\epsilon 1}$ to 1.6 helps reducing the jet-decay over-estimation [4, 28, 54], such a modification lacks generality. Pope [54] suggested a correction to the standard k-ε model, adding an additional term to the kinetic energy dissipation rate transport equation:

$$Corr_{Pope} = C_{\epsilon 3}\frac{\tilde{\epsilon}^2}{\tilde{k}}\psi, \tag{8}$$

with $\psi = \omega_{ij}\omega_{jk}S_{ki}$, measuring the vortex stretching:

$$\omega_{ij} = \frac{1}{2}\frac{\tilde{k}}{\tilde{\epsilon}}\left(\frac{\partial U_i}{\partial x_j} + \frac{\partial U_j}{\partial x_i}\right), \tag{9}$$

$$S_{ki} = \frac{1}{2}\frac{\tilde{k}}{\tilde{\epsilon}}\left(\frac{\partial U_i}{\partial x_j} - \frac{\partial U_j}{\partial x_i}\right). \tag{10}$$

The impact of the choice of the turbulent Schmidt number and of the turbulence model is discussed in Section 4.

2.2. Combustion Model — PaSR Model

The PaSR model [48, 55], assumes that each computational cell is separated into two zones: one where reactions take place, and another characterized by mixing alone. Turbulence drives the exchange between the two zones. The final species concentration of the cell is the weighted mean value between the reactive zone and the mixing zone. A conceptual drawing of the PaSR model is shown in Fig. 1.

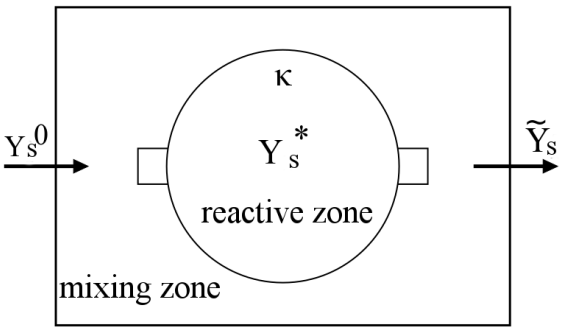

Figure 1: Conceptual drawing of the PaSR model (adapted from Li et al. [35]).

Figure 1 depicts one computational cell, in which Y_s^0 is the initial s_{th} species mass fraction in the non-reactive region, $\widetilde{Y}_s$ is the final averaged s_{th} species mass fraction in the cell and Y_s^* is the s_{th} species mass fraction in the reactive zone. The term κ is the mass fraction of the reactive zone in the cell, which is estimated with [56]:

$$\kappa = \frac{\tau_c}{\tau_c + \tau_{mix}}, \tag{11}$$

where τ_c and τ_{mix} are the characteristic chemical and mixing timescales, respectively. The complexity of the model lies, therefore, in the estimation of τ_c and τ_{mix}, as described in previous publications [35, 51].

In the present work, the mixing timescale is evaluated with a dynamic approach [35, 51]—as the ratio of the scalar variance, $\widetilde{\phi''^2}$, and the scalar dissipation rate, $\widetilde{\epsilon_\phi}$ [57]:

$$\tau_{mix_{Dynamic}} = \frac{\widetilde{\phi''^2}}{\widetilde{\epsilon_\phi}}. \tag{12}$$

The mixture fraction Z is selected to describe the mixing process of a scalar. Therefore, the scalar variance and dissipation rate take the form of the mixture fraction variance ($\widetilde{Z''^2}$) and mixture fraction dissipation rate ($\widetilde{\chi}$). They are obtained by solving the following transport equations [58, 59]:

$$\frac{\partial \bar{\rho}\widetilde{Z}}{\partial t} + \frac{\partial \bar{\rho}\widetilde{u_j}\widetilde{Z}}{\partial x_j} = \frac{\partial}{\partial x_j}\Big(\bar{\rho}(D_s + D_t)\frac{\partial \widetilde{Z}}{\partial x_j}\Big), \tag{13}$$

$$\frac{\partial \bar{\rho}\widetilde{Z''^2}}{\partial t} + \frac{\partial \bar{\rho}\widetilde{u_j}\widetilde{Z''^2}}{\partial x_j} = \frac{\partial}{\partial x_j}\Big(\bar{\rho}(D_s + D_t)\frac{\partial \widetilde{Z''^2}}{\partial x_j}\Big) + 2\rho D_t\Big(\frac{\partial \widetilde{Z}}{\partial x_j}\Big)^2 - \bar{\rho}\widetilde{\chi}, \tag{14}$$

$$\frac{\partial \rho \widetilde{\chi}}{\partial t} + \frac{\partial \rho \widetilde{u_j} \widetilde{\chi}}{\partial x_j} = \frac{\partial}{\partial x_j}\left(\bar{\rho}(D_s + D_t)\frac{\partial \widetilde{\chi}}{\partial x_j}\right) - C_1 \bar{\rho}\frac{\widetilde{\chi}^2}{\widetilde{Z''^2}} - C_2 \bar{\rho}^2 \frac{C_\mu \widetilde{k}}{\mu_t}\widetilde{\chi} + C_3 \frac{\bar{\rho} C_\mu \widetilde{k}}{S c_t}\left(\frac{\partial \widetilde{Z}}{\partial x_j}\right)^2 + C_4 \mu_t \frac{\widetilde{\chi}}{\widetilde{k}}|\widetilde{S}|^2. \tag{15}$$

In the present work, the molecular diffusivity D is estimated with thermal diffusivity α, given the absence of species such as H_2. The turbulent diffusivity is calculated using $D_t = \mu_t/(\bar{\rho} S c_t)$. In Eqn. 15, C_1, C_2, C_3 and C_4 are model constants. They are set to $C_1 = 1.0$, $C_2 = 1.8$, $C_3 = 1.7$ and $C_4 = 1.4$ [58] in the current study.

The chemical timescale can be obtained from the Jacobian matrix (**J**) of the chemical source terms [60, 61]. The decomposition of the source term Jacobian matrix is accurate but time consuming, especially when a large mechanism is used. As an alternative, the formation rates can be used. The chemical timescale of each chemical species can be approximated with the ratio of the species mass fraction and formation rate in the reactive structure [14, 62]:

$$\tau_{c,s} = \frac{Y_s^*}{|dY_s^*/dt|}. \tag{16}$$

After removing the dormant species (characterised formation rate smaller than $1 \times 10^{-16} s^{-1}$), the slowest chemical time is chosen as the characteristic chemical timescale:

$$\tau_c = max(\tau_{c,s}). \tag{17}$$

More details about the choice of chemical timescale are presented in Supplementary Material.

Finally, the mean source term $\overline{\dot{\omega}}_s$ in the species transport equation is expressed as:

$$\overline{\dot{\omega}}_s = \kappa \frac{\widetilde{\rho}\left(Y_s^* - Y_s^0\right)}{\tau^*}, \tag{18}$$

where τ^* is the residence time in the reactive structure. In the present work, the mixing timescale is used as the residence time τ^*. A time-splitting approach is used to obtain the value of Y_s^*. The reactive zone is modelled as an ideal reactor evolving from the initial value of Y_s^0:

$$\frac{dY_s^*}{dt} = \frac{\dot{\omega}_s}{\rho}. \tag{19}$$

The term $\dot{\omega}_s$ represents the instantaneous formation rate of species s. The final integration of $\frac{dY_s^*}{dt}$ over the residence time of τ^* is Y_s^*.

3. Methodology

3.1. Experimental Approach

The experimental validation data are newly obtained and presented here for the first time. These experimental data complement those reported by Ye et al. [8], undertaken in the same JHC burner using *n*-heptane as fuel. The JHC burner used in this study has a cooled central jet with the inner diameter of D_j = 4.6 mm [8]. The liquid *n*-heptane fuel is mixed with carrier air and then preheated by a controlled evaporator and mixer (CEM). The temperature of the mixture at the central jet exit plane is 412 K, which is higher than the *n*-heptane boiling point (371 K). A secondary burner located 90 mm upstream of the exit plane has an inner diameter of 82 mm. The secondary burner produces the hot combustion products from a lean mixture of natural gas, hydrogen, air and nitrogen. Changing the ratios of these gases allows the coflow oxygen level and temperature to be varied independently. The mean gas temperature, mean velocity and Reynolds number of the central jet and hot coflow are reported in Table 1. The equilibrium composition for species of O_2, N_2, H_2O, CO_2 and OH are obtained from equilibrium calculations with coflow adiabatic temperature are provided in Table 2.

Table 1: Jet and coflow characteristics

Profiles	Central jet	Hot coflow
Velocity	50 m/s	2.4 m/s
Temperature	412 K	1250 K
Reynolds number	10,000	1000

Table 2: Species mass fractions from equilibrium calculation

Species	nC_7H_{16}	O_2	N_2	H_2O	CO_2	OH
Fuel stream	0.398	0.462	0.140	0	0	0
Coflow 3 %	0	0.0347	0.8382	0.0697	0.0573	2.27×10-06
Coflow 6 %	0	0.0703	0.8034	0.0693	0.0570	2.68×10-06
Coflow 9 %	0	0.1045	0.7696	0.0691	0.0568	2.96×10-06

The mean and RMS values of temperature and species are measured using the optical techniques of Rayleigh scattering and planar laser-induced fluorescence (PLIF), respectively [8, 19]. Temperature, semi-quantified number density of OH as well as the normalized CH_2O-PLIF signal are reported at the axial locations of 14.5 mm ($3.2D_j$), 22.5 mm ($4.9D_j$),

29.5 mm (6.4D_j), and 59.5 mm (12.9D_j). The CH_2O-PLIF signal is not quantified due to challenges with determining the quenching rates.

3.2. Numerical Configuration

Figure 2 presents a two-dimensional schematic of the axisymmetric domain. The axial direction is denoted with *z*, and the radial direction marked with *r*. The bulk mean velocities used for the jet and coflow streams are given in Table 1, with corresponding Reynolds numbers, and compositions are given in Table 2.

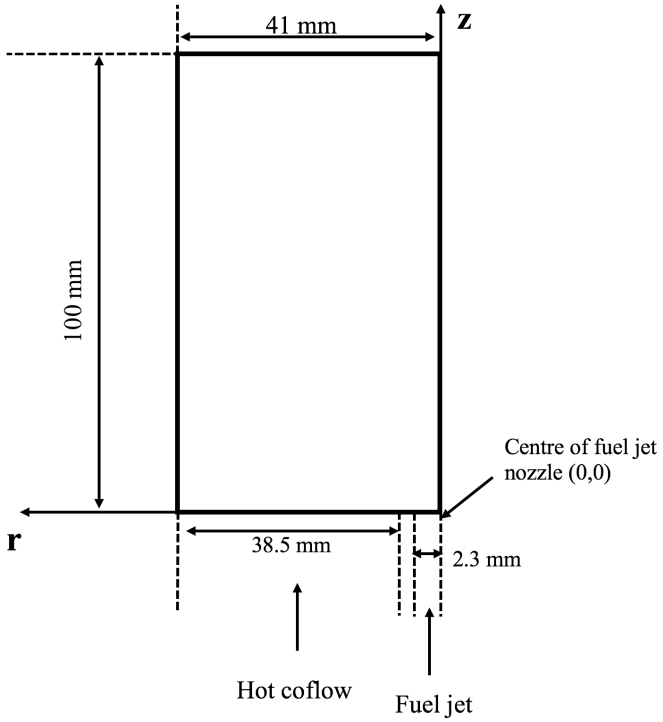

Figure 2: Two-dimensional schematic of the JHC burner.

A two-dimensional structured mesh is used in the simulation. The mesh has 4450 hexahedral cells and 100 prisms. A pre-inlet with the length of 100 mm including the burner wall is used. The computational domain extends 100 mm further downstream. Only the fuel jet and hot coflow streams are considered in the simulation, since the experimental data are available up to 59.5 mm downstream of the jet outlet, and mixing with fresh air from the surroundings (quiescent air) only has an effect from 100 mm above the jet exit plane [8], .

Because the turbulent Schmidt number Sc_t is varied according to the specific flow nature, there is no universally-accepted formulation in the literature [63]. According to Tominaga [64] et al., optimum values for Sc_t are widely distributed in the range from 0.2 to 1.3. In

the present discussion, a sensitivity study for the choice of the turbulent Schmidt number is first presented, setting the Sc_t to 0.7, 1.0, 1.2 and 1.3. The Pope correction [54] is used here in combination with the standard k-ε turbulence model, to correct the spreading rate of the jet. The PaSR combustion model with the dynamic calculation of mixing timescale is adopted. The temperature, velocity and species mass fractions from Tables 1 and 2 are used as boundary conditions. A reduced *n*-heptane mechanism with 106 species and 1738 reactions [65–67] is used for most simulations. Indeed, numerical results using a detailed mechanism with 654 species and 2827 reactions [68, 69] showed minor differences when compared with the results provided by the reduced one and they are presented in the Supplementary Material.

4. Results and Discussion

4.1. Turbulence Model Parameters

The influence of the turbulent Schmidt number on the mean temperature and OH distribution is presented in Figs. 3–5, for each of the three coflow O_2 levels considered. Note that the temperature in the fuel jet is not measured, therefore the experimental temperature values close to the centerline at axial locations of 14.5, 22.5 and 29.5 mm are not available. Moreover, it should be noted that the OH measured along the jet centerline is an artefact of interference from fuel Raman and is not indicative of OH; however, this interference does not affect the location or value of the peak OH intensity.

Figure 3 shows that using a turbulent Schmidt number $Sc_t = 0.7$ results in early ignition of the jet flame for the case with coflow oxygen level of 9 %. A generalized over-prediction of mean temperature profiles is observed at axial locations z = 22.5, 29.5 and 59.5 mm. The location of peak temperature is shifted slightly to the right (away from the centerline) for z = 59.5 mm. Furthermore, the region with temperature above that of the coflow temperature (1250 K) is broader than observed experimentally. On the other hand, using $Sc_t = 1.3$ leads to a 140 K under-prediction of the mean temperature at z = 59.5 mm. Low turbulent Schmidt numbers increase the scalar diffusivity (see Eq. 4), leading to enhanced mixing between the fuel and oxidizer species, thus promoting chemical reactions. However, high turbulent Schmidt number influences the flow in the opposite way; as a result, the flame ignition is delayed. Setting Sc_t to 1.0 or 1.2 provides satisfactory mean temperature predictions.

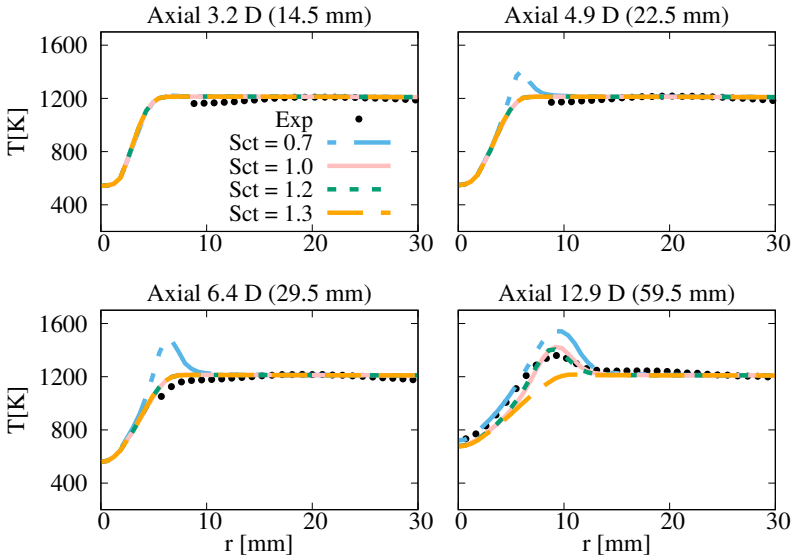

Figure 3: Mean temperature profiles obtained with various turbulent Schmidt numbers (0.7, 1.0, 1.2 and 1.3), compared with the experimental data at several axial locations. Coflow oxygen level of 9 %.

The differences between choosing Sc_t = 1.0 and Sc_t = 1.2 is revealed through the OH distributions in coflows with oxygen levels of 3 % and 6 % (shown in Fig. 4 and 5). No experimental data are available at z = 22.5 mm for 3 % and 6 % O_2 cases—the numerical values are shown as a comparison with the 9 % case. Since the OH number density (molecules/cm^3) is measured experimentally, the mole fractions of OH are extracted from the simulations and converted for directed comparison. At locations far from the centerline (r $\geq$ 15 mm), the predicted OH level is close to the experimental value with both Sc_t = 1.0 and Sc_t = 1.2. However, the calculated OH peaks at z = 14.5, 29.5 and 59.5 mm are higher than the experimental data when Sc_t = 1.0 is chosen. Particularly at z = 59.5 mm, showing more than six times over-prediction. Choosing Sc_t = 1.2 keeps the OH peak value closer to the experimental data for both the 3 % and 6 % cases, especially at z = 14.5 mm. At z = 59.5 mm, using Sc_t = 1.2 still over-predicts OH for the coflow oxygen level of 3 %, although significantly less than with Sc_t = 1.0. Based on this analysis, a turbulent Schmidt number of 1.2 was chosen for the remainder of the simulations.

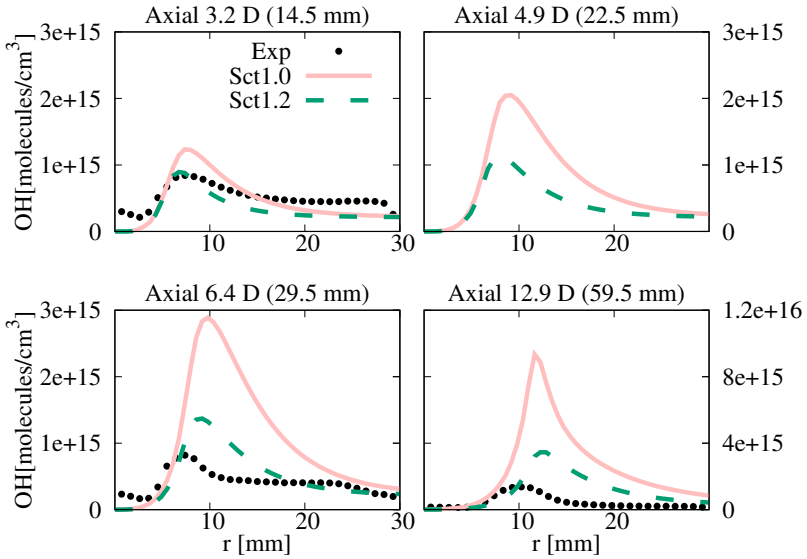

Figure 4: Mean experimental and numerical OH number density profiles at several axial locations. Coflow oxygen level of 3 %.

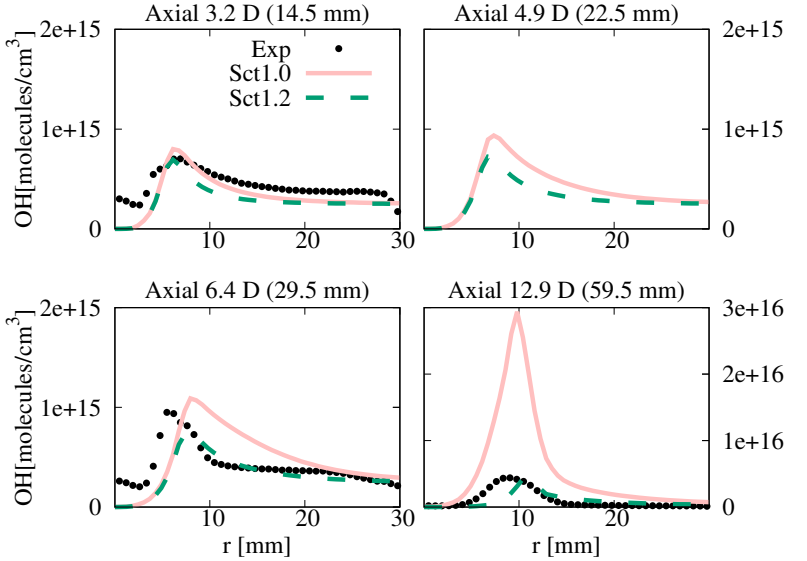

Figure 5: Mean experimental and numerical OH number density profiles at several axial locations. Coflow oxygen level of 6 %.

Adoption of the Pope correction has major influence on the flow field of the jet. Figure 6 shows the mean temperature profiles for the 9 % O_2 case, with and without the Pope correction. Very similar predicted profiles are obtained at z = 14.5/22.5/29.5 mm. At z = 59.5 mm, the standard k-ε models fails to predict the peak temperature location correctly, while results

with the Pope correction closely follow the experimental profile. Comparing the jet decay on the centerline in Fig. 7, a faster jet decay is featured after z = 30 mm if no Pope correction is used. Moreover, Fig. 8 indicates that the spread rate is higher without Pope correction, which shifts the stoichiometric mixture location further away from the centerline. Ultimately, the combination of $Sc_t = 1.2$ and Pope correction is chosen in the current study.

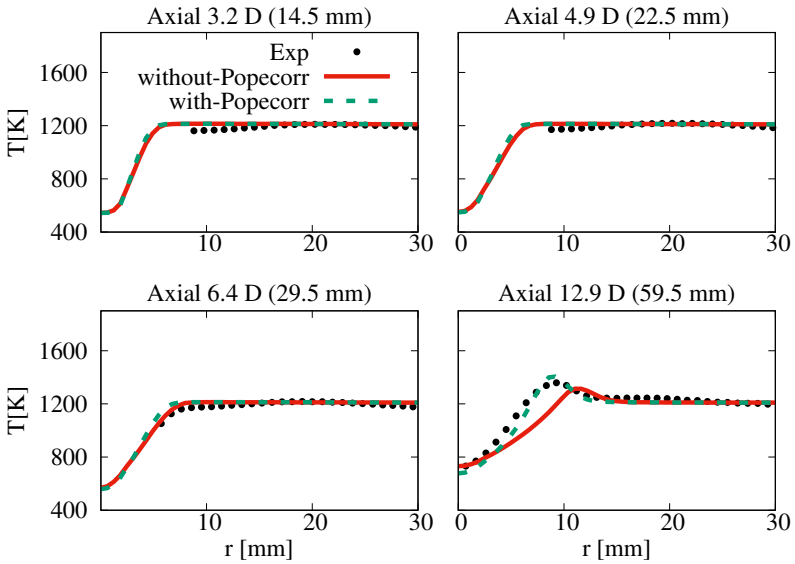

Figure 6: Mean temperature profiles obtained with and without Pope correction, compared with the experimental data at several axial locations. Coflow oxygen level of 9 %.

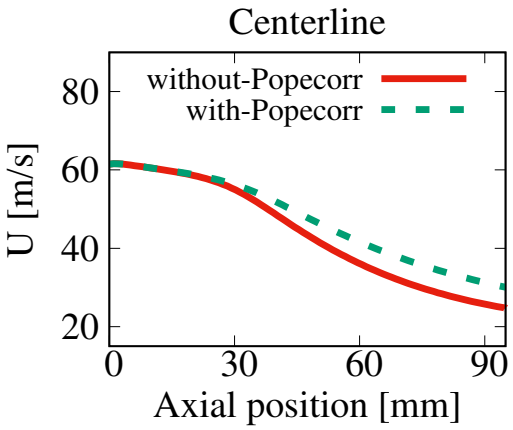

Figure 7: Mean velocity profile on the centerline obtained with and without Pope correction. Coflow oxygen level of 9 %.

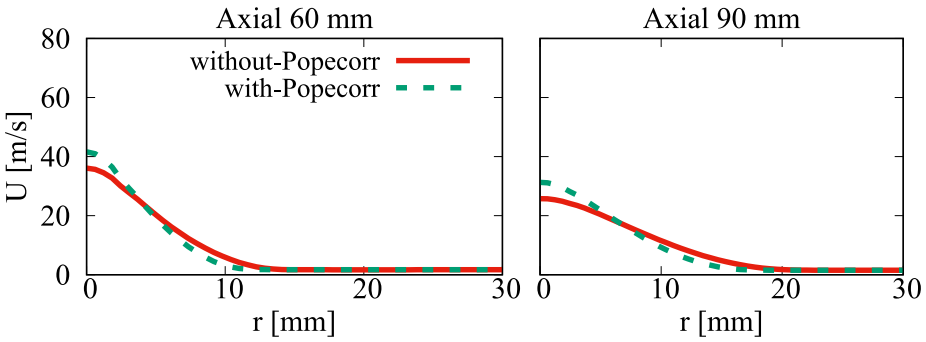

Figure 8: Mean velocity profile at 60 mm and 90 mm axial locations, obtained with and without Pope correction. Coflow oxygen level of 9 %.

4.2. The influence of oxygen level

Figure 6 shows that the mean temperature profiles for the 9 % case are very well predicted with the turbulent and combustion models chosen. The predicted temperature profiles obtained for the 3 % O_2 and 6 % O_2 cases are compared to the available experimental measurements in Fig. 9 and Fig. 10. The 3 % O_2 and 6 % O_2 cases show peak temperature at z = 59.5 mm of about 1230 K and 1240 K, respectively: more than 100 K lower than the maximum measured temperature for 9 % O_2 (around 1360 K). The numerical model can capture the temperature levels quite well, showing remarkable agreement with the measured data. As previously indicated, no experimental data are available at z = 22.5 mm.

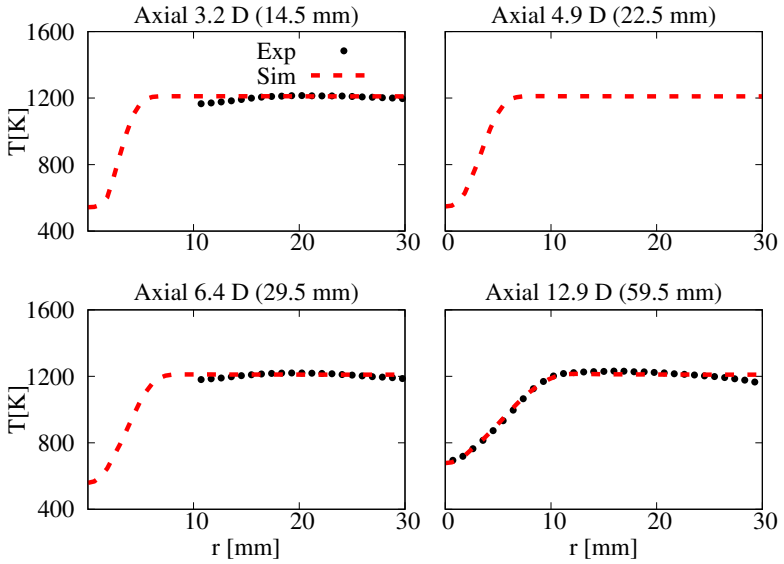

Figure 9: Mean experimental and numerical temperature profiles, at different axial locations. Coflow oxygen level of 3 %.

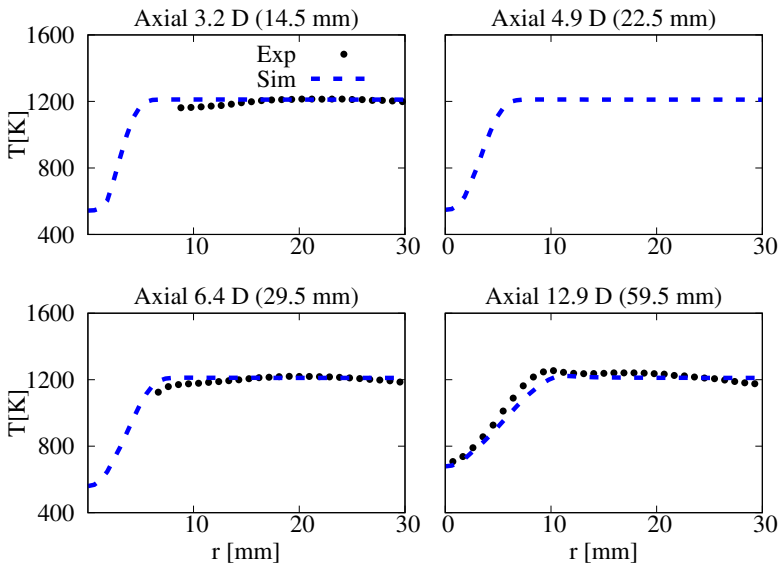

Figure 10: Mean experimental and numerical temperature profiles, at different axial locations. Coflow oxygen level of 6 %.

In Section 4.1, the OH number density distribution for the 3 % O_2 and 6 % O_2 cases was presented with two different turbulent Schmidt numbers. The OH profile of the 9 % O_2 case is shown in Fig. 11 with Sc_t = 1.2. Slightly under-predicted OH number density levels are shown at axial locations of z = 14.5, 22.5 and 29.5 mm. However, a significant over-estimation (approximately four times) can be observed at z = 59.5 mm, different from the 3 % O_2 (around two times over-prediction) and 6 % O_2 cases (no obvious over-prediction).

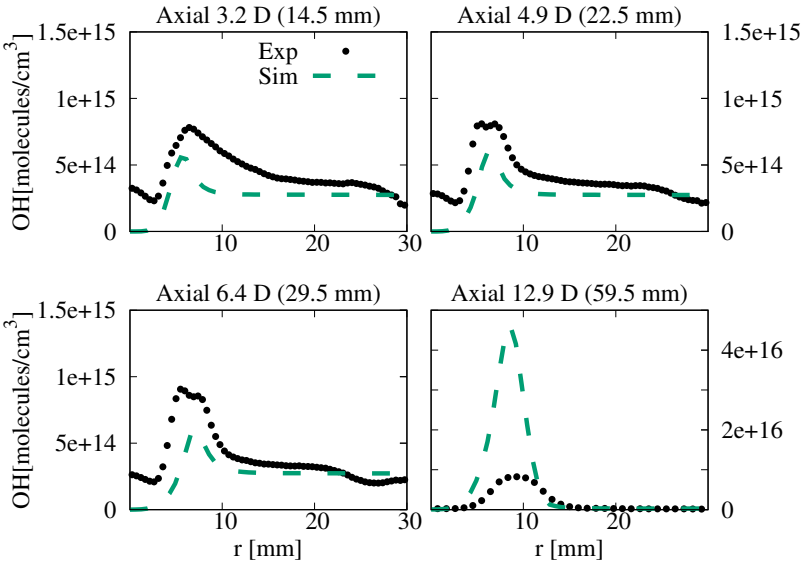

Figure 11: Mean experimental and numerical OH number density profiles at several axial locations. Coflow oxygen level of 6 %.

The predicted CH_2O levels are compared with the experimentally measured PLIF signals, in Figs. 12, 13 and 14. Both experimental and numerical CH_2O profiles are normalized between 0 and 1. The peak values are generally well predicted for $z \leqslant 30$ mm. However, a generalized under-prediction close to the centerline location is observed at all the four axial locations. CH_2O has been identified as an important precursor in controlling the initiation of reaction in methane flames, as explained by Gordon et al. [70]. In the present *n*-heptane flame, the lack of production of CH_2O along the centerline is directly linked to the formation of CO (see Fig. 22), thus to heat release and flame ignition. However, since the CH_2O signals are not quantified, it is not possible to draw further conclusion based on the comparison of experimental and numerical CH_2O profiles.

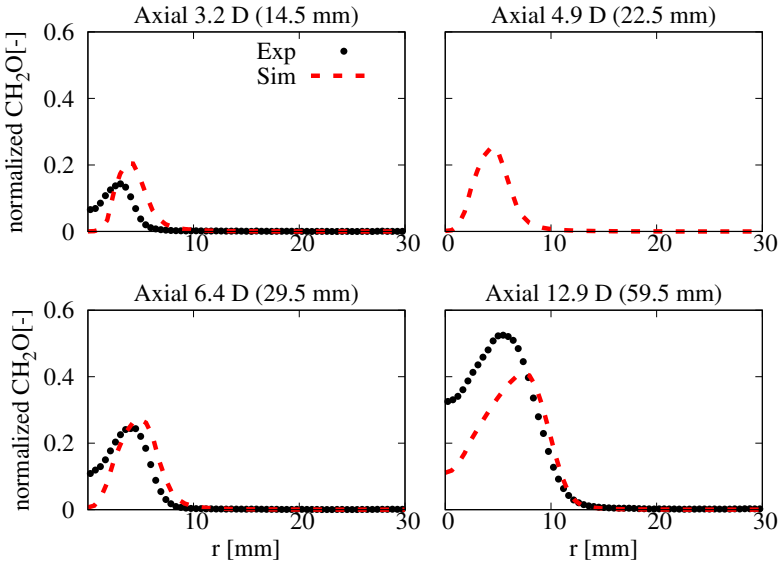

Figure 12: Mean experimental and numerical normalized CH_2O number density profiles, at different axial locations. Coflow oxygen level of 3 %.

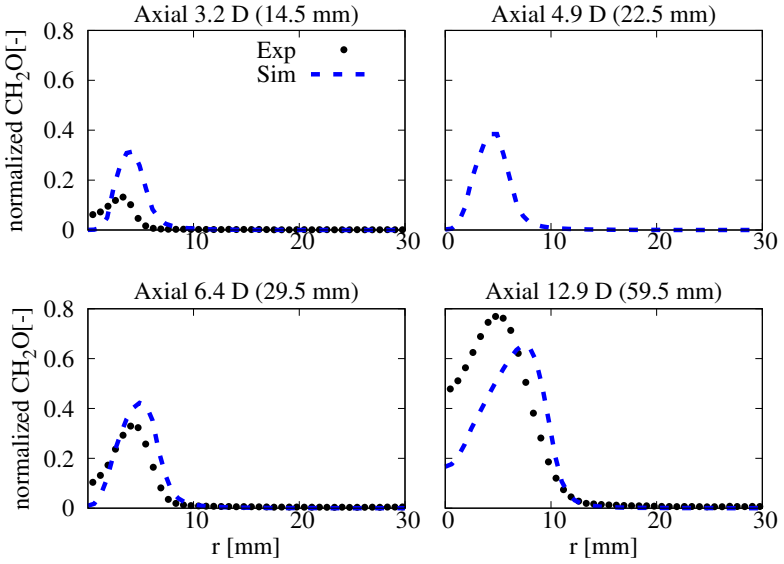

Figure 13: Mean experimental and numerical normalized CH_2O number density profiles, at different axial locations. Coflow oxygen level of 6 %.

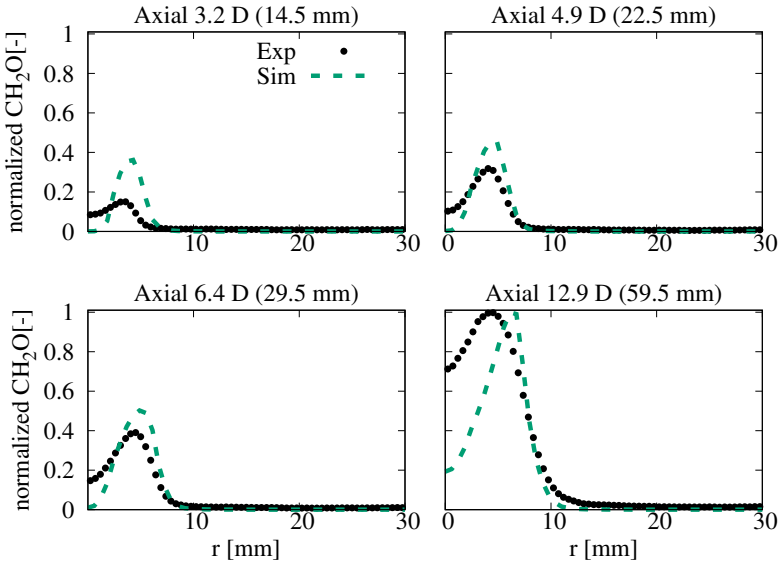

Figure 14: Mean experimental and numerical normalized CH_2O number density profiles, at different axial locations. Coflow oxygen level of 9 %.

4.3. OH distribution

When analyzing the OH distributions in the three flames, a weak-to-strong transition is observed, for the 3 % and 6 % cases [8], both numerically and experimentally (Fig. 17). This indicates that the 3 % and 6 % cases do not reach MILD conditions [8, 10], and that the corresponding flames are lifted. To characterize such behaviour, the "weak-to-strong transition height" is used. Numerically, it is defined as the height at which the OH number density signal is first captured, based on different threshold values (as indicated in the legend). Experimentally, the height is inferred from the photographs shown in Fig. 16, based on the intensity of the captured signal.

A summary of the experimentally measured and modelled flame transition heights is shown in Fig. 15. When the OH number density threshold value is set to 1×10^{15} or 5×10^{14} molecules/cm^3, a monotonic trend relating the flame transition height and coflow oxygen level is observed. Moreover, the transition height for the 3 % case is marginally affected by the threshold value. However, the monotonic trend is lost when the threshold value is further reduced to 1×10^{14} molecules/cm^3. In this case, the transition height for the 3 % case is much lower than for the other two cases, indicating that this case is the closest to MILD conditions.

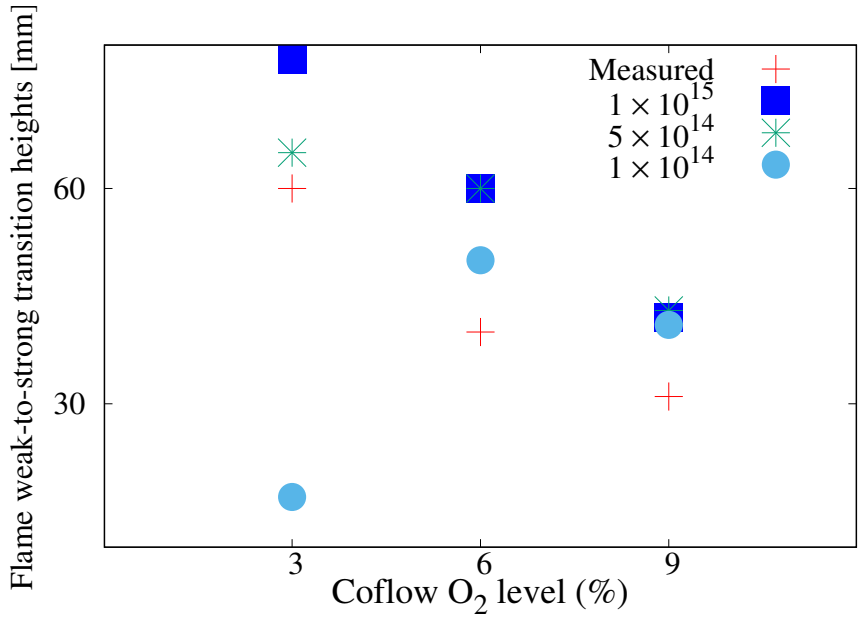

Figure 15: Flame weak-to-strong transition heights in mm. The threshold values of 1×10^{15}, 5×10^{14} and 1×10^{14}m, in molecules/cm^3 of OH, are used to identify the flame transition heights. The reference measurements are obtained from photographs.

To compare the flame weak-to-strong transition heights, Fig. 16 shows the modelled OH number density distributions from all three cases and experimental flame photographs. The threshold OH number density is set to 5×10^{14} molecules/cm^3, that shows similar trend of flame weak-to-strong transition heights. The height above the jet exit plane is marked and annotated. The location starting with strong signal is identified and highlighted with a star. The transitional structure can be observed for the 3 % case between the star and diamond, both on the experimental photograph (40–60 mm) and on the numerical simulation contour plot (65–78 mm). This phenomenon is more apparent when the threshold OH number density is reduced to 1×10^{14} molecules/cm^3, as presented in Fig. 17, where the instantaneous experimental OH-LIF images are compared with the simulations. Figure 17 also indicates the existence of a transitional structure for the 6 % case. However, it is not as obvious as for the 3 % case. The experimental OH-LIF images show the existence of the transitional structure for the 3 % case, at height below 20 mm from the jet exit plane. Such structure is not evident for the 9 % case. Thus, the numerical analysis confirms the occurrence of a transitional flame structure, observed experimentally at low coflow oxygen level, and it can capture the experimental trend associated to the weak-to-strong transition.

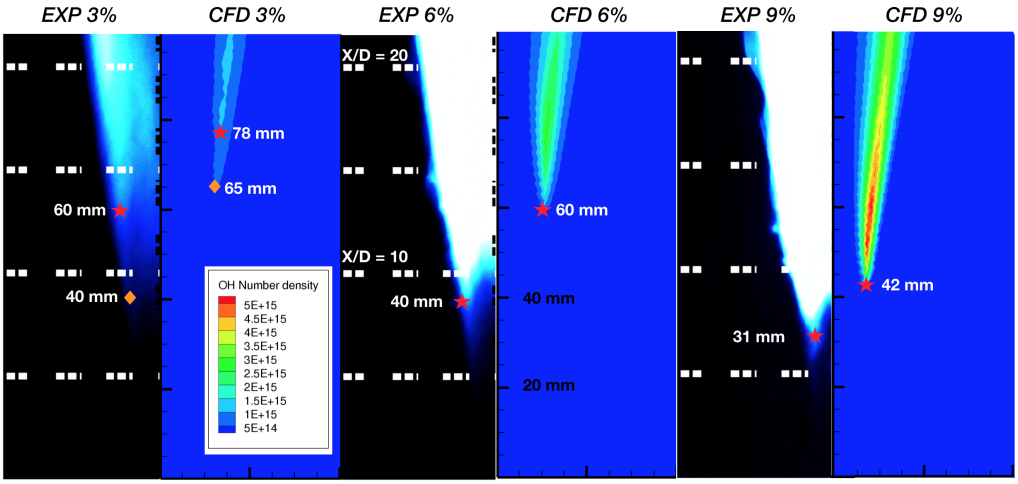

Figure 16: Mean OH number density distribution for 3 %, 6 % and 9 % coflow oxygen levels compared with the experimental flame photographs taken with an ISO sensitivity of 1600, exposure time of 1/15 second and an f-number of 2 [8]. The diamond and star denote the starting points of the weak and strong signals, respectively. The 3 % case shows transitional OH signal.

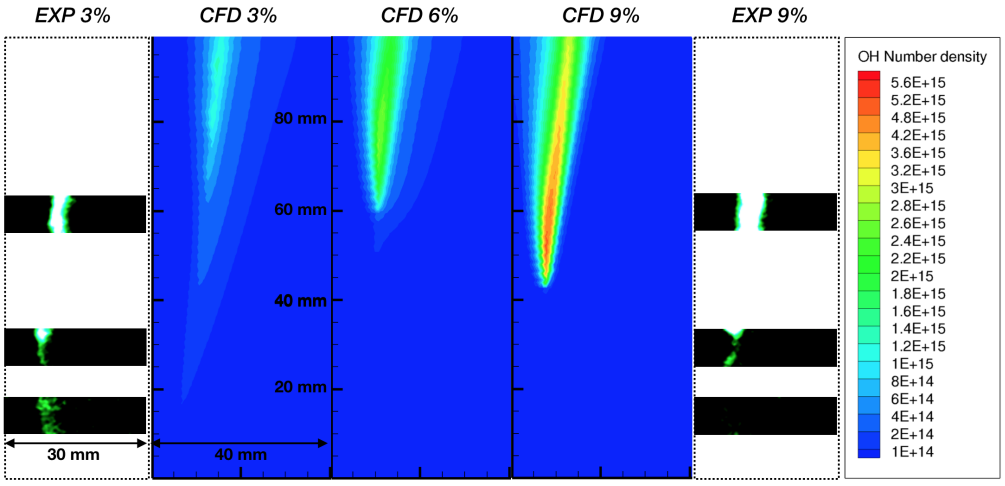

Figure 17: Mean OH number density distribution for the 3 %, 6 % and 9 % coflow oxygen levels, compared with the experimental OH-LIF images. The 6 % OH-LIF instantaneous image is not available. The threshold OH number density of the numerical contour plot is set to 1×10^{14} molecules/cm^3.

4.4. Chemical timescale analysis

When the coflow oxygen level is reduced from 9 % to 3 %, the higher dilution of the fuel-oxidiser mixture reduces the reactivity, and this results in higher values of the characteristic chemical timescale. Figure 18 shows the chemical timescale distributions for the three cases.

The region with chemical timescale longer than 1 s, covering most of the area far away from the centerline, represents the chemically inactive zone. As discussed in Section 2.2, the chemical timescale is evaluated as $\tau_{c,s} = \frac{Y_s^*}{|dY_s^*/dt|}$ (s denotes the s_{th} species in the chemical mechanism), and is clipped at 1 s. The 3 % O_2 case exhibits a wider active region (chemical timescale smaller than 1 s) near the jet exit plane (z = 0 mm) than the 6 % or 9 % O_2 cases. Despite the differences in the width of these regions, the chemical timescales are similar in magnitude for all three cases, for z ≤ 40 mm.

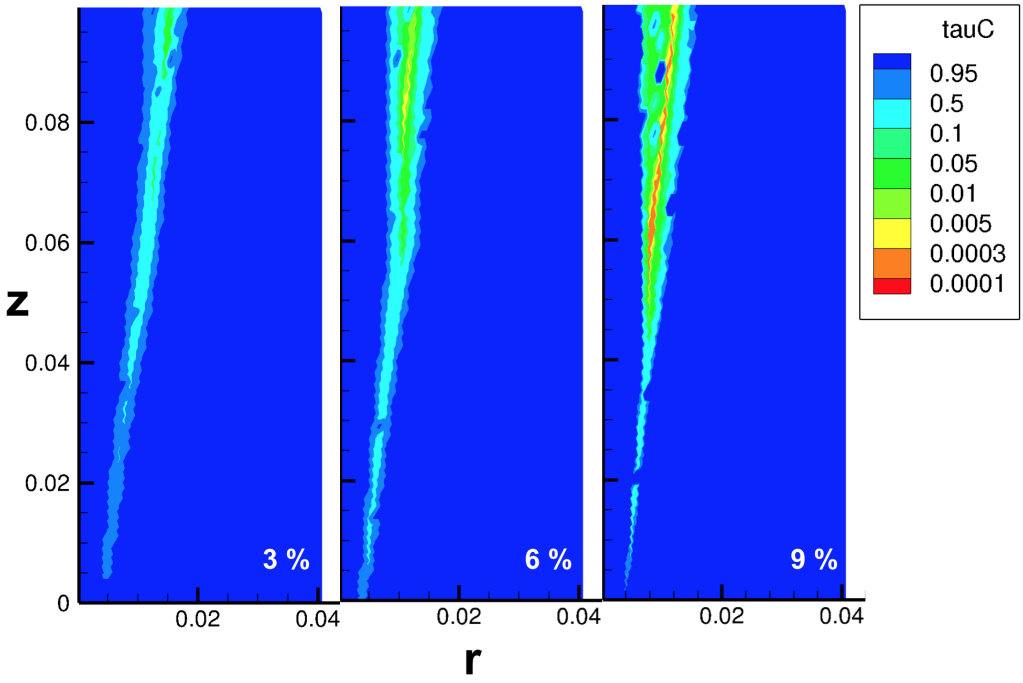

Figure 18: Chemical timescale distribution for the 3 %, 6 % and 9 % coflow oxygen levels. The active chemical time clipping value is set at 1 s.

Figure 18 also shows that the active region of the 9 % O_2 case tends to expand—and becomes chemically faster than the other two cases—in the region z ≥ 45 mm, with shorter chemical timescales (below 5 ms). On the other hand, the 3 % and 6 % cases show narrower chemically active zones. This is due to the fact that higher coflow oxygen levels push the stoichiometric reaction zone towards the fuel stream side [71]. Furthermore, the higher reactivity of the mixture leads to a larger heat release. As a result, the fuel is decomposed faster and the reaction zone is propagated further into the fuel stream [72]. Increased reactivity results in higher heat release peak for the 9 % O_2. This matches the high OH number density at around z = 45 mm (Fig. 16, 9 % case). The widening of the region of low chemical timescale (high reactivity) for the 6 % O_2 is localised at around z = 60 mm (Fig. 18). For the 3 %

O_2 case, an area with low chemical timescale is visible only after z = 80 mm, showing the transitional features of this case.

Figure 19 shows line plots with the minimum chemical timescale value along the axial direction. For all the three cases, there exists a slow decrease of chemical time starting from z = 0 mm and a drastic drop at around z = 45/60/80 mm, for 3/6/9 % coflow levels, respectively. Such observation concurs with the 2D contour plot in Fig. 18.

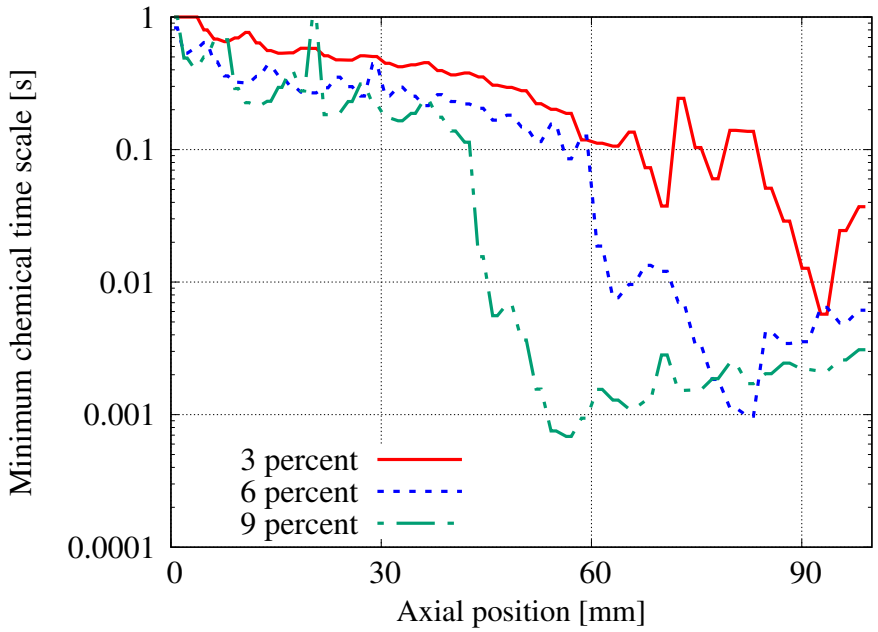

Figure 19: Minimum chemical timescale values along the axial direction for the cases with 3 %, 6 % and 9 % coflow oxygen levels.

The contours of chemical timescale distribution for the three oxygen levels show the effect of the increased availability of oxygen on the reactivity of the system. This directly impacts the combustion model via the reacting fraction κ. Indeed, the analysis of the mixing timescale (shown in Supplementary Material) for the three cases indicates very similar distributions regardless of the oxygen level. The same was reported by Evans et al. on C_2H_4 and CH_4/H_2 JHC flames with varied coflow oxygen levels [71, 72]. Therefore, the chemical timescale becomes the controlling parameter for the determination of κ and the final mean reaction rate, $\overline{\dot{\omega}}_s$.

4.5. Investigations on negative heat release rate

Previous numerical studies on methane by de Joannon and co-workers [3, 41] demonstrated the absence of a net negative heat release region in MILD combustion, because of the

suppression of pyrolytic reactions. Line and contour plots of the heat release rate with three different coflow oxygen levels are presented in Figs. 20 and 21. Both figures show that a negative heat release region exists for all the cases. This conclusion agrees with that of Ye et al. [8], who also demonstrated the dependence of the net heat release rate profile on strain-rate. Furthermore, studies of laminar opposed-flow flames noted that the net negative heat release region only vanished for *n*-heptane in highly diluted conditions (99% N_2 by volume [73]). In contrast to this, additional two-dimensional simulations with coflow O_2 concentrations of 1 % and 2 % (shown in Supplementary Material) suggest that the negative heat release region still exists if the coflow oxygen level is reduced to 2% and 1% in the numerical simulations (profiles shown in Supplementary Material) and the absolute value for negative heat release is even higher with lower oxygen content, thus following the trend shown by the 3%, 6% and 9% cases. Moreover, reducing the coflow oxygen level below 3% leads to very weak transitional OH signals.

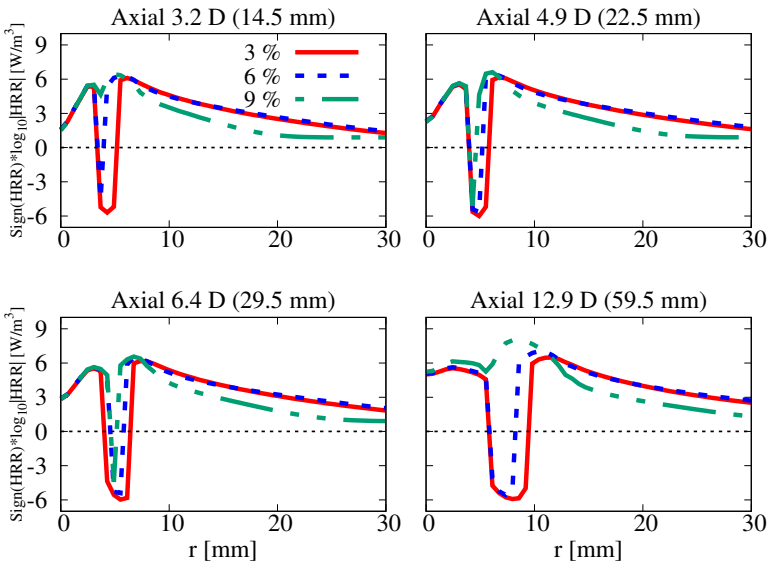

Figure 20: Heat release rate (HRR) for the cases with 3 %, 6 % and 9 % coflow oxygen levels at several axial locations. Note the heat release rates are plotted in logarithmic scale (base 10) and multiplied with the HRR sign.

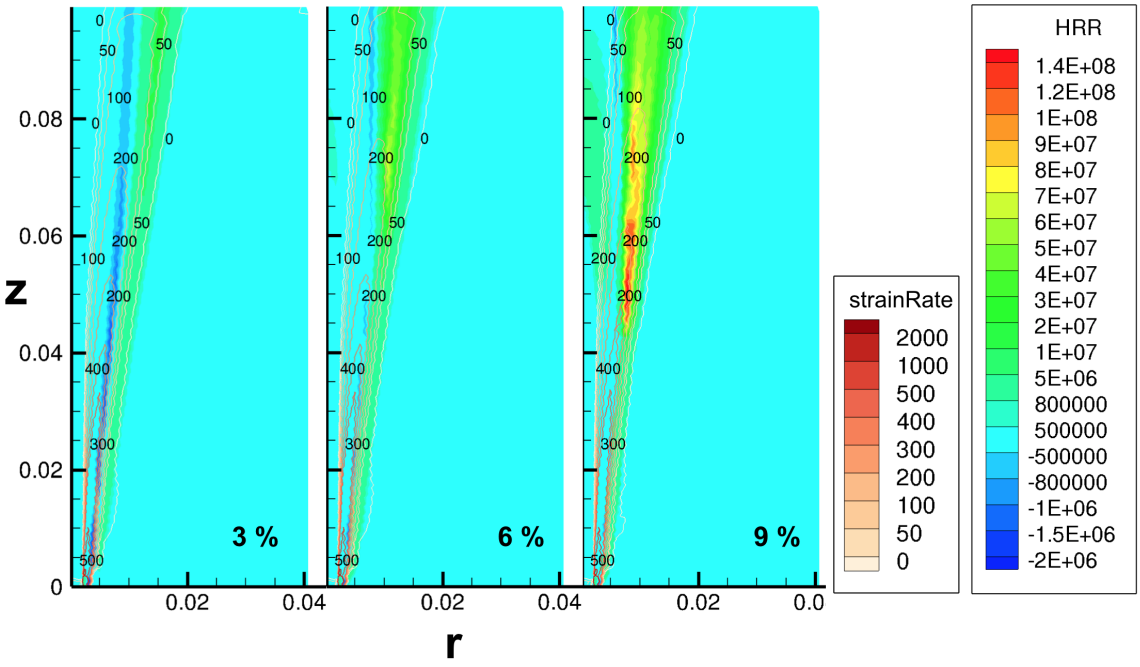

Figure 21: Heat release rate (HRR) for the 3 %, 6 % and 9 % coflow oxygen cases, with superimposed axial strain rate streamlines. The units for strain rate and HRR are s^{-1} and W/m^3, respectively.

The influence of strain rate on the net heat release in laminar opposed-flow flames was analysed by Ye et al. [8], spanning several orders of magnitude. Their results showed that the 9 % O_2 case was always characterised by a larger absolute value of negative heat release rate than the 3 % O_2 case. One significant difference between different oxygen dilutions is the trend between the absolute value of negative heat release rate and the strain rate. For the 9 % O_2 case, the absolute value of HRR increases monotonically as the strain rate is increased from 80 s^{-1} to 320 s^{-1}, whereas it decreases monotonically for the 3 % O_2 case in the same range.

In Fig. 21, the heat release is represented with filled color maps, with superimposed lines of strain rate values. In the 3 % O_2 case, a region of negative heat release extends along the whole simulation domain, over a wide range of axial strain rates (up to 500 s^{-1}), parallel to the positive heat release region. In the 6 % and 9 % O_2 cases, the area of positive heat release rate becomes wider while the net negative region shrinks. The regions of negative heat release in the 6 % and 9 % O_2 cases are located mainly around the low and medium strain rates. This observation does not concur with the results from Ye et al. [8], in which the 9 % O_2 tends to have more negative heat release when larger strain rate is applied. However, the strain rate from Ye et al. [8] is perpendicular to the flame front direction, while the strain rate discussed

in this paper is in the axial direction. Furthermore, the axial and radial strain rate profiles are very similar across all cases (as shown in the Supplementary Material). It is therefore reasonable to conclude that the existence of the negative heat release is not dominated by the flow-field, but rather by chemical reactions.

As explained by Ye et al. [8], the negative heat release region for the 3 % case appears because the *n*-heptane fuel pyrolysis process is not suppressed by the low temperature and low oxygen concentration, it can proceed through alternative paths which are featured by lower activation energy. Figure 22 shows the chemical pathways of the *n*-heptane fuel. It is found that two parent fuel pyrolysis paths exist to produce C_7H_{15} isomers or alkyl radicals, such as pC_4H_9 and nC_3H_7. Then, through secondary pyrolysis, smaller hydrocarbon molecules such as C_2H_4 and C_2H_5 are formed.

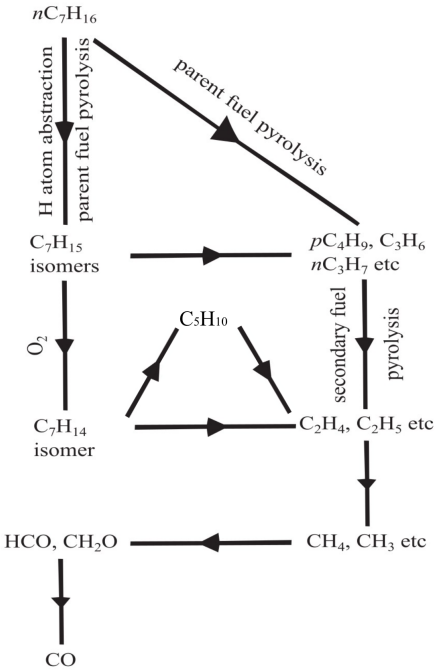

Figure 22: Chemical pathways of *n*-heptane fuel [8, 74].

Figure 23 presents selected key species involved in *n*-heptane pyrolysis and oxidation. The production of nC_7H_{15} from H atom abstraction (left path in Fig. 22) is highest close to the burner exit for all the three cases. The H atoms are consumed by O_2 to produce HO_2, as indicated by the H and HO_2 species distribution and formation rate in Fig. 24. In particular, the amount of H radical close to the jet exit is higher for the 3 % case than the other two cases and the regions showing a peak of HO_2 formation rate overlap with the location of high nC_7H_{15} concentration. HO_2 is produced from H via the reaction H + O_2 + N_2 $\leftrightharpoons$ HO_2

+ N_2. Moreover, the backward reaction of OH + HO_2 $\leftrightharpoons$ O_2 + H_2O further contributes to the production of HO_2. According to the investigation of non-premixed methane/hydrogen flames by Evans et al. [75], an increase in the availability O_2 in the coflow promotes the backward reaction rate of OH + HO_2 $\leftrightharpoons$ O_2 + H_2O and the forward rate of 2OH (+M) $\leftrightharpoons$ O + H_2O (+M).

The distribution of nC_7H_{15} (left path in Fig. 22) and nC_3H_7 (right path in Fig. 22), close to the burner exit is very similar for all oxygen levels, until z = 60 mm (Figs. 23a and 23b). Above z = 60 mm, the production of nC_7H_{15} and nC_3H_7 are increased with the elevated level of oxygen in the coflow. Similar observations can be made for C_2H_5, which is a product from the secondary fuel pyrolysis (Fig. 23c). When the temperature is low, the endothermic reactions are not suppressed for the lower oxygen level cases, as occurs with simple fuels under MILD condition [3, 41], because of the existence of multi-path pyrolysis processes. Moreover, the production of CO is quite low, especially upstream (see Fig. 23d). The oxidation of CO to CO_2 results in the largest positive heat release. Without the heat release from CO_2 formation, the negative heat release due to pyrolytic processes cannot be compensated, resulting in the observed higher absolute values of the negative heat release region for the lower coflow oxygen levels.

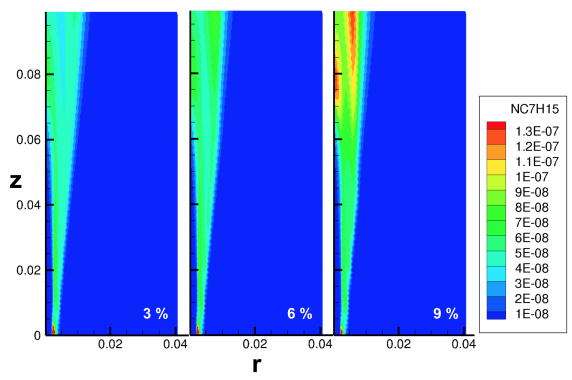

(a) nC_7H_{15} mass fraction

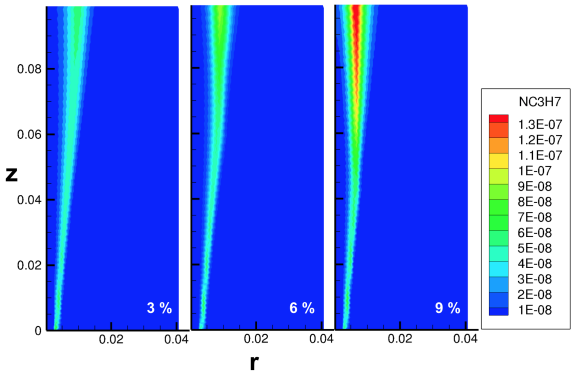

(b) nC_3H_7 mass fraction

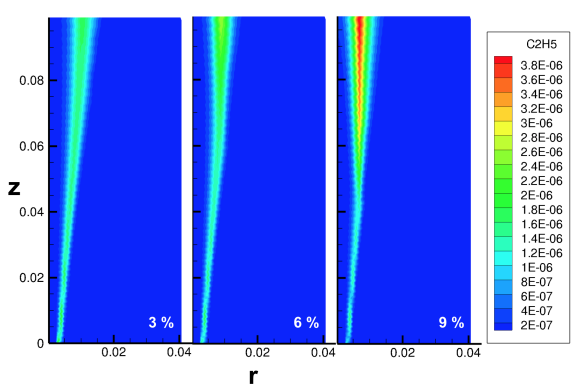

(c) C_2H_5 mass fraction

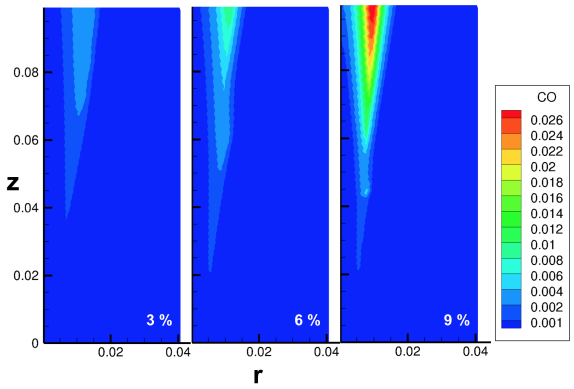

(d) CO mass fraction

Figure 23: Mass fractions of species involved in the *n*-heptane chemical pathways for 3 %, 6 % and 9 % coflow oxygen levels.

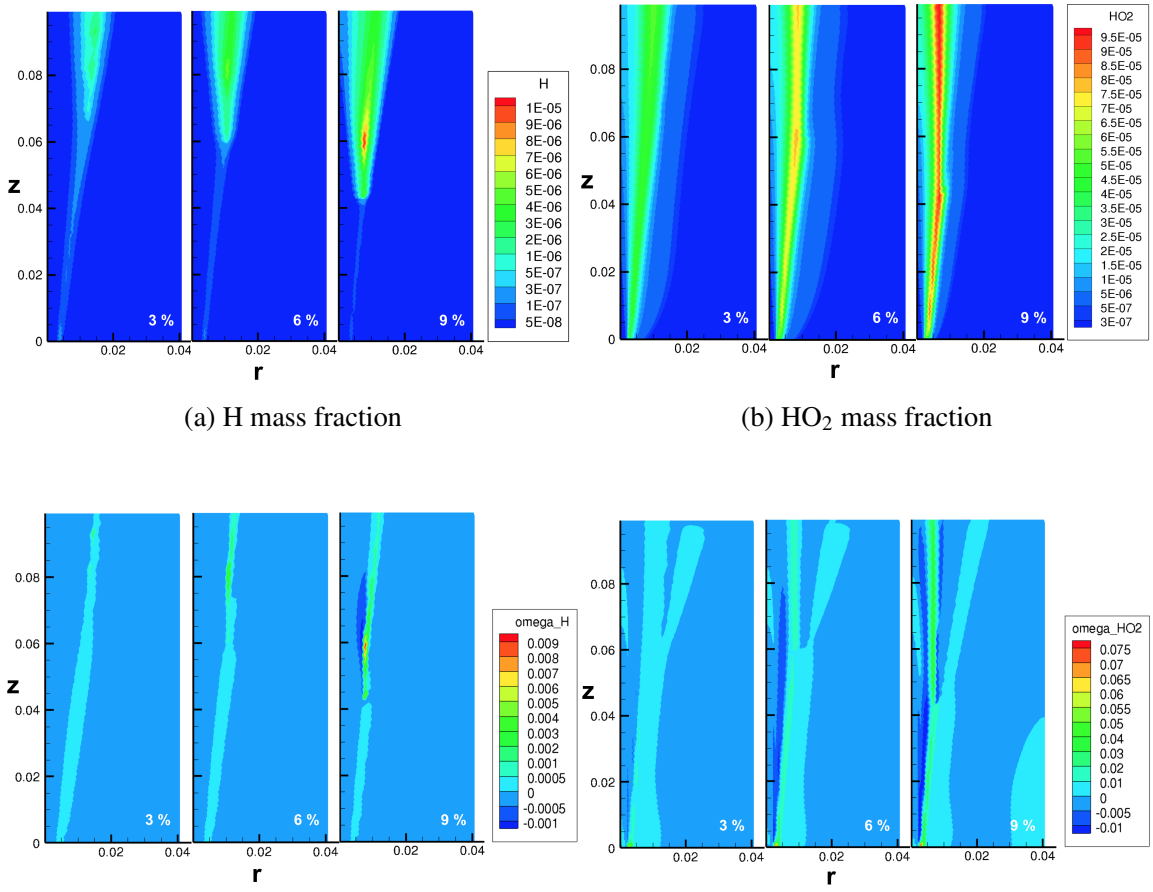

(a) H mass fraction

(b) HO_2 mass fraction

(c) H formation rate

(d) HO_2 formation rate

Figure 24: Mass fractions and formation rates of H and HO_2 for 3 %, 6 % and 9 % coflow oxygen levels.

5. Conclusions

Unsteady RANS simulations were carried out to investigate the characteristics of the *n*-heptane turbulent flames in a jet-in-hot-coflow (JHC) burner. The PaSR combustion model was used with detailed chemistry and a dynamic evaluation of the mixing timescale. The results of these simulations were validated using newly available experimental data from laser-based diagnostics. A detailed CFD analysis was carried out to develop a validated modelling approach and support the interpretation of the experimental findings. The conclusions from this work can be summarized as:

– A turbulent Schmidt number of 1.2 and the use of the Pope correction for the jet spreading rate provide the most satisfactory predictions on mean temperature, OH and CH_2O. The turbulent Schmidt number used in the present work helps decreasing the turbulent

diffusivity of the chemical species, retarding ignition in agreement with the experimental observations.

– The numerically modelled flame weak-to-strong transition height depends on the threshold value used for the OH number density. For threshold values above $5{\times}10^{14}$ molecules/cm^3, a monotonic decreasing trend is observed as a function of the increasing oxygen level in the coflow. However, such observation is not valid when the threshold OH number density value is further reduced to 1×10^{14} molecules/cm^3. In this case, non-monotonic trend between flame weak-to-strong height and the coflow oxygen level is captured. Therefore, changing the threshold of OH number density value can affect the interpretation of the current flame weak-to-strong height trend, and hence it also impacts the classification of the flame.

– A transitional flame structure can be observed for the 3 % O_2 case, based on the distribution of OH number density (threshold set to 1×10^{14} molecules/cm^3), and on the chemical timescale distribution. This is in agreement with the experimental findings.

– Two chemical pathways in *n*-heptane allow an alternative pyrolysis path with lower activation energy in low temperature and low oxygen conditions. This leads to expanded negative heat release region as the coflow oxygen level decreases; and such region is not associated to a specific range of strain rates. Such observation indicates that none of the three coflow oxygen level cases reach fully MILD condition.

It is more difficult to achieve MILD combustion using *n*-heptane than that with the simple fuels like methane and ethylene. Due to the existence of two pyrolysis chemical pathways, the appearance of the transitional structure in *n*-heptane flames happens at lower coflow oxygen level compared to simpler fuels.

6. Acknowledgement

This project has received funding from the European Union′s Horizon 2020 research and innovation program under the Marie Skłodowska-Curie grant agreement No. 643134; the European Research Council, Starting Grant No. 714605; the Australian Research Council (ARC) through the Discovery (DP and DECRA) programme; the United States Air Force Asian Office of Aerospace Research and Development (AOARD) and the China Scholarship Council.

References

[1] J. A. Wünning and J. G. Wünning. Flameless oxidation to reduce thermal NO-formation. *Progress in Energy and Combustion Science*, 23:81–94, 1997.

[2] A. Cavaliere and M. de Joannon. MILD combustion. *Progress in Energy and Combustion Science*, 30:329–366, 2004.

[3] M. de Joannon, G. Sorrentino, and A. Cavaliere. MILD combustion in diffusion-controlled regimes of hot diluted fuel. *Combustion and Flame*, 159:1832–1839, 2012.

[4] Alessandro Parente, Mohammad Rafi Malik, Francesco Contino, Alberto Cuoci, and Bassam B. Dally. Extension of the Eddy Dissipation Concept for turbulence/chemistry interactions to MILD combustion. *Fuel*, 163:98–111, 2015.

[5] E. Oldenhof, Mark J. Tummers, E.H. van Veen, and D.J.E.M. Roekaerts. Ignition kernel formation and lift-off behaviour of Jet-in-Hot-Coflow flames. *Combustion and Flame*, 157:1167–1178, 2010.

[6] B. B. Dally, A. N. Karpetis, and R. S. Barlow. Structure of turbulent non-premixed jet flames in a diluted hot coflow. *Proceedings of the Combustion Institute*, 29:1147–1154, 2002.

[7] P.A.M. Kalt and B.B. Dally. The effect of jet preheating on turbulence in a premixed jet in hot coflow. *Proceedings of the Australian Combustion Symposium*, 2013.

[8] Jingjing Ye, Paul R. Medwell, Michael J. Evans, and Bassam B. Dally. Characteristics of turbulent n-heptane jet flames in a hot and diluted coflow. *Combustion and Flame*, 183:330–342, 2017.

[9] Paul R. Medwell and Bassam B. Dally. Effect of fuel composition on jet flames in a heated and diluted oxidant stream. *Combustion and Flame*, 159:3138–3145, 2012.

[10] Michael John Evans, Paul Ross Medwell, and Zhao Feng Tian. Modelling lifted jet flames in a heated coflow using an optimised Eddy Dissipation Concept model. *Combustion Science and Technology*, 187(7):1093–1109, 2015.

[11] E. Oldenhof, Mark J. Tummers, E. H. van Veen, and D. J. E. M. Roekaerts. Role of entrainment in the stabilisation region of Jet-in-Hot-Coflow flames. *Combustion and Flame*, 158(8):1553–1563, 2011.

[12] Ashoke De, Ernst Oldenhof, Pratap Sathiah, and Dirk Roekaerts. Numerical simulation of Delft-Jet-in-Hot-Coflow (DJHC) flames using the Eddy Dissipation Concept model for turbulence chemistry interaction. *Flow Turbulence Combustion*, 87:537–567, 2011.

[13] Matthias Ihme and Yee Chee See. Prediction of autoignition in a lifted methane/air flame using an unsteady flamelet/progress variable mode. *Combustion and Flame*, 157:1850–1862, 2010.

[14] Zhiyi Li, Alberto Cuoci, Amsini Sadiki, and Alessandro Parente. Comprehensive numerical study of the Adelaide Jet in Hot-Coflow burner by means of RANS and detailed chemistry. *Energy*, 139:555–570, 2017.

[15] Paul R. Medwell, Peter A.M. Kalt, and Bassam B. Dally. Imaging of diluted turbulent ethylene flames stabilized on a Jet in Hot Coflow (JHC) burner. *Combustion and Flame*, 152:100–113, 2007.

[16] Jingjing Ye, Paul Medwell nd Michael J. Evans, and Bassam B. Dally. The impact of carrier gas on ethanol flame behaviour in a Jet in Hot Coflow (JHC) burner. In *The Australian Combustion Symposium 2015*, 2015.

[17] Jingjing Ye, Paul R. Medwell, Bassam B. Dally, and Michael J. Evans. The transition of ethanol flames from conventional to MILD combustion. *Combustion and Flame*, 171:173–184, 2016.

[18] Eric M. Walters. Stability and liftoff of non-premixed large hydrocarbon flames in mild conditions. Master's thesis, Oregon State University, 2017.

[19] Jingjing Ye, Paul R. Medwell, Konstantin Kleinheinz, Michael J. Evans, Bassam B. Dally, and Heinz G. Pitsch. Structural differences of ethanol and dme jet flames in a hot diluted coflow. *Combustion and Flame*, 192:473 – 494, 2018.

[20] Stephan Kruse, Jingjing Ye, Zhiwei Sun, Antonio Attili, Bassam Dally, Paul Medwell, and Heinz Pitsch. Experimental investigation of soot evolution in a turbulent non-premixed prevaporized toluene flame. *Proceedings of the Combustion Institute*, 37:849–857, 2018.

[21] Michael J. Evans, Paul R. Medwell, Zhiwei Sun, Alfonso Chinnici, Jingjing Ye, Qing N. Chan, and Bassam B. Dally. Downstream evolution of n-heptane/toluene flames in hot and vitiated coflows. *Combustion and Flame*, 202:78 – 89, 2019.

[22] Paul R. Medwell and Bassam B. Dally. Effect of fuel composition on jet flames in a heated and diluted oxidant stream. *Combustion and Flame*, 159(10):3138–3145, 2012.

[23] Jingjing Ye, Paul R. Medwell, Emilien Varea, Stephan Kruse, Bassam B. Dally, and Heinz G. Pitsch. An experimental study on mild combustion of prevaporised liquid fuels. *Applied Energy*, 151:93–101, 2015.

[24] Roman Weber, John P. Smart, and Willem vd Kamp. On the (MILD) combustion of gaseous, liquid, and solid fuels in high temperature preheated air. *Proceedings of the Combustion Institute*, 30(2):2623–2629, 2005.

[25] V. Mahendra Reddy, Pratim Biswas, Prateek Garg, and Sudarshan Kumar. Combustion characteristics of biodiesel fuel in high recirculation conditions. *Fuel Processing Technology*, 118:310 –317, 2014.

[26] F. C. Christo and B. B. Dally. Modelling turbulent reacting jets issuing into a hot and diluted coflow. *Combustion and Flame*, 142:117–129, 2005.

[27] Robert L. Gordon, Assaad R. Masri, Stephen B. Pope, and Graham M. Goldin. Transport budgets in turbulent lifted flames of methane autoigniting in a vitiated co-flow. *Combustion and Flame*, 151(3):495–511, 2007.

[28] Alessio Frassoldati, Pratyush Sharma, Alberto Cuoci, Tiziano Faravelli, and Eliseo Ranzi. Kinetic and fluid dynamics modeling of methane/hydrogen jet flames in diluted coflow. *Applied Thermal Engineering*, 30:376–383, 2009.

[29] Amir Mardani, Sadegh Tabejamaat, and Mohsen Ghamari. Numerical study of influence of molecular diffusion in the MILD combustion regime. *Combustion Theory and Modelling*, 14(5):747–774, 2010.

[30] Seyed Reza Shabanian, Paul Ross Medwell, Masoud Rahimi, Alessio Frassoldati, and Alberto Cuoci. Kinetic and fluid dynamic modeling of ethylene jet flames in diluted and heated oxidant stream combustion conditions. *Applied Thermal Engineering*, 52:538–554, 2012.

[31] Javad Aminian, Chiara Galletti, and Leonardo Tognotti. Extended EDC local extinction model accounting finite-rate chemistry for MILD combustion. *Fuel*, 165:123–133, 2016.

[32] Amir Mardani. Optimization of the Eddy Dissipation Concept (EDC) model for turbulence-chemistry interactions under hot diluted combustion of ch4/h2. *Fuel*, 191:114–129, 2017.

[33] M.J. Evans, A. Chinnici, P.R. Medwell, and J. Ye. Ignition features of methane and ethylene fuel-blends in hot and diluted coflows. *Fuel*, 203:279–289, 2017.

[34] Z. Chen, V.M. Reddy, S. Ruan, N.A.K. Doan, W.L. Roberts, and N. Swaminathan. Simulation of MILD combustion using perfectly stirred reactor model. *Proceedings of the Combustion Institute*, 36(3):4279 –4286, 2017.

[35] Zhiyi Li, Marco Ferrarotti, Alberto Cuoci, and Alessandro Parente. Finite-rate chemistry modelling of non-conventional combustion regimes using a partially-stirred reactor closure: Combustion model formulation and implementation details. *Applied Energy*, 225:637–655, 2018.

[36] M. Ihme and Y. C. See. LES flamelet modeling of a three-stream MILD combustor: Analysis of flame sensitivity to scalar inflow conditions. *Proceeding of the Combustion Institute*, 33(1):1309–1317, 2011.

[37] Matthias Ihme, Jian Zhang, Guowei He, and Bassam Dally. Large Eddy Simulation of a Jet-in-Hot-Coflow burner operating in the oxygen-diluted combustion regime. *Flow, Turbulence and Combustion*, 89:449–464, 2012.

[38] P. Domingo, L. Vervisch, and D. Veynante. Large-eddy simulation of a lifted methane jet flame in a vitiated coflow. *Combustion and Flame*, 152(3):415–432, 2008.

[39] Zhiyi Li, Alberto Cuoci, and Alessandro Parente. Large eddy simulation of mild combustion using finite rate chemistry: Effect of combustion sub-grid closure. *Proceedings of the Combustion Institute*, 37:4519–4529, 2018.

[40] Chun Sang Yoo, Edward S. Richardson, Ramanan Sankaran, and Jacqueline H. Chen. A dns study on the stabilization mechanism of a turbulent lifted ethylene jet flame in highly-heated coflow. *Proceedings of the Combustion Institute*, 33(1):1619–1627, 2011.

[41] M. de Joannon, P. Sabia, G. Sorrentino, and A. Cavaliere. Numerical study of mild combustion in hot diluted diffusion ignition (HDDI) regime. *Proceedings of the Combustion Institute*, 32(2):3147–3154, 2009.

[42] Manabendra Saha, Bassam B. Dally, Paul R. Medwell, and Emmet M. Cleary. Moderate or Intense Low oxygen Dilution (MILD) combustion characteristics of pulverized coal in a self-recuperative furnace. *Energy & Fuels*, 28(9):6046–6057, 2014.

[43] Jingjing Ye, Paul R. Medwell, Emilien Varea, Stephan Kruse, Bassam B. Dally, and Heinz G. Pitsch. An experimental study on MILD combustion of prevaporised liquid fuels. *Applied Energy*, 151:93–101, 2015.

[44] Y. Minamoto and N. Swaminathan. Subgrid scale modelling for MILD combustio. *Proceedings of the Combustion Institute*, 35(3):3529–3536, 2015.

[45] Bjørn F. Magnussen. On the structure of turbulence and a generalized Eddy Dissipation Concept for chemical reaction in turbulent flow. In *19th AIAA Aerospace Science Meeting*, St. Louis, Missouri, USA, January 1981.

[46] I.R. Gran and B. F. Magnussen. A numerical study of a bluff-body stabilized diffusion flame, part 2: Influence of combustion modelling and finite-rate chemistry. *Combustion Science and Technology*, 119(1-6):191–217, 1996.

[47] Bj/orn F. Magnussen. The Eddy Dissipation Concept a bridge between science and technology. In *ECCOMAS Thematic Conference on Computational Combustion*, Lisbon, Portugal, 2005.

[48] J. Chomiak. *Combustion: A Study in Theory, Fact and Application*. Abacus Press/Gorden and Breach Science Publishers, 1990.

[49] Norbert Peters. *Turbulent Combustion*. Cambridge University Press, 2000.

[50] B.F. Magnussen and B.H. Hjertager. On mathematical modeling of turbulent combustion with special emphasis on soot formation and combustion. *Symposium (International) on Combustion*, 16(1):719 – 729, 1977.

[51] Marco Ferrarotti, Zhiyi Li, and Alessandro Parente. On the role of mixing models in the simulation of MILD combustion using finite-rate chemistry combustion models. *Proceeding of the Combustion Institute*, 000:1–8, 2018.

[52] Zhiyi Li, Marco Ferrarotti, Alberto Cuoci, and Alessandro Parente. Finite-rate chemistry modelling of non-conventional combustion regimes using a partially-stirred reactor closure: Combustion model formulation and implementation details. *Applied Energy*, 225:637–655, 2018.

[53] Dmitry A. Lysenko, Ivar S. Ertesvåg, and Kjell Erik Rian. Numerical simulation of non-premixed turbulent combustion using the Eddy Dissipation Concept and comparing with the steady laminar flamelet model. *Flow, Turbulence and Combustion*, 53:577–605, 2014.

[54] S. B. Pope. An explanation of the turbulent round-jet/plane-jet anomaly. Technical report, Imperial College London, 1978.

[55] V. Golovitchev and J. Chomiak. Numerical modeling of high temperature air flameless combustion. In *The 4th international symposium on high temperature air combustion and gasification*, 2001.

[56] Fabian Peng Kärrholm. *Numerical Modelling of Diesel Spray Injection, Turbulence Interaction and Combustion*. Phd thesis, Chalmers University of Technology, Chalmers, Sweden, 2008.

[57] Venkatramanan Raman and Heinz Pitsch. A consistent LES/filtered-density function formulation for the simulation of turbulent flames with detailed chemistry. *Proceedings of the Combustion Institute*, 31(2):1711– 1719, 2007.

[58] I.K. Ye. *Investigation of the scalar variance and scalar dissipation rate in URANS and LES*. Phd thesis, University of Waterloo, Ontario, Canada, Waterloo, Ontario, Canada, 2011.

[59] J. P. H. Sanders and I. Gökalp. Scalar dissipation rate modelling in variable density turbulent axisymmetric jets and diffusion flames. *Physics of Fluids*, 10(4):938–948, 1998.

[60] Benjamin J. Isaac, Alessandro Parente, Chiara Galletti, Jeremy N. Thornock, Philip J. Smith, and Leonardo Tognotti. A novel methodology for chemical time scale evaluation with detailed chemical reaction kinetic. *Energy Fuels*, 27(4):2255–2265, 2013.

[61] R. O. Fox. *Computational Models for Turbulent Reacting Flows*. Cambridge University Press, Cambridge, UK, 2003.

[62] J. Chomiak and A. Karlsson. Flame liftoff in diesel sprays. In *Twenty-Sixth Symposium (International) on Combustion*, pages 2557–2564. The Combustion Institute, 1996.

[63] Riccardo Longo, Magnus Fürst, Aurélie Bellemans, Marco Ferrarotti, Marco Derudi, and Alessandro Parente. CFD dispersion study based on a variable schmidt formulation

for flows around different configurations of ground-mounted buildings. *Building and Environment*, 2019.

[64] Yoshihide Tominaga and Ted Stathopoulos. Turbulent schmidt numbers for CFD analysis with various types of flowfield. *Atmospheric Environment*, 41:8091–8099, 2007.

[65] E. Ranzi, A. Frassoldati, A. Stagni, M. Pelucchi, A. Cuoci, and T. Faravelli. Reduced kinetic schemes of complex reaction systems: Fossil and biomass-derived transportation fuels. *International Journal of Chemical Kinetics*, 46(9):512–542, 2014.

[66] A. Stagni, A. Cuoci, A. Frassoldati, T. Faravelli, and E. Ranzi. Lumping and reduction of detailed kinetic schemes: An effective coupling. *Industrial and Engineering Chemistry Research*, 53(22):9004–9016, 2014.

[67] A. Stagni, A. Frassoldati, A. Cuoci, T. Faravelli, and E. Ranzi. Skeletal mechanism reduction through species-targeted sensitivity analysis. *Combustion and Flame*, 163:382–393, 2016.

[68] Marco Mehl, William J. Pitz, Charles K. Westbrook, and Henry J. Curran. Kinetic modeling of gasoline surrogate components and mixtures under engine conditions. *Proceedings of the Combustion Institute*, 33(1):193 – 200, 2011.

[69] H.J. Curran, P. Gaffuri, W.J. Pitz, and C.K. Westbrook. A comprehensive modeling study of n-heptane oxidation. *Combustion and Flame*, 114(1):149 – 177, 1998.

[70] Robert L. Gordon, Assaad R. Masri, and Epaminondas Mastorakos. Simultaneous rayleigh temperature, OH- and CH2O-LIF imaging of methane jets in a vitiated coflow. *Combustion and Flame*, 155:181–195, 2008.

[71] M.J. Evans, P.R. Medwell, H. Wu, A. Stagni, and M. Ihme. Classification and lift-off height prediction of non-premixed MILD and autoignitive flames. *Proceedings of the Combustion Institute*, 36(3):4297 – 4304, 2017.

[72] M.J. Evans, C. Petre, P.R. Medwell, and A. Parente. Generalisation of the eddy-dissipation concept for jet flames with low turbulence and low Damöhler number. *Proceedings of the Combustion Institute*, 37(4):4497 – 4505, 2019.

[73] M. de Joannon, P. Sabia, and A. Cavaliere. Alternative ignition systems. Technical Report 133-150, Verlag ProcessEng Engineering GmbH.

[74] Lars Seidel, Kai Moshammer, Xiaoxiao Wang, Thomas Zeuch, Katharina Kohse-Hinghaus, and Fabian Mauss. Comprehensive kinetic modeling and experimental study of a fuel-rich, premixed n-heptane flame. *Combustion and Flame*, 162(5):2045–2058, 2015.

[75] Michael J. Evans, Paul R. Medwell, Zhao F. Tian, Jingjing Ye, Alessio Frassoldati, and Alberto Cuoci. Effects of oxidant stream composition on non-premixed laminar flames with heated and diluted coflows. *Combustion and Flame*, 178:297–310, 2017.

5.5 Journal paper 5

This paper was published in the Proceedings of the Combustion Institute:

Zhiyi Li, Alberto Cuoci and Alessandro Parente, Large Eddy Simulation of MILD combustion using finite rate chemistry: effect of combustion sub-grid closure, Proceedings of the Combustion Institute 37(4), 4519-4529 (2019).

Large Eddy Simulation of MILD combustion using finite rate chemistry: effect of combustion sub-grid closure

Zhiyi Li[a,*], Alberto Cuoci[b], Alessandro Parente[a,**]

[a]*Aero-Thermo-Mechanics Department, Université Libre de Bruxelles, Avenue Franklin Roosevelt 50, 1050 Brussels, Belgium*
[b]*Department of Chemistry, Materials, and Chemical Engineering, Politecnico di Milano, P.zza Leonardo da Vinci, 20133 Milano, Italy*

Abstract

In this work, we present a detailed comparison between the conventional Partially Stirred Reactor (PaSR) combustion model and two implicit combustion models named Quasi Laminar Finite Rate (QLFR) model and Laminar Finite Rate (LFR) model, respectively. Large Eddy Simulation (LES) is employed and the Adelaide Jet in Hot Co-flow (AJHC) burner is chosen as validation case. In the implicit combustion models, the filtered source term comes directly from the chemical term, without inclusion of the turbulent effect. Results have demonstrated that the two implicit models have very similar behaviour compared with the conventional PaSR model concerning the mean and root-mean-square of the temperature and species mass fraction fields and they all give satisfactory predictions, especially the mean values. This justifies the usage of implicit combustion models in low Damköhler number (Da $\leqslant$ 1.0) systems. The QLFR model is able to save ~3 times computational time compared with the LFR model. Moreover, the comparison between two 4-step global mechanisms and a reduced 17 species 58 reactions skeletal mechanism proves the importance of using finite rate chemistry approach in MILD combustion regime.

Keywords:
MILD combustion, Partially Stirred Reactor, Implicit sub-grid models, Adelaide JHC burner, Detailed chemistry

1. Introduction

Moderate or Intense Low oxygen Dilution (MILD) combustion has the advantages of uniformly distributed temperature field, reduced NO_x and soot formation, as well as higher fuel

*Corresponding author: Zhiyi.Li@ulb.ac.be
**Corresponding author: Alessandro.Parente@ulb.ac.be

flexibility compared to the conventional combustion technologies [1, 2]. In MILD combustion, reaction can occur over a wide range of turbulent scales instead of the smallest scale in conventional combustion [3]. The system evolves towards a distributed reaction regime and low temperatures, because of the high dilution level and the intense mixing between fuel and hot-diluted oxidiser. This leads to higher chemical and lower mixing time scales, thus to characteristic Damköhler number of order ∼1 [1, 2]. As a result, combustion progress in such systems cannot be described using models based on the principle of time scale separation [4], and models accounting for finite rate chemistry should be considered. In the present paper, the Partially Stirred Reactor (PaSR) model [5] is considered. In PaSR, the influence of the sub-grid fluctuations on the reaction rate is expressed with a factor κ, defined as the ratio between the characteristic chemical time scale and the sum of the chemical and mixing time scales. Recently, it was shown that κ approaches 1 in MILD combustion, suggesting that reacting structures can be fully resolved on the Large Eddy Simulation (LES) grid using a laminar finite rate model [6].

Successful predictions of MILD systems are reported in the literature. Many contributions refer to lifted jet flames in vitiated co-flow [7], for which several investigations have been carried out using Reynolds Averaged Navier-Stokes (RANS) simulation. In the context of RANS simulation, different authors particularly focused on the over-prediction of temperature obtained using standard EDC constants. Adjusted EDC constants [8, 9] based on a fitting procedure were used to alleviate the over-predicted temperature. Parente et al. [10] proposed a dynamic expression of the EDC constants based on local values of turbulent Reynolds number Re_T and Damköhler number, proving the importance of considering chemical time scale in MILD combustion. However, despite high computational efficiency of RANS simulation, steady-state assumptions are not able to capture non-equilibrium phenomena, such as local extinction and re-ignition. To this end, Large Eddy Simulation (LES) can provide superior results with respect to RANS. Ihme et al. [11, 12] carried out LES on the Adelaide Jet in Hot Co-flow (AJHC) burner using a three-stream Flamelet Progress Variable (FPV) formulation. Good agreement with the experimental measurements was observed for the mean temperature and specie mass fraction profiles. Afarin et al. [13] used PaSR to investigate the reaction zone structure as well as the distribution of temperature and minor species mass fractions, showing acceptable accuracy.

The present paper focuses on the applicability of different implicit combustion model formulations under the framework of MILD combustion. The work focuses, in particular, on MILD combustion, where finite-rate chemistry effects are more relevant. The PaSR model is benchmarked against two implicit formulations, the Laminar Finite Rate (LFR) and the Quasi-Laminar Finite Rate (QLFR) formulations. In the LFR model, the mean source term is

directly retrieved from the Arrhenius expression, while in the QLFR model, a time-splitting approach is used, solving an Ordinary Differential Equation (ODE) to describe the evolution of species mass fractions within the LES residence time. The AJHC burner [7] is chosen as the test case, as it provides high-fidelity measurements of mean and root-mean-square (rms) temperature, mixture fraction, and species mass fraction for a MILD combustion prototype system. All simulations are carried out using OpenFOAM, where the different models (PaSR, QLFR and LFR) are implemented [10, 14]. Finite rate chemistry and multi-component molecular species diffusion are included in the calculation. The assessment of the model performances is based on both the mean and variance of the temperature and species mass fraction profiles.

2. Numerical Models

2.1. Turbulent Model

The one Equation Eddy Viscosity (`oneEqnEddy`) is chosen as the sub-grid turbulent model [15]. In LES, the Favre-filtered governing equations of continuity, momentum, energy and species are solved. The sub-grid stress tensor for the Favre-filtered momentum field, expressed as

$$\overline{\tau_{ij}} = \rho\widetilde{u_i u_j} - \rho\tilde{u}_i\tilde{u}_j, \tag{1}$$

requires a turbulence model. In `oneEqnEddy` model, $\overline{\tau_{ij}}$ is estimated by an subgrid-scale eddy viscosity ν_{sgs} and a resolved scale strain rate $\overline{S}_{ij}$:

$$\overline{\tau_{ij}} \approx -2\nu_{sgs}\overline{S}_{ij}. \tag{2}$$

The sub-grid scale viscosity is computed as:

$$\nu_{sgs} = C_k\sqrt{k_{sgs}}\Delta, \tag{3}$$

where $C_k = 0.094$, Δ is the grid size and k_{sgs} is the sub-grid scale kinetic energy which is solved through a dedicated transport equation [16].

2.2. Combustion Model

Two implicit models are compared with the conventional PaSR model. Their main features and differences are presented in Table 1.

Table 1: Characteristics of different combustion models (scaled CPU time based on KEE58 mechanism)

Combustion model	PaSR	QLFR	LFR
Turbulent effect	Explicit	Implicit	Implicit
ODE integration	Yes	Yes	No
Detailed chemistry	Yes	Yes	Yes
Scaled CPU time	1	0.86	2.66

2.2.1. Partially Stirred Reactor model

The Partially Stirred Reactor (PaSR) [5] separates each computational cell into two zones. Reaction happens only in a fraction of the cell, identified by the reacting fraction κ [17]. Thus, the mean source term can be expressed as:

$$\overline{\dot{\omega}}_k = \kappa \dot{\omega}_k^*(\widetilde{\boldsymbol{Y}}, \widetilde{T}). \tag{4}$$

In Equation 4, $\dot{\omega}_k^*(\widetilde{\boldsymbol{Y}}, \widetilde{T})$ represents the formation rate of species k based on the Favre-averaged mass fractions of species in the cell. The term κ is a coefficient which considers the non-perfect mixing, calculated as:

$$\kappa = \frac{\tau_c}{\tau_c + \tau_{mix}}, \tag{5}$$

where τ_c is the characteristic chemical time scale in each cell and τ_{mix} is the mixing time scale. In the present study, the chemical time scale of each species is estimated by $\tau_{c,k} = Y_k^*/(dY_k^*/dt)$, where Y_k^* and dY_k^*/dt are mass fraction of the k_{th} species and the corresponding formation rate in the reacting zone, respectively. The highest limiting value is chosen as the characteristic chemical time scale, considering only active species (the species characterized by an absolute rate of change (dY_k^*/dt) higher than a given threshold). The mixing time scale is represented with the geometrical mean of the sub-grid velocity stretch time ($\Delta/v^{'}$) and the Kolmogorov time scale ($(\nu/\epsilon_{sgs})^{1/2}$) [18].

2.2.2. Quasi Laminar Finite Rate model

Based on the PaSR model, the QLFR model is formulated merely by forcing $\kappa = 1.0$ [19], under the hypothesis that the mixing time scale is much smaller than the chemical time scale. Therefore, the turbulent eddies are assumed to be able to penetrate into the flame structures and the whole cell is like a Perfectly Stirred Reactor (PSR) [6]. In this time-splitting approach, the reactive zone is modelled as a reactor:

$$\frac{dY_k}{dt} = \frac{\dot{\omega}_k}{\rho}. \tag{6}$$

The term $\dot{\omega}_k$ is the instantaneous formation rate of species k. The final integration of $\frac{dY_k}{dt}$ over the residence time τ in the reactor is Y_k^* introduced in Section 2.2.1. The term $\dot{\omega}_k^*(\widetilde{\boldsymbol{Y}}, \widetilde{T})$ in Equation 4 is thus estimated with:

$$\dot{\omega}_k^*(\widetilde{\boldsymbol{Y}}, \widetilde{T}) = (Y_k^* - \widetilde{Y}_k)/\tau. \tag{7}$$

In the present work, τ equals to CFD time step. As far as the CPU requirements are concerned, the QLFR model allows saving additional time compared to PaSR model, as it does not need any chemical time scale estimation for the evaluation of κ.

2.2.3. Laminar Finite Rate model

The Laminar Finite Rate model does not directly account for the effect of turbulence in the mean source term, and the mean formation rates are determined by Arrhenius expressions [20]:

$$\overline{\dot{\omega}}_k = M_k \sum_{r=1}^{N_r} \hat{R_{k,r}}. \tag{8}$$

In Equation 8, M_k is the molecular weight of species k and $\hat{R_{k,r}}$ is the Arrhenius rate of creation/destruction of species k in reaction r. The LFR model is generally used for laminar reacting flows [21] or in the context of Direct Numerical Simulation (DNS). In LES applications, the LFR model is valid when the grid size is sufficiently small and the flame structure is thick enough (low Damköhler number system). It is worth mentioning that the direct coupling of source terms without a time splitting scheme imposes to use smaller time steps with respect to the one required from the PaSR and QLFR models, to ensure simulation stability.

3. Validation Case

The Adelaide Jet in Hot Co-flow (AJHC) burner [7] emulates the MILD combustion with a simple geometry. It is thus suitable for the LES analysis.

3.1. Experimental Basis

The AJHC burner has a central jet with the inner diameter of 4.25 mm and an annulus pipe providing the hot co-flow with the inner diameter of 82 mm. The burner is mounted in the wind tunnel (air is used as tunnel gas) with the cross section of 254 mm × 254 mm. The central jet provides an equi-molar mixture of CH_4 and H_2. A secondary burner is mounted upstream of the annulus pipe exit plane, providing the hot combustion products which mix with air and nitrogen. The oxygen level is controlled to 3%, 6% and 9% by adjusting the amount of air and nitrogen.

Table 2: Boundary conditions for the AJHC burner

Profiles	Central jet	Annulus	Tunnel
Velocity	58.74 m/s	3.2 m/s	3.3 m/s
Temperature	294 K	1300 K	294 K

The gas temperature and velocity profiles of the central jet, annulus and wind tunnel are presented in Table 2. In this paper, the condition corresponding to a Reynolds number of 10,000 and and co-flow oxygen content of 3% is studied. The mean and rms profiles of temperature, mixture fraction and mass fractions of species (CH_4, H_2, H_2O, CO_2, N_2, O_2, NO, CO, and OH) along the centerline as well as on the axial positions of 4/30/60/120/200 mm are available for model validation. The mean experimental measurements data shown in the validation work include the 99.99% confidence intervals as well.

3.2. Numerical Set-up

The simulation domain starts from the jet exit and extends 180 mm further downstream. The radial direction expands 90 mm away from the centerline. The whole domain is discretized with a 3D cylinder structured mesh containing ~1.5 million cells. The energy resolved in the grid reaches at least 80% and more than 90% at several locations of interest, indicating a sufficient small grid size.

The LEMOS [22] inflow generation method for velocity field is applied on all the three streams. The `WaveTransmissive` [23] boundary condition is used for pressure outlet. Experimentally measured profiles (H_2O, CO_2 O_2 species mass fractions and temperature) are directly used as inflow data for the simulation. The Chapman-Enskog formulation is employed for multi-component diffusion. Three different chemical mechanisms, the 4-step global mechanism from Jones and Lindstedt (JL) [24], the modified JL mechanism from Wang et al. [25], as well as a reduced skeletal mechanism KEE58 [26] are considered. The sampling locations are the centerline and 30/60/120 mm axial locations. Both mean and variance profiles are sampled. The mean value is obtained from the time averaged instantaneous profiles. A 2D axi-symmetric sketch of the simulation domain and the sampling positions are shown in Figure 1.

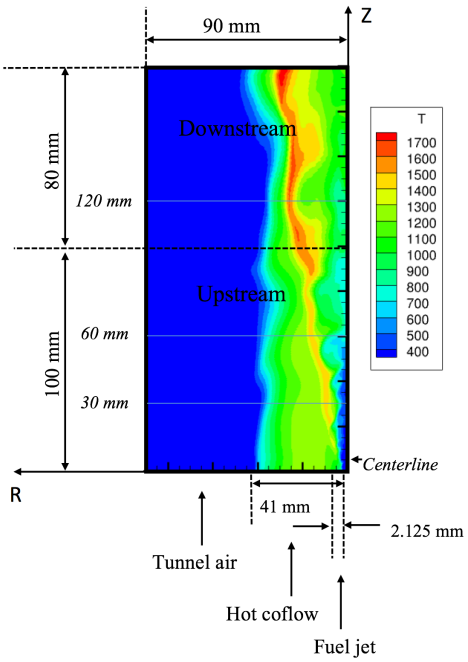

Figure 1: 2D axi-symmetric sketch of the AJHC burner with the instantaneous temperature profile and sampling locations.

4. Results and Discussion

In Section 4.1, the simulation results from the two implicit combustion models are compared with the PaSR model and the experimental data. The comparison between a global and a skeletal chemistry is discussed in Section 4.2, demonstrating the importance of finite rate chemistry in MILD combustion.

4.1. Conventional and implicit combustion models

Firstly, the mixture fraction profiles provided by the three models are compared in Figure 2, using Bilger's definition [26], to assess the ability of the different approaches to describe the mixing process. The mean mixture fractions (f_{mean}) provided by the different models are almost identical. One can conclude that the mixing field is well predicted, even though slight under-prediction is observed close to jet exit position for $z \leqslant 45$ mm.

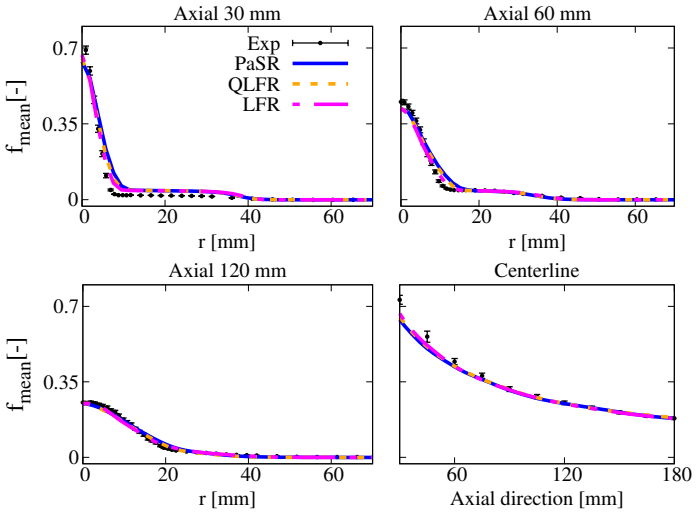

Figure 2: Mean mixture fraction (f_{mean}) profile provided by the conventional PaSR model, PaSR based QLFR model and LFR model at several sampling locations compared to the experimental measurements. Kinetic mechanism: KEE58.

In order to assess the possibility of using implicit combustion models, the averaged values of κ and Damköhler number obtained with the PaSR model are presented. In Figure 3, the averaged κ values are shown with mean temperature profile in background. It can be observed that, in the areas where combustion takes place (from z = 30 mm onward), κ values are in the range from 0.9 to 1.0, indicating that most of the cell is occupied by reacting structures. In Figure 4, the radial profiles of κ and Damköhler number are plotted at selected axial locations (30/120 mm). It can be observed that κ is always larger than 0.9 and Damköhler number is always smaller than 0.15 at both locations.

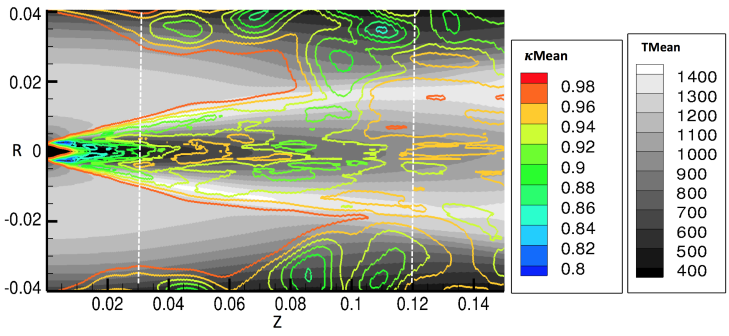

Figure 3: mean κ field (mean temperature in background, axis unit: m).

The mean temperature profiles provided by the three combustion models are compared to the experimental data at different sampling locations in Figure 5. The temperature profiles

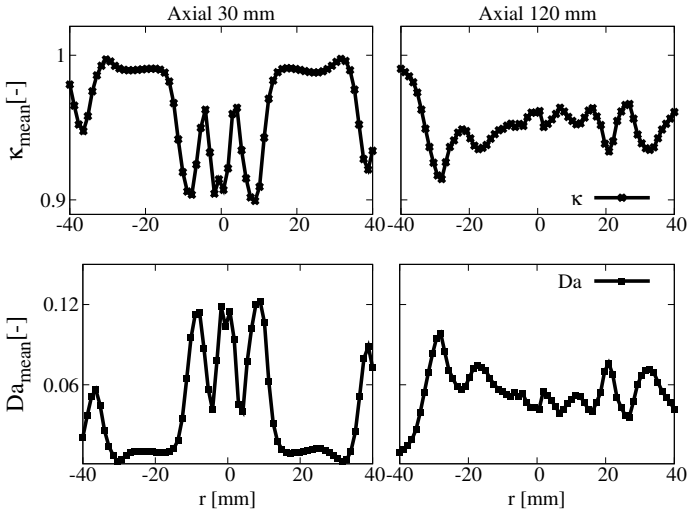

Figure 4: mean κ and mean Damköhler number at 30 mm and 120 mm axial locations

are similar, showing only minor differences between each other and very good predictions of experimental data. At 30 mm axial position (z = 30 mm), the LFR model underpredicts the mean temperature peak by 100 K, and the peak temperature is only slightly higher than the co-flow temperature, suggesting later ignition with respect to the other models. This is confirmed by the analysis of the OH contour plots (see Supplementary Material), showing higher lift-off height for the LFR model. Very satisfactory agreement with the measurement data is observed at 120 mm axial location for all the three models. The QLFR model predicts the peak temperature exactly (1 K difference), while PaSR and LFR models over-predict and under-predict the value by 15 K and 40 K, respectively. Regarding the centerline profile, the later ignition predicted by LFR model corrects the slight over-prediction (around 7%) of mean temperature by the other two models. Interestingly, the results obtained with the PaSR and QLFR models are almost overlapping, indicating that the approximation of $\kappa = 1.0$ is appropriate and thus the assumption of an implicit closure is suitable for the investigated system. The mean profiles obtained are also similar compared to the ones presented in the research work of Ihme et al. [12]. In the present work, more accurate temperature predictions are obtained at the 30 mm and 60 mm axial locations.

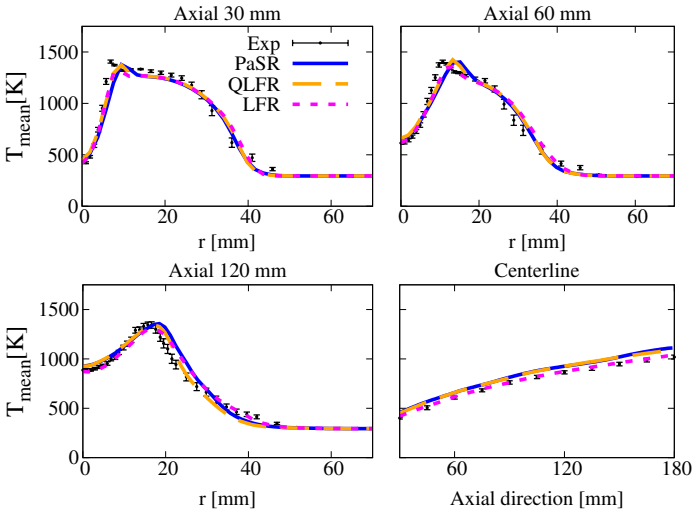

Figure 5: Mean temperature profile provided by the conventional PaSR model, PaSR based QLFR model and LFR model at several sampling locations compared to the experimental measurements. Kinetic mechanism: KEE58.

The rms value of temperature is shown in Figure 6. The first peak at axial 30 mm and 60 mm locations are well predicted by all the three models. Some under-predictions can be observed for the prediction of the second peak, indicating that the interaction between co-flow and air stream is under-estimated by the model. At 120 mm axial location, the PaSR model over-predicts the peak value by 13 % while LFR model under-predicts by 24 %. The QLFR model predicts the peak value better than the previous two models, showing an under-prediction of 8 %.

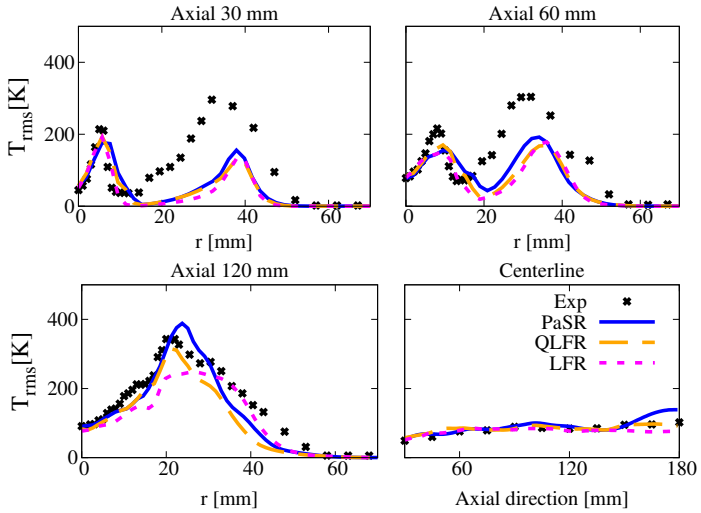

Figure 6: Root-mean-square (rms) temperature profile provided by the conventional PaSR model, PaSR based QLFR model and LFR model at several sampling locations compared to the experimental measurements. Kinetic mechanism: KEE58.

The mean and rms of species mass fraction of the oxidizer and products are shown in Figures 7 - 9 as well. All models show good agreement with the experimental data at 120 mm axial location for the mean O_2 and H_2O profiles (Figure 7). Slight shifting of the peak value is observed at axial 60 mm for the mean H_2O plot when using the PaSR approach. As far as the O_2 and H_2O rms values are concerned (Figure 8), some under-predictions are observed at z = 60 mm, although the qualitative trend is well captured. At z = 120 mm, the QLFR model well captures the H_2O rms peak value, while PaSR and LFR models over-predict and under-predict the experimental peak value by 11 % and 18.5 %, respectively.

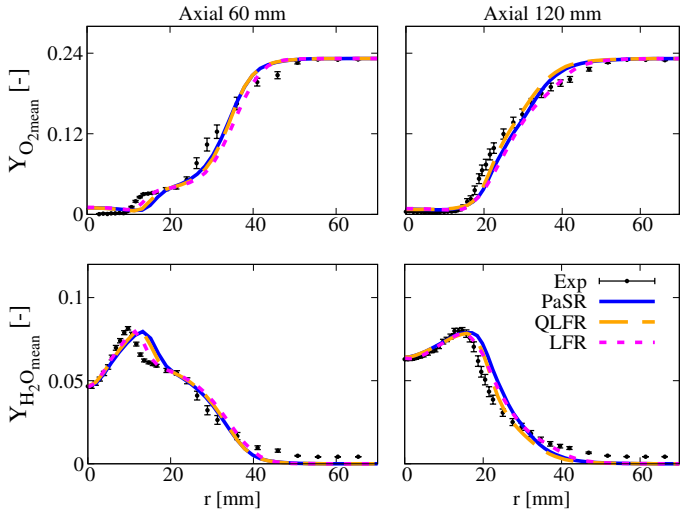

Figure 7: Mean O_2 and H_2O mass fraction profile provided by the conventional PaSR model, PaSR based QLFR model and LFR model at two sampling locations (axial 60/120 mm) compared to the experimental measurements. Kinetic mechanism: KEE58.

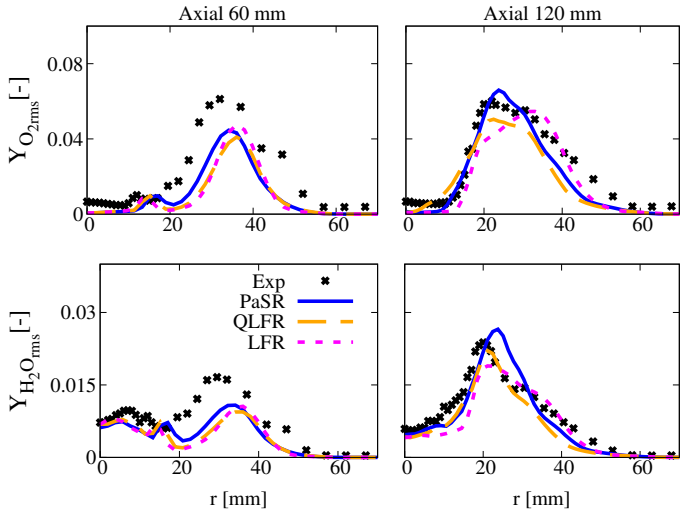

Figure 8: Root-mean-square (rms) O_2 and H_2O mass fraction profile provided by the conventional PaSR model, PaSR based QLFR model and LFR model at two sampling locations (axial 60/120 mm) compared to the experimental measurements. Kinetic mechanism: KEE58.

The CO mass fraction distribution is generally hard to capture in the AJHC system [12], because the hot and diluted conditions modify the CO/CO_2 conversion rates [27]. In Figure 9, both the mean and rms value of CO are presented. The PaSR model estimates well the mean and variance peak value at z = 120 mm and centerline profile, except for variance when

$z \geqslant 150$ mm. The QLFR model provides results very close to PaSR, thus confirming the pertinence of the hypothesis of $\kappa = 1$. The LFR model underestimates the mean CO peak value by 17 % at z = 120 mm as well as the centerline profile. The CO profiles obtained from LFR model confirm that using this approach leads to an under-estimation of the intensity of turbulence/chemistry interactions with respect to the other two models.

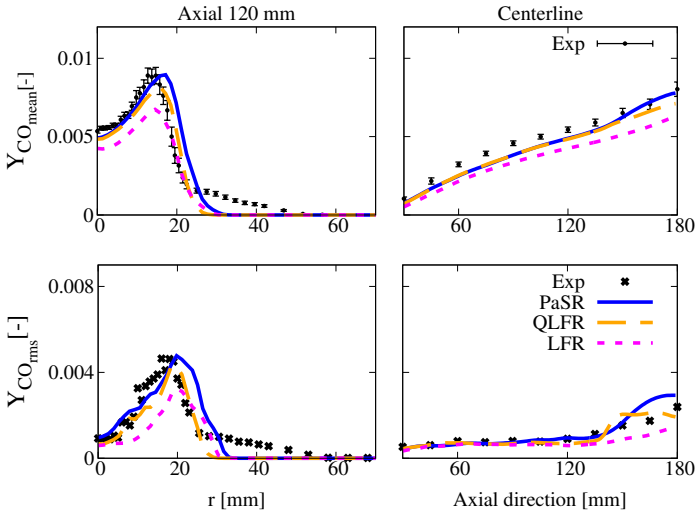

Figure 9: Mean and root-mean-square (rms) CO mass fraction profile provided by the conventional PaSR model, PaSR based QLFR model and LFR model at two sampling locations (centerline and axial 120 mm) compared with the experimental measurements. Kinetic mechanism: KEE58.

4.2. Detailed chemistry approach

To investigate the relevance of the kinetic mechanism on the results, two global 4-step mechanism are benchmarked against the KEE58 mechanism in Figure 10, using the conventional PaSR model. In Figure 10, 4step denotes the original JL mechanism [24], 4step-mod represents the modified JL mechanism from Wang et al. [25] and KEE58 indicates the KEE mechanism [26].

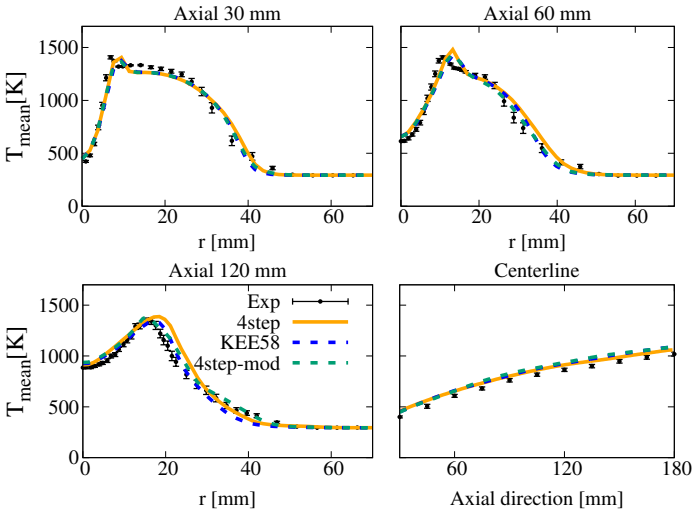

Figure 10: Mean temperature profile provided by the conventional PaSR model using a global chemistry and a skeletal mechanism at several sampling locations compared to the experimental measurements.

The original JL mechanism provides acceptable predictions of the temperature field, although slight over predictions are observed for the mean radial temperature profiles at both z = 60 mm and z = 120 mm, by 45 K and 74 K, respectively. The modified JL mechanism is able to correct the over-prediced temperature peak from the original one, showing results closer to that obtained with the KEE58 mechanism. However, the main advantage associated to the use of more detailed mechanism can be found when looking at the species mass fraction profiles of the products. In Figure 11, the centerline and downstream (120 mm) radial profiles of CO_2 and H_2O mean species mass fraction are compared to the experimental data. It can be appreciated how the use of the original JL mechanism leads to a significant over-prediction of the mean CO_2 mass fraction while under-predicting H_2O levels. On the opposite, the modified JL mechanism provides a strong under-prediction of the mean CO_2 values and over-predicting H_2O mass fraction.

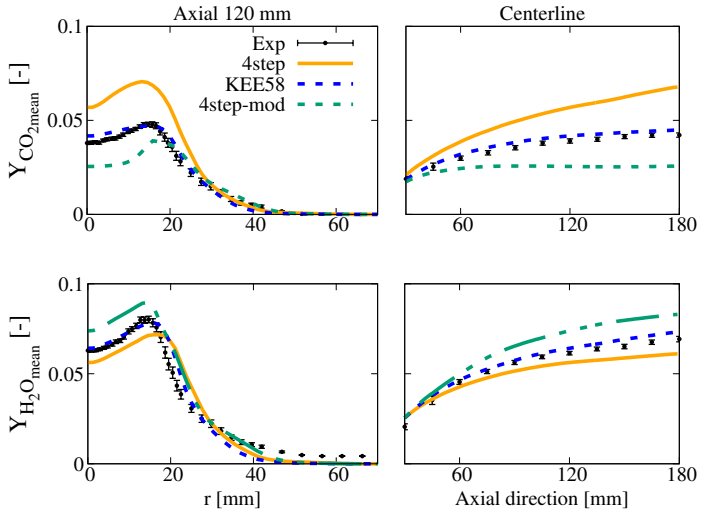

Figure 11: Mean CO_2 and H_2O mass fraction provided by the conventional PaSR model using a global chemistry and a skeletal mechanism at two sampling locations (axial 120 mm and centerline) compared to the experimental measurements.

To further compare the global and skeletal mechanisms, Figure 12 presents the contour plot of mean CO mass fraction, as provided by the KEE58 (left) and the original JL (right) mechanisms, respectively. Figure 12 clearly shows that the global scheme predicts a very fast CO/CO_2 conversion and fails in predicting any CO formation downstream of the flame, thus leading to the over-estimation of CO_2 levels observed in Figure 11.

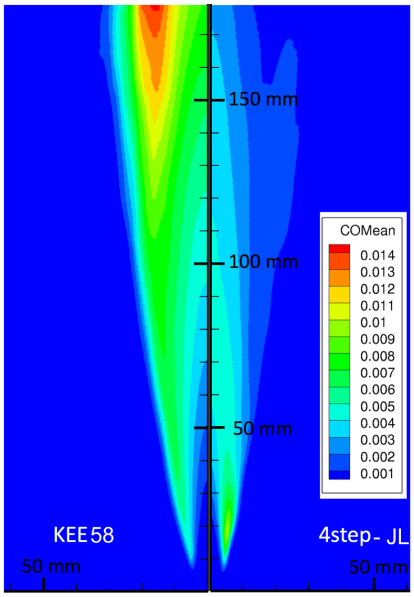

Figure 12: Contour plot of mean CO mass fraction profile obtained using a skeletal (left) mechanism and a global (right) mechanism.

5. Conclusions

In the present work, Large Eddy Simulations of AJHC burner are carried out with the purpose of investigating the applicability of implicit combustion models in MILD combustion. Two implicit combustion models, (QLFR and LFR) are benchmarked against the PaSR approach for turbulence/chemistry interactions. Two 4-step global mechanisms and a skeletal mechanism are used. The conclusion can be summarized as follow:

– High κ (close to 1.0) and low Damköhler number ($\leqslant 0.15$) values are shown by the PaSR model in the reaction zones.

– Among the two implicit combustion models, the QLFR model provides results that are very close to the PaSR model, thus confirming that κ values are close to 1.0. The LFR model generally under-predicts the level of turbulence/chemistry interactions in the flame. However, it predicts the centerline mean temperature correctly.

– Global mechanisms cannot faithfully predict the main products mass fractions, confirming the need of finite rate chemistry in MILD combustion.

The obtained results and conclusions justify the application of implicit closures in the context of MILD combustion. The choice between the different approaches shown here in

realistic configurations will depend on the local Da and Re numbers as well as on the size of the chemical mechanism employed.

Acknowledgments

This project has received funding from the European Union′s Horizon 2020 research and innovation program under the Marie Skłodowska-Curie grant agreement No. 643134. The research of the last author was sponsored by the European Research Council, Starting Grant No. 714605.

References

[1] J. A. Wünning, J. G. Wünning, Prog. Energy Combust. Sci. 23 (1997) 81–94.

[2] A. Cavaliere, M. de Joannon, Prog. Energy Combust. Sci 30 (2004) 329–366.

[3] Y. Minamoto, N. Swaminathan, R. S. Cant, T. Leung, Combust. Sci. Technol. 186 (2014) 1075–1096.

[4] Y. Minamoto, N. Swaminathan, Proc. Combust. Inst. 35 (2015) 3529–3536.

[5] J. Chomiak, Combustion: A Study in Theory, Fact and Application, Abacus Press/Gorden and Breach Science Publishers, New York, 1990.

[6] C. Duwig, P. Iudiciani, Fuel 123 (2014) 256–273.

[7] B. B. Dally, A. N. Karpetis, R. S. Barlow, Proc. Combust. Inst. 29 (2002) 1147–1154.

[8] J. Aminian, C. Galletti, S. Shahhosseini, L. Tognotti, Flow Turbul. Combust. 88 (2012) 597–623.

[9] M. J. Evans, P. R. Medwell, Z. F. Tian, Combust. Sci. Technol. 187 (2015) 1093–1109.

[10] A. Parente, M. R. Malik, F. Contino, A. Cuoci, B. B. Dally, Fuel 163 (2015) 98–111.

[11] M. Ihme, Y. C. See, Proc. Combust. Inst. 33 (2011) 1309–1317.

[12] M. Ihme, J. Zhang, G. He, B. Dally, Flow Turbul. Combust. 89 (2012) 449–464.

[13] Y. Afarin, S. Tabejamaat, A. Mardani, in: Seventh Mediterranean Combustion Symposium, Naples, Italy.

[14] A. Cuoci, A. Frassoldati, T. Faravelli, E. Ranzi, Comput. Phys. Commun 192 (2015) 237–264.

[15] A. Yoshizawa, K. Horiuti, J. Phys. Soc. Jpn. 54 (1985) 2834–2839.

[16] S. Huang, Q. S. Li, Int. J. Numer. Methods Eng. 81 (2010) 835–865.

[17] F. P. Kärrholm, Numerical Modelling of Diesel Spray Injection, Turbulence Interaction and Combustion, Phd thesis, Chalmers University of Technology, Chalmers, Sweden, 2008.

[18] V. Sabelnikov, C. Fureby, Progress in Propulsion Physics 4 (2013) 539–568.

[19] C. Fureby, in: 45th AIAA Aerospace Sciences Meeting and Exhibit, American Institute of Aeronautics and Astronautics, 2007.

[20] C. Duwig, K. J. Nogenmyr, C. K. Chan, M. J. Dunn, Combust. Theor. Model. 15 (2011) 537–568.

[21] Z. Gao, C. Jiang, C. H. Lee, Int. J. Hydrogen Energy 41 (2016) 13238–13253.

[22] N. Kornev, H. Kröger, E. Hassel, Commun. Numer. Meth. Engng 24 (2008) 875–877.

[23] T. J. Poinsot, S. K. Lele, J. Comput. Phys. 101 (1993) 104–129.

[24] W. P. Jones, R. P. Lindstedt, Combust. Flame 73 (1988) 233–249.

[25] L. Wang, Z. Liu, S. Chen, C. Zheng, Combustion Science and Technology (2012).

[26] R. W. Bilger, S. H. Stårner, R. J. KEE, Combust. Flame 80 (1990) 135–149.

[27] J. Andersen, C. L. Rasmussen, T. Giselsson, P. Glarborg, Energy Fuels 23 (2009) 1379–1389.

5.6 Journal paper 6

This paper is in preparation.

Large Eddy Simulation of MILD combustion with dynamic Partially Stirred Reactor combustion closure

Zhiyi Li[a,b,*], Alberto Cuoci[c], Alessandro Parente[a,b,**]

[a] *Université Libre de Bruxelles, Ecole Polytechnique de Bruxelles, Aero-Thermo-Mechanics Laboratory, Bruxelles, Belgium*
[b] *Université Libre de Bruxelles and Vrije Universiteit Brussel, Combustion and Robust Optimization Group (BURN), Bruxelles, Belgium*
[c] *Department of Chemistry, Materials, and Chemical Engineering, Politecnico di Milano, Piazza Leonardo da Vinci, 20133 Milano, Italy*

Abstract

The present paper focuses on the Large Eddy Simulation of a jet-in-hot-coflow burner operating in MILD condition. Several operating conditions with varied coflow oxygen levels and jet Reynolds numbers are considered. The conventional Partially Stirred Reactor combustion model is compared with two implicit models and one dynamic formulation, evaluating the mixing time scale with the ratio of mixture fraction sub-grid fluctuation and mixture fraction dissipation rate. Results from the cases with different coflow oxygen levels (3%/6%/9% by mass, Reynolds number = 10 k) demonstrate that the two implicit models provide predictions of the mean and root-mean-square of the temperature and species mass fraction fields very similar to the conventional PaSR model. Moreover, they all give satisfactory predictions compared to experimental data, especially the mean values. When the jet Reynolds number is increased from 10 k to 20 k, the conventional estimation of the mixing time scale does not allow capturing the typical extinction and re-ignition behaviour of the flame at 3% O_2 level. On the other hand, the dynamic mixing model is able to capture the re-ignition process, improving the accuracy of predictions.

Keywords: MILD combustion, dynamic Partially Stirred Reactor model, mixing time scale, Large Eddy Simulation, jet-in-hot-coflow burner

1. Introduction

Novel combustion technologies with low emissions, high efficiency and fuel flexibility have become essential under the current challenges of energy shortage and increasing air

*Corresponding author: Zhiyi.Li@ulb.ac.be
**Corresponding author: Alessandro.Parente@ulb.ac.be

pollution. Among them, Moderate or Intense Low oxygen Dilution (MILD) combustion has gained increasing attention for the past few decades [1–3]. In industrial applications, MILD combustion is often achieved by promoting strong flue gas recirculation within the reaction region, by means of high velocity fuel jets [4]. The mixture is heated above the self-ignition temperature, leading to distributed oxidation conditions and reduced combustion noise [1]. The reactivity is reduced because of dilution and this results in a more uniform temperature field. The absence of temperature peaks strongly inhibit thermal NO_x production [1, 2]. Such conditions are favorable to complete combustion with very low CO [5, 6] and soot emissions [7, 8].

Simplified lab-scale axis-symmetric jet burners are generally used to emulate MILD condition, to decrease the influence of geometric complexity encountered in practical devices—for example, the jet-in-hot-coflow (JHC) burners [9, 10]. Dally et al. [10] carried out experiments on this burner using an equimolar fuel mixture of CH_4 and H_2. Different oxygen levels (3%, 6% and 9%) in the oxidiser coflow were achieved with the addition of nitrogen. They concluded that the production of CO, NO and OH are suppressed by reducing the oxygen level in the hot and diluted coflow. Numerical investigations on the JHC burners with a hot coflow stabilizing the flame were carried out mostly using Reynolds Averaged Navier-Stokes (RANS) [4, 11–22] simulation. There are only a few with Large Eddy Simulation (LES) [23–26]. Labahn et al. and Bhaya et al. [26] investigated the JHC burner with Dutch natural gas as fuel with two different Reynolds numbers. Ihme et al. [24] showed LES predictions of the JHC burner fed with CH_4/H_2 as fuel using a three streams flamelet/progress variable approach.

The distinguishing feature of MILD combustion is the very strong interactions between the fluid mixing and chemical kinetics, so that models based on the separation between turbulent and chemical time scales are not suitable to describe the complex interactions occurring in such a regime [27]. Therefore, models that account for finite-rate chemistry effects must be considered. Considering the balance between the accuracy of detailed chemistry and the request of CPU hour, there are several models available. For example, reactor-based models such as the Eddy Dissipation Concept (EDC) [28–30] model and the Partially Stirred Reactor (PaSR) [31] model. In EDC and PaSR, each computational cell is separated into two zones, the reactive zone for chemical reactions and the surrounding fluid representing mixing process. The closure of the mean reaction term is then based on a factor accounting for mixing and chemical time scales. Recently, several studies have focused on the use of implicit combustion models [32, 33] in the context of LES. The assumption here is that the LES grid is fine enough to resolve the flame structure. While this appears as a very rough assumption for several combustion applications, the use of implicit models have been proven

appropriate in the context of MILD combustion [32, 33], due to the distributed features of such a combustion regime. As a result, the whole cell can be considered as a Perfectly Stirred Reactor (PSR) and the filtered source term comes directly from the chemical term, without inclusion of the turbulent effect. On the other hand, in the PaSR approach, the interaction between turbulence and chemistry is represented with a factor κ, which is defined as the ratio between the chemical time scale and the sum of mixing and chemical time scales. PaSR models the combustion process as a sequence of reaction and mixing processes in local uniform regions. Both the chemical and mixing time scales are included in the model explicitly, allowing more comprehensive descriptions on turbulence/chemistry interactions. Therefore, its performances strongly depend on the accurate estimation of mixing and chemical time scales.

Regarding the evaluation of mixing time scale, Kärrholm [34] and Nordin [35] estimated the mixing time scale as a certain fraction of the integral one, using a mixing constant C_{mix} ranging from 0.001 to 0.3 [35]. Chomiak [36] estimated the mixing time from the geometric mean of integral and Kolmogorov mixing time scales. Ferraroti and Li et al. [22, 37] proposed a dynamic estimation of the mixing time scale in PaSR using the ratio of variance of mixture fraction and mixture fraction dissipation rate which come from solving three extra transport equations. Improvements on the predictions of species mass fractions and temperature were observed with the dynamic method [22, 37] in the Reynolds Averaged Navier-Stokes (RANS) framework. For the choice of mixing time scale in Large Eddy Simulation (LES), Afarin et al. [38] related the characteristic time scale to the effective viscosity, mean density and sub-grid scale turbulent dissipation. Fureby et al. [39] estimated the mixing time with the geometric mean of Kolmogorov time scale and sub-grid velocity stretch time. Li et al. [33] tested such approach on the LES of the Adelaide JHC burner. However, most of the above mentioned mixing models are defined globally and they are limited by the filter width. Moreover, the dynamic mixing model formulation validated in RANS has not yet been extended and validated in the context of LES.

To further test different formulations of the finite-rate models and to validate a dynamic model for mixing time scale estimation in LES, numerical simulations of the JHC burner with various coflow oxygen levels and fuel jet Reynolds numbers were carried out and the results are presented in the current article. A mesh resolution convergence study is first presented. Following that, effect of the increasing oxygen level in the coflow is analysed. Following up on a previous study by the same Authors [33]on the effect of the combustion closures for the 3% oxygen coflow level case, the analysis for the 6 and 9% cases is carried out. Finally, a dynamic estimation of mixing time scale in LES is tested and compared with the conventional definitions of mixing time in PaSR. Two fuel jet Reynolds number cases are chosen, the 10 k

and 20 k. The objective of the present article is to provide a comprehensive view on finite-rate chemistry approaches for the LES simulation under MILD conditions.

2. Methodology

2.1. Turbulence Model

In LES simulations, the filtered (denoted with ˜) governing equations of mass, momentum, chemical species and energy are solved [40] :

$$\frac{\partial \bar{\rho}}{\partial t} + \frac{\partial}{\partial x_i}\left(\bar{\rho}\tilde{u}_i\right) = 0, \tag{1}$$

$$\frac{\partial}{\partial t}\left(\bar{\rho}\tilde{u}_i\right) + \frac{\partial}{\partial x_i}\left(\bar{\rho}\tilde{u}_i\tilde{u}_j\right) = -\frac{\partial \bar{p}}{\partial x_j} + \frac{\partial}{\partial x_i}\left[\bar{\tau}_{ij} - \bar{\rho}\left(\widetilde{u_i u_j} - \tilde{u}_i\tilde{u}_j\right)\right]. \tag{2}$$

$$\frac{\partial}{\partial t}\left(\bar{\rho}\widetilde{Y_s}\right) + \frac{\partial}{\partial x_i}\left(\bar{\rho}\widetilde{Y_s}\tilde{u}_i\right) = \frac{\partial}{\partial x_i}\left[\overline{V_{s,i}Y_s} - \bar{\rho}\left(\widetilde{u_i Y_s} - \tilde{u}_i\widetilde{Y_s}\right)\right] + \bar{\dot{\omega}}_s, \tag{3}$$

$$\frac{\partial}{\partial t}\left(\bar{\rho}\tilde{h}\right) + \frac{\partial}{\partial x_i}\left(\bar{\rho}\tilde{h}\tilde{u}_i\right) - \overline{\frac{Dp}{Dt}} = \frac{\partial}{\partial x_i}\left[\overline{\lambda\frac{\partial T}{\partial x_i}} - \bar{\rho}\left(\widetilde{u_i h} - \tilde{u}_i\tilde{h}\right)\right] + \overline{\tau_{ij}\frac{\partial u_i}{\partial x_j}} - \frac{\partial}{\partial x_i}\left(\overline{\rho\sum_{s=1}^{N} V_{s,i}Y_s h_s}\right) - \bar{\dot{\omega}}_T. \tag{4}$$

In Eqn. 1 - 4, ρ, $\mathbf{u}$, p represent the density, velocity and pressure respectively; h is the enthalpy; λ is the thermal conductivity. The terms $\overline{V_{s,i}Y_s}$ and $\overline{\lambda\frac{\partial T}{\partial x_i}}$ are filtered laminar diffusion fluxes for species and enthalpy which is modelled through a simple gradient assumption.

The unresolved Reynolds stresses need to be modelled:

$$\overline{\mathrm{T}_{ij}} = \left(\widetilde{u_i u_j} - \tilde{u}_i\tilde{u}_j\right), \tag{5}$$

which requires a turbulence model. The one Equation Eddy Viscosity (`oneEqnEddy`) is chosen as the sub-grid turbulent model [41]. In `oneEqnEddy` model, $\overline{\mathrm{T}_{ij}}$ is estimated by an subgrid-scale eddy viscosity ν_{sgs} and a resolved scale strain rate $\overline{S}_{ij}$:

$$\overline{\mathrm{T}_{ij}} = -2\nu_{sgs}\overline{S}_{ij} + \frac{1}{3}\tau_{ii}^{sgs}\delta_{ij}. \tag{6}$$

The sub-grid scale viscosity is computed as:

$$\nu_{sgs} = C_k\sqrt{k_{sgs}}\Delta, \tag{7}$$

where $C_k = 0.094$, Δ is the grid size and k_{sgs} is the sub-grid scale kinetic energy which is solved through a dedicated transport equation [42]:

$$\frac{\partial(\rho k_{sgs})}{\partial t} + \frac{\partial(\rho \overline{u}_j k_{sgs})}{\partial x_j} - \frac{\partial}{\partial x_j}\left[\rho\left(\nu + \nu_{sgs}\right)\frac{\partial k_{sgs}}{\partial x_j}\right] \tag{8}$$

$$= -\rho\tau_{ij} : \overline{S}_{ij} - C_\epsilon \frac{\rho k_{sgs}^{3/2}}{\Delta}, \tag{9}$$

in which where the operator : is a double inner product and C_ϵ is a constant qhich equals to 1.048.

2.2. Partially-Stirred Reactor model and implicit LES combustion models

2.2.1. Partially-Stirred Reactor model

In the assumption of the Partially Stirred Reactor (PaSR) [31] model, each computational cell is separated into two zones, the reactive zone and surrounding fluid zone. Reaction happens only in a fraction of the cell which is represented by the term κ [34]. The mean source term is obtained from the mixing between the products from the reactive zone and surrounding fluid:

$$\overline{\dot{\omega}}_s = \kappa \dot{\omega}_s^*(\widetilde{\boldsymbol{Y}}, \widetilde{T}). \tag{10}$$

In Equation 10, $\dot{\omega}_s^*(\widetilde{\boldsymbol{Y}}, \widetilde{T})$ represents the formation rate of species s based on the filtered mass fractions of species in the reactive zone that is modelled as a Perfectly Stirred Reactor (PSR) [43]:

$$\frac{dY_s}{dt} = \frac{\dot{\omega}_s}{\rho}. \tag{11}$$

The term $\dot{\omega}_s$ is the instantaneous formation rate of species s. The final integration of $\frac{dY_s}{dt}$ over the residence time τ in the reactor is Y_s^*, the species mass fraction in the reactive zone. The term $\dot{\omega}_k^*(\widetilde{\boldsymbol{Y}}, \widetilde{T})$ in Equation 10 is thus estimated with:

$$\dot{\omega}_s^*(\widetilde{\boldsymbol{Y}}, \widetilde{T}) = (Y_s^* - \widetilde{Y}_s^0)/\tau, \tag{12}$$

where $\widetilde{Y}_s$ is the species mass fraction in the surrounding fluid. In the present work, τ equals to CFD time step.

The term κ is calculated as:

$$\kappa = \frac{\tau_c}{\tau_c + \tau_{mix}}, \tag{13}$$

in which τ_c and τ_{mix} are the characteristic chemical time scale and mixing time scale, respectively.

2.2.2. Quasi-Laminar Finite Rate model

Based on the PaSR model, the QLFR model is formulated merely by forcing $\kappa = 1.0$ [44], under the hypothesis that the mixing time scale is much smaller than the chemical time scale. Therefore, the turbulent eddies are assumed to be able to penetrate into the flame structures and the whole cell is like a Perfectly Stirred Reactor (PSR) [43].

2.2.3. Laminar Finite Rate model

The Laminar Finite Rate model does not directly account for the effect of turbulence in the mean source term, and the mean formation rates are determined by Arrhenius expressions [32]:

$$\overline{\dot{\omega}}_k = M_k \sum_{r=1}^{N_r} \hat{R_{k,r}}. \tag{14}$$

In Equation 14, M_k is the molecular weight of species k and $\hat{R_{k,r}}$ is the Arrhenius rate of creation/destruction of species k in reaction r.

2.3. Mixing time scale evaluation

The mixing time scale can be evaluated with various forms [22, 37]. Under current LES frame, three approaches are considered:

Kolmogorov time scale. In combustion systems, it is often assumed that reactions happen at the dissipation scales, of the order of the Kolmogorov one, $\tau_{mix_K} = \sqrt{\nu/\epsilon_{sgs}}$ [4], where ν is the kinematic viscosity and ϵ_{sgs} is the turbulence kinetic energy dissipation rate. In MILD combustion, reactions can occur over a wide range of flow scales [2], and the use of the Kolmogorov mixing time scale might lead to inaccurate predictions [45], as shown in some RANS simulations [22].

Geometric mean of Kolmogorov time scale and sub-grid velocity stretch time. Since the flame structures in a 3D volume are generally anisotropic (sheets, ribbons, and tubes), the influence from the sub-grid velocity stretch shall be considered [39] in mixing time calculation. Therefore, another approach is to use the geometrical mean of the sub-grid velocity stretch time $(\Delta/v^{'})$ and the Kolmogorov time scale $((\nu/\epsilon_{sgs})^{1/2})$ [39]:

$$\tau_{mix} = \sqrt{\frac{\Delta}{v^{'}} \frac{\nu}{(\epsilon_{sgs})^{1/2}}}. \tag{15}$$

Dynamic mixing time. A more comprehensive approach consists in the dynamic estimation of mixing time scale. It is based on the ratio of the scalar variance, $\widetilde{\phi''^2}$, to the scalar dissipation rate, $\widetilde{\epsilon_\phi}$ [46]:

$$\tau_{mix_{Dynamic}} = \frac{\widetilde{\phi''^2}}{\widetilde{\epsilon_\phi}}. \tag{16}$$

The scalar of mixture fraction f is selected here. Therefore, the scalar variance and dissipation rate take the form of the mixture fraction sub filter variance ($\widetilde{f''^2}$) and mixture fraction dissipation rate ($\widetilde{\chi}$). Transport equations are solved to get these values.

In LES of reacting flows, transport equation for scalar dissipation rate $\widetilde{\chi}$ requires additionally closures for the gradients of diffusivity and density [47]. To limit the appearance of unclosed terms, instead, $\widetilde{|\nabla f|^2}$ is solved, by using Eqn. 17 [47]:

$$\begin{aligned}
\frac{D}{D_t}\left(\overline{\rho}\widetilde{|\nabla f|^2}\right) = & \frac{\partial}{\partial x_j}\left(\overline{\rho}(\widetilde{D}_f + D_t)\frac{\partial}{\partial x_j}(\widetilde{|\nabla f|^2})\right) \\
& - 2\overline{\rho}\left(\frac{\partial \widetilde{u_i}}{\partial x_j}\frac{\partial \widetilde{f}}{\partial x_i}\frac{\partial \widetilde{f}}{\partial x_j}\right) \\
& - 2\overline{\rho}\widetilde{D}_f\left(\frac{\partial^2 \widetilde{f}}{\partial x_i \partial x_j}\right)^2 \\
& - \frac{2}{\overline{\rho}}\frac{\overline{\rho}}{\partial x_i}\frac{\widetilde{f}}{\partial x_i}\left(\frac{\partial}{\partial x_j}\left(\overline{\rho}\widetilde{D}_f\frac{\partial}{\partial x_j}(\widetilde{f})\right)\right) \\
& + 2\frac{\partial(\overline{\rho}\widetilde{D}_f)}{\partial x_i}\frac{\partial \widetilde{f}}{\partial x_i}\left(\frac{\partial^2 \widetilde{f}}{\partial x_j \partial x_j}\right) \\
& + 2\frac{\partial \widetilde{f}}{x_i}\frac{\partial \widetilde{f}}{x_j}\left(\frac{\partial^2(\overline{\rho}\widetilde{D}_f)}{\partial x_i \partial x_j}\right) \\
& + C_{prd}\cdot\overline{\rho}\cdot\frac{32\cdot\nu_t}{\Delta^2}\cdot\left(\widetilde{|\nabla f|^2} - |\nabla\widetilde{f}|^2\right) \\
& - C_{dis}\cdot\overline{\rho}\cdot\frac{\widetilde{D}_f}{\widetilde{f''^2}}\left(\widetilde{|\nabla f|^2} - |\nabla\widetilde{f}|^2\right)^2,
\end{aligned} \tag{17}$$

in which D_f is the scalar diffusivity. In Eq. 17, $C_{prd=1.0}$ and C_{dis} is determined by the sub-filter scalar variance coefficient: $C_{dis} = 12C_{var}$. In the present approach, C_{var} is evaluated with [47]:

$$C_{var} = \widetilde{f''^2}/(\Delta^2|\nabla\widetilde{f}|^2). \tag{18}$$

The scalar dissipation rate is then calculated as $\widetilde{\chi} = 2D_f\widetilde{|\nabla f|^2}$.

The sub-filter mixture fraction variance $\widetilde{f''^2}$ can not be obtained directly by solving a transport equation as what is often done in RANS, because it is the sub-grid value under LES framework. Therefore, Eqn. 19 is used:

$$\widetilde{f''^2} = \widetilde{f^2} - (\widetilde{f})^2. \tag{19}$$

The term $\widetilde{f^2}$ is then obtained from solving a transport equation:

$$\frac{D}{D_t}\left(\overline{\rho}\widetilde{f^2}\right) = \frac{\partial}{\partial x_j}\left(\overline{\rho}(\widetilde{D}_f + D_t)\frac{\partial}{\partial x_j}(\widetilde{f^2})\right) - \rho\widetilde{\chi}, \tag{20}$$

and the filtered mixture fraction transport equation shall be solved to get $\widetilde{f}$:

$$\frac{\partial\bar{\rho}\widetilde{f}}{\partial t} + \frac{\partial\bar{\rho}\widetilde{u}_j\widetilde{f}}{\partial x_j} = \frac{\partial}{\partial x_j}\Big(\rho(D_f + D_t)\frac{\partial\widetilde{f}}{\partial x_j}\Big). \tag{21}$$

In the end, the dynamic mixing time scale is expressed as:

$$\tau_{mix_{Dynamic}} = \frac{\widetilde{f''^2}}{\widetilde{\chi}} = \frac{\widetilde{f^2} - (\widetilde{f})^2}{2D_f\widetilde{|\nabla f|^2}}. \tag{22}$$

2.4. Chemical time scale evaluation

For the evaluation of chemical time scale, Fox [48, 49] suggested using the eigenvalues of the Jacobian matrix **J** of the chemical source terms. After the decomposition of the Jacobian matrix, the chemical time scale is estimated with the inverse of the eigenvalues λ_s:

$$\tau_{c,s} = \frac{1}{|\lambda_s|}. \tag{23}$$

The decomposition of the source term Jacobian matrix is accurate but time consuming, especially when large scale simulations with much detailed mechanism is used. The formation rate based characteristic time scale evaluation is a simplified approach. Instead of getting the chemical time scale for each species from the Jacobian matrix decomposition, the ratio of species mass fraction and formation rate in the reactive structure is directly used [21, 36], approximating the Jacobian diagonal terms:

$$\tau_{c,s} = \frac{Y_s^*}{|dY_s^*/dt|}, \tag{24}$$

where Y_s^* and dY_s^*/dt are mass fraction of the s_{th} species and the corresponding formation rate in the reacting zone, respectively. In Eqn. 24, $\tau_{c,s}$ is the characteristic time scale of a single species. After removing the dormant species (characterised by infinite time scale values), the slowest chemical time scale τ_c is chosen as leading scale for the evaluation of κ.

3. Model validation

3.1. Experimental data

The JHC burner emulates MILD combustion with a simplified geometry. There is an insulated and cooled central jet with the inner diameter of 4.25 mm, and it provides an equi-molar mixture of CH_4 and H_2. The burner has an annulus pipe with a secondary burner mounted upstream. The burner provides hot combustion products, which are further mixed with air and nitrogen to control the oxygen levels to 3%, 6% and 9% in mass fraction. Only the 3% coflow case reaches MILD condition before the entrainment of higher concentration of oxygen in the air stream, starting from around the axial location of 100 mm. The annulus that provides hot coflow has the inner diameter of 82 mm. The whole burner is located in a wind tunnel with the cross section of 254 mm $\times$ 254 mm. In Fig. 2, a 2D simple sketch of the investigated area in the numerical modelling is presented. In the current study, four cases with three different co-flow oxygen contents and two fuel jet Reynolds numbers are investigated, as highlighted in Table 1. The central jet, annulus and wind tunnel gas temperatures and velocities are presented in Table 2.

Table 1: Investigated cases

Co-flow oxygen level:	3%	6%	9%
Re = 10 k	✓	✓	✓
Re = 20 k	✓		

Table 2: Physical properties of the jet (Central jet velocity is for the Re = 10 k case.)

Profiles	Central jet	Annulus	Tunnel
Velocity (10 k)	58.74 m/s	3.2 m/s	3.3 m/s
Velocity (20 k)	117.48 m/s	3.2 m/s	3.3 m/s
Temperature	294 K	1300 K	294 K

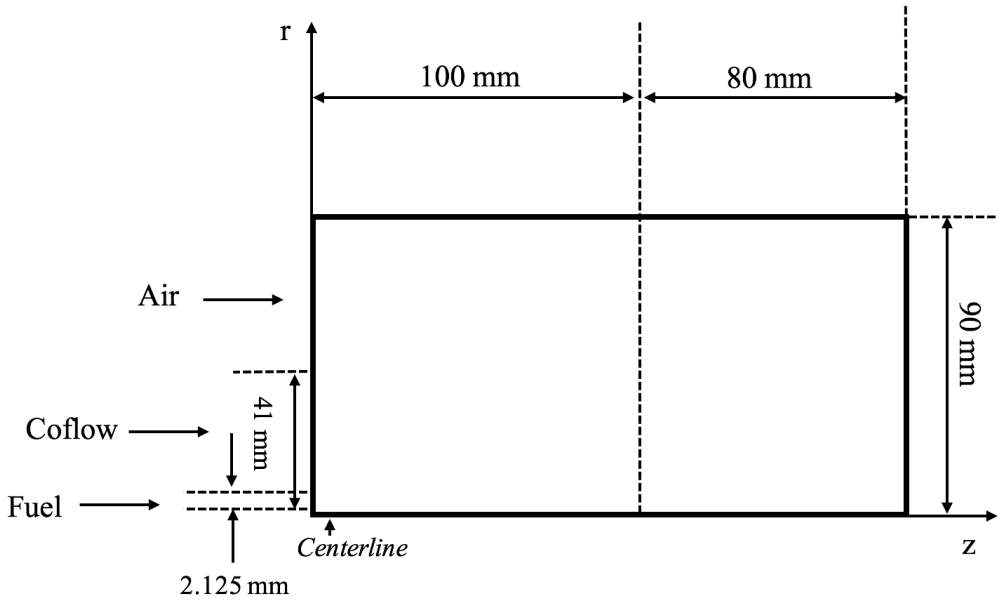

Figure 1: two-dimensional sketch of the Jet in Hot Co-flow burner.

The mean, variance (RMS) and scattered data of temperature and various species mass fractions (CH_4, H_2, H_2O, CO_2, N_2, O_2, NO, CO, and OH), along the centerline as well as on the different axial locations of 30/60/120/200 mm (z = 30/60/120/200 mm), are available for validation. The experimental profiles used for comparison include both the mean values and the error bar with 99.99% confidence interval associated with a Student′s distribution for the true mean value [50].

3.2. Numerical set-up

The simulation domain starts from the jet exit and extends 180 mm further downstream. The radial direction expands 90 mm away from the centerline. The whole domain is discretized with a three-dimensional cylinder structured mesh. Four meshes with different resolution are used. They have ~0.5/1.0/1.5/2.0 containing million cells. The LEMOS [51] inflow generation method for velocity field is applied on all the three streams-jet, coflow and tunnel air. Experimentally measured profiles (H_2O, CO_2 O_2 species mass fractions and temperature) at the axial location of 4 mm are directly used as inflow data for the simulation. A reduced skeletal mechanism KEE58 [52] is used for finite-rate chemistry calculations. The sampling locations are at the centerline and 30/60/120 mm axial locations. Both mean and variance profiles are sampled after more than 16 times of flow through of the jet.

4. Results and discussion

In this section, the modelling results from various mesh resolution, coflow oxygen level and the mixing time scale evaluation method are presented and validated against the experimental data.

4.1. Mesh resolution test

The proper choice of mesh resolution is of great important in the current simulation. Firstly, the mesh size should be fine enough so that the assumptions on implicit models are valid—distributed flame structure can be resolved with the LES grid. Regarding this, more detailed discussion based on the Damköhler number and κ value distribution have been provided in the paper published by the authors [33]. On the other hand, mixing time scale evaluation using the Kolmogorov chemical time scale $\tau_{mix_K} = \sqrt{\nu/\epsilon_{sgs}}$ and geometric mean of Kolmogorov time scale and sub-grid velocity stretch time $\sqrt{\frac{\Delta}{v'}\frac{\nu}{(\epsilon_{sgs})^{1/2}}}$ limits the cell size. When the cell size is reduced, the sub-grid turbulent energy dissipation rate ϵ_{sgs} is decreased accordingly, so does the filter size Δ. Therefore, with sufficiently small grid size, the two above mentioned approaches for the estimation of mixing time scale is not valid. So does the estimation of κ: $\kappa = \dfrac{\tau_c}{\tau_c + \tau_{mix}}$.

In Figure 1, the mean temperature profiles from simulations with different mesh resolution for the 3% oxygen level and 10 k Reynolds number case is presented. The axial locations of z = 30/60/120 mm and centerline are sampled and compared with the experimental data. There is no evident difference regarding the mean temperature values on z = 30/60 mm and centerline. On z = 120 mm, the mean temperature peak value is over-predicted by ~100 K with the 0.5 million mesh and ~50 K with the 1.0 and 2.0 million meshes. The prediction from the 1.5 million mesh keeps within the errorbar range.

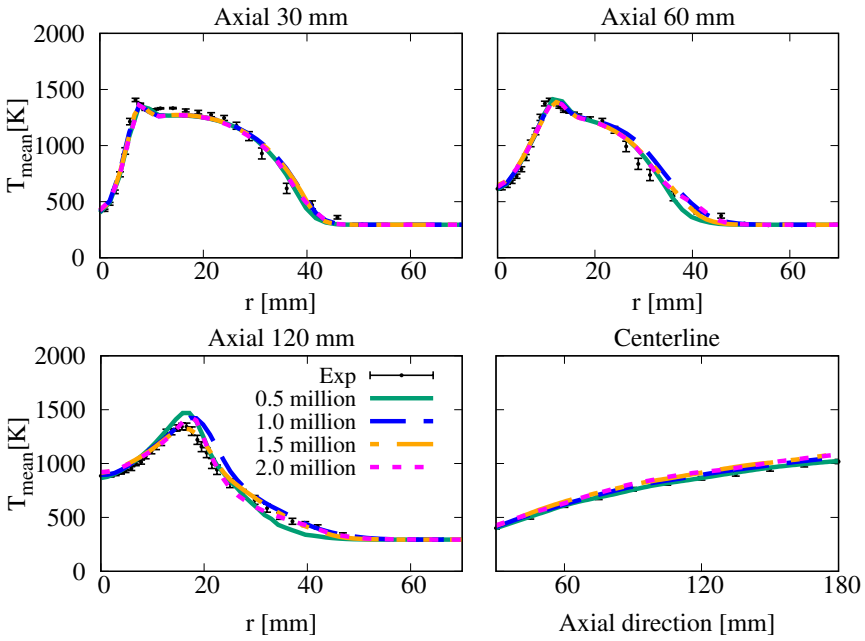

Figure 2: Mean temperature profiles from simulations with different mesh resolutions (~0.5/1.0/1.5/2.0 million cells) for the 3% oxygen level and 10 k Reynolds number case compared with experimental data.

For the root-mean-square (RMS) temperature profiles at z = 120 mm, the differences can be further captured. The value for the RMS temperature is increasing with finer mesh, until the mesh with 1.5 million cells—good agreement with the measurement data can be obtained. For the 2.0 million cells mesh, similar RMS peak value is shown while slight under prediction can be seen at around r = 20 mm.

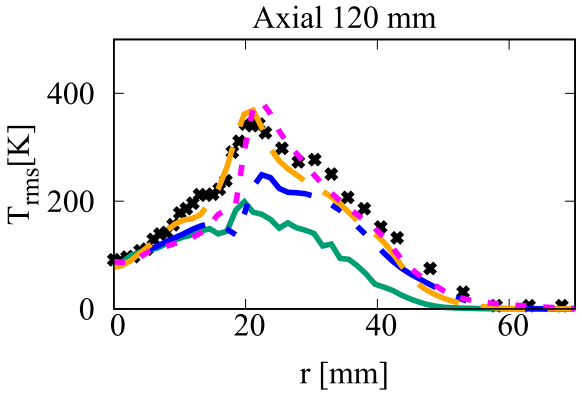

Figure 3: RMS temperature profiles from simulations with different mesh resolutions (~0.5/1.0/1.5/2.0 million cells) for the 3% oxygen level and 10 k Reynolds number case compared with experimental data.

The mean species mass fraction of H_2O from the four meshes are also compared in Fig-

ure 4. No major difference is found and so does the prediction for mean CO and CO_2 mass fraction (not shown here for brevity). However, for the RMS profiles in Figure 5, as it has been observed with the temperature RMS, the low resolution meshes (0.5 million and 1.0 million) are not able to predict the sub-grid fluctuations well. For the peak value, the 1.5 and 2.0 million meshes are preferred compared with the experimental data—yet, the 2.0 million mesh presents under-prediction at the location between r = 10 mm and 20 mm.

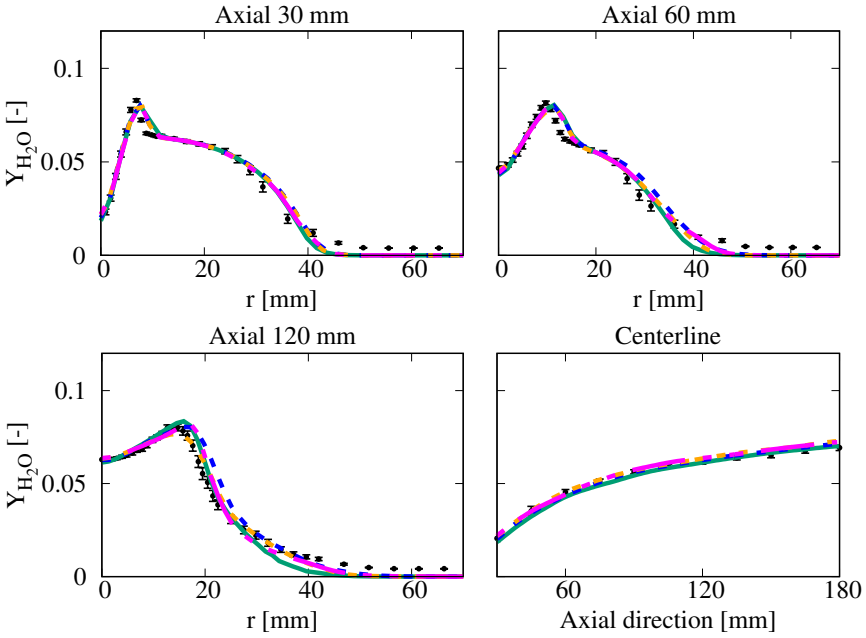

Figure 4: Mean H_2O mass fraction profiles from simulations with different mesh resolutions (~0.5/1.0/1.5/2.0 million cells) for the 3% oxygen level and 10 k Reynolds number case on z = 120 mm compared with experimental data.

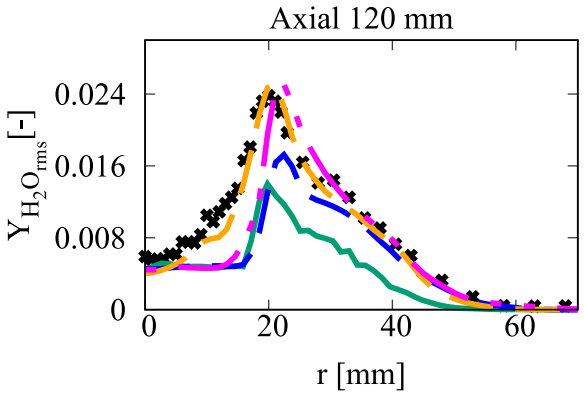

Figure 5: RMS H_2O mass fraction profiles from simulations with different mesh resolutions (~0.5/1.0/1.5/2.0 million cells) for the 3% oxygen level and 10 k Reynolds number case compared with experimental data.

The energy resolved at selected locations (z = 60/120 mm) with the four meshes is demonstrated in Figure 6. The coarse meshes (0.5 and 1.0 million) resolve low amount of energy which falls below 80% at some radial locations, especially for r $\leqslant$ 40 mm. The higher resolution meshes (1.5 and 2.0 million) have similar amount of energy resolved with each other at the selected locations and it is above 80%. Therefore, in summary, considering the accuracy and efficiency of simulation, as well as the mixing time scale evaluation and the application of implicit combustion models, the 1.5 million mesh is more suitable than the other ones in the current research work. It is therefore used for the rest of simulations.

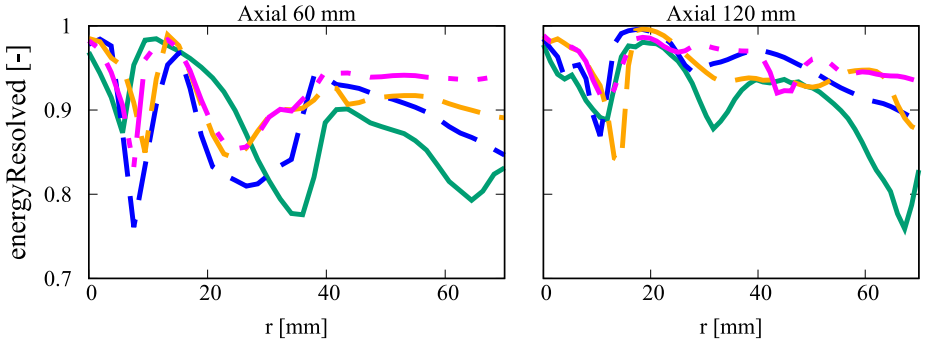

Figure 6: Amount of energy solved from simulations with different mesh resolutions (~0.5/1.0/1.5/2.0 million cells) for the 3% oxygen level and 10 k Reynolds number case.

4.2. The influence of coflow oxygen level

The investigated case include three oxygen levels, fixing jet Reynolds number at Re = 10 k. Increased oxygen level in the coflow could lead to earlier ignition of the flame and more heat release. In Figure 7, the mean OH mass fraction distribution for the three coflow oxygen cases along with the heat release rate (HRR) contour plots at the level of 1×10^{16},

1×10^{17} as well as 2×10^{17} W/m^3 are presented. Compared to the other two higher oxygen level cases, the 3% case shows very weak mean OH mass fraction profile, especially at around z = 0.11 m. After z = 0.12 m, the OH level is increased, because that the oxygen from the air stream starts to penetrate and react with the fuel. Such transition can also be observed from the contour lines of HRR. Starting from z = 0.11 m until z = 0.14 m, there is a break for the HRR contour line of 1×10^{17} and 2×10^{17} W/m^3, implying that the lack of oxygen in the coflow has lead to slight local extinction. For the 6% case, the 1×10^{17} W/m^3 level HRR is continuous. However, the 2×10^{17} W/m^3 shows short break between z = 0.11 m and z = 0.12 m. Close to the jet exit location, based on the OH mass fraction value, all of the three cases are slightly lifted. The 9% case is ignited and releases heat faster than the other two cases—the contour lines of the HRR values of 1×10^{16}, 1×10^{17} and 2×10^{17} W/m^3 almost overlap with each other. On the contrary, for the 3% case, larger distance is observed between the 1×10^{16} and 1×10^{17} contour lines. Compared to the 9%, the ignition of the low oxygen level case is less intense.

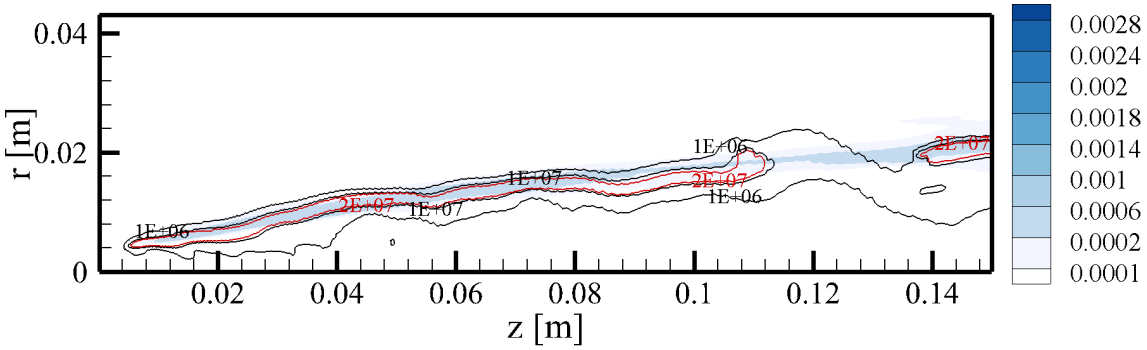

(a) 3%, Re = 10 k

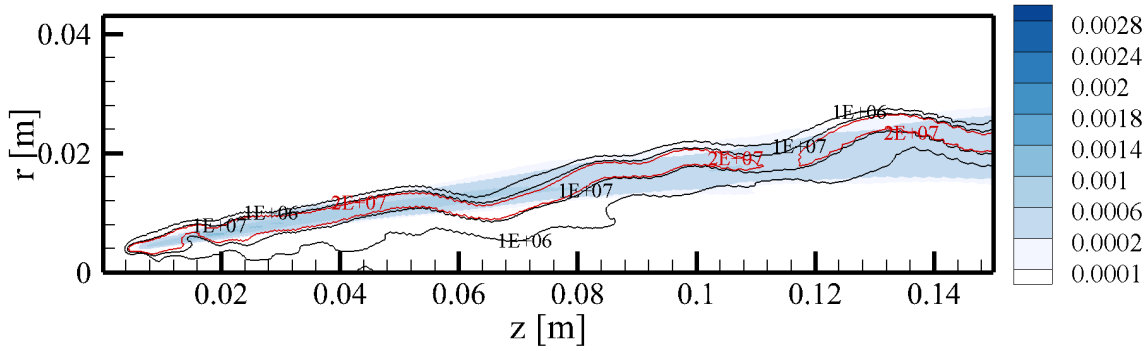

(b) 6%, Re = 10 k

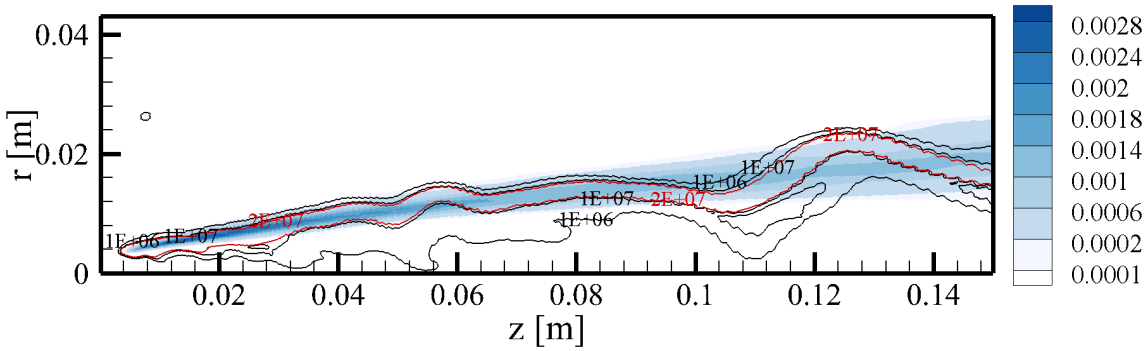

(c) 9%, Re = 10 k

Figure 7: Mean OH mass fraction contour plot with heat release rate (HRR) contour lines from the three oxygen level cases. The unit of HRR is W/m^3.

The difference in HRR is revealed on temperature directly. In Figure 8, the mean temperature profiles from simulations with PaSR model are validated against the experimental data for oxygen levels of 3/6/9%. The geometric mean of Kolmogorov time scale and the sub-grid velocity stretching time is used for the mixing time scale to evaluate κ. Both numerical and experimental results show elevated mean temperature peak value with increased coflow oxy-

gen level. Satisfactory agreement with the measured data is obtained for the peak value and location at z = 30/60 mm for all the cases. At z = 120 mm, the 3% is better predicted than the other two cases, for which the mean temperature is over-predicted both by around 110 K. For the H_2O production, as shown in Figure 9, good agreement is obtained at all sampled locations for all the three oxygen level cases.

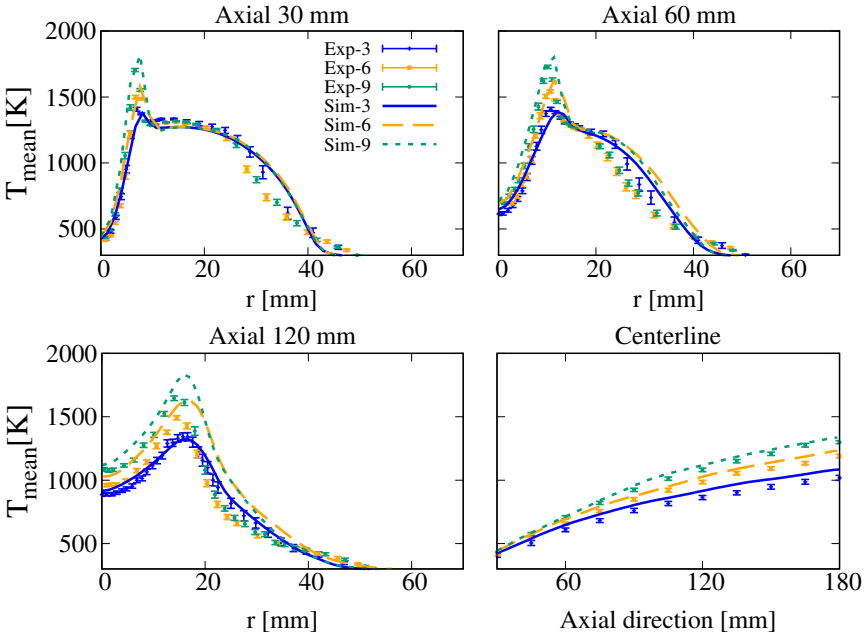

Figure 8: Mean temperature plot at sampled locations from the three oxygen level cases compared with the experimental data.

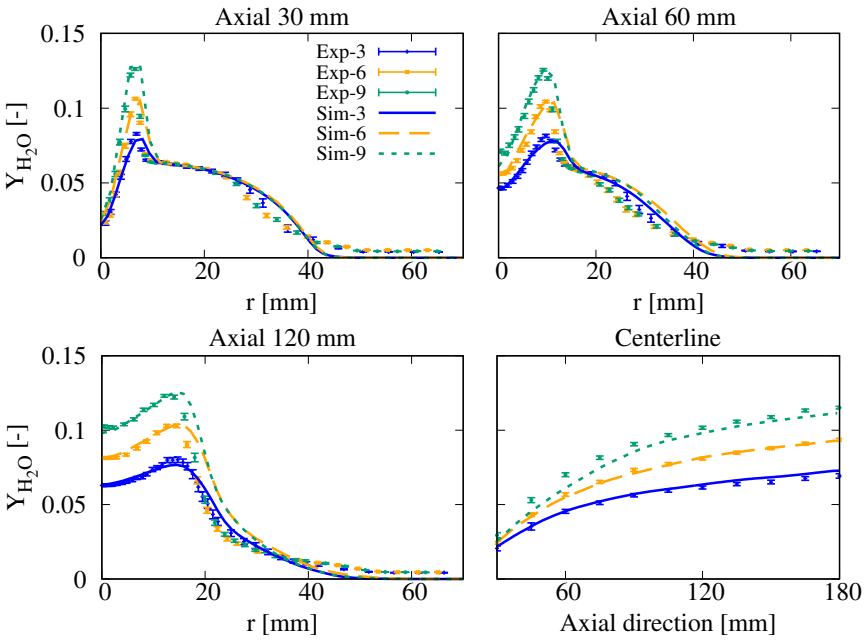

Figure 9: Mean mass H_2O fraction plot at sampled locations from the three oxygen level cases compared with the experimental data.

In Figure 8 and 9, the modelled profiles from only PaSR is presented. The two implicit models, QLFR and LFR provide simulation results very similar with the PaSR model. They are not presented here. Such similarity is not only valid for mean temperature and major species like CO_2 and H_2O, but also minor species like CO and the rms value of CO, shown in Figure 10 and 11. The mean CO mass fraction value before z = 60 mm has two peak values. The second one comes from the combustion products mixing with the air in the coflow region. Concerning the first peak, all three models provide numerical values that are very close to the experimental data, for the 3% and 6% cases. Over-predictions are captured at z = 30/60 mm for the 9% case, by 38% and 17%, respectively. At z = 120 mm, the selected models predict all three cases with satisfaction.For the RMS CO mass fraction, no over-prediction is observed, while under-prediction exist, particularly at the location of the second peak. Since the RMS value is not provided directly as boundary condition, the under-prediction of the second peak indicates that the interaction between the air and coflow stream may not be well simulated.

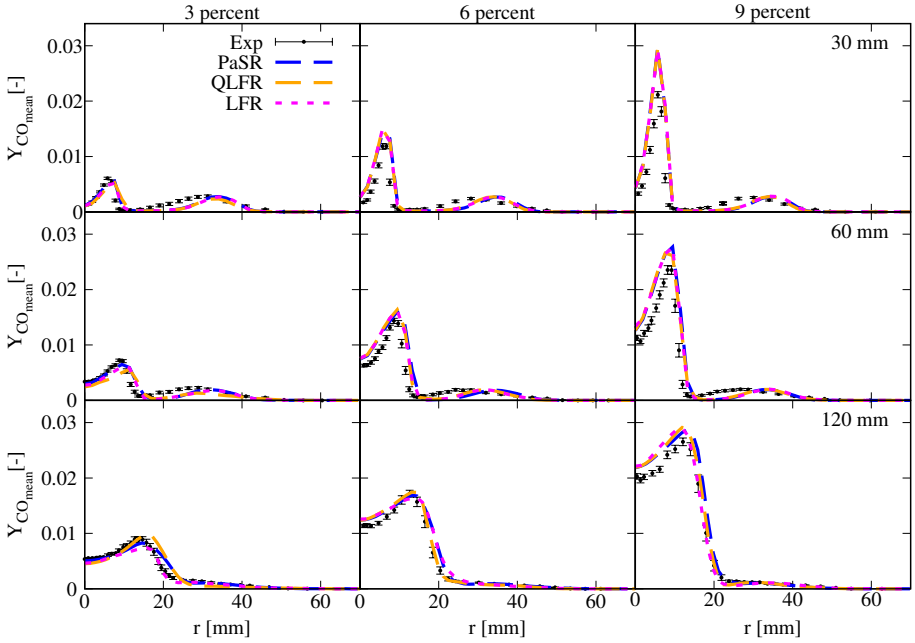

Figure 10: Mean CO mass fraction plot at sampled locations from the three oxygen level cases compared with the experimental data. Three combustion models: PaSR, QLFR and LFR are used.

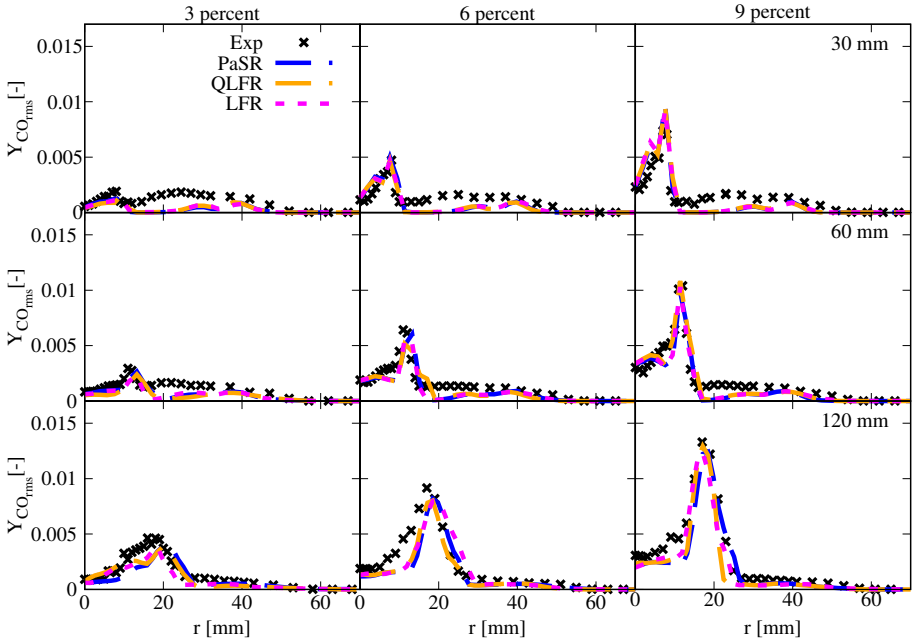

Figure 11: RMS CO mass fraction plot at sampled locations from the three oxygen level cases compared with the experimental data. Three combustion models: PaSR, QLFR and LFR are used.

From the line plot in Figure 10, it is observed that the CO peak value at the selected axial

locations is reduced with decreased coflow oxygen levels. The CO production in the whole system can be better appreciated with the 2D contour plot in Figure 12. All three sub-figures show low level of CO in the coflow stream, coming from the boundary condition. On the reaction layer with high HRR, it is the same for all the coflow oxygen level cases that not much CO can be maintained after produced. They are mostly converted to CO_2. However, in the fuel stream, the 9% is showing much higher value of CO mass fraction compared to the other lower oxygen cases—three times of the 3% case. Such conclusion agrees with the experimental findings from Dally et al. [10] and it is also an important characteristic of MILD combustion.

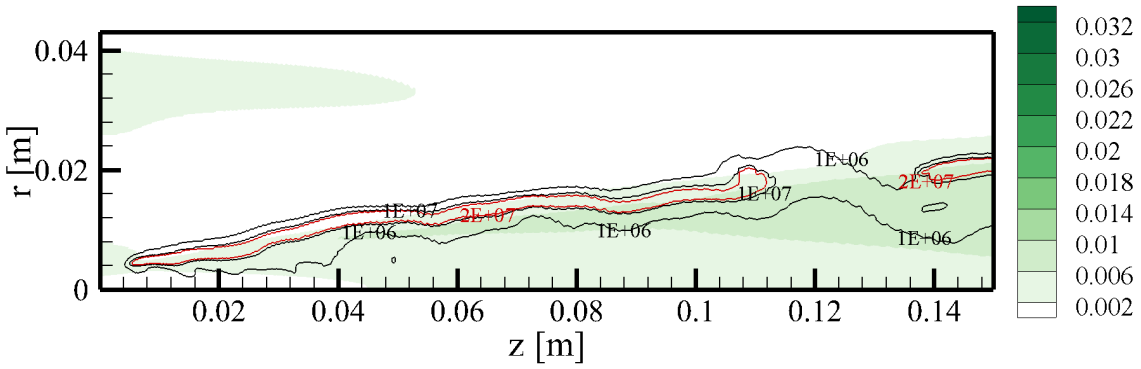

(a) 3%, Re = 10 k

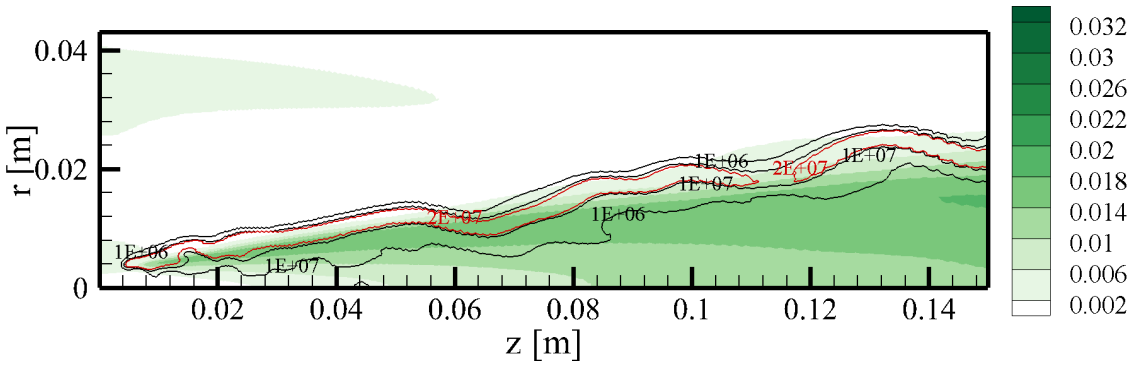

(b) 6%, Re = 10 k

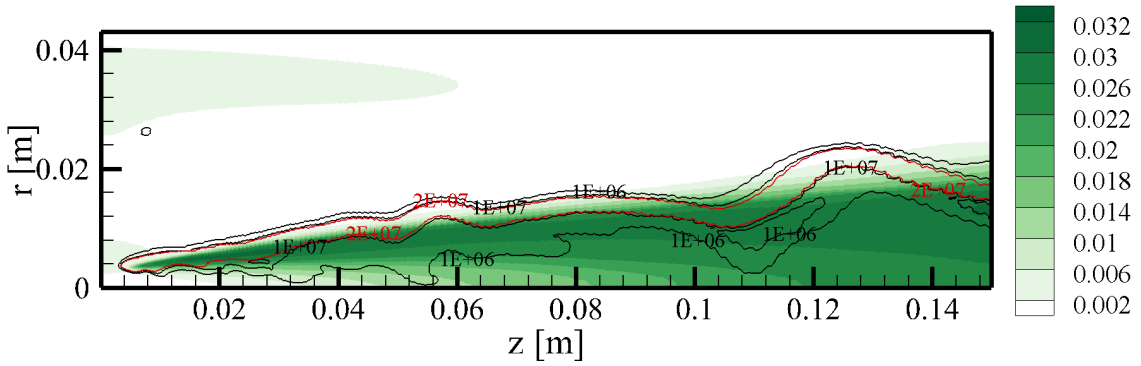

(c) 9%, Re = 10 k

Figure 12: Mean CO mass fraction contour plot with heat release rate (HRR) contour lines from the three oxygen level cases. The unit of HRR is W/m^3.

In summary, the observations obtained above implies that the increased coflow oxygen level promotes the ignition of the current flame and the entrainment of air into the fuel stream helps the local extinguished flame to re-ignite downstream for the 3% case. The OH and CO

production are suppressed when reducing the coflow oxygen level. The two implicit models show very similar numerical profiles comparing with the PaSR model, even for higher oxygen level cases.

4.3. The choice of mixing time scale

Three approaches for the estimation of mixing time in LES were introduced in Section 2.3. The first two approaches which are based on the time scale of the flow are termed as conventional methods. The dynamic approach is first introduced by the authors here in PaSR model with LES. They are compared in the present Section on the validation of the 3% oxygen level and Re = 10 k case. No major difference is captured on the mean temperature and major species like CO_2 and H_2O predictions. They are therefore not shown here. Instead, the rms values of temperature and species mass fractions of O_2 and H_2O are presented in Figure 13 and 14. On z = 30/60 mm, all mixing models tend to under-predict the second peak of the temperature fluctuations, while using the dynamic and Kolmogorov mixing time scale show slightly better profiles. On z = 120 mm, the results from using dynamic and geometric mean scales are closer to the experimental one. Similar trend is captured on the O_2 and H_2O rms values. The dynamic estimation of mixing time scale predict rms values in general better than the other two approaches.

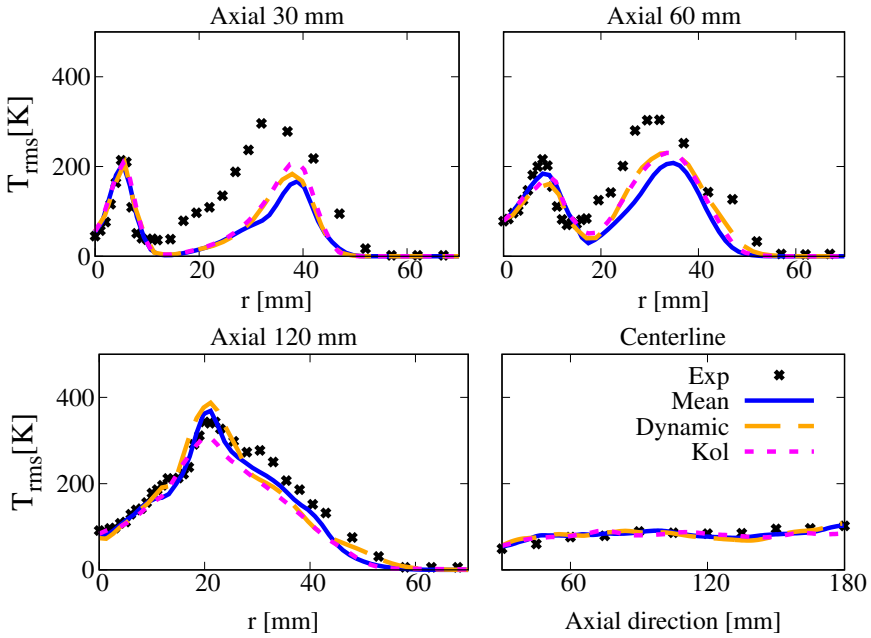

Figure 13: RMS temperature profiles at sampled locations from the three approaches for the evaluation of mixing time scale compared with the experimental data. Mean: geometric mean of the Kolmogorov time scale and sub-grid velocity stretch time; Dynamic: dynamic mixing time scale; Kol: Kolmogorov mixing time scale.

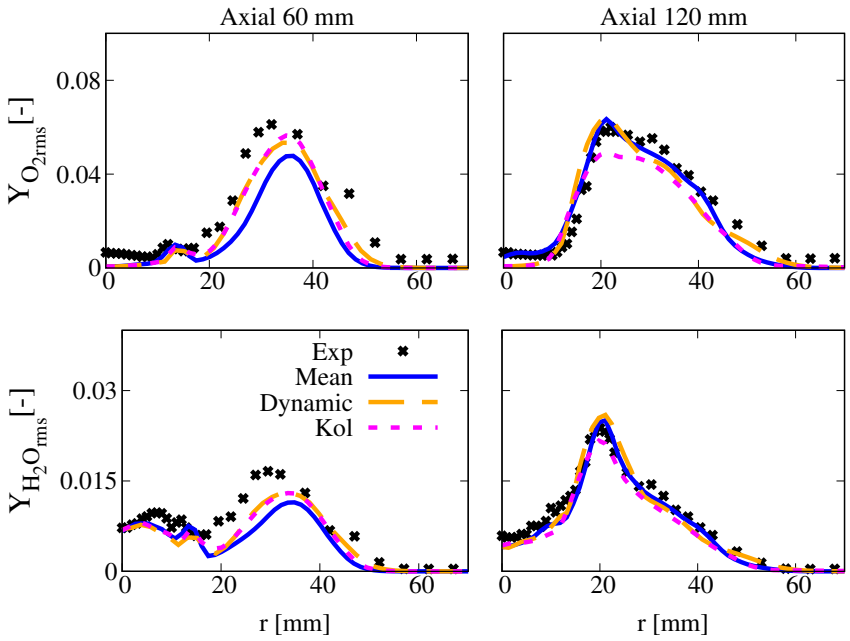

Figure 14: RMS O_2 and H_2O mass fraction profiles at sampled locations from the three approaches for the evaluation of mixing time scale compared with the experimental data. Mean: geometric mean of the Kolmogorov time scale and sub-grid velocity stretch time; Dynamic: dynamic mixing time scale; Kol: Kolmogorov mixing time scale.

Moreover, the mean and rms values for minor species of OH are shown in Figure 15. The peak values are overall well predicted with all the mixing models. From the experimental data, there is also high OH intensity at the centerline, however, such data could be erroneous because of an artefact of interference from the fuel.

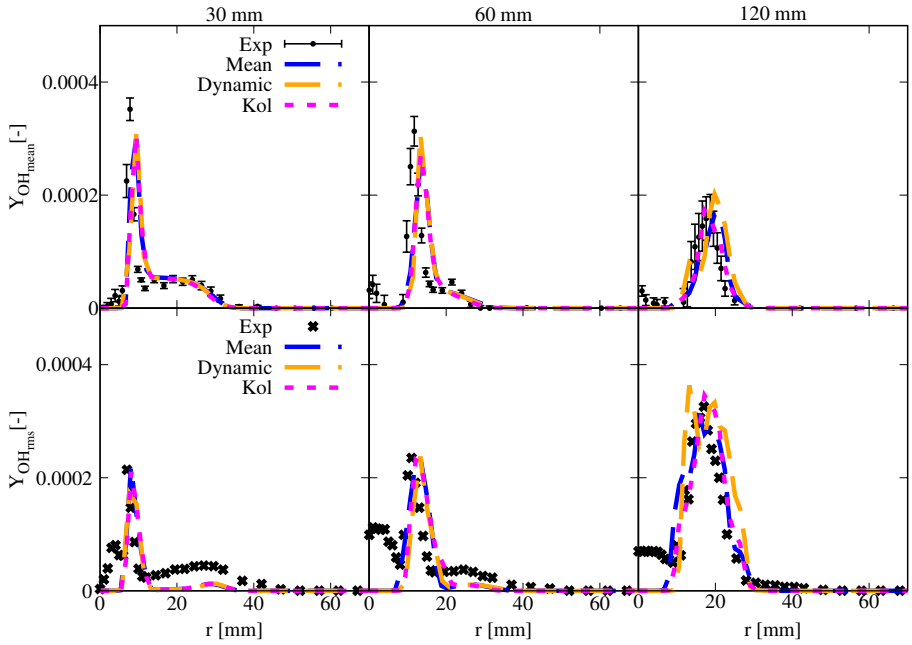

Figure 15: Mean and RMS OH mass fraction profiles at sampled locations from the three approaches for the evaluation of mixing time scale compared with the experimental data. Mean: geometric mean of the Kolmogorov time scale and sub-grid velocity stretch time; Dynamic: dynamic mixing time scale; Kol: Kolmogorov mixing time scale.

4.4. Dynamic PaSR model with high turbulence

From Section 4.3, the dynamic model presents slightly better performance than the other two mixing models, however, its advantage is not well appreciated. Therefore, in this section, the jet Reynolds number is increased to 20 k, leading to a more intense interactions between the turbulence and chemical reactions, as depicted by the temperature scatter data in Figure 16. At z = 60 and 120 mm as well as at the centerline, more data points fall in the low temperature area. Some points even reach around 500 K at the stoichiometric mixture fraction. Such case with high level of local extinction brings challenges to the numerical simulation and at the same time, the advanced estimation of mixing time in the combustion model becomes more important.

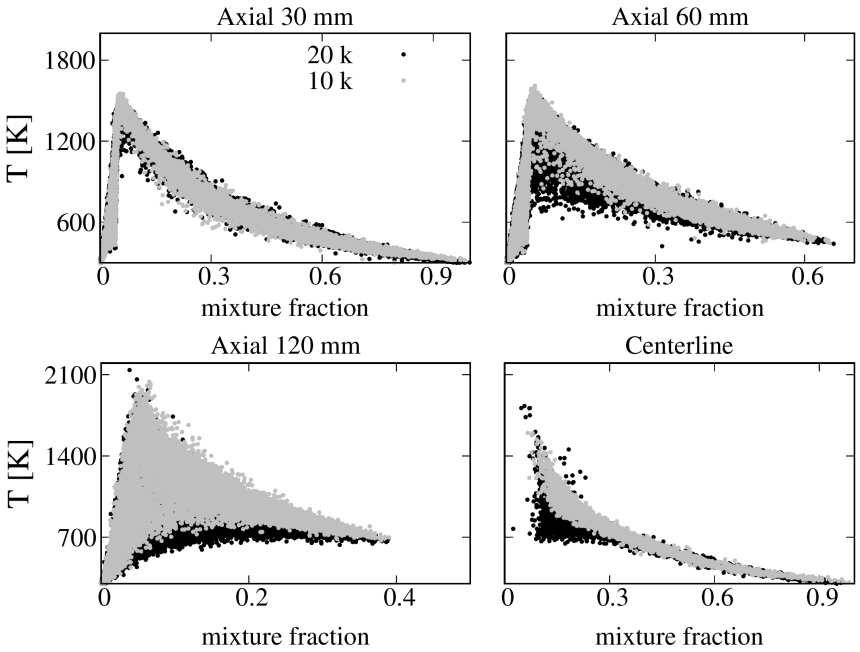

Figure 16: Scatter data of temperature for the cases with Reynolds number of 20 k and 10 k.

The comparison between the averaged OH mass fraction and HRR from the conventional evaluation of the mixing time (geometric mean of Kolmogorov scale and sub-grid stretching time) and the dynamic formulation are demonstrated in Figure 17. Three contour lines for HRR are shown in Figure 17a, the 5×10^5, 1×10^7 and 5×10^7 W/m^3. Apparently they all break in the middle of the domain, at around z = 0.1 - 0.13 m. The mean OH distribution disappear from z = 0.07 m. Such observations indicate that the flame tends to extinguish. Further downstream, the entrainment of high concentration of oxygen from air stream doe not help the flame to ignite again. On the contrary, in Figure 17b, using the dynamic mixing model re-ignites the flame after z = 0.08 m. The contour lines of 1×10^7 and 5×10^7 W/m^3 are also shown. The 1×10^7 W/m^3 level of heat release does not break, as depicted in Figure 17a.

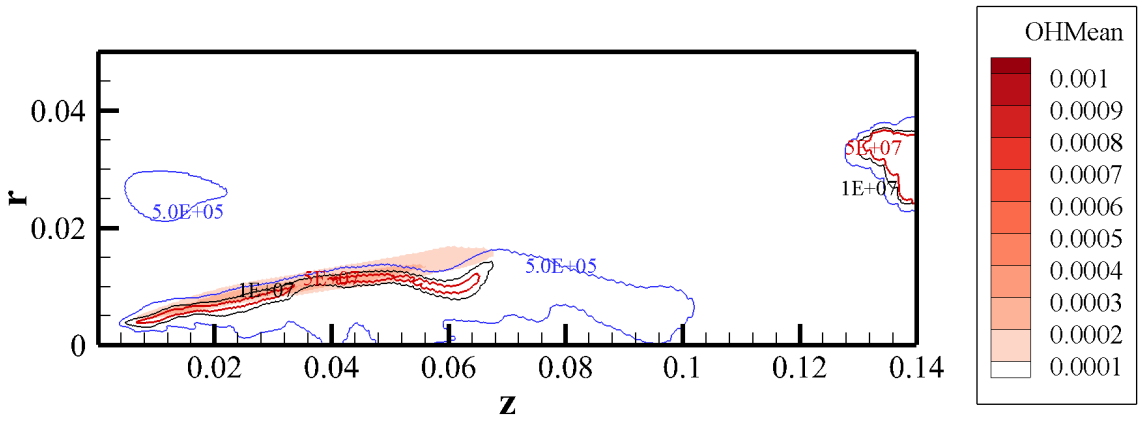

(a) Mean

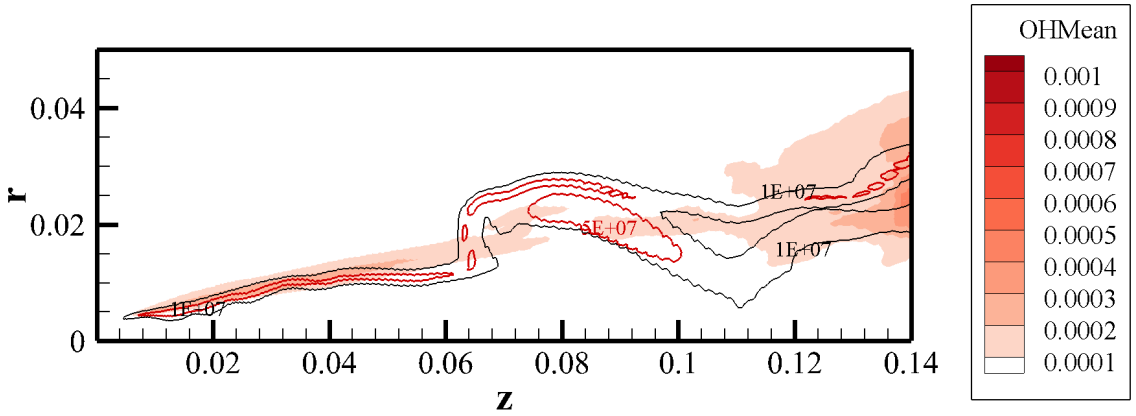

(b) Dynamic

Figure 17: Mean OH mass fraction contour plot with heat release rate (HRR) contour lines from the geometric mean and dynamic evaluation of mixing time scale. The unit of HRR is W/m^3.

The mixture fraction line plots are first validated against the experimental data, showing the prediction of the flow field (the measured data for velocity field is not available). The two mixing models show very similar mixture fraction profiles for the at 30/60/120 mm axial location. However, at the centerline, after around z = 130 mm, the case with conventional estimation of mixing time scale under-predicts the centerline mean mixture fraction. According to the mean OH distribution and HRR contour lines, even though there is still heat release captured after z = 130 mm for the case with conventional evaluation of mixing time, the OH does not appear again—the flame fails to re-ignite.

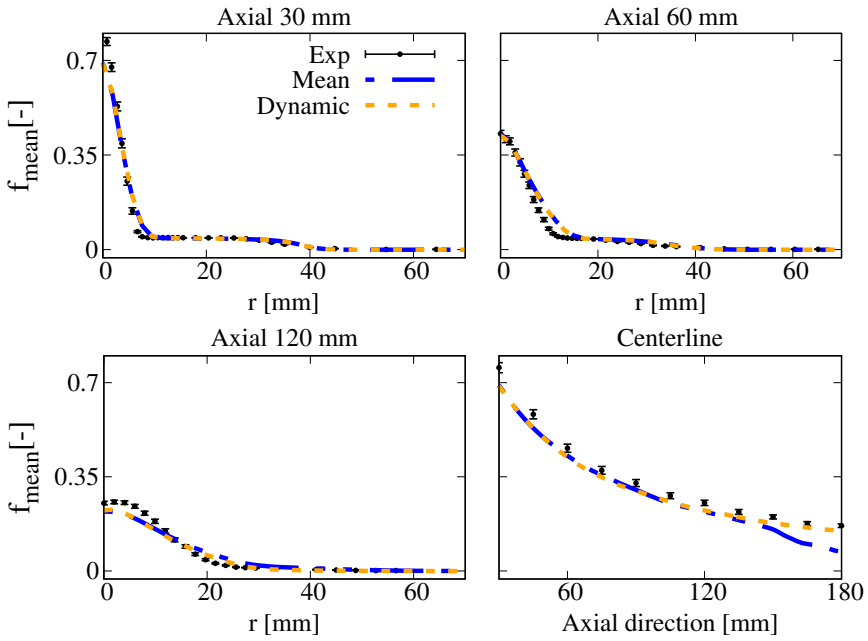

Figure 18: Mean mixture fraction profiles from simulations with conventional and dynamic evaluation of mixing time scale for the 3% oxygen level, 20 k Reynolds number case compared with experimental data. Mean: conventional evaluation, geometric mean of Kolmogorov scale and sub-grid stretching time. Dynamic: dynamic estimation of mixing time scale.

The high turbulence with low oxygen level in the coflow could also lead to instabilities in the flame without a proper choice of the mixing model. In Figure 19, the mean temperature profile is presented. Both models present slightly shifted (by about 4 mm) peak value location at z = 30 mm and z = 60 mm. At z = 120 mm, the dynamic model shows excellent agreement with regard to the experimental profile, while the other one has over-prediction at radial location after 20 mm—it comes probably from the instability problem of the system. Such problem can be further identified by the RMS temperature profiles, in Figure 20. At z = 120 mm and the centerline, the RMS temperature value from conventional mixing model increases drastically, implying the oscillation of flame that causes extinction downstream.

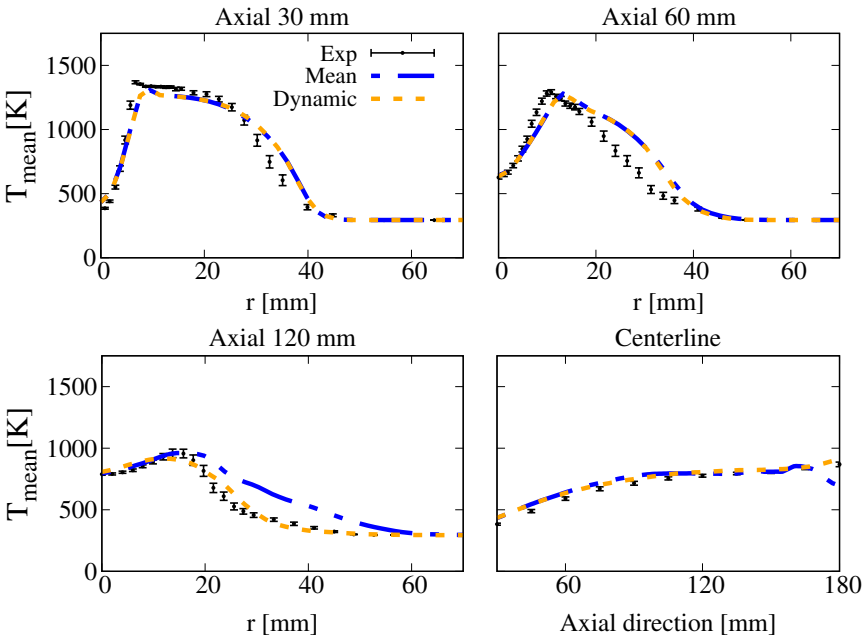

Figure 19: Mean temperature profiles from simulations with conventional and dynamic evaluation of mixing time scale for the 3% oxygen level, 20 k Reynolds number case compared with experimental data. Mean: conventional evaluation, geometric mean of Kolmogorov scale and sub-grid stretching time. Dynamic: dynamic estimation of mixing time scale.

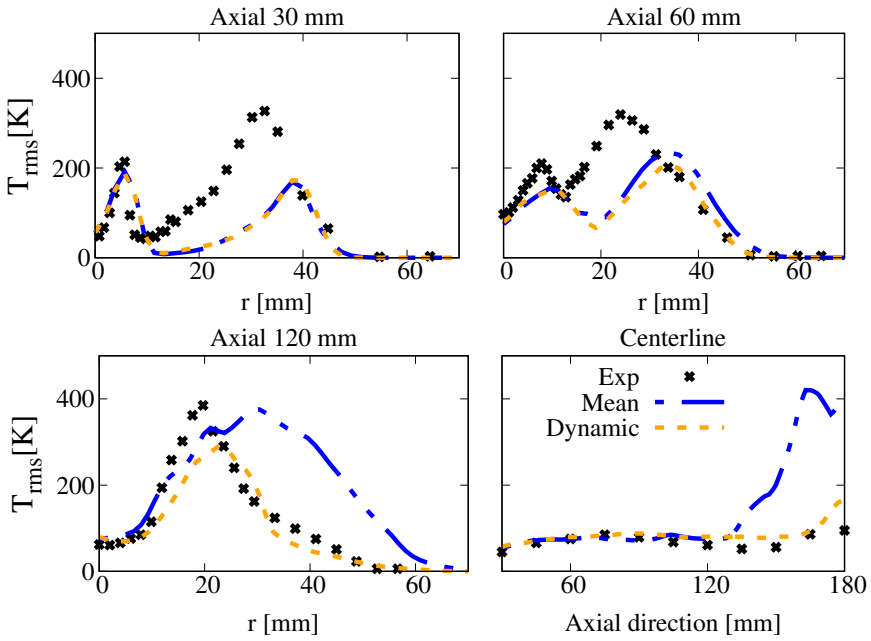

Figure 20: RMS temperature profiles from simulations with conventional and dynamic evaluation of mixing time scale for the 3% oxygen level, 20 k Reynolds number case compared with experimental data. Mean: conventional evaluation, geometric mean of Kolmogorov scale and sub-grid stretching time. Dynamic: dynamic estimation of mixing time scale.

Similar observations are captured from Figure 21, on the mean H_2O species mass fraction profiles. On the other hand, the dynamic model follows the trend of H_2O production with satisfaction, especially on the centerline. The experimental data from the jet Reynold number of 10 k case is compared with the 20 k one for the centerline profile. The availability of the experimental data starts from z = 30 mm. Beginning with the same boundary condition of mean H_2O mass fraction, the 10 k case has the trend of increasing H_2O production. However, the 20 k case keeps the trend until z = 100 mm and the H_2O level decreases slightly after. At around z = 150 mm, the production of H_2O increases again. Such tendency is well captured with the dynamic mixing model.

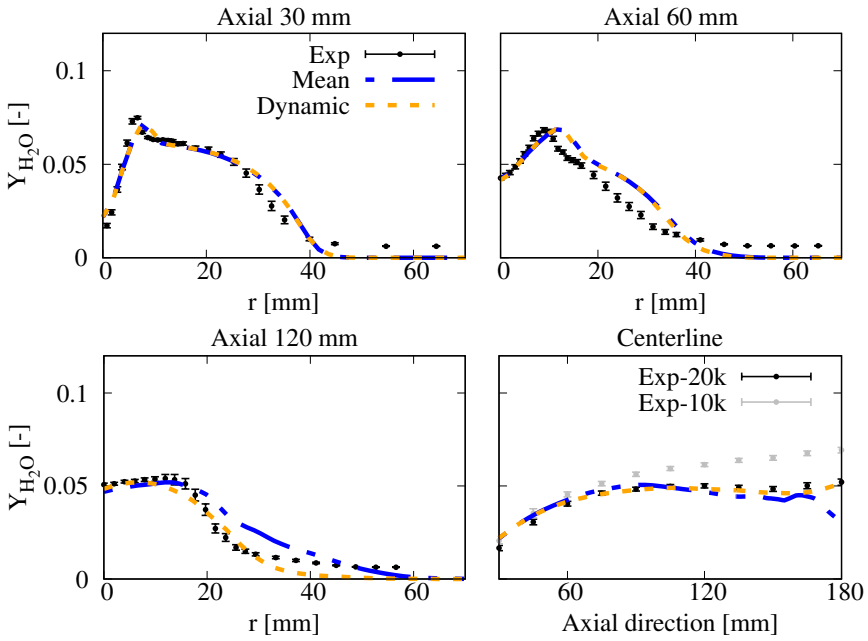

Figure 21: Mean H_2O species mass fraction profiles from simulations with conventional and dynamic evaluation of mixing time scale for the 3% oxygen level, 20 k Reynolds number case compared with experimental data. Mean: conventional evaluation, geometric mean of Kolmogorov scale and sub-grid stretching time. Dynamic: dynamic estimation of mixing time scale.

5. Conclusion

Large Eddy Simulation (LES) with finite-rate combustion models is carried out on the jet-in-hot-coflow (JHC) burner having three different coflow oxygen levels and two fuel jet Reynolds numbers, reaching the following conclusions:

- Suppressed production of OH, CO and heat release is observed when the coflow oxygen level is reduced from 9% to 3%. Such numerical profiles agrees with the experimental observations. The local extinction that can be captured for the 3% case is not shown for the 9% case.

- The implicit combustion models offer satisfactory prediction on the all three cases with different coflow oxygen levels. The profiles obtained with implicit models are very similar to the ones with PaSR.

- Compared to the mixing time scale estimation using the conventional definition (based on Kolmogorov or/and sub-grid stretching time), the dynamic evaluation provides numerical results closer to the experimental data. This is especially obvious for the RMS

valus. More importantly, there is no obvious increase of CPU time when the dynamic model is used, even though three more transport equations need to be solved.

– When the fuel jet Reynolds number is increased from 10 k to 20 k, the conventional definition for mixing time scale fails to predict the re-ignition of the flame downstream. Under-prediction is captured on the centerline. The dynamic model captured the trend well, with good agreement compared to the experimental data.

These results demonstrate the applicability of implicit LES combustion models on wider range of JHC flames and proves the capabilities of dynamic mixing model in PaSR regarding the simulation of MILD flames with higher turbulence level.

Acknowledgments

This project has received funding from the European Union′s Horizon 2020 research and innovation program under the Marie Skłodowska-Curie grant agreement No. 643134. The research of the last author is sponsored by the European Research Council, Starting Grant No. 714605.

References

[1] J. A. Wünning and J. G. Wünning. Flameless oxidation to reduce thermal NO-formation. *Progress in Energy and Combustion Science*, 23:81–94, 1997.

[2] A. Cavaliere and M. de Joannon. MILD combustion. *Progress in Energy and Combustion Science*, 30:329–366, 2004.

[3] M. de Joannon, G. Sorrentino, and A. Cavaliere. MILD combustion in diffusion-controlled regimes of hot diluted fuel. *Combustion and Flame*, 159:1832–1839, 2012.

[4] Alessandro Parente, Mohammad Rafi Malik, Francesco Contino, Alberto Cuoci, and Bassam B. Dally. Extension of the Eddy Dissipation Concept for turbulence/chemistry interactions to MILD combustion. *Fuel*, 163:98–111, 2015.

[5] Yizhuo He, Chun Zou, Yu Song, Yang Liu, and Chuguang Zheng. Numerical study of characteristics on NO formation in methane MILD combustion with simultaneously hot and diluted oxidant and fuel (HDO/HDF). *Energy*, 112:1024–1035, 2016.

[6] Marco Ferrarotti, Chiara Galletti, Alessandro Parente, and Leonardo Tognotti. Development of reduced NOx models for flameless combustion. In *18th IFRF Members Conference*, 2015.

[7] G. G. Szegö, B. B. Dally, and G. J. Nathan. Scaling of NOx emissions from a laboratory-scale MILD combustion furnace. *Combustion and Flame*, 154:281–295, 2008.

[8] Amir Mardani, Sadegh Tabejamaat, and Shahla Hassanpour. Numerical study of CO and CO2 formation in CH4/H2 blended flame under MILD condition. *Combustion and Flame*, 160:1636–1649, 2013.

[9] E. Oldenhof, Mark J. Tummers, E.H. van Veen, and D.J.E.M. Roekaerts. Ignition kernel formation and lift-off behaviour of Jet-in-Hot-Coflow flames. *Combustion and Flame*, 157:1167–1178, 2010.

[10] B. B. Dally, A. N. Karpetis, and R. S. Barlow. Structure of turbulent non-premixed jet flames in a diluted hot coflow. *Proceedings of the Combustion Institute*, 29:1147–1154, 2002.

[11] F. C. Christo and B. B. Dally. Modelling turbulent reacting jets issuing into a hot and diluted coflow. *Combustion and Flame*, 142:117–129, 2005.

[12] Alessio Frassoldati, Pratyush Sharma, Alberto Cuoci, Tiziano Faravelli, and Eliseo Ranzi. Kinetic and fluid dynamics modeling of methane/hydrogen jet flames in diluted coflow. *Applied Thermal Engineering*, 30:376–383, 2009.

[13] Amir Mardani, Sadegh Tabejamaat, and Mohsen Ghamari. Numerical study of influence of molecular diffusion in the MILD combustion regime. *Combustion Theory and Modelling*, 14(5):747–774, 2010.

[14] Ashoke De, Ernst Oldenhof, Pratap Sathiah, and Dirk Roekaerts. Numerical simulation of Delft-Jet-in-Hot-Coflow (DJHC) flames using the Eddy Dissipation Concept model for turbulence-chemistry interaction. *Flow Turbulence Combustion*, 87:537–567, 2011.

[15] Seyed Reza Shabanian, Paul Ross Medwell, Masoud Rahimi, Alessio Frassoldati, and Alberto Cuoci. Kinetic and fluid dynamic modeling of ethylene jet flames in diluted and heated oxidant stream combustion conditions. *Applied Thermal Engineering*, 52:538–554, 2012.

[16] Michael John Evans, Paul Ross Medwell, and Zhao Feng Tian. Modelling lifted jet flames in a heated coflow using an optimised eddy dissipation concept model. *Combustion Science and Technology*, 187(7):1093–1109, 2015.

[17] Javad Aminian, Chiara Galletti, and Leonardo Tognotti. Extended EDC local extinction model accounting finite-rate chemistry for MILD combustion. *Fuel*, 165:123–133, 2016.

[18] Amir Mardani. Optimization of the Eddy Dissipation Concept (EDC) model for turbulence-chemistry interactions under hot diluted combustion of ch4/h2. *Fuel*, 191:114–129, 2017.

[19] M.J. Evans, A. Chinnici, P.R. Medwell, and J. Ye. Ignition features of methane and ethylene fuel-blends in hot and diluted coflows. *Fuel*, 203:279–289, 2017.

[20] Z. Chen, V.M. Reddy, S. Ruan, N.A.K. Doan, W.L. Roberts, and N. Swaminathan. Simulation of MILD combustion using perfectly stirred reactor model. *Proceedings of the Combustion Institute*, 36(3):4279 –4286, 2017.

[21] Zhiyi Li, Alberto Cuoci, Amsini Sadiki, and Alessandro Parente. Comprehensive numerical study of the Adelaide Jet in Hot-Coflow burner by means of RANS and detailed chemistry. *Energy*, 139:555–570, 2017.

[22] Zhiyi Li, Marco Ferrarotti, Alberto Cuoci, and Alessandro Parente. Finite-rate chemistry modelling of non-conventional combustion regimes using a partially-stirred reactor closure: Combustion model formulation and implementation details. *Applied Energy*, 225:637–655, 2018.

[23] M. Ihme and Y. C. See. LES flamelet modeling of a three-stream MILD combustor: Analysis of flame sensitivity to scalar inflow conditions. *Proceeding of the Combustion Institute*, 33(1):1309–1317, 2011.

[24] Matthias Ihme, Jian Zhang, Guowei He, and Bassam Dally. Large Eddy Simulation of a Jet-in-Hot-Coflow burner operating in the oxygen-diluted combustion regime. *Flow, Turbulence and Combustion*, 89:449–464, 2012.

[25] Rohit Bhaya, Ashoke De, and Rakesh Yadav. Large eddy simulation of mild combustion using pdf-based turbulencechemistry interaction models. *Combustion Science and Technology*, 186(9):1138–1165, 2014.

[26] J.W. Labahn and C.B. Devaud. Large eddy simulations (les) including conditional source-term estimation (cse) applied to two delft-jet-in-hot-coflow (djhc) flames. *Combustion and Flame*, 164:68–84, 2016.

[27] Y. Minamoto and N. Swaminathan. Subgrid scale modelling for MILD combustio. *Proceedings of the Combustion Institute*, 35(3):3529–3536, 2015.

[28] Bjørn F. Magnussen. On the structure of turbulence and a generalized Eddy Dissipation Concept for chemical reaction in turbulent flow. In *19th AIAA Aerospace Science Meeting*, St. Louis, Missouri, USA, January 1981.

[29] I.R. Gran and B. F. Magnussen. A numerical study of a bluff-body stabilized diffusion flame, part 2: Influence of combustion modelling and finite-rate chemistry. *Combustion Science and Technology*, 119(1-6):191–217, 1996.

[30] Bj/orn F. Magnussen. The Eddy Dissipation Concept a bridge between science and technology. In *ECCOMAS Thematic Conference on Computational Combustion*, Lisbon, Portugal, 2005.

[31] J. Chomiak. *Combustion: A Study in Theory, Fact and Application*. Abacus Press/Gorden and Breach Science Publishers, 1990.

[32] Christophe Duwig, Karl Johan Nogenmyr, Cheong Ki Chan, and Matthew J. Dunn. Large eddy simulations of a piloted lean premix jet flame using finite-rate chemistry. *Combustion Theory and Modelling*, 15(4):537–568, 2011.

[33] Zhiyi Li, Alberto Cuoci, and Alessandro Parente. Large eddy simulation of mild combustion using finite rate chemistry: Effect of combustion sub-grid closure. *Proceedings of the Combustion Institute*, 37 (4):4519–4529, 2018.

[34] Fabian Peng Kärrholm. *Numerical Modelling of Diesel Spray Injection, Turbulence Interaction and Combustion*. Phd thesis, Chalmers University of Technology, Chalmers, Sweden, 2008.

[35] P. A. Niklas Nordin. *Comple Chemistry Modeling of Diesel Spray Combustio*. PhD thesis, Chalmers University of Technology, 2001.

[36] J. Chomiak and A. Karlsson. Flame liftoff in diesel sprays. In *Twenty-Sixth Symposium (International) on Combustion*, pages 2557–2564. The Combustion Institute, 1996.

[37] Marco Ferrarotti, Zhiyi Li, and Alessandro Parente. On the role of mixing models in the simulation of MILD combustion using finite-rate chemistry combustion models. *Proceeding of the Combustion Institute*, 000:1–8, 2018.

[38] Y. Afarin, S. Tabejamaat, and A. Mardani. Large eddy simulation study of H2/CH4 flame structure at MILD condition. In *Seventh Mediterranean Combustion Symposium*, Naples, Italy, 2011.

[39] V. Sabelnikov and C. Fureby. Extended les-pasr model for simulation of turbulent combustion. *Progress in Propulsion Physics*, 4:539–568, 2013.

[40] Thierry Poinsot and Denis Veynante. *Theoretical and Numerical Combustion*. R. T. Edwards, 2000.

[41] A. Yoshizawa and K. Horiuti. A statistically-derived subgrid-scale kinetic energy model for the large-eddy simulation of turbulent flows. *Journal of the Physical Society of Japan*, 54:2834–2839, 1985.

[42] S. Huang and Q. S. Li. A new dynamic one-equation subgrid-scale model for large eddy simulations. *International Journal for Numerical Methods in Engineering*, 81:835–865, 2010.

[43] C. Duwig and P. Iudiciani. Large eddy simulation of turbulent combustion in a stagnation point reverse flow combustor using detailed chemistry. *Fuel*, 123:256–273, 2014.

[44] C. Fureby. Comparison of flamelet and finite rate chemistry les for premixed turbulent combustion. In *45th AIAA Aerospace Sciences Meeting and Exhibit*. American Institute of Aeronautics and Astronautics, 2007.

[45] L. Kjäldman, A. Brink, and M. Hupa. Micro mixing time in the Eddy Dissipation Concept. *Combustion Science and Technology*, 154:207–227, 2007.

[46] Venkatramanan Raman and Heinz Pitsch. A consistent LES/filtered-density function formulation for the simulation of turbulent flames with detailed chemistry. *Proceedings of the Combustion Institute*, 31(2):1711– 1719, 2007.

[47] E. Knudsen, E. S. Richardson, E. M. Doran, H. Pitsch, and J. H. Chen. Modeling scalar dissipation and scalar variance in large eddy simulation: Algebraic and transport equation closures. *Physics of Fluids*, 24(055103), 2012.

[48] Benjamin J. Isaac, Alessandro Parente, Chiara Galletti, Jeremy N. Thornock, Philip J. Smith, and Leonardo Tognotti. A novel methodology for chemical time scale evaluation with detailed chemical reaction kinetic. *Energy Fuels*, 27(4):2255–2265, 2013.

[49] R. O. Fox. *Computational Models for Turbulent Reacting Flows*. Cambridge University Press, Cambridge, UK, 2003.

[50] William L. Oberkampf and Matthew F. Barone. Measures of agreement between computation and experiment: Validation metrics. *Journal of Computational Physics*, 217(1):5–36, 2006.

[51] Nikolai Kornev, Hannes Kröger, and Egon Hassel. Synthesis of homogeneous anisotropic turbulent fieldswith prescribed second-order statisticsby the random spots method. *Communications in Numerical Methods in Engineering*, 24:875–877, 2008.

[52] R. W. Bilger, S. H. Stårner, and R. J. KEE. On reduced mechanisms for methane-air combustion in nonpremixed flames. *Combustion and Flame*, 80(2):135–149, 1990.

5.7 Journal paper 7

This paper was published in Combustion and Flame.

Characterization of turbulent combustion at MILD conditions using tangential stretching rate

Zhiyi Li[a,b,*], Riccardo Malpica Galassi[c], Pietro Paolo Ciottoli[c], Alessandro Parente[a,b,**], Mauro Valorani[c]

[a] *Université Libre de Bruxelles, Ecole polytechnique de Bruxelles, Aero-Thermo-Mechanics Laboratory, Brussels, Belgium*

[b] *Université Libre de Bruxelles and Vrije Universiteit Brussel, Combustion and Robust Optimization Group (BURN), Brussels, Belgium*

[c] *Mechanical and Aerospace Engineering Department, Sapienza University of Rome, Via Eudossiana, 18, Rome 00184, Italy*

Abstract

This article presents a numerical study of a jet-in-hot-coflow (JHC) burner which emulates Moderate or Intense Low-oxygen Dilution (MILD) conditions. Such combustion regime offers reduction in pollutant emissions and improvements in efficiency. However, some phenomena like the relations between auto-ignition and flame propagation, local extinction and re-ignition are not easily detected by experimental analysis or through the inspection of CFD calculations. The advanced post-processing tools based on the theories of computational singular perturbation and tangential stretching rate are adopted to investigate the large eddy simulation results of the JHC burner with different coflow oxygen levels. A topological characterization of the flowfield is achieved employing the local number of chemically exhausted modes, highlighting regions that share similar dynamical features. Strong chemical activity, denoted by a small number of exhausted modes, is found in the fuel/coflow mixing layer and, to a minor extent, in the coflow/air mixing layer, exhibiting correlation with the higher heat release rate zones. The analysis of the reactive layers with the tangential stretching rate suggests that the flame under MILD condition is initiated by auto-ignition; The ignited flame kernels are transported further downstream by propagation phenomenon. Moreover, the investigation of the TSR participation indices (PIs) mark the local extinction and re-ignition zone for the low oxygen level case, indicating that the lack of oxygen in the coflow suppresses the path to produce final combustion products and heat—thus reducing the reactivity of the whole system.

[*] Zhiyi.Li@ulb.ac.be

[**] Alessandro.Parente@ulb.ac.be

Keywords: Computational Singular Perturbation, MILD combustion, Tangential Stretching Rate, Large Eddy Simulation, jet-in-hot-coflow burner

1. Introduction

The limited availability of fossil fuels and the increasing environmental concerns associated to pollutant emissions and climate change have pushed the development of new combustion technologies that feature high fuel flexibility, increased efficiency and low pollution emissions. One of the novel technology is termed as Moderate or Intense Low oxygen Dilution (MILD) combustion, and has drawn increasing attention for the past few decades [1, 2]. Because of its diluted conditions, non-visible or audible flames and uniform distributed temperature field [3–5], MILD combustion ensures complete combustion while suppressing the formation of pollutants such as CO, NO_x [6, 7] and soot [8].

MILD combustion technology has been applied in several industrial applications [1]. It was introduced originally in industrial furnaces for methane combustion [9] and later extended to other gaseous fuels like hydrogen [10], ethanol [11] as well as liquid [12] and solid [13] fuels. MILD technology has been also proved in gas turbines [11, 14] and hybrid solar thermal devices [15], leading to increased thermal performances with respect to conventional systems.

However, because of its complex features, it is difficult to predict the features from one configuration to another. As a result, to alleviate the dependency on the burner geometry and allow for high-fidelity experiments, model flames like the jet-in-hot-coflow (JHC) [16–18] were built to emulate MILD conditions. The JHC burner has a central high speed jet and a secondary burner providing hot exhaust products mixing with air. Dally et al. [16] used planar laser-induced fluorescence (PLIF) and Rayleigh scattering techniques with an equimolar mixture of CH_4 and H_2. Different oxygen levels (3%, 6% and 9%) were achieved with the addition of nitrogen in the hot coflow. They concluded that the production of CO, NO and OH is suppressed by reducing the oxygen level in the hot coflow. Medwell et al. [19, 20] carried out experiments to reveal the distribution of hydroxyl radical (OH), formaldehyde (CH_2O), and temperature under hydrogen addition. They observed a "lift-off" height based on the weak-to-strong transition of OH and the existence of pre-ignition in the apparent lifted region of these flames. They also revealed that a reduction of O_2 coflow level leads to reduced CH_2O production. In addition to experimental investigations, increasing attention has been paid to the numerical modelling of the JHC burner. Most numerical investigations were carried out using Reynolds Averaged Navier-Stokes (RANS) simulations [21–32], while only a few studies were based on Large Eddy Simulation (LES) [33, 34]. Despite low CPU re-

source requirement of RANS simulation, steady-state assumptions are not able to capture non-equilibrium phenomena, such as local extinction and re-ignition [33]. As a result, Large Eddy Simulation (LES) can potentially reveal more about the fundamental characteristics of MILD combustion.

Due to the strong mixing and the reduced temperature levels in MILD combustion, a stronger competition between chemical reactions and mixing exists in this regime, leading to a Damköhler numbers of order one. As a result, the importance of turbulence-chemistry interactions becomes of paramount importance—which brings to the discussion between autoignition and self-propagation in such combustion regime. MILD conditions are generally achieved by means of exhaust gas recirculation (EGR), driven by the internal burner aerodynamics, or emulated by hot and vitiated co-flows. Given that the temperature of the exhaust gases is higher than the fuel self ignition temperature, autoignition is likely to play an important role in such a regime [1, 2, 35]. Previous DNS results [36, 37] under MILD conditions also substantiate the extensive existence of autoignition, rather than flame propagation. However, some studies reported on the presence of ignition kernels convecting downstream of the flame and towards stoichiometric and richer mixtures [17, 38, 39]. Such studies indicate the strong role of both autoignition and flame self-propagation in MILD regime. De Joannon et al. also found the important role that diffusion plays to initiate the chemical reaction [4, 40] in hot diluted diffusion ignition (HDDI) regime. Furthermore, Doan et al. [41] conducted DNS on non-premixed MILD combustion with interal EGR. They indicated that autoignition occurs in regions with lean mixtures having low ignition delay times, and that ignition kernels propagate into richer mixtures moving downstream.

In order to study turbulence-chemistry interactions and the relationship between flame autoignition and propagation under MILD condition, advanced post-processing tools are required.

The computational singular perturbation (CSP) method [42, 43] enables the definition of rigorous mathematical tools capable of extracting local information from chemically reactive flow fields. It takes advantage of an eigenmode decomposition of the chemical source term to determine the intrinsic chemical timescales, a proper distinction between fast and slow scales, and the dimension of the slow invariant manifold (SIM), which is an attractive low-dimensional subspace where the system evolves according to the slow scales. The dimension of the SIM is related to the number of fast/exhausted chemical modes, being those giving a negligible net contribution to the dynamics, and it is a fair indicator of the actual local degrees of freedom of the chemical system under study.

The slow subspace, which is spanned by the slow modes, contains the active chemical scales, which can be either dissipative or explosive, characterizing an attractive dynamics

towards the SIM and in turn equilibration, or a departing dynamics that drives the system away from equilibrium. The tangential stretching rate (TSR) is able to select, among the slow modes, those where the actual energy propagation takes place. The TSR approach, already employed for the characterization of laminar [44] and turbulent flames [45–47], is a representative of the driving chemical timescale, being either explosive or dissipative. In turn, proper indices are able to select the chemical reactions mostly participating to the dominant chemical eigenmodes, giving the opportunity to further characterize the underlying physics.

The objective of this article is to use the CSP analysis and the concept of TSR to shade light on the intrinsic characteristics of MILD combustion. LES simulations of the JHC burner with coflow oxygen levels of 3%, 6% and 9% are first compared with the available experimental data and observations, showing the validity of the numerical results. The separation between fast and slow modes is then presented, indicating the chemically active and frozen regions forr the system of interest. Furthermore, the chemical and extended TSR with the inclusion of diffusive terms are used to identify the explosive and contractive nature of the system, giving insights on the relations between flame auto-ignition and propagation. Finally, the participation indices (PIs) of each process contributing to the TSR time scale are examined. The large PIs from different coflow oxygen level cases are compared.

2. Theoretical framework

2.1. CSP fundamentals

The species and energy equations that govern the evolution of a reactive-transport system can be cast in the general form of:

$$\frac{\partial \boldsymbol{z}}{\partial t} = \boldsymbol{L}(\boldsymbol{z}) + \boldsymbol{g}(\boldsymbol{z}), \tag{1}$$

where $\boldsymbol{g}(\boldsymbol{z})$ is the chemical source term of the system, $\boldsymbol{L}(\boldsymbol{z})$ is a spatial differential operator (convection and/or diffusion), $\boldsymbol{z}$ is the (N+1)-dimensional state vector including the mass fractions of N species and the temperature. The chemical source term in Eq.(1) can always be written with respect to a new basis, spanned by a set of basis vectors, or modes, $\boldsymbol{a}_i$ (i=1, N+1), to yield:

$$\boldsymbol{g}(\boldsymbol{z}) \; = \sum_{i=1,N+1} \boldsymbol{a}_i(\boldsymbol{z}) f^i(\boldsymbol{z}). \tag{2}$$

where $f^i(\boldsymbol{z}) = f^i(\boldsymbol{g}(\boldsymbol{z})) := \boldsymbol{b}^i \cdot \boldsymbol{g}(\boldsymbol{z})$ is the amplitude of the i-th mode and $\boldsymbol{b}^i$ denotes the dual basis vector, such that $\boldsymbol{b}^i \cdot \boldsymbol{a}_j = \delta^j_i$ and $\sum_i \boldsymbol{a}_i \boldsymbol{b}^i = \mathbf{I}$, with $i = 1, N+1$. The bi-orthonormality condition allows to recover the original representation of $\boldsymbol{g}(\boldsymbol{z})$. Based on CSP, the basis vectors $\boldsymbol{a}_i$ and covectors $\boldsymbol{b}^i$ can be approximated to leading order, by the right and left eigenvectors

of the Jacobian $\boldsymbol{J}_{\boldsymbol{g}}$ of $\boldsymbol{g}(z)$, respectively. This set of basis vectors is traditionally employed in CSP to decouple the chemical modes time-evolution, i.e., each mode amplitude $f^i(\boldsymbol{g})$ evolves in time independently, enabling in turn to define a spectrum of intrinsic local time scales of the reactive system based on $\boldsymbol{g}(z)$, which are defined as the reciprocal of the eigenvalues λ_i of $\boldsymbol{J}_{\boldsymbol{g}}$.

It is well established that dissipative fast time scales, which are associated to the largest negative eigenvalues of $\boldsymbol{J}_{\boldsymbol{g}}$, develop. In purely reactive systems, the CSP modal decomposition enables a fast/slow subspaces partitioning of the original N+1-dimensional tangent space. Ordering the modes based on their associated timescale, from the fastest to the slowest, so that the first ($i = 1$) mode refers to the fastest chemical time scale (largest eigenvalue), the number M of fast modes is defined as the number of modes whose amplitude f^i gives a zero net contribution ($f^i \approx 0$) to the state evolution over a scale of the order τ^{M+1} [48–50]. Hence, the first M timescales are considered exhausted, allowing for the definition of an attractive local subspace - the slow invariant manifold (SIM) - where the system evolves according to the slow scales. The slow time scales can be either dissipative or explosive, characterizing an attractive dynamics towards the SIM and in turn equilibration, or a departing dynamics that drives the system away from equilibrium.

It is worth noting that $f^i \approx 0$ occurs because of cancellations of balancing reactions at equilibrium. Among the fast modes, there might be a subset of modes whose $f^i \approx 0$ occurs because of absence of contributions. We will refer to these modes as frozen modes.

In reactive-transport systems, it is still of interest to obtain information from the chemical source term alone, since it describes the chemical dynamics that interacts with transport [51]. Hence, the SIM dimension becomes a measure of how far is the reactive system away from equilibrium because of transport. At the same time, it may be worth understanding how transport affects the chemical modes. On this regard, the extension of the CSP eigendecomposition to the full reactive-transport system is pursued with a local approach [52] by keeping the purely reactive system's eigen-structure and by projecting the full right-hand-side onto the CSP chemical modes $\boldsymbol{a}_i$, yielding:

$$\frac{\partial z}{\partial t} = \sum_{i=1,N+1} \boldsymbol{a}_i(z) h^i(z). \tag{3}$$

where $h^i(z) = h^i(\boldsymbol{g}(z), \boldsymbol{L}(z)) := \boldsymbol{b}^i \cdot (\boldsymbol{L}(z) + \boldsymbol{g}(z))$ is the modified amplitude of the i-th mode. According to this approach, transport affects the mode amplitudes, i.e., not their directions, within the hypothesis that transport timescales are much slower than the fastest reactive time scales that are associated to the emergence of the low dimensional manifold. In this case, transport only perturbs the system off the chemical manifold, while the fast chemical pro-

cesses rapidly relax the system back onto it.

Consistently with Eq. (3), the effect of transport on the mode amplitudes reveals itself in a different partition of the tangent space, determining the number H of exhausted modes/timescales as the number of modes whose amplitude h^i gives a zero net contribution to the state evolution over a scale of the order of τ^{H+1}. All the considerations that followed the definition of M are naturally extended to a reactive-transport system, e.g. fast/slow species and frozen modes, according to the behavior of h^i. The introduction of the mode amplitudes $h^i(\boldsymbol{z})$ will be central in the definition of the TSR, as detailed in the following section.

2.2. Tangential Stretching Rate

Given a modal decomposition that enables the recognition of a spectrum of intrinsic timescales, M of which are declared exhausted, the important question then becomes how to sort out the most relevant time scales among the $N - M$ intrinsic slow time scales of the system: in fact, it might happen that no or little energy is associated to a specific time scale. In other words, although there might exist a *potential* channel to propagate energy through a mode (at the associated time scale), it might well happen that the system does not select that mode for the *actual* energy propagation. The TSR is a measure of how much the dynamics stretches/contracts in the direction of the vector field and it is employed to characterize the most *energy-containing* scales developing in the system, where the *energy* is the square of the mode amplitude. Based on the TSR approach [44, 53], the local stretching rate of the system dynamics in the direction tangential to the vector field $\boldsymbol{L}(\boldsymbol{z}) + \boldsymbol{g}(\boldsymbol{z})$, is given by

$$\omega_{\tilde{\tau}}(\boldsymbol{L}, \boldsymbol{g}) := \sum_{i=1}^{N} W_i(\boldsymbol{L}, \boldsymbol{g})\ \lambda_i, \tag{4}$$

with λ_i being the eigenvalue of the i-th mode, and the weight, W_i, of each chemical eigenvalue defined as:

$$W_i(\boldsymbol{L}, \boldsymbol{g}) := \frac{h^i(\boldsymbol{L}, \boldsymbol{g})}{|\boldsymbol{L} + \boldsymbol{g}|} \sum_{k=1}^{N} \frac{h^k(\boldsymbol{L}, \boldsymbol{g})}{|\boldsymbol{L} + \boldsymbol{g}|} \left(\boldsymbol{a}_k \cdot \boldsymbol{a}_i\right), \tag{5}$$

where $|\boldsymbol{L} + \boldsymbol{g}|$ is the norm of the RHS of Eq. (1). It follows that the tangential stretching rate $\omega_{\tilde{\tau}}$ is essentially a time scale obtained as a weighted average of all slow time scales[1], with the weight depending on the mode amplitude associated with that scale, and on the relative

[1] The contribution to $\omega_{\tilde{\tau}}$ of an eigenvalue λ_i is of the order $|(h^i)^2\ \lambda_i|$; the mode amplitude of a fast mode, by definition, should be negligibly small, $h^i \sim 0$; however, it can happen that because of numerical inaccuracies h^i is small but finite, say $h^i \sim O(10^{-12})$; this implies that $|(h^i)^2\ \lambda_i| > O(1)$ for $|\lambda_i| > O((h^i)^{-2})$, instead of remaining negligibly small. To prevent this source of contamination, it is safer to restrict the summation in Eqs. (4) and (5) over the slow subspace only.

orientation of the direction of the basis vector associated with that scale and the direction of the vector field. The magnitude of the TSR represents the reciprocal of the most energy containing time scale of the system, while its positive or negative sign indicates an explosive or non-explosive/dissipative nature of the dynamics.

We will refer to the purely reactive *chemical TSR* as $\omega_{\boldsymbol{g}} := \omega_{\tilde{\tau}}(\boldsymbol{L} = 0, \boldsymbol{g})$ and to the reactive-transport *extended TSR* as $\omega_{\boldsymbol{g}+\boldsymbol{L}} := \omega_{\tilde{\tau}}(\boldsymbol{L} \neq 0, \boldsymbol{g})$. When transport is absent, $\omega_{\boldsymbol{g}}$ provides the stretching rate along the unit vector oriented in the direction of the chemical source term. While in a purely reactive system, only $\omega_{\boldsymbol{g}}$ is defined, in a reactive-transport system both quantities are defined and meaningful, $\omega_{\boldsymbol{g}+\boldsymbol{L}}$ being the stretching along the reactive-transport vector field and $\omega_{\boldsymbol{g}}$ the stretching along the chemical source term direction, i.e., the direction the system would follow if transport were abruptly removed. The latter is useful in the characterization of the chemistry budget in a reactive-transport system, i.e. to gain insights into the chemical dynamics that competes against transport. In the current case, it is helpful to give insights on the interactions between flame auto-ignition and self-propagation in the combustion system.

The TSR is contributed by the most energy containing modes, which can be identified by resorting to a participation index of the i-th mode to the TSR, defined as

$$P^{\omega_{\tilde{\tau}}}_{\text{mode}_i}(\boldsymbol{L}, \boldsymbol{g}) := \frac{\bar{W}_i(\boldsymbol{L}, \boldsymbol{g})\ |\lambda_i|}{\sum_{j'=1}^{N} \left|\bar{W}_{j'}(\boldsymbol{L}, \boldsymbol{g})\ \left|\lambda_{j'}\right|\right|} \qquad \text{no sum on i.} \tag{6}$$

It is of interest to quantify the relative contribution of each physical process most contributing to the development of $\omega_{\tilde{\tau}}$, either a chemical reaction or a transport process. Hence, an index is introduced that relates the k–th process to $\omega_{\tilde{\tau}}$, $P^{\omega_{\tilde{\tau}}}_{\text{process}_k}$, as the product of the participation index of the *i*-th mode to the TSR, $P^{\omega_{\tilde{\tau}}}_{\text{mode}_i}$, times the CSP participation index [54, 55] of the k–th process to the i–th mode, $P^{\text{mode}_i}_{\text{process}_k}$, that is:

$$P^{\omega_{\tilde{\tau}}}_{\text{process}_k}(\boldsymbol{L}, \boldsymbol{g}) := \sum_{\text{mode}_i=1}^{N+1} P^{\omega_{\tilde{\tau}}}_{\text{mode}_i}(\boldsymbol{L}, \boldsymbol{g})\ P^{\text{mode}_i}_{\text{process}_k}(\boldsymbol{L}, \boldsymbol{g}). \tag{7}$$

Since the CSP participation indices to each mode $P^{\text{mode}_i}_{\text{process}_k}$ and the indices $P^{\omega_{\tilde{\tau}}}_{\text{mode}_i}$ sum to 1 by construction, it follows that $\sum_{k=1}^{N_{proc}} P^{\omega_{\tilde{\tau}}}_{\text{process}_k} = 1$ as well, in virtue of the following:

$$\sum_{\text{process}_k=1}^{N_{proc}} P^{\omega_{\tilde{\tau}}}_{process_k} = \sum_{\text{process}_k=1}^{N_{proc}} \left(\sum_{\text{mode}_i=1}^{N+1} P^{\omega_{\tilde{\tau}}}_{\text{mode}_i} P^{\text{mode}_i}_{\text{process}_k} \right) = \left(\sum_{\text{mode}_i=1}^{N+1} P^{\omega_{\tilde{\tau}}}_{\text{mode}_i} \right) \left(\sum_{\text{process}_k=1}^{N_{proc}} P^{\text{mode}_i}_{\text{process}_k} \right) = 1. \tag{8}$$

There exist other metrics that allow to identify the processes most contributing to a time scale. On this regard, we have to stress that - by construction - the indices $P^{\omega_{\tilde{\tau}}}_{\text{process}_k}$ select

the processes that are associated with (i) the time scale provided by $\omega_{\tilde{\tau}}$, and (ii) all and only the (active) modes that contribute the most to the "energy" of the system during both the explosive and contractive phases of its dynamics. This way, the user is not requested to make any a-priori assumptions about the specific system of interest.

3. Large Eddy Simulation dataset

The Large Eddy Simulation (LES) dataset used in the present work is taken from the numerical simulation of the jet-in-hot-coflow (JHC) burner [16]. The JHC burner has an insulated and cooled central jet with the inner diameter of 4.25 mm providing an equimolar mixture of CH_4 and H_2. A secondary burner mounted upstream of the exit plane has the inner diameter of 82 mm and provides the hot combustion products. The combustion products are mixed with air and nitrogen, to control the oxygen levels to 3%, 6% and 9%. The 3% case reaches MILD conditions, while the 6% and 9% cases are transitional between MILD and conventional regimes. The burner is mounted in a wind tunnel with the cross section of 254 mm $\times$ 254 mm. The gas temperature and velocity profiles of the central jet, coflow and wind tunnel can be found in Table 1. The experimental data (mean and root-mean-square) of temperature and mass fractions of species (CH_4, H_2, H_2O, CO_2, N_2, O_2, NO, CO, and OH) along the centerline as well as at the radial position of 30/60/120/200 mm are available for validation. More details about the Adelaide JHC burner experiments can be found in [16].

Table 1: Boundary conditions

Profiles	Central jet	Coflow	Tunnel
Velocity	58.74 m/s	3.2 m/s	3.3 m/s
Temperature	294 K	1300 K	294 K

The numerical domain starts from the jet exit location and extends 180 mm axially. The radial direction expands 90 mm from the centerline. The whole domain is discretized with a 3D cylinder structured mesh having ~1.5 million cells. 52 cells are used to discretize the jet diameter. The LEMOS [56] inflow generator for velocity field is used on all the three streams—fuel, coflow and air. The measured mean species mass fraction, temperature and velocity taken 4 mm downstream of the burner exit are used as boundary condition for the simulation. An instantaneous temperature profile is shown on a two-dimensional axisymmetric plane in Figure 1. A reduced skeletal mechanism KEE58 [57] with 17 species and 58 reactions is used in combination with the Laminar Finite Rate (LFR) combustion model [58, 59]. In LFR model, the filtered source term comes directly from the chemical term,

without inclusion of the turbulent effect. The application of the LFR model on JHC burner is compared with the conventional Partially stirred Reactor (PaSR) model in the research work of Li et al. [59], showing that the numerical results obtained with LFR model are very similar to the ones with PaSR model. Then, the CSP analysis is applied on the filtered LES data. The mean temperature and species mass fractions are obtained from averaging the instantaneous profiles after around 16 jet flowthroughs, and 1 coflow and air flowthroughs.

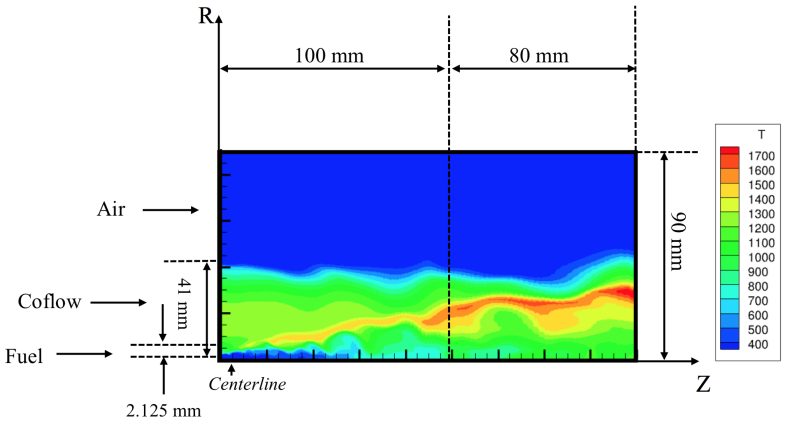

Figure 1: Instantaneous two-dimensional temperature distribution for the JHC burner

4. LES dataset validation

In this section, the LES data obtained with the LFR model are validated against experimental data. In Figure 2 and Figure 3, the mean experimental and numerical temperature and H_2O mass fraction profiles are compared. Overall, a very good agreement is found for both the temperature and H_2O mass fraction. Regarding the mean temperature prediction, slight under-prediction (around 2 %) can be observed at 30 mm axial location, for the 3 % case, while an over-prediction (approximately 11 %) is visible at z 120 mm, for the 9 % case. For the H_2O mass fraction, a better prediction is obtained, showing in general close profiles compared with the experimental ones.

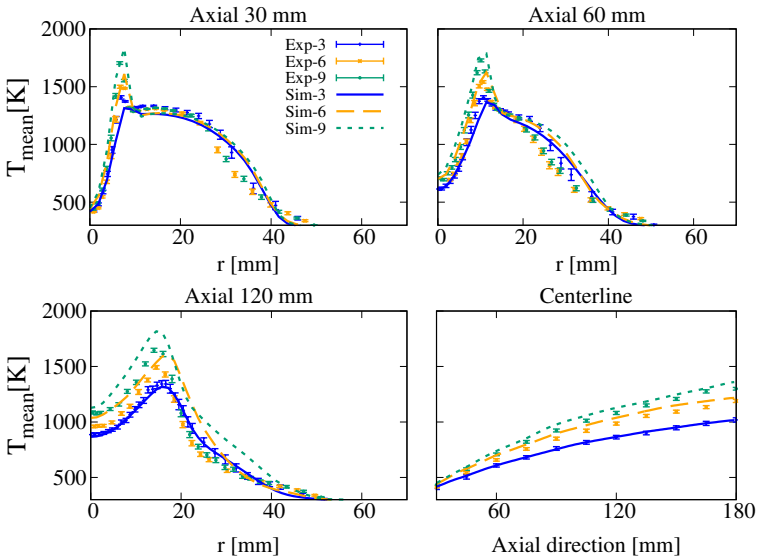

Figure 2: Mean experimental and numerical temperature profiles for the 3 %, 6 % and 9 % O_2 cases.

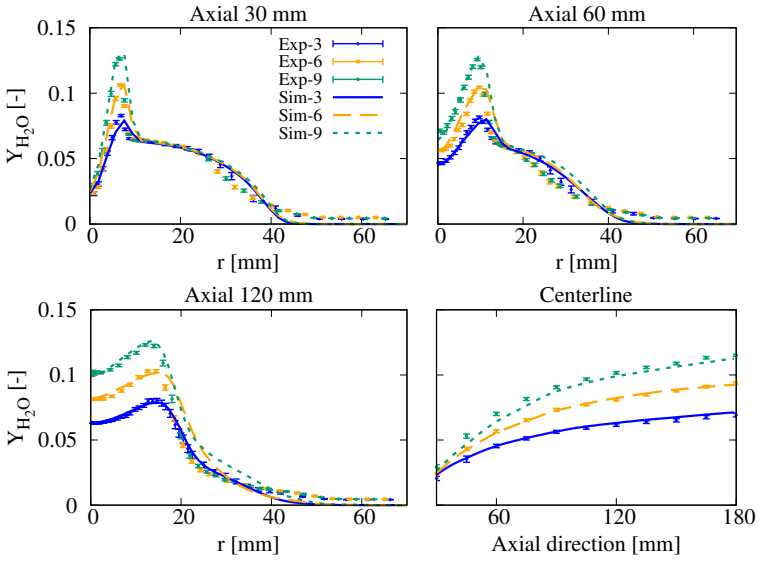

Figure 3: Mean experimental and numerical H_2O mass fraction profiles for the 3 %, 6 % and 9 % O_2 cases.

The mean OH distribution on the axis-symmetric plane (the radius is limited at R = 0.05 m) contour plot is also shown here in Figure 4. All the three flames are slightly lifted. The identified lift-off heights decrease with increasing oxygen levels, from 0.007 m to 0.0045 m and to 0.0042 m. However, since the lift-off heights for the 3 % case (0.0042 m) and 6 % case (0.0045 m) are very close, the conclusion that leads to a monotonic trend between the lift-off height and coflow oxygen level can not be well justified. The lifted characteristic

of the flames can serve to analyse the role of autoignition and self flame propagation in MILD combustion, as further discussed in Section 6.2. The analysis of OH mass fraction profiles (Fig. 4) indicate that OH production is suppressed for the 3 % case, compared to the higher coflow oxygen levels. The 3 % OH mass fraction contour becomes thinner starting from Z = 0.09 m up until Z = 0.13 m; after Z = 0.13 m, the OH layer expands again until the end of the domain. For the other two cases, such phenomenon is not observed, thus indicating the occurrence of local extinction, due to the lack of oxygen in the coflow. The local extinction and flame re-ignition for the 3 % case is also captured by the instantaneous LES results.

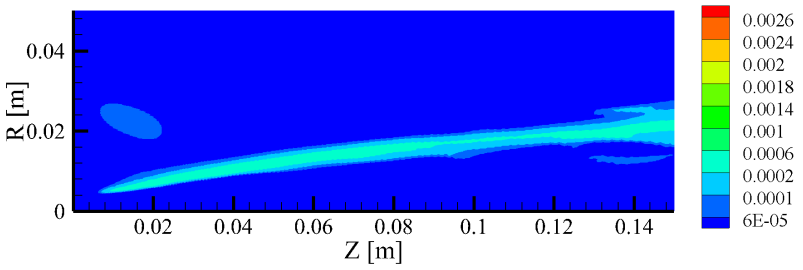

(a) 3 %

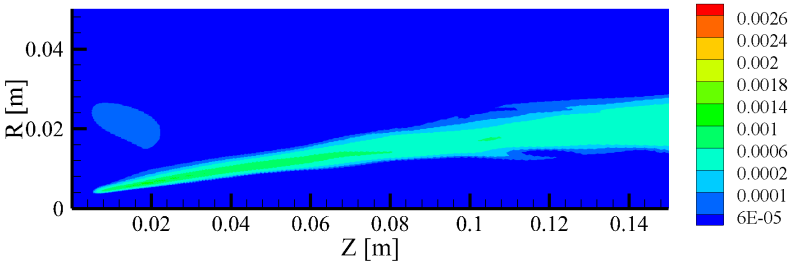

(b) 6 %

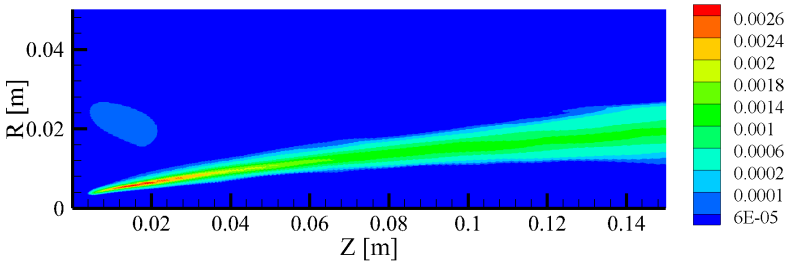

(c) 9 %

Figure 4: Contour plots of mean OH mass fraction for the 3 %, 6 % and 9 % O_2 cases.

5. Flowfield topology based on exhausted modes

The chemical composition space (CCS) is an 18-dimensional (17 species plus temperature) space, which undergoes a local fast/slow partition based on the CSP analysis of the chemical source term. The number M of fast (exhausted) chemical modes gives information about the dimension of the Slow Invariant Manifold (SIM), i.e. how far is the mixture from chemical equilibrium. The spatial distribution of M is a fair candidate for the recognition of zones that share similar dynamical features. The higher M, the closer the mixture to equilibrium. Hence, a large number of slow modes (N-M) indicates energetic chemical activity, whose faster time scale is τ^{M+1}. The number of fast (exhausted) modes M, in representative snapshots of the domain for the 3 % and 9 % cases, is shown in Figure 5 (the radius direction is limited to R = 0.06 m).

The fast/slow partition allows to topologically subdivide the domain, as shown in Figure 6. Moving radially outward from the centerline, the three streams, namely fuel, coflow and air, are injected in the field in different thermochemical states. Fuel and air are mixtures in equilibrium, hence chemically inactive, and are identified as frozen (white in Fig. 5) by the CSP analysis. Indeed, such mixtures remain frozen as these are convected downstream, until mixing with the coflow takes place. On the other hand, the coflow stream is injected in a non-equilibrium state. As soon as it enters the field, the hot reaction products mixture, composed of CO, O_2, H_2O and CO_2, starts to react, activating a number of slow (energetic) chemical scales and exhibiting a fast subspace of dimension 3−4. This region with M=3−4 persists until Z≈0.01 m, where an increase in the heat release rate is observed, and will be referred to as Region 1. Proceeding downstream, the dynamics of the coflow, still unmixed with fuel and air, evolves in a distinctive triangle-shaped region, referred to as Region 2. In this region, as the mixture flows downstream, the fast subspace dimension grows up to 11 fast modes, indicating a reduction of the slow manifold dimensionality, hence the evolution towards chemical equilibrium, and a reduction of the heat release rate, whose local minima overlap the region of largest fast subspace dimension. Transport keeps the chemical composition off the manifold, leaving 3 active (slow) chemical modes which compete against transport, establishing a balance. This condition persists in the region until Z = 0.1 m for the 3 % case and Z = 0.08 m for the 9 % case.

The high concentration of O_2 in the air stream starts to penetrate through the coflow stream and reacts with the fuel stream, breaking such equilibrium condition, and this is indicated by the decrease of M. Even though fuel and air streams come into contact at this location, both the air/coflow and fuel/coflow mixing layers exhibit chemical activity. These two layers will be referred to as Region 3 and 4, respectively. Note first that the two mixing

layers, which surround Region 2, show the smallest numbers of exhausted modes in the field, indicating fast and energetic chemical processes.

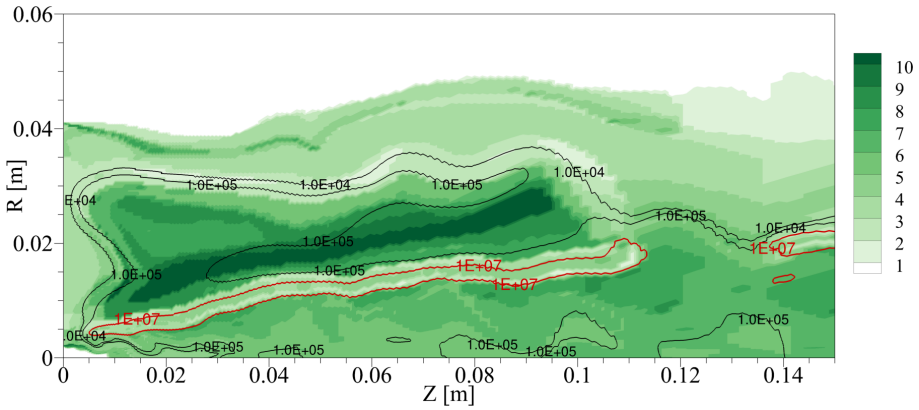

(a) 3%

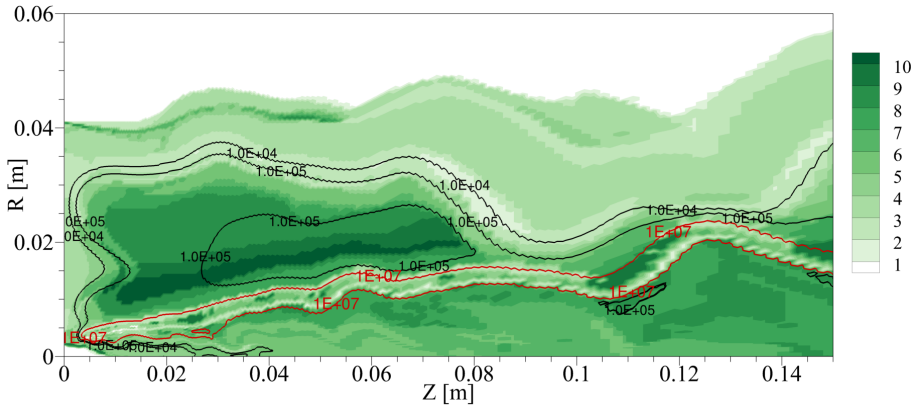

(b) 9%

Figure 5: Number of fast modes, with contour lines of heat release rate for the 3% (a) and 9% (b) O_2 cases

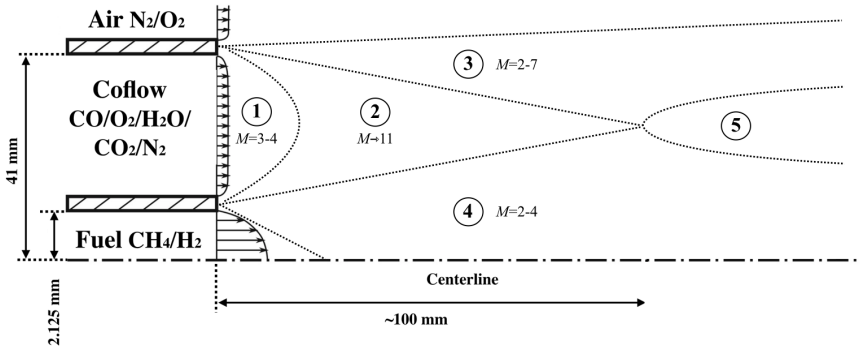

Figure 6: 2D axi-symmetric sketch of the AJHC burner with topology (adapted from [34]).

Region 3 features the mixing layer between the air and coflow streams. This layer is characterized by a rather low number of fast modes (2−7), indicating medium-to-intense chemical activity due to the interaction between the hot reaction products and the diluted air. A moderate heat release rate (10^{4-5} W/m^3) is found in this layer with a steep increase where the number of fast modes has a minimum, i.e. closer to the hot coflow. Different from Region 4, the chemical activities in Region 3 do not have flame structures, because of the lack of fuel.

The zone between the fuel stream and coflow stream, indicated as Region 4, is characterized by another layer exhibiting a minimum of the number of fast modes, between 2 and 4. This is also the reaction layer which is deemed to reach MILD condition for the 3 % case experimentally. Here, the chemical system evolves with a large number of slow degrees of freedom, indicating high energetic chemical activity. Moreover, this layer features the largest positive heat release rate (10^{7-8} W/m^3, indicated with a red contour line in Fig. 5).

Downstream the entrainment point of the air in the fuel stream, denoted by the end of Region 2 (Z $\simeq$ 0.11 m and Z $\simeq$ 0.08 m for the 3% and 9% cases, respectively), the 3% and 9% cases behave differently. This region will be referred to as Region 5. The 3 % case shows a break in the minimum-M layer and a sudden decrease of HRR, which increases again downstream. The 9 % case, instead, exhibits a continuous minimum-M layer, which merges with the other one originating from the air/coflow mixing layer. Moreover, there seems to persist an inner region between the two, with a larger M, which shrinks and spreads according to the turbulent flowfield, downstream of Z $\simeq$ 0.08 m.

6. TSR analysis

Further insights on the local dynamics of the reacting flow field are gained with the tangential stretching rate analysis. The TSR identifies, among the slow chemical scales, the

most energetic ones, based on (i) the chemical source term alone (chemical TSR) and (ii) the chemical source plus the diffusion term (extended TSR). Convection is not included in the extended TSR computation, as the fluid particle is observed from a lagrangian point of view. The outcomes of the analysis are: (i) the identification of a local driving chemical timescale, and its explosive/dissipative nature; (ii) the characterization of the local combustion regime, based on the influence of transport on the chemical dynamics, obtained via a comparison between chemical and extended TSRs; (iii) the identification of the chemical reactions mostly participating to the chemical TSR scale, shedding light on the driving chemical processes.

Figures 7 and 8 show the fields of chemical TSR, extended TSR and fastest explosive eigenvalue λ_e, for the 3 and 9 % cases. The role of the fastest explosive mode, typically recognized as the only dominant mode in explosive chemical processes, is discussed and compared with the TSR.

6.1. Chemical TSR

The chemical TSR (ω_g) field along with heat release rate contour lines on the jet axisymmetric plane for the cases with coflow oxygen levels of 3 % and 9 % are presented in Figure 7(a) and 8(a). Most of the domain in both cases show negative ω_g levels, which indicate the dissipative/non-explosive nature of the active chemical processes. Positive values of ω_g are captured in Regions 1, 4 and 5, the latter being for the 3 % case only.

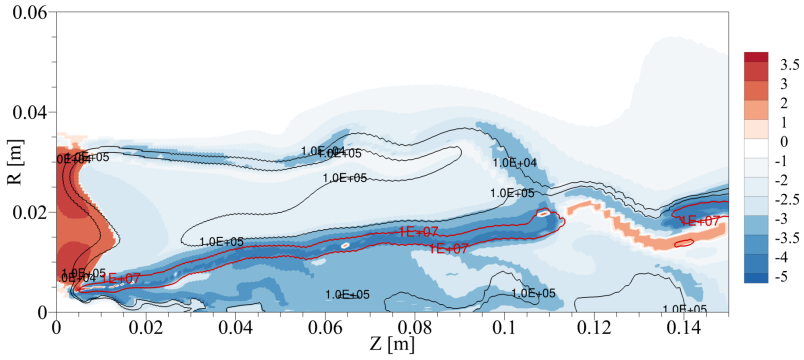

(a) chemical TSR

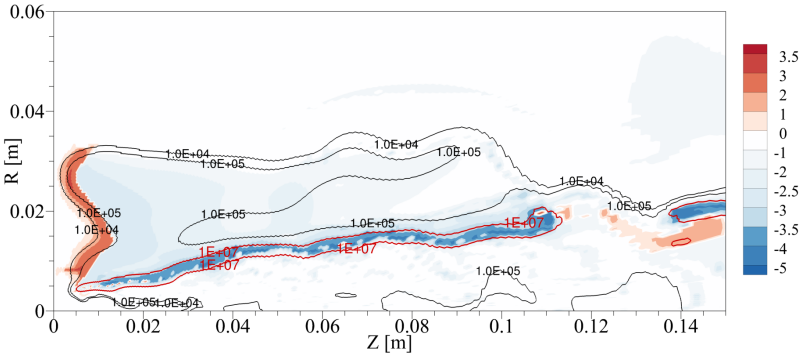

(b) extended TSR

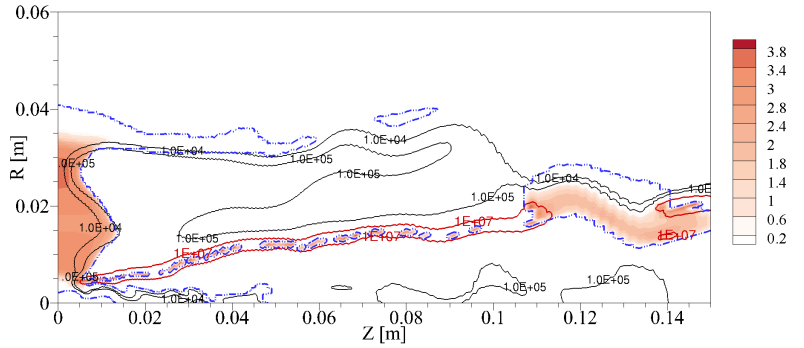

(c) Fast explosive eigenvalue

Figure 7: Contour plots of the chemical TSR, extended TSR and fastest explosive eigenvalue λ_e for the 3 % coflow oxygen level. Heat release rate values are shown with contour lines. The TSR values are shown in logarithmic form, as: sign(TSR) $\times \log_{10} |$ TSR $|$. Zero (white) regions refer to values smaller than 10^0=1 s^{-1}, hence time scales larger than 1 s. Blue dashed contour line in (c) tracks the transition of λ_e to negative values.

Close to the hot coflow exit location upstream (Region 1), positive values for the chemical TSR (ω_g) can be observed, pointing out a chemically explosive area. Since the boundary condition provided in the coflow stream is not a strictly equilibrium mixture and there is no

pre-inlet pipe used for the current LES, the components (CO, O_2, H_2O and CO_2) in the coflow stream show a propensity to evolve on a rather slow explosive timescale of the order of 10^{-3} s, and then to reach their equilibrium state. The equilibrium state is partially reached at around Z = 0.01 m, before the entrainment of air, as discussed in Section 5.

The most negative ω_g region overlaps with the high heat release rate Region 4. The magnitude of ω_g indicates that the timescale associated with the active chemical processes in this region is of the order of $10^{(-5)-(-6)}$ seconds, being the fastest chemical processes in the field. The inner structure of Region 4 shows a distinctive two-branches behavior, which might resemble the lean (upper) and rich (lower) branches of a triple-flame structure [60]. In addition to the interaction zone between the fuel stream and the coflow stream, a fast chemical contractive region can be seen where the mixing between the coflow stream and air stream takes place (Region 3), conforming to the low number of fast modes previously observed. However, the chemical activity develops on slower time scales with respect to Region 4.

A closer inspection of Region 4 reveals the presence of positive values of ω_g. The chemical TSR contour plots for the 3 %, 6 % and 9 % cases are magnified for the location of Z = 0−0.04 m and R = 0−0.03 m, as shown in Figure 10. The area with positive ω_g values in the coflow diminishes from the 3 % to 9 % case; this means that the coflow stream reaches a quasi-equilibrium state earlier in the case with higher coflow oxygen level than that with lower. Apart from the chemically explosive region in the coflow stream, a chain-shaped area with positive ω_g can be seen on the 3 % and 6 % cases in the fuel-coflow mixing layer, revealing a thin region where explosive chemistry takes place. This structure locates where the heat release rate starts to increase. Such observation suggests that the initial ignition of the flame for the 3 % and 6 % cases is chemistry-driven, hence it is led by auto-ignition. This chain structure is not evidently captured in the 9 % case.

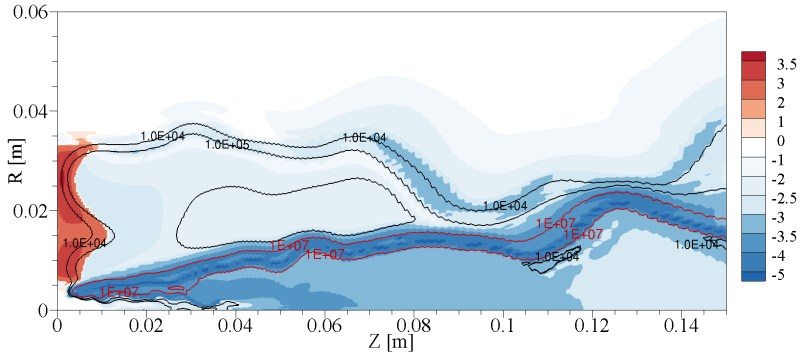

(a) chemical TSR

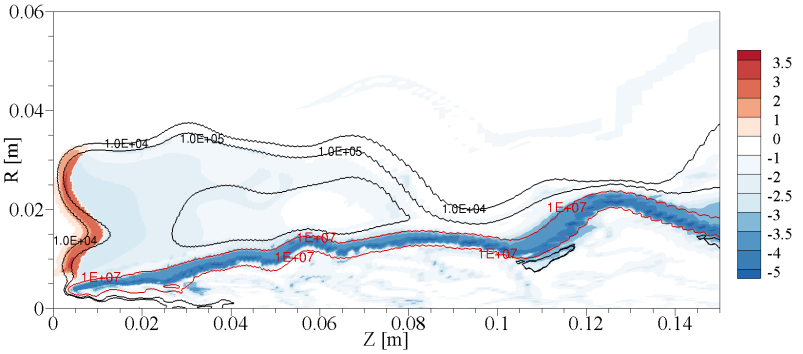

(b) extended TSR

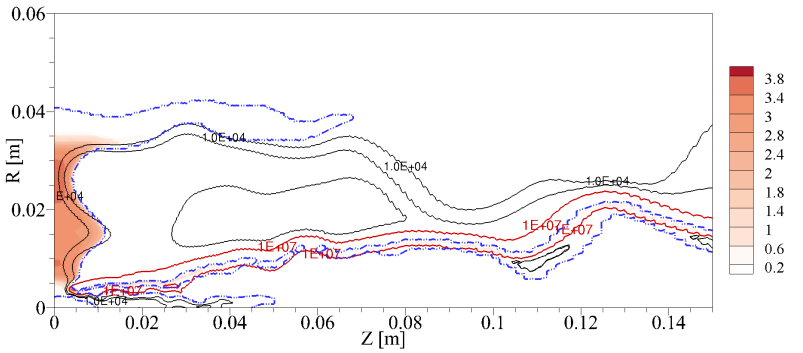

(c) Fast explosive eigenvalue

Figure 8: Contour plots of the chemical TSR, extended TSR and fastest explosive eigenvalue λ_e for the 9 % coflow oxygen level. Heat release rate values are shown with contour lines. The TSR values are shown in logarithmic form, as: sign(TSR) $\times \log_{10} |$ TSR $|$. Zero (white) regions refer to values smaller than 10^0=1 s^{-1}, hence time scales larger than 1 s. Blue dahsed contour line in (c) tracks the transition of λ_e to negative values.

For the 3 % case, positive ω_g values are observed downstream of the jet, starting from around Z = 0.112 m, in Region 5. This indicates local extinction and explosive re-ignition of the flame around that locations, as also supported by the observation of the OH profiles

in Sec. 3. A break between the contour lines of heat release rate is also found in this region. The re-ignition comes from the entrainment of air into the heated fuel stream, as indicated by the oxygen concentration in Figure 9. The entrainment of air for the 3 % case happens at around Z = 0.12 m, which is much later than the 9 % case, at around Z = 0.09 m. The lack of O_2 in the coflow stream and late entrainment of air lead to local extinction for the 3 % case, as indicated by the continuous instantaneous OH mass fraction profiles. Because of slightly increased oxygen levels, local extinction is not present in the 6 % and 9 % cases. This is also confirmed later in Section 6.5, focused on the discussion of chemical reaction participation indices.

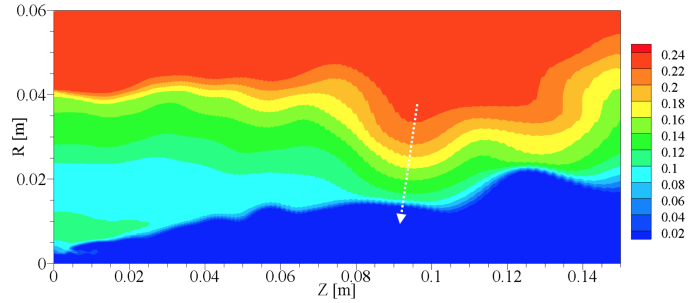

(a) 3 %

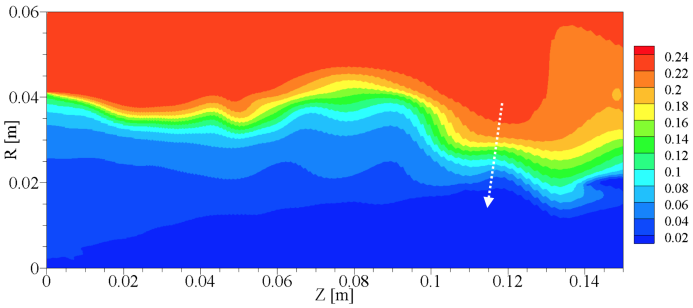

(b) 9 %

Figure 9: Contour plots oxygen levels for the 3 % and 9 % cases.

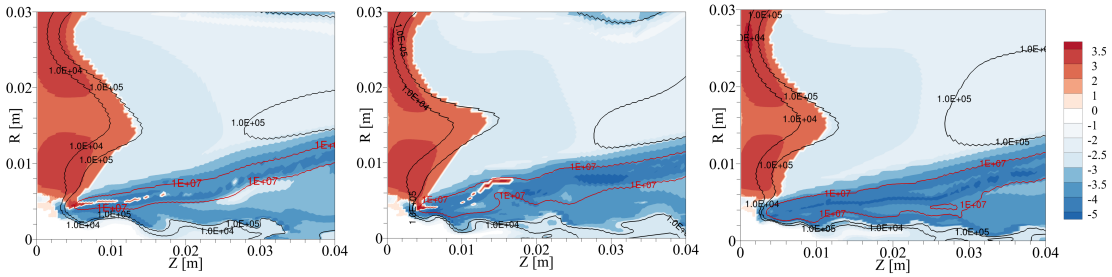

(a) 3 % (b) 6 % (c) 9 %

Figure 10: Chemical TSR contour plots close to jet exit location for the cases with coflow oxygen levels of 3 %, 6 % and 9 %

6.2. Extended TSR

The extended TSR is the measure that allows to quantify the influence of transport on the chemical modes. As discussed in Section 2, transport alters the chemical mode amplitudes, moving the energy content across the modes spectrum. Typically, the comparison of TSR and extended TSR gives insights on the role of transport. For example, in auto-ignitive flames the role of diffusion is negligible and ignition is promoted by chemistry. In this case, TSR and extended TSR (reaction plus diffusion) are comparable and both positive—the influence of transport is minor. On the other hand, in propagating flames, it is the diffusion of radicals that promotes ignition. Hence the TSR and extended TSR are expected to be different—typically negative the first and positive the latter, highlighting the diffusive nature of the driving explosive process.

Figures 7(b) and 8(b) show the field of extended TSR for the 3 % and 9 % cases, respectively. Comparing the extended TSR with the chemical TSR, we observe that: (i) fast chemistry is mitigated by transport, which lowers the magnitude of the driving scale in most of the field, and (ii) there are no purely diffusion-driven fast explosive regions. More specifically, the coflow injection Region 1 appears to be influenced by transport: diffusion mitigates the chemical ignition propensity. This is substantiated by a reduction of both the magnitude and the spatial extension of the positive extended TSR region with respect to the chemical TSR. Region 2 remains almost unaltered by transport. In the mixing layer with diluted air (Region 3), fast chemistry (chemical scale $\sim 10^{-4}$ s) is completely balanced by transport: extended TSR approaches zero. Actually, in this area, the extended TSR tracks the positive eigenvalue λ_e, which however is of order $10^0 = 1$ s^{-1}, yielding a very slow explosive dynamics (not appreciable in the logarithmic scale of the figures). The same equilibrating effect is found in Region 4, specifically in the rich branch of the flame, where λ_e is again tracked by the

extended TSR. These two regions, even though characterized by extremely slow timescales, represent diffusion-driven explosive zones.

The high heat release rate layer of Region 4, instead, maintains its fast contractive character. It appears that transport is shifting the system's dynamics towards slower scales: the major chemically explosive regions, as pointed out by the chemical TSR, appear less explosive and reduced in size, due to the activation of other contractive and slow modes. The chain-shaped explosive area at the leading edge of the flame is tracked by the extended TSR as well, supporting the auto-igniting nature of the regime at that location, with diffusion that plays an opposing role.

A number of positive eigenvalue spots along the high HRR layer, which are not tracked by the chemical TSR, are partially tracked by the extended TSR, however other contractive modes maintain equal importance and the overall value of the extended TSR remains slightly negative. Such observations are substantiate the findings from the research work of Doan et al. [41], who discussed the role of turbulent transport in propagating the flame and distributing the ignition kernels produced from auto-ignition further downstream.

The re-ignition region of the 3% case's Region 5 maintains its explosive character, denoting the chemical nature of the dynamics.

6.3. Explosive eigenvalue

Figures 7(c) and 8(c) show the fastest positive eigenvalue λ_e in logarithmic scale. The blue dashed iso-contour line shows the transition to a negative value. It can be seen that: (i) λ_e exists in wide regions of the field, such as in the fuel stream (rich branch of the flame), in the reaction layer with high HRR (lean branch of the flame), close to the coflow exit location, on the coflow-air mixing layer and, in the 3% case, in the re-ignition region, in agreement with the findings in [61]; (ii) its value is larger than 10^0 s^{-1} only in the red-coloured regions of Figs. 7(c) and 8(c), meaning that λ_e is extremely slow everywhere else inside the blue line; (iii) the chemical TSR coincides with λ_e only in the coflow inlet region and in sub-regions of the fuel-coflow mixing layer, implying that other modes with negative eigenvalue are more important in the regions where the two don't overlap, especially where λ_e is small; (iv) the extended TSR tracks λ_e more extensively in the rich branch of the flame and in the air-coflow mixing layer, denoting a role of transport in the explosivity of the mixture in those locations, which however result to be extremely slow.

6.4. Modes participation to chemical/extended TSR

Additional insights on the nature of the TSRs can be obtained by inquiring the participation indices of each mode to the development of the TSRs, as defined in Eq.6, in selected

1-dimensional slices of the field. In particular, one radial slice is taken at Z = 0.015 m to show the contributions to the positive TSR chain structure in the mixing layer of Region 4, already depicted in Fig. 10.

The participation indices of modes to TSR and extended TSR in a slice taken at Z = 0.015 m for the 3 % and 9 % cases are presented in Figure 6.4. The N_s+1 eigenvalues are shown with grey symbols. The participation to the TSR, which is an index between 0 and 1, is denoted by blue/red markers for chemical/extended TSR, where darker color implies larger participation index.

The 3 % oxygen level case is shown in Fig. 6.4 (a-b). Three zones can be recognized by looking at the number of fast modes, from left to right: the first, with 5-6 exhausted modes, is the rich branch of the flame of Region 4. Chemistry is contractive on a scale of the order of 10^{-4} s, with modes #7 and #8 mostly contributing. Note that λ_e exists in this region, however it is extremely small, collapsing in the zero logarithmic value. The central region, with 3-4 exhausted modes, is the high HRR layer of Region 4 and chemically most active area of the field. In the middle of this region, one point with a couple of positive eigenvalues, belonging to the chain structure, appears at around R = 0.0055 m. The chemical TSR (blue) gets almost full contribution by the large positive eigenvalue. The third region, which lies in the coflow's Region 2, features the increase in the number of exhausted modes observed in Section 5, with the chemical TSR entirely contributed by a negative eigenvalue with a slow scale of the order of 10^{-2} s. The effect of transport can be observed in Fig. 6.4(b). In the first region, transport balances chemistry, yielding a very small extended TSR (zero in the logarithmic scale) that tracks the small positive eigenvalue. In the high HRR central region, the overall effect is to slow down the dynamics, with timescales reduced by approximately 2 orders of magnitude. The explosivity is also reduced, since the major contributor in the positive eigenvalue spot is shifted to the slower positive eigenvalue of the couple. Therefore, conclusion can be drawn that the explosive nature in the high HRR layer is chemistry-driven.

On the other hand, in the 9 % oxygen case, which features a similar topological structure, the positive eigenvalue is not contributing to the chemical TSR. Instead, the addition of transport in the computation of the TSR shifts the contribution towards the positive eigenvalue. Hence, explosivity is more diffusion-driven, even though quite slow (order of 10^{-2} s). However, other contractive modes are important as well. This finding highlights the advantage of using the TSR to select the most energy-containing modes. Tables 2 and 3 show eigenvalues and weights to both chemical and extended TSR in select points of the slice, for the 3% and 9% cases. In particular, two points are investigated: one in the rich (lower) branch and one in the lean (upper) branch of Region 4. The latter is picked where the fast positive eigenvalues show up. The tables highlight how transport shifts the weights across the modes, by mod-

ifying the mode amplitudes. In the 3% case, both the TSRs capture the couple of positive eigenvalues in the lean branch, however transport shifts importance towards the slowest one. In the 9% case, both TSRs don't assign importance to the small positive eigenvalue in the rich branch. Moreover, the extended TSR is capturing the positive eigenvalue in the lean branch whilst the chemical TSR gives importance to fast contractive modes. Note that there are in total 6% importance given to modes #10 and #11 and it translates into large participation of these modes, due to their higher value of λ_i with respect to mode #14.

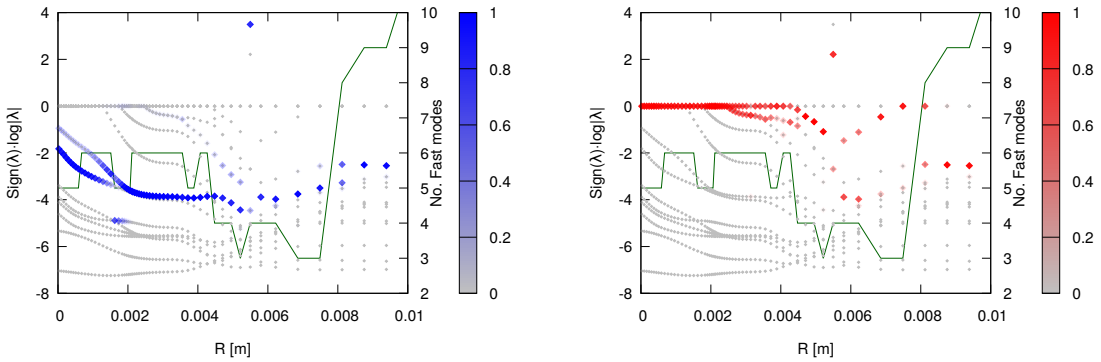

(a) chemical TSR 3 %

(b) extended TSR 3 %

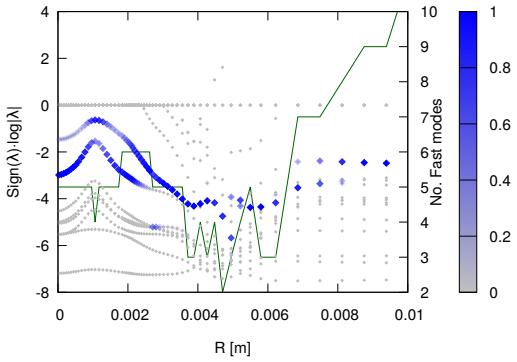

(c) chemical TSR 9 %

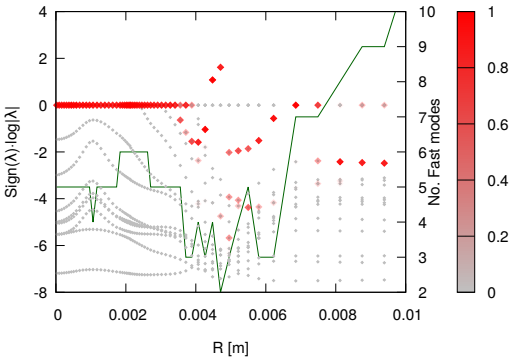

(d) extended TSR 9 %

Figure 11: Participation indices of eigenvalues for the chemical/extended TSR. 3 % and 9 % cases on Z = 0.015 m. Eigenvalues are shown with grey symbols, their participation is denoted by blue/red markers. Number of fast modes is represented with green solid line. Radial direction is clipped at R=0.01 m. Note that the grey symbols show all the eigenvalues, including the fast and conserved ones that do not contribute to TSR.

In summary, both cases (3 % and 9 %) show simultaneous appearance of positive eigenvalues. In these locations, the dynamics of both systems is explosive, since the extended TSR identifies the positive eigenvalues as dominant, however they substantially differ in nature. In the 3 % case, the explosivity is due to chemistry, while in the the 9 % case it originates

Rich branch (R = 0.0021)				Lean branch (R = 0.0055)			
Mode #	λ_i	$W_i(\mathbf{g})$	$W_i(\mathbf{g}+\mathbf{L})$	Mode #	λ_i	$W_i(\mathbf{g})$	$W_i(\mathbf{g}+\mathbf{L})$
1	$-1.53 \cdot 10^{7}$	0 % (fast)	0 % (fast)	1	$-7.55 \cdot 10^{6}$	0 % (fast)	0 % (fast)
2	$-2.71 \cdot 10^{6}$	0 % (fast)	0 % (fast)	2	$-2.81 \cdot 10^{6}$	0 % (fast)	0 % (fast)
3	$-3.68 \cdot 10^{5}$	0 % (fast)	0 % (fast)	3	$-1.42 \cdot 10^{6}$	0 % (fast)	0 %(fast)
4	$-2.85 \cdot 10^{5}$	0 % (fast)	0 % (fast)	4	$-9.40 \cdot 10^{5}$	0 % (fast)	0 %(fast)
5	$-2.34 \cdot 10^{5}$	0 % (fast)	0 % (fast)	5	$-6.14 \cdot 10^{5}$	0 %	0 %
6	$-9.23 \cdot 10^{4}$	0 % (fast)	0 %	6	$-5.69 \cdot 10^{5}$	0 %	0 %
7	$-5.18 \cdot 10^{3}$	0.1 %	0 %	7	$-4.09 \cdot 10^{5}$	0.8 %	0 %
8	$-4.34 \cdot 10^{3}$	98.3 %	0 %	8	$-1.22 \cdot 10^{5}$	0.2 %	0 %
9	$-6.44 \cdot 10^{1}$	0 %	0 %	9	$-1.03 \cdot 10^{5}$	0 %	0 %
10	$-3.44 \cdot 10^{0}$	0 %	0 %	10	$-2.88 \cdot 10^{4}$	5.4 %	0.5 %
11	$-1.91 \cdot 10^{-1} + 9.59 \cdot 10^{-1}\, i$	0.8 %	48.8 %	11	$\mathbf{+2.25 \cdot 10^{3}}$	72.5 %	7.7 %
12	$-1.91 \cdot 10^{-1} + 9.59 \cdot 10^{-1}\, i$	0.8 %	48.8 %	12	$\mathbf{+9.50 \cdot 10^{2}}$	21.8 %	83.8 %
13	$-2.69 \cdot 10^{-2}$	0 %	0 %	13	$-6.53 \cdot 10^{2}$	0 %	0 %
14	$-3.42 \cdot 10^{-4}$	0 %	2.5 %	14	$-1.16 \cdot 10^{2}$	0 %	7.8 %
15	0	0 % (cons)	0 % (cons)	15	0	0 % (cons)	0 % (cons)
16	0	0 % (cons)	0 % (cons)	16	0	0 % (cons)	0 % (cons)
17	0	0 % (cons)	0 % (cons)	17	0	0 % (cons)	0 % (cons)
18	0	0 % (cons)	0 % (cons)	18	0	0 % (cons)	0 % (cons)

Table 2: Eigenvalues and weights to chemical and extended TSR as per Eq.(4) in select points of the slice Z = 0.015m, picked at R = 0.0021 m and R = 0.0055 m. Positive eigenvalues are in bold. Fast and conserved (denoted with cons) modes don't contribute to the TSR because of vanishing amplitude and eigenvalue, respectively. 3% coflow oxygen level case.

from transport. In both cases, the extended TSR tracks the very slow positive eigenvalue in the rich branch of the flame, where the chemical TSR is instead contractive.

6.5. TSR participation indexes

The CSP decomposition allows to quantify the contributions of each chemical reaction to a given CSP mode. In turn, the capability of the TSR to select the energy-carrying modes gives the opportunity to compute a single set of indices, through Eq. 7, that assess the participation of each reaction to the dominant chemical dynamics. Note that, by definition, the fast reactions that concur to the development of the SIM, and that are associated to exhausted modes, are not participating to the TSR.

Figure 12 shows the high TSR participation indices (PIs) developing in the field, in the 3% coflow oxygen level case. The topology already observed in the previous sections is again highlighted by the persistence of the TSR PIs in distinct regions of the field.

Figure 12(a) depicts the forward/backward competition in Region 4 of reaction R3: $CH_4 + H \Leftrightarrow CH_3 + H_2$ (purple/orange). This is expected, being the fuel stream an equi-molar mixture of CH_4 and H_2 which gets heated by the hot coflow. According to Law [62], the forward step of R3, which destructs methane, plays also an inhibiting role in the ignition process,

Rich branch (R = 0.0021)				Lean branch (R = 0.0047)			
Mode #	λ_i	$W_i(\mathbf{g})$	$W_i(\mathbf{g}+\mathbf{L})$	Mode #	λ_i	$W_i(\mathbf{g})$	$W_i(\mathbf{g}+\mathbf{L})$
1	$-1.58 \cdot 10^7$	0 % (fast)	0 % (fast)	1	$-2.58 \cdot 10^7$	0 % (fast)	0 % (fast)
2	$-5.10 \cdot 10^5$	0 % (fast)	0 % (fast)	2	$-1.01 \cdot 10^7$	0 % (fast)	0 % (fast)
3	$-2.60 \cdot 10^5$	0 % (fast)	0 % (fast)	3	$-7.44 \cdot 10^6$	0 %	0 %
4	$-1.14 \cdot 10^5$	0 % (fast)	0 % (fast)	4	$-5.85 \cdot 10^6$	0.1 %	0 %
5	$-9.53 \cdot 10^4$	0 % (fast)	0 % (fast)	5	$-2.55 \cdot 10^6$	0 %	0 %
6	$-5.51 \cdot 10^4$	0 % (fast)	0 % (fast)	6	$-2.53 \cdot 10^6$	0 %	0 %
7	$-1.44 \cdot 10^3$	60.2 %	0 %	7	$-1.64 \cdot 10^6$	0.8 %	0 %
8	$-5.41 \cdot 10^1$	39.6 %	0 %	8	$-1.47 \cdot 10^6 + 9.58 \cdot 10^3\, i$	0 %	0 %
9	$-7.66 \cdot 10^{-2}$	0 %	0 %	9	$-1.47 \cdot 10^6 - 9.58 \cdot 10^3\, i$	0 %	0 %
10	$-5.67 \cdot 10^{-3} + 7.87 \cdot 10^{-3}\, i$	0 %	22.8 %	10	$-5.56 \cdot 10^4 + 6.55 \cdot 10^3\, i$	49.5 %	3 %
11	$-5.67 \cdot 10^{-3} - 7.87 \cdot 10^{-3}\, i$	0 %	22.8 %	11	$-5.56 \cdot 10^4 - 6.55 \cdot 10^3\, i$	49.5 %	3 %
12	$-1.42 \cdot 10^{-3}$	0 %	53.7 %	12	$-6.96 \cdot 10^3$	0 %	0 %
13	$-2.04 \cdot 10^{-4}$	0 %	0 %	13	$-1.28 \cdot 10^3$	0 %	0.1 %
14	$\mathbf{+5.34 \cdot 10^{-6}}$	0 %	0 %	14	$\mathbf{+2.93 \cdot 10^1}$	0 %	94 %
15	0	0 % (cons)	0 % (cons)	15	0	0 % (cons)	0 % (cons)
16	0	0 % (cons)	0 % (cons)	16	0	0 % (cons)	0 % (cons)
17	0	0 % (cons)	0 % (cons)	17	0	0 % (cons)	0 % (cons)
18	0	0 % (cons)	0 % (cons)	18	0	0 % (cons)	0 % (cons)

Table 3: Eigenvalues and weights to chemical and extended TSR as per Eq.(4) in select points of the slice Z = 0.015m, picked at R = 0.0021 m and R = 0.0047 m. Positive eigenvalues are in bold. Fast and conserved (denoted with cons) modes don't contribute to the TSR because of vanishing amplitude and eigenvalue, respectively. 9% coflow oxygen level case.

since it competes with the chain-branching step Rf41: H + O_2 → OH + O (blue, Fig. 12(b)), for the H production, and converts the active H atoms to the less active CH_3 radicals. Reaction Rf3 is enhanced by the methane concentration. It appears that the backward step is dominant in the two branches of the flame in Region 4, towards increasing heat release rate. In the layer of minimal fast subspace dimension occurring in the fuel/coflow mixing region, reactions Rf6: CH_3 + O → CH_2O + H (green, Fig. 12(a)), and Rf41 become dominant. Reaction Rf6 is the typical methyl radical consumption pathway of methane flames, triggered by the O atom abundance due to back diffusion and fed by the CH_3 produced by the methane destruction step of Rf3, while reaction Rf41 is the chain-branching step that involves the H radical produced by Rb3 and by the coflow region activity, which will be described later on. Also, recombination reaction Rf1: CH_3 + H (+M) → CH_4 (+M) (orange, Fig. 12(c)) is captured as dominant in the fuel stream, in between the two flame branches. The highest heat release rate region overlaps with the dominance of Rf40: OH + H_2 → H_2O + H (red, Fig. 12(b)).

The coflow region is characterized by large PIs of reaction Rf41 near the inflow and the chain propagation step Rf36: CO + OH → CO_2 + H (green, Fig. 12(c)) throughout the

entire Region 2. Also, reaction Rf41 is the most participating along both the air/coflow and fuel/coflow mixing layers, especially near the inflow, where the explosive TSR is captured. Together with Rf41 and with similar participation intensity, Rf43 (purple, Figs. 12(b-c)), which is a termination step of the radical chain process, dominates in both the mixing layers. The chain initiation forward reaction Rf37: CO + O2 $\Leftrightarrow$ CO_2 + O (not shown), captured close to the coflow exit location, activates the reactivity in the coflow stream, and the O radical is produced. Further downstream, the O radical reacts with H_2O and produces OH radicals by the reaction Rb47: 2OH $\Leftrightarrow$ O + H_2O. The produced OH radical activates reaction Rf36, which is largely dominant in the area. Finally, the H radical produced by Rf36 activates Rf41 and Rf43, which consume the oxygen present in the coflow. It is likely that the H radical that feeds Rf41 and Rf43 results from both the coflow activity and the fuel stream activity of R3 discussed before.

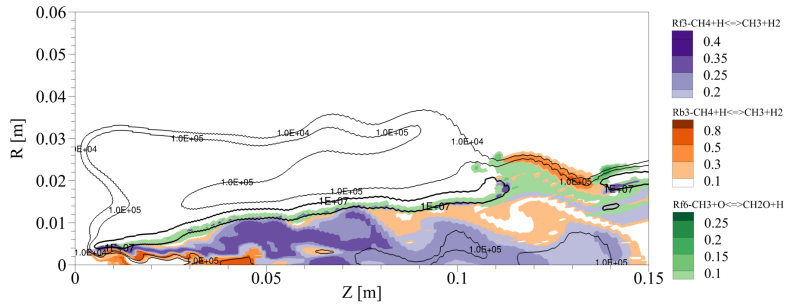

(a)

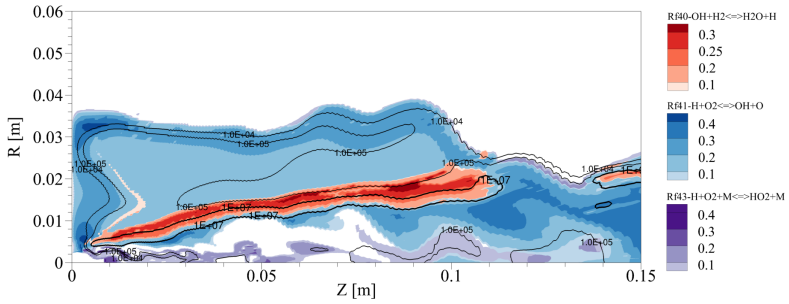

(b)

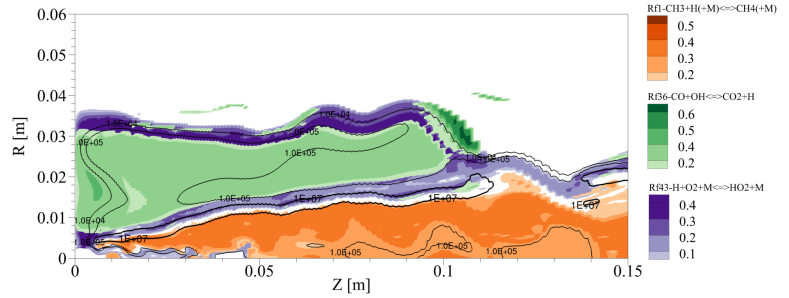

(c)

Figure 12: Dominant participation indices of reactions to the chemical TSR, in the 3 % oxygen case with heat release rate contours (black lines).

The local extinction/re-ignition zone of Region 5 is clearly visible in Fig. 12(b). The high participation of Rf40 suddenly drops, indicating an interruption in the conversion of H_2 into H_2O, due to the oxygen and radicals depletion in the coflow stream. Consequently, the heat release rate diminishes, as well as temperature, which drops by approximately 200 K, due to the mixing with the fresh fuel stream. The simultaneous presence of a higher fuel concentration, the entrainment of air from the air-stream and the high temperature leads to the re-activation of the chain-branching reaction Rf41. A broad explosive region is then

generated, as discussed with the chemical TSR index.

As with the 9 % oxygen case, similar profiles are shown for the dominant participation indices of most reactions, showing only slight differences quantitatively. However, regarding the one which is relevant to the H_2O production, as indicated in Figure 13, the high participation of Rf40 keeps until the end of the stream. With higher availability of oxidizer in the coflow, the reactions with the involvement of O_2 show higher participation. For exmaple, in Figure 14 and 15, the Rf2: $CH_4 + O_2 \Leftrightarrow CH_3 + HO_2$ and Rf21: $CH_2 + O_2 \Leftrightarrow CH_2O + O$ are shown. Both reactions tends to contribute more with the increase of oxygen content in the coflow. The relative large PI of Rf21 also breaks after Z = 0.12 m for the 3 % case. In methane combustion, the chain reaction is initiated by Rf2 [62] and radicals are produced for further chain branching and propagation steps, like Rf21. The produced CH_2O is then transferred to HCO, CO and finally to CO_2 and heat. The highly diluted condition suppresses such chain reactions and they react with reduced chemical activity. As a result, less heat is produced and the system is kept at lower peak temperature.

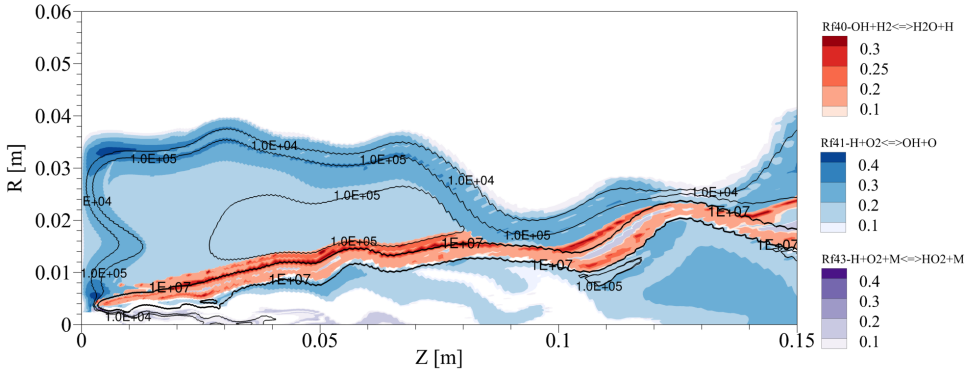

Figure 13: Dominant participation indices of reactions to the chemical TSR, in the 9 % oxygen case with heat release rate contours (black lines).

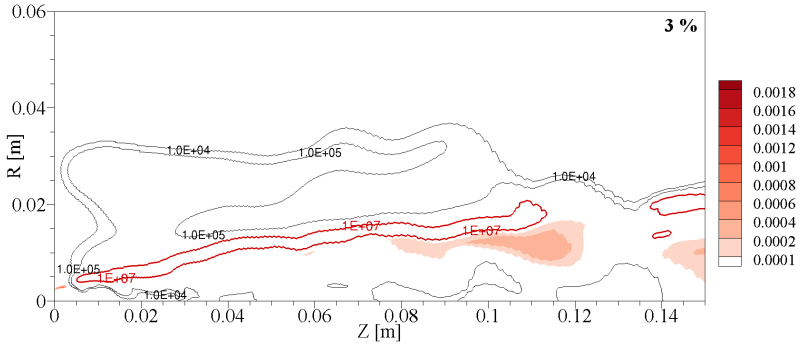

(a)

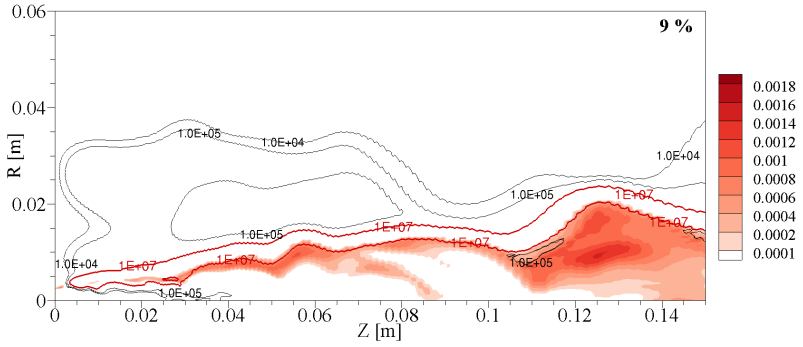

(b)

Figure 14: Participation indices of Rf2: $CH_4 + O_2 \Leftrightarrow CH_3 + HO_2$ for the 3 % and 9 % oxygen cases.

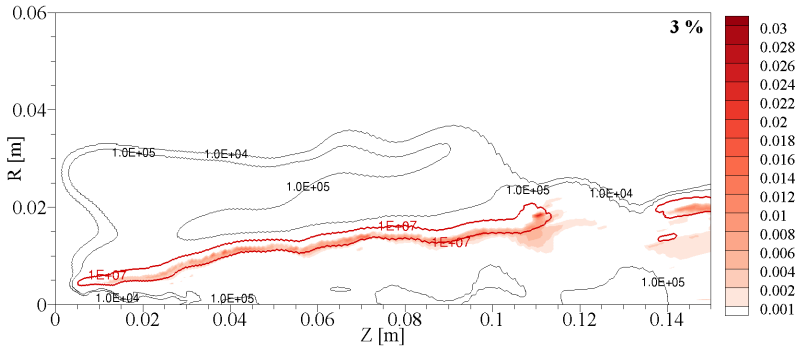

(a)

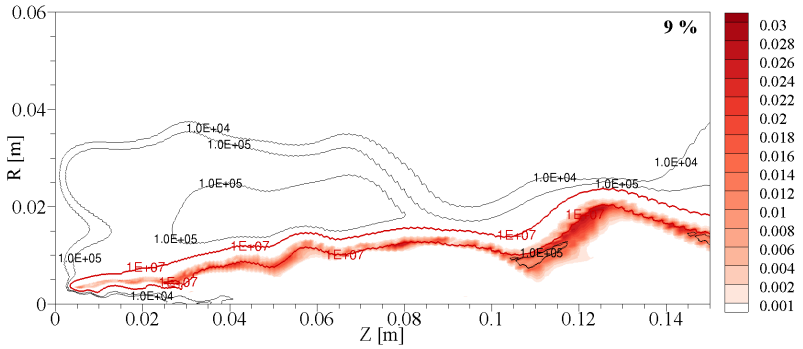

(b)

Figure 15: Participation indices of Rf21: $CH_2 + O_2 \Leftrightarrow CH_2O + O$ for the 3 % and 9 % oxygen cases.

7. Conclusions

In the present article, Computational Singular Perturbation (CSP) and Tangential Stretching Rate (TSR) analysis are carried out on the Large Eddy Simulation (LES) results of a jet-in-hot-coflow (JHC) burner, to investigate the nature of turbulence-chemistry interactions under Moderate or Intense Low oxygen Dilution (MILD) combustion condition. The LES data consists of the JHC simulation results under three different coflow oxygen levels: 3 %, 6 % and 9 % by mass. The validation of the LES results against the experimental data, the fast-slow modes of the system, the TSR & extended TSR analysis results as well as the participation indices (PIs) of chemical reactions are shown. The conclusions obtained can be summarized as:

– Satisfactory agreement is obtained by comparing the LES results of the mean temperature and species mass fraction with the experimental data.

– A region which reaches equilibrium featuring high number of the fast modes is identified inside the coflow region (Region 2). At the same time, low number of fast modes reveals the reactive layers with high heat release rate where the coflow mixes with fuel stream.

– Local flame extinction and re-ignition are found in the 3 % case, because of the low availability of oxygen in the coflow and the entrainment of air.

– The extended TSR with diffusive term shows the importance of both autoignition and flame propagation under MILD conditions. The observations substantiate findings from previous research works stating that the initiated ignition kernels from autoignition are transported further downstream by flame propagation.

– At the location close to the flame ignition point, the 3 % case is more chemical reaction driven while the 9 % case is transport driven.

– By looking at the participation indices of the chemical reactions, the processes which contribute to the equilibrium state in the coflow stream are identified. Similar profiles are obtained by looking at the large PIs that contribute to the chemical TSR for the 3 % and 9 % cases. However, because of higher availability of O_2 in the coflow for the 9 % case, the PIs of the reactions with the contribution of O_2 is slightly higher than that with the 3 % case.

The advanced analysis using the CSP and TSR tools reveal the intrinsic features of turbulence-chemistry interactions in MILD combustion and demonstrate the major role that both autoignition and flame propagation play. For the perspective of the current research, a refined mesh concentrating on the axial location before 0.06 m is expected to be used, in order to capture more phenomena involving the ignition process of the flame.

Acknowledgments

This project has received funding from the European Research Council (ERC) and the European Union′s Horizon 2020 research and innovation program under the Marie Skłodowska-Curie grant agreement No. 643134, Starting Grant No. 714605. This work was also supported by a STSM Grant from COST Action SMARTCATs.

References

[1] J. A. Wünning and J. G. Wünning. Flameless oxidation to reduce thermal NO-formation. *Progress in Energy and Combustion Science*, 23:81–94, 1997.

[2] A. Cavaliere and M. de Joannon. MILD combustion. *Progress in Energy and Combustion Science*, 30:329–366, 2004.

[3] B. B. Dally, E. Riesmeier, and N. Peters. Effect of fuel mixture on moderate and intense low oxygen dilution combustion. *Combustion and Flame*, 137:418–431, 2004.

[4] M. de Joannon, G. Sorrentino, and A. Cavaliere. MILD combustion in diffusion-controlled regimes of hot diluted fuel. *Combustion and Flame*, 159:1832–1839, 2012.

[5] Xuan Gao, Fei Duan, Seng Chuan Lim, and Mee Sin Yip. NOx formation in hydrogen-emethane turbulent diffusion flame under the moderate or intense low-oxygen dilution conditions. *Energy*, 59:559–569, 2013.

[6] Yizhuo He, Chun Zou, Yu Song, Yang Liu, and Chuguang Zheng. Numerical study of characteristics on NO formation in methane MILD combustion with simultaneously hot and diluted oxidant and fuel (HDO/HDF). *Energy*, 112:1024–1035, 2016.

[7] Marco Ferrarotti, Chiara Galletti, Alessandro Parente, and Leonardo Tognotti. Development of reduced NOx models for flameless combustion. In *18th IFRF Members Conference*, 2015.

[8] G. G. Szegö, B. B. Dally, and G. J. Nathan. Scaling of NOx emissions from a laboratory-scale MILD combustion furnace. *Combustion and Flame*, 154:281–295, 2008.

[9] Chiara Galletti, Alessandro Parente, and Leonardo Tognotti. Numerical and experimental investigation of a mild combustion burner. *Combustion and Flame*, 151:649–664, 2007.

[10] A. Parente, C. Galletti, and L. Tognotti. Effect of the combustion model and kinetic mechanism on the MILD combustion in an industrial burner fed with hydrogen enriched fuels. *International Journal of Hydrogen Energy*, 33:7553–7564, 2008.

[11] F. Xing, A. Kumar, Y. Huang, S. Chan, C. Ruan, S. Gu, and X. Fan. Flameless combustion with liquid fuel: A review focusing on fundamentals and gas turbine application. *Applied Energy*, 193:28–51, 2017.

[12] Jingjing Ye, Paul R. Medwell, Emilien Varea, Stephan Kruse, Bassam B. Dally, and Heinz G. Pitsch. An experimental study on MILD combustion of prevaporised liquid fuels. *Applied Energy*, 151:93–101, 2015.

[13] W. P. Adamczyk, R. A. Bialecki, M. Ditaranto, P. Gladysz, N. E. L. Haugen, A. Katelbach-Wozniak, A. Klimanek, S. Sladek, A. Szlek, and G. Wecel. CFD modelling and thermodynamic analysis of a concept of a MILD-Oxy combustion large scale pulverized coal boiler. *Energy*, 140(1):1305–1315, 2017.

[14] Stephan Kruse, Bruno Kerschgens, Lukas Berger, Emilien Varea, and Heinz Pitsch. Experimental and numerical study of MILD combustion for gas turbine applications. *Applied Energy*, 148:456–465, 2015.

[15] A. Chinnici, Z. F. Tian, J. H. Lim, G. J. Nathan, and B. B. Dally. Comparison of system performance in a hybrid solar receiver combustor operating with MILD and conventional combustion. Part II: Effect of the combustion mode. *Solar Energy*, 147:478–488, 2017.

[16] B. B. Dally, A. N. Karpetis, and R. S. Barlow. Structure of turbulent non-premixed jet flames in a diluted hot coflow. *Proceedings of the Combustion Institute*, 29:1147–1154, 2002.

[17] E. Oldenhof, Mark J. Tummers, E.H. van Veen, and D.J.E.M. Roekaerts. Ignition kernel formation and lift-off behaviour of Jet-in-Hot-Coflow flames. *Combustion and Flame*, 157:1167–1178, 2010.

[18] E. Oldenhof, Mark J. Tummers, E. H. van Veen, and D. J. E. M. Roekaerts. Role of entrainment in the stabilisation region of Jet-in-Hot-Coflow flames. *Combustion and Flame*, 158(8):1553–1563, 2011.

[19] Paul R. Medwell, Peter A.M. Kalt, and Bassam B. Dally. Imaging of diluted turbulent ethylene flames stabilized on a Jet in Hot Coflow (JHC) burner. *Combustion and Flame*, 152:100–113, 2007.

[20] Paul R. Medwell and Bassam B. Dally. Effect of fuel composition on jet flames in a heated and diluted oxidant stream. *Combustion and Flame*, 159:3138–3145, 2012.

[21] F. C. Christo and B. B. Dally. Modelling turbulent reacting jets issuing into a hot and diluted coflow. *Combustion and Flame*, 142:117–129, 2005.

[22] Alessio Frassoldati, Pratyush Sharma, Alberto Cuoci, Tiziano Faravelli, and Eliseo Ranzi. Kinetic and fluid dynamics modeling of methane/hydrogen jet flames in diluted coflow. *Applied Thermal Engineering*, 30:376–383, 2009.

[23] Amir Mardani, Sadegh Tabejamaat, and Mohsen Ghamari. Numerical study of influence of molecular diffusion in the MILD combustion regime. *Combustion Theory and Modelling*, 14(5):747–774, 2010.

[24] Seyed Reza Shabanian, Paul Ross Medwell, Masoud Rahimi, Alessio Frassoldati, and Alberto Cuoci. Kinetic and fluid dynamic modeling of ethylene jet flames in diluted and heated oxidant stream combustion conditions. *Applied Thermal Engineering*, 52:538–554, 2012.

[25] Alessandro Parente, Mohammad Rafi Malik, Francesco Contino, Alberto Cuoci, and Bassam B. Dally. Extension of the Eddy Dissipation Concept for turbulence/chemistry interactions to MILD combustion. *Fuel*, 163:98–111, 2015.

[26] Michael John Evans, Paul Ross Medwell, and Zhao Feng Tian. Modelling lifted jet flames in a heated coflow using an optimised Eddy Dissipation Concept model. *Combustion Science and Technology*, 187(7):1093–1109, 2015.

[27] Javad Aminian, Chiara Galletti, and Leonardo Tognotti. Extended EDC local extinction model accounting finite-rate chemistry for MILD combustion. *Fuel*, 165:123–133, 2016.

[28] Amir Mardani. Optimization of the Eddy Dissipation Concept (EDC) model for turbulence-chemistry interactions under hot diluted combustion of ch4/h2. *Fuel*, 191:114–129, 2017.

[29] M.J. Evans, A. Chinnici, P.R. Medwell, and J. Ye. Ignition features of methane and ethylene fuel-blends in hot and diluted coflows. *Fuel*, 203:279–289, 2017.

[30] Z. Chen, V.M. Reddy, S. Ruan, N.A.K. Doan, W.L. Roberts, and N. Swaminathan. Simulation of MILD combustion using perfectly stirred reactor model. *Proceedings of the Combustion Institute*, 36(3):4279 –4286, 2017.

[31] Zhiyi Li, Alberto Cuoci, Amsini Sadiki, and Alessandro Parente. Comprehensive numerical study of the Adelaide Jet in Hot-Coflow burner by means of RANS and detailed chemistry. *Energy*, 139:555–570, 2017.

[32] Zhiyi Li, Marco Ferrarotti, Alberto Cuoci, and Alessandro Parente. Finite-rate chemistry modelling of non-conventional combustion regimes using a partially-stirred reactor closure: Combustion model formulation and implementation details. *Applied Energy*, 225:637–655, 2018.

[33] M. Ihme and Y. C. See. LES flamelet modeling of a three-stream MILD combustor: Analysis of flame sensitivity to scalar inflow conditions. *Proceeding of the Combustion Institute*, 33(1):1309–1317, 2011.

[34] Matthias Ihme, Jian Zhang, Guowei He, and Bassam Dally. Large Eddy Simulation of a Jet-in-Hot-Coflow burner operating in the oxygen-diluted combustion regime. *Flow, Turbulence and Combustion*, 89:449–464, 2012.

[35] Masashi Katsuki and Toshiaki Hasegawa. The science and technology of combustion in highly preheated air. *Symposium (International) on Combustion*, 27(2):3135–3146, 1998.

[36] J.A. van Oijen. Direct numerical simulation of autoigniting mixing layers in mild combustion. *Proceedings of the Combustion Institute*, 34(1):1163–1171, 2013.

[37] M. Ugur Göktolga, Jeroen A. van Oijen, and L. Philip H. de Goey. 3d dns of mild combustion: A detailed analysis of heat loss effects, preferential diffusion, and flame formation mechanisms. *Fuel*, 159:784–795, 2015.

[38] J. Sidey and E. Mastorakos. Visualization of mild combustion from jets in cross-flow. *Proceedings of the Combustion Institute*, 35(3):3537–3545, 2015.

[39] Ebrahim Abtahizadeh, Alexey Sepman, Francisco Hernández-Pérez, Jeroen van Oijen, Anatoli Mokhov, Philip de Goey, and Howard Levinsky. Numerical and experimental investigations on the influence of preheating and dilution on transition of laminar coflow diffusion flames to mild combustion regime. *Combustion and Flame*, 160(11):2359–2374, 2013.

[40] M. de Joannon, P. Sabia, G. Sorrentino, and A. Cavaliere. Numerical study of mild combustion in hot diluted diffusion ignition (HDDI) regime. *Proceedings of the Combustion Institute*, 32:3147–3154, 2009.

[41] Nguyen Anh Khoa Doan and Nedunchezhian Swaminathan. Autoignition and flame propagation in non-premixed mild combustion. *Combustion and Flame*, 201:234–243, 2019.

[42] Sau-Hai Lam and Dimitris A. Goussis. Understanding complex chemical kinetics with computational singular perturbation. *Proc. Comb. Inst.*, 22:931–941, 1988.

[43] S.H. Lam. Using CSP to Understand Complex Chemical Kinetics. *Combustion Science and Technology*, 89:375–404, 1993.

[44] Mauro Valorani, Pietro Paolo Ciottoli, and Riccardo Malpica Galassi. Tangential stretching rate (TSR) analysis of non premixed reactive flows. *Proceedings of the Combustion Institute*, 36(1):1357–1367, 2017.

[45] Pinaki Pal, Mauro Valorani, Paul G. Arias, Hong G. Im, Margaret S. Wooldridge, Pietro Paolo Ciottoli, and Riccardo Malpica Galassi. Computational characterization of ignition regimes in a syngas/air mixture with temperature fluctuations. *Proceedings of the Combustion Institute*, 36(3):3705–3716, 2017.

[46] Dimitrios Manias, Alexandros-Efstathios Tingas, Francisco E Hernández Pérez, Hong G Im, Riccardo Malpica Galassi, Pietro Paolo Ciottoli, and Mauro Valorani. Analysis of hydrogen/air turbulent premixed flames at different karlovitz numbers using computational singular perturbation. In *2018 AIAA Aerospace Sciences Meeting*, page 0364, 2018.

[47] Dimitris M. Manias, Efstathios-Al. Tingas, Francisco E. Hernández Pérez, Riccardo Malpica Galassi, Pietro Paolo Ciottoli, Mauro Valorani, and Hong G. Im. Investigation of the turbulent flame structure and topology at different Karlovitz numbers using the tangential stretching rate index. *Combustion and Flame*, 200:155–167, 2019.

[48] S.H. Lam and D.A. Goussis. The CSP Method for Simplifying Kinetics. *International Journal of Chemical Kinetics*, 26:461–486, 1994.

[49] Mauro Valorani, Pietro Paolo Ciottoli, Riccardo Malpica Galassi, Samuel Paolucci, Temistocle Grenga, and Emanuele Martelli. Enhancements of the G-Scheme Framework. *Flow, Turbulence and Combustion*, 101(4):1023–1033, 2018.

[50] Mauro Valorani, Samuel Paolucci, Pietro Paolo Ciottoli, and Riccardo Malpica Galassi. Entropy production and timescales. *Combustion Theory and Modelling*, 21(1):137–157, 2017.

[51] Pietro Paolo Ciottoli, Pasquale Eduardo Malpica Galassi, Riccardo abd Lapenna, Giuseppe Leccese, Daniele Bianchi, Francesco Nasuti, Francesco Creta, and Mauro Valorani. CSP-based chemical kinetics mechanisms simplification strategy for non-premixed combustion: An application to hybrid rocket propulsion. *Combustion and Flame*, 186:83–93, 2017.

[52] Dimitris A. Goussis, Mauro Valorani, Francesco Creta, and Habib N. Najm. Reactive and reactive-diffusive time scales in stiff reaction-diffusion systems. *Progress in Computational Fluid Dynamics, An International Journal*, 5(6):316, 2005.

[53] Mauro Valorani, Samuel Paolucci, Emanuele Martelli, Temistocle Grenga, and Pietro Paolo Ciottoli. Dynamical system analysis of ignition phenomena using the Tangential Stretching Rate concept. *Combustion and Flame*, 162(8):2963–2990, 2015.

[54] J. Prager, H.N. Najm, M. Valorani, and D. Goussis. Structure of n-Heptane/Air Triple Flames in Partially-Premixed Mixing Layers. *Combustion and Flame*, 158:2128–2144, 2011.

[55] Saurabh Gupta, Hong G Im, and Mauro Valorani. Analysis of n-heptane auto-ignition characteristics using computational singular perturbation. *Proceedings of the Combustion Institute*, 34(1):1125–1133, 2013.

[56] Nikolai Kornev, Hannes Kröger, and Egon Hassel. Synthesis of homogeneous anisotropic turbulent fields with prescribed second-order statistics by the random spots method. *Communications in Numerial Methods in Engineering*, 24:875–877, 2008.

[57] R. W. Bilger, S. H. Stårner, and R. J. KEE. On reduced mechanisms for methane-air combustion in nonpremixed flames. *Combustion and Flame*, 80(2):135–149, 1990.

[58] C. Duwig and P. Iudiciani. Large eddy simulation of turbulent combustion in a stagnation point reverse flow combustor using detailed chemistry. *Fuel*, 123:256–273, 2014.

[59] Zhiyi Li, Alberto Cuoci, and Alessandro Parente. Large eddy simulation of mild combustion using finite rate chemistry: Effect of combustion sub-grid closure. *Proceedings of the Combustion Institute*, 2018.

[60] H.N. Najm, M. Valorani, D.A. Goussis, and J. Prager. Analysis of Methane-Air Edge Flame Structure. *Combustion Theory and Modelling*, 14(2):257–294, 2010.

[61] Luis Cifuentes, Ehsan Fooladgar, and Christophe Duwig. Chemical Explosive Mode Analysis for a Jet-in-Hot-Coflow burner operating in MILD combustion. *Fuel*, 232(September 2017):712–723, 2018.

[62] Chung K. Law. *Combustion Physics*. Cambridge University Press, 2006.

5.8 Conference paper 8

This paper was accepted for the 12th International ERCOFTAC Symposium on Engineering Turbulence Modelling and Measurements.

Numerical investigation of lifted turbulent flame with PaSR and FPV models

Zhiyi Li[a,c,*], Rihab Mahmoud[b], Amsini Sadiki[b], Alessandro Parente[a,c,**]

[a] *Université Libre de Bruxelles, Ecole polytechnique de Bruxelles, Aero-Thermo-Mechanics Laboratory, Belgium*
[b] *Technische Universität Darmstadt, Institute of Energy and Powerplant technology, Germany*
[c] *Université Libre de Bruxelles and Vrije Universiteit Brussel, Combustion and Robust Optimization Group, Belgium*

Abstract

The current study focuses on the Unsteady Reynolds Averaged Navier-Stokes (URANS) simulation of a lifted methane flame with vitiated co-flow. The combustion models of Partially Stirred Reactor (PaSR) and Flamelet Progress Variable (FPV) are adopted and compared. Three kinetic mechanisms (KEE58, GRI3.0 and San-Diego) with increasing number of species and reactions are used with PaSR model. Results have shown that using the San-Diego mechanism provides better simulation results regarding the mean temperature and species mass fraction, which reveals the importance of chemistry kinetics on the lifted flame. The PaSR model is able to predict the current flame with satisfaction. However, the FPV models shows its limitation on the case when transient phenomenon like extinction and re-ignition exist.

1. Introduction

In order to meet the objective of low-emission energy strategy, techniques such as the combustion of lean and diluted fuel-air mixture have been proposed [1]. To achieve the diluted condition, Exhaust Gas Recirculation (EGR) is often used in applicational combustion systems [2]. The mixing of the fresh gases and the hot products leads to auto-ignition of the flame and the temperature field is homogenized because of reduced reactivity. As a result, the amount of NO_x emission is highly reduced. Furthermore, the thermal energy contained in the hot products helps to stabilize the flame [3].

*Corresponding author: Zhiyi.Li@ulb.ac.be
**Corresponding author: Alessandro.Parente@ulb.ac.be

If the central jet has enough high velocity, the auto-ignited flame will be lifted. The lifted and diluted condition can lead to reduced Damköhler numbers, which indicates a strong multi-scale interaction between the chemistry kinetics and turbulent mixing [1]. Predicting such flames in industrial level with complex geometry is a great challenge to the turbulent and combustion models used. The Cabra [4] vitiated co-flow flame provides a simplification, by using a jet with simple geometry. Moreover, the co-flow area with large diameter isolates the contact of central fuel with ambient air for a long distance, avoiding complexities with three streams.

The stabilization of Cabra flame is a balance between chemical reactions and fluid dynamics [5]. Therefore, unlike mixing-controlled flames, models that exclude detailed kinetics are not able to capture the multi-scale process. The Partially Stirred Reactor (PaSR) [6] has been reported to handle the turbulence-chemistry interaction well, not only in conventional combustion regime [7–10], but also under non-conventional condition, like MILD combustion[11]. In PaSR, the influence of the turbulence on the reaction rate is expressed with a factor κ, defined as the ratio between the characteristic chemical time scale and the sum of the chemical and mixing time scales. On the other hand, the flamelet-like models are one of the most commonly used models in turbulent combustion. The relation between turbulence and chemistry is described with several representative variables, and it requires low computational cost. In the present work, the Flamelet Progress Variable (PFV) model proposed by Pierce & Moin (2001, 2004) [12, 13] is chosen to compare with the PaSR model regarding their abilities on turbulence-chemistry interaction prediction.

The objective of the current article is to demonstrate the importance of chemistry kinetics in the diluted and lifted flame and to evaluate the performance of combustion models in multi-scale reacting flows. Two combustion models, the finite-chemistry based Partially Stirred Reactor (PaSR) model and the tabulated chemistry based Flamelet Progress Variable (PFV) model are validated against high fidelity experimental data from Cabra et al (2005) [4]. Three chemical mechanisms, the KEE58 [14], GRI3.0 [15] and San-Diego [16] are used. Finite Volume Method (FVM) based URANS (Unsteady Reynolds Averaged Navier-Stokes) simulation is applied on all the cases.

2. Methodology

2.1. PaSR model

In the PaSR model [6, 11], each computational cell is split into two zones: one where reactions take place, and another characterized by only mixing. The final average species concentration of the cell is determined by the mass exchange between the two zones, driven

by the turbulence. The mean chemical source term is formulated as:

$$\overline{\dot{\omega}_i} = \kappa \frac{\widetilde{\rho}\left(Y_i^* - Y_i^0\right)}{\tau^*}, \tag{1}$$

where τ^* represents the residence time in the reactive zone, Y_i^0 is the initial i_{th} species mass fraction in the non-reactive region and Y_i^* is the i_{th} species mass fraction in the reactive zone. The quantity κ is the mass fraction of the reaction zone in the computational cell, which is evaluated as [7]:

$$\kappa = \frac{\tau_c}{\tau_c + \tau_{mix}}, \tag{2}$$

where τ_c and τ_{mix} are the characteristic chemical and mixing time scale in each cell, respectively.

In order to get the value of Y_i^*, a time-splitting approach is applied. The reactive zone is modelled as an ideal reactor evolving from Y_i^0, during a residence time τ^*:

$$\frac{dY_i^*}{dt} = \frac{\dot{\omega}_i}{\rho}. \tag{3}$$

The term $\dot{\omega}_i$ is the instantaneous formation rate of species i. The final integration of $\frac{dY_i^*}{dt}$ over the residence time τ^* in the reactor is Y_i^*. The characteristic of PaSR model lies in the fact that the Ordinary Differential Equations (ODEs) of the reactions and the transport equations of scalar quantities are solved to obtain the composition space.

2.1.1. Dynamic estimation of mixing time scale

For the estimation of mixing time scale τ_{mix} in PaSR model, a dynamic approach which involves solving the transport equations are adopted. It is based on the ratio of the scalar variance, $\widetilde{\phi''^2}$, to the scalar dissipation rate, $\widetilde{\epsilon_\phi}$ [17]:

$$\tau_{mix} = \frac{\widetilde{\phi''^2}}{\widetilde{\epsilon_\phi}}. \tag{4}$$

The mixture fraction Z is selected to describe the mixing process. Therefore, the mixture fraction variance ($\widetilde{Z''^2}$) and mixture fraction dissipation rate ($\widetilde{\chi}$) are used. They are obtained from solving the transport equations[18, 19]. In the transport equations, there are four constants used: C_1, C_2, C_3 and C_4. Different combination of values are available in the literature [18, 19]. In the present article, the second set ($C_1 = 1.0$, $C_2 = 1.8$, $C_3 = 3.4$ and $C_4 = 1.4$) and third set ($C_1 = 2.0$, $C_2 = 1.8$, $C_3 = 3.4$ and $C_4 = 1.4$) from Ye et al (2011) is used. They are referred to as dyn2 and dyn3, respectively.

2.1.2. Chemical time scale estimation from formation rates

For the evaluation of chemical time scale, the ratio of species mass fraction and formation rate in the reactive zone is used [20]:

$$\tau_{c,i} = \frac{Y_i^*}{|dY_i^*/dt|}. \tag{5}$$

In Eqn. 5, $\tau_{c,i}$ is the characteristic time scale of a single species; after removing the dormant species (characterised by infinite time scale values), the slowest chemical time scale is chosen as leading scale for the evaluation of the PaSR parameter κ.

2.2. FPV model

Based on the assumption of the flamelet model [21], which considers a turbulent diffusion flame as an ensemble of laminar flamelets, the FPV model obtains the composition space from solving scalar transport equations of mixture fraction Z and progress variable C [13]:

$$\frac{\partial \bar{\rho}\widetilde{Z}}{\partial t} + \nabla \cdot \bar{\rho}\widetilde{\mathbf{u}}\widetilde{Z} = \nabla \cdot \left[\bar{\rho}(\widetilde{D}_Z + D_t)\nabla\widetilde{Z}\right], \tag{6}$$

$$\frac{\partial \bar{\rho}\widetilde{C}}{\partial t} + \nabla \cdot \bar{\rho}\widetilde{\mathbf{u}}\widetilde{C} = \nabla \cdot \left[\bar{\rho}(\widetilde{D}_C + D_t)\nabla\widetilde{C}\right] + \bar{\rho}\widetilde{\omega}_C, \tag{7}$$

where D_t is the turbulent diffusivity and the $\widetilde{\ }$ denotes the favre averaged values. The favre averaged specie mass fraction $\widetilde{y}_i$ and chemical source term $\widetilde{\omega}_C$ are calculated by integrating laminar composition state from flamelet library over the joint PDF of Z and C:

$$\widetilde{y}_i = \int y_i\,(Z, C)\,\widetilde{P}\,(Z, C)\,dZdC, \tag{8}$$

$$\widetilde{\omega}_C = \int \omega_C\,(Z, C)\,\widetilde{P}\,(Z, C)\,dZdC. \tag{9}$$

The joint PDF $\widetilde{P}\,(Z, C)$ is modelled by:

$$\widetilde{P}\,(Z, C) = \widetilde{P}\,(C|Z)\,\widetilde{P}\,(Z)\,, \tag{10}$$

where $\widetilde{P}\,(Z)$ is described by a beta PDF and $\widetilde{P}\,(C|Z)$ is determined by a delta function:

$$\widetilde{P}\,(C|Z) = \delta(C - \widetilde{C|Z}). \tag{11}$$

The definition of Progress Variable (PV) C is defined using the mass fraction of CO, CO_2 and H_2O in the current work.

3. Experimental and numerical details

The lifted flame with vitiated co-flow [4] has a central jet with the inner diameter of d = 4.57 mm, containing a mixture of 33 % CH_4 and 67 % air by volume. A coaxial flow with hot combustion products from a lean H_2-air flame is provided. The bulk velocity of the fuel and co-flow are 100 m/s and 5.4 m/s, receptively, and the co-flow mean temperature is 1350 K. A 2D schematic drawing of the Cabra lifted flame can be seen in Figure 1

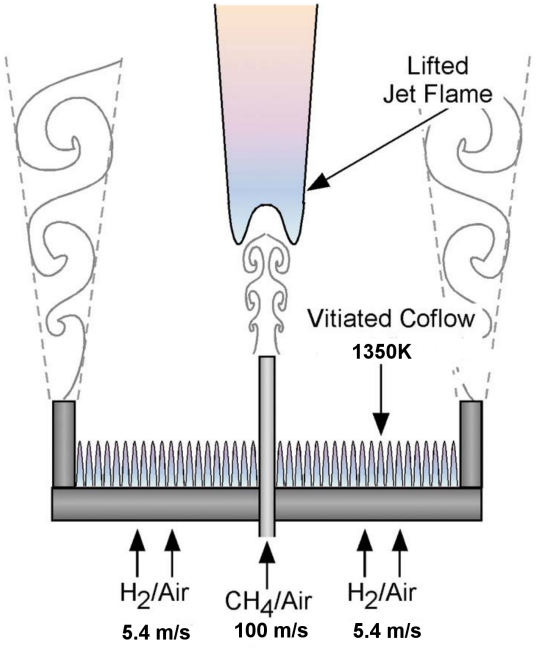

Figure 1: 2D schematic drawing of Cabra lifted flame (adapted from Cabra et al. [4]).

An axi-symmetric 2D structured mesh containing 30840 cells is used for URANS simulation. It extends 70 d downstream of the fuel nozzle exit and 20 d radially. Pre-inlet pipe is constructed for the fuel jet, which is discretized with 12 cells. The standard k-ϵ model is adopted as turbulence model. The KEE58 (17 species, 58 reactions) [14], GRI3.0 (53 species, 325 reactions) [15] and San-Diego(50 species, 247 reactions) [16] kinetic mechanisms with increasing complexity are chosen for detailed chemistry approach. The sampling locations are z/d (z is the axial direction) = 15, 30, 40, 50 70 and the centerline.

4. Results and discussion

4.1. The influence of chemical kinetics

In this section, the PaSR model with dyn2 constants is used for simulation with three different kinetic mechanisms. The mean temperature profiles on the sampling locations are

compared to the experimental measurement data in Figure 2. The radial (z/d = 15, 30, 40, 50 and 70) mean temperature profiles shows that the flame is not ignited when KEE58 mechanism is used. A slight increase of temperature can be captured with GRI3.0. However, there is a huge under-prediction of temperature compared to the experimental value. When it comes to the San-Diego mechanism, though early ignition is observed on z/d = 30, the flame is fully ignited. This is especially obvious when looking at the centerline value.

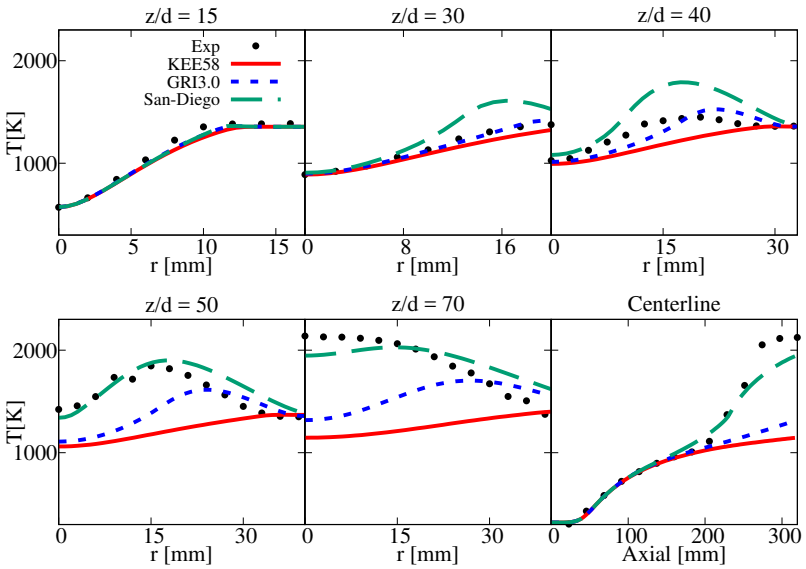

Figure 2: Mean temperature profiles on z/d = 15, 30, 40, 50, 70 and the centerline with three different mechanisms (KEE58, GRI3.0 and San-Diego) in creasing complexity.

The influence of flame ignition can be revealed from the flow field properties as well. Figure 3 shows the mixture fraction distribution from the cases using the three different mechanisms. Similar profiles are shown for z/d $\leq$ 40. Obvious discrepancies are captured on z/d = 70 and z $\geq$ 250 mm, with using San-Diego mechanism provides closer results to the measured profiles.

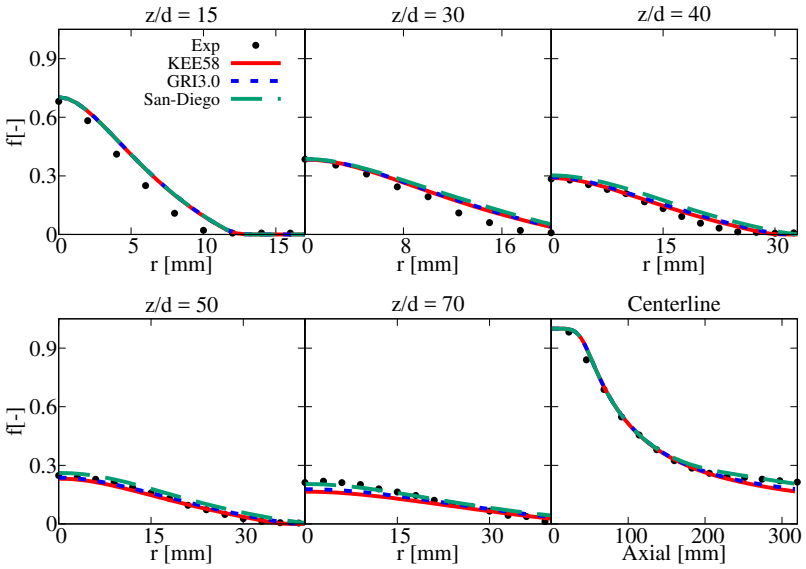

Figure 3: Mean mixture fraction profiles on z/d = 15, 30, 40, 50, 70 and the centerline with three different mechanisms (KEE58, GRI3.0 and San-Diego) in creasing complexity.

The heat release rate contour plot in Figure 4 provides more visual look on the flame ignition. From KEE58 to San-Diego (from left to right), the heat release happens earlier and the absolute amount is increased as well. Furthermore, heat release is captured close to the centerline downstream of the jet ($z \geq 220$ mm) only when San-Diego mechanism is used.

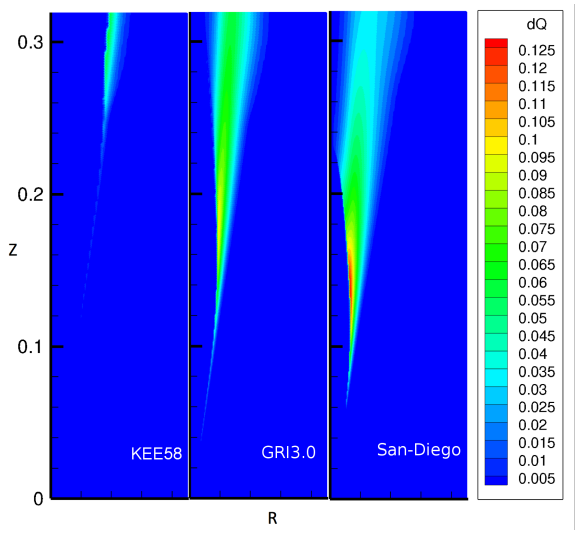

Figure 4: Contour plot of heat release rate (J/s) with three different mechanisms (KEE58, GRI3.0 and San-Diego) in creasing complexity. Unit: m.

4.2. Comparison of PaSR and FPV models

The dyn3 constants are used in this section in order to increase the accuracy of prediction with PaSR model. The San-Diego mechanism is chosen and the other numerical properties are kept the same except combustion model adopted. The FlameMaster [22] toolkit is used and 1D diffusion steady flamelets are generated to construct the lookup-table for FPV model. The S curve obtained by plotting the maximum temperature of each flamelet versus the scalar stoichiometric dissipation rate is presented in Figure 5. Since the temperature of co-flow is 1350 K, the lower branch of the non-burning solutions reaches a plateau at around 1350 K. The middle branch which represents unstable burning condition is also included in the current calculation.

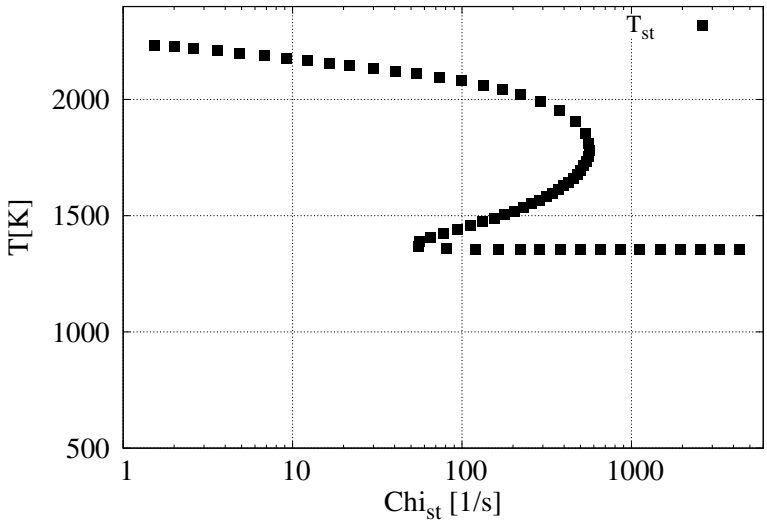

Figure 5: S curve obtained by plotting the maximum temperature of each flamelet versus the scalar stoichiometric dissipation rate.

Figure 6 shows the comparison of mean temperature profiles obtained from cases using PaSR and FPV models. It is obvious to see that the FPV model provides very early ignition, a sudden increase of temperature is observed at around z = 100 mm on the centerline. Upstream ($z/d \leq 50$) temperature field is highly over-predicted. On the contrary, the PaSR model gives reasonable predictions for upstream region, although slight over-prediction is captured on z/d = 50. Further downstream, at z/d = 70 and after, FPV model shows its advantage by predicting mean temperature better than PaSR model.

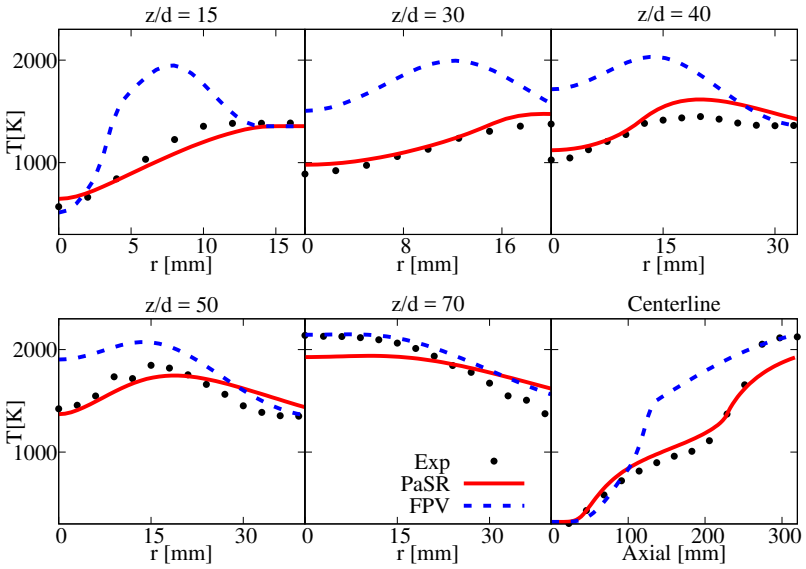

Figure 6: Mean temperature profiles on z/d = 15, 30, 40, 50, 70 and the centerline obtained from cases using PaSR anf FPV combustion models.

The process of combustion process can be revealed by the oxidiser distribution as well. In Figure 7, when the FPV model is used, O_2 is rapidly consumed from around axial location of z = 80 mm, according to the centerline profile. While as with the PaSR model, in agreement with the experimental data, the sharp decrease of O_2 centerline value happens until z = 200 mm. Such trend can be observed for z/d = 15, 30, 40 and 50 as well. As with z/d = 70, similar to the mean temperature profile, using FPV models provides better prediction. Using the PaSR model is not able to consume enough O_2 for $z \geq 250$ mm, and this results in reduced production of CO_2 (not shown here) and H_2O (see Figure 8). On the other hand, the FPV models seems to be failed to handle the intense turbulence and chemistry interaction region (100 mm $\leq z \leq$ 250 mm).

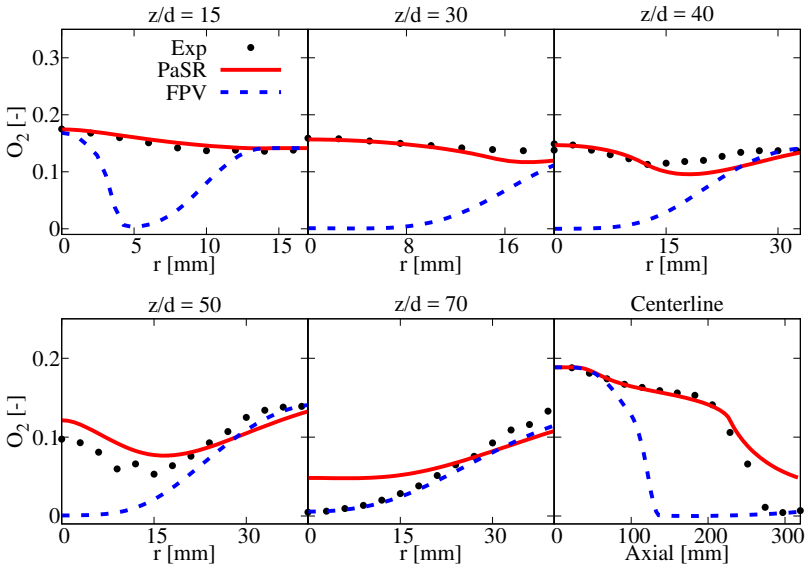

Figure 7: Mean O_2 mass fraction profiles on z/d = 15, 30, 40, 50, 70 and the centerline obtained from cases using PaSR anf FPV combustion models.

In Figure 8, the PaSR model predicts the mean H_2O with good agreement to the experimental data on most sampled locations, except on the centerline direction from z = 250 mm downward. The FPV model still shows obvious over-prediction, especially upstream.

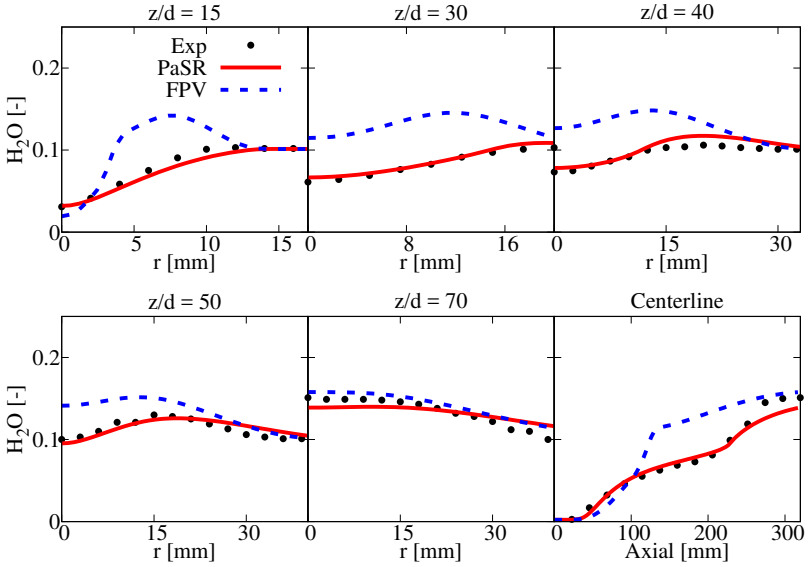

Figure 8: Mean H_2O mass fraction profiles on z/d = 15, 30, 40, 50, 70 and the centerline obtained from cases using PaSR anf FPV combustion models.

The choice of combustion model has influence on flow field as well. Satisfactory agree-

ment with the experimentally measured value is found for mean mixture fraction using the PaSR model. When it comes to the FPV model, much slower jet decay is presented and the only well predicted location locates at z/d = 70, as it is with T and O_2.

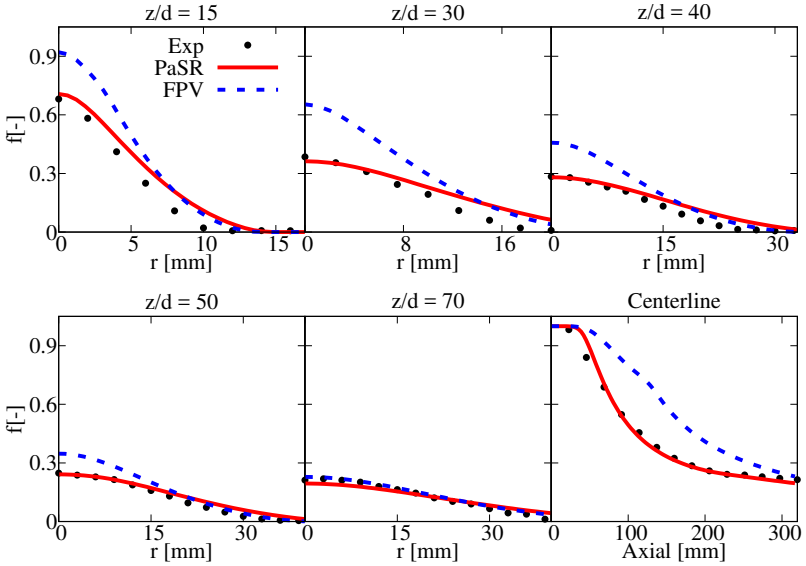

Figure 9: Mean mixture fraction profiles on z/d = 15, 30, 40, 50, 70 and the centerline obtained from cases using PaSR anf FPV combustion models.

The OH distribution from the cases with PaSR and FPV model is shown in Figure 10. The flame is lifted to around 100 mm when PaSR model is used. Such flame lift off height corresponds to around 22 d, which is lower than the experimental measured height, 35 d. Regarding the case with FPV model, the flame is ignited almost immediately at the jet outlet location, showing no lift-off of the flame.

The lifted flame is caused by the high velocity, indicating the existence of flame extinction between the length from jet outlet to flame stabilization location. Since PaSR models the reactive region in each cell by solving the Ordinary Differential Equations (ODEs) of the reactions and τ_{mix} is included explicitly in the calculation of κ, the interaction of chemistry and turbulence is updated for each time step. However, the FPV model reads the lookup-table which is obtained from steady diffusion flame. Unsteady situations (flame extinction and re-ignition) can not be fully covered with the generated table.

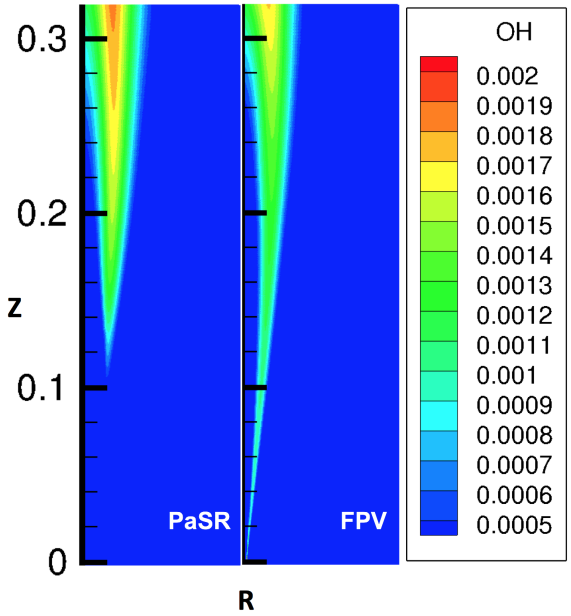

Figure 10: Contour plot of OH mass fraction obatined from cases with PaSR and FPV models. Unit: m.

5. Conclusions

The present article compares three different mechanism with increasing complexity with Partially Stirred Reactor (PaSR) model. The performance of PaSR and Flamelet Progress Variable (FPV) model are evaluated regarding their predictions on mean temperature, species mass fraction and mixture fraction of the Cabra flame. The conclusion can be summarized as:

- The Cabra methane flame is very sensitive to the chemistry kinetics used because of the strong interaction between chemistry and turbulence. Therefore detailed mechanism is required for simulating such flame.
- The case with PaSR model provides overall better predicted profiles than that with FPV model. The FPV model fails to handle the complex multi-scale situation.
- Neither of the models give correct flame lift-off height, indicating further work on the turbulence model and properties used.
- Even though full S-curve is included in the flamelet table, the current steady FPV model does not predict the lifted flame well. The generated flamelets come from a steady solution; however, extinction and reignition phenomena driven by turbulence create transient states which are away from the steady solutions. Therefore, the steady FPV

model shows limited performance on flames with strong turbulence-chemistry interaction. For the prospectives, the Unsteady Flamelet Progress Variable (UFPV) [1, 23] is expected to be used on the current flame. A new definition of Progress Variable (PV) using Principle Component Analysis (PCA) [24] is planned to be implemented as well.

Acknowledgments

This project has received funding from the European Union′s Horizon 2020 research and innovation program under the Marie Skłodowska-Curie grant agreement No. 643134. The research of the last author is sponsored by the European Research Council, Starting Grant No. 714605.

References

[1] Matthias Ihme and Yee Chee See. Prediction of autoignition in a lifted methane/air flame using an unsteady flamelet/progress variable mode. *Combustion and Flame*, 157:1850–1862, 2010.

[2] P. Domingo, L. Vervisch, and D. Veynante. Large-eddy simulation of a lifted methane jet flame in a vitiated coflow. *Combustion and Flame*, 152(3):415–432, 2008.

[3] Hongda Zhang, Zhou Yu, Taohong Ye, Majie Zhao, and Ming Cheng. Large eddy simulation of turbulent lifted flame in a hot vitiated coflow using tabulated detailed chemistry. *Applied Thermal Engineering*, 128:1660–1672, 2018.

[4] R. Cabra, J.-Y.Chen, R.W. Dibble, A.N.Karpetis, and R.S. Barlow. Lifted methane-air jet flames in a vitiated coflow. *Combustion and Flame*, 143:491–506, 2005.

[5] S. Navarro-Martinez and A. Kronenburg. Les-cmc simulations of a lifted methane flame. *Proceedings of the Combustion Institute*, 32(1):1509–1516, 2009.

[6] J. Chomiak. *Combustion: a study in theory, fact and application*. Abacus press/gorden and breach science publishers, 1990.

[7] Fabian Peng Kärrholm. *Numerical modelling of diesel spray injection, turbulence interaction and combustion*. PhD thesis, Chalmers University of Technology, 2008.

[8] P. A. Niklas Nordin. *Complex chmisrey modeling of diesel sparay combustion*. PhD thesis, Chalmers University of Technology, 2001.

[9] V. Sabelnikov and C. Fureby. Extended les-pasr model for simulation of turbulent combustion. *Progress in Propulsion Physics*, 4:539–568, 2013.

[10] Vladimir Sabelnikov and Christer Fureby. Les combustion modeling for high re flames using a multi-phase analogy. *Combustion and Flame*, 160:83–96, 2013.

[11] V.I. Golovitchev and J. Chomiak. Numerical modelling of high temperature air "flameless" combustion. In *the 4th international symposium on high temperature air combustion and gasification*, Rome, Italy, 2001. the 4.

[12] C. D. Pierce and P. Moin. *Progress-Variable Approach for Large Eddy Simulation of Turbulent Combustion*. PhD thesis, Stanford University, 2001.

[13] C. D. Pierce and P. Moin. Progress-variable approach for large eddy simulation of non-premixed turbulent combustion. *Journal of Fluid Mechanics*, 504:73–97, 2004.

[14] R. W. Bilger, S. H. Stårner, and R. J. KEE. On reduced mechanisms for methane-air combustion in nonpremixed flames. *Combustion and Flame*, 80(2):135–149, 1990.

[15] Gregory P. Smith, David M. Golden, Michael Frenklach, Nigel W. Moriarty, Boris Eiteneer, Mikhail Goldenberg, C. Thomas Bowman, Ronald K. Hanson, Soonho Song, William C. Gardiner, Jr., Vitali V. Lissianski, and Zhiwei Qin.

[16] University of California at San Diego. Chemical-kinetic mechanisms for combustion applications.

[17] Venkatramanan Raman and Heinz Pitsch. A consistent LES/filtered-density function formulation for the simulation of turbulent flames with detailed chemistry. *Proceedings of the Combustion Institute*, 31(2):1711– 1719, 2007.

[18] I.K. Ye. *Investigation of the scalar variance and scalar dissipation rate in URANS and LES*. Phd thesis, University of Waterloo, Ontario, Canada, Waterloo, Ontario, Canada, 2011.

[19] J. P. H. Sanders and I. Gökalp. Scalar dissipation rate modelling in variable density turbulent axisymmetric jets and diffusion flames. *Physics of Fluids*, 10(4):938–948, 1998.

[20] J. Chomiak and A. Karlsson. Flame liftoff in diesel sprays. In *Twenty-Sixth Symposium (International) on Combustion*, pages 2557–2564. The Combustion Institute, 1996.

[21] N. Peters. Laminar diffusion flamelet models in non-premixed turbulent combustion. *Progress in Energy and Combustion Science*, 10:319–339, 1984.

[22] H. Pitsch. *FlameMaster, A C++ Computer Program for 0D Combustion and 1D Laminar Flame Calculations.*

[23] Heinz Pitsch and Matthias Ihme. An unsteady/flamelet progress variable method for les of nonpremixed turbulent combustion. In *43rd AIAA Aerospace Sciences Meeting and Exhibit*, Reno, NV, 2005.

[24] I. T. Jolliffe. *Principal component analysis*. Springer, New York, NY, 2002.

References

[1] Francesco Contino, Hervé Jeanmart, Tommaso Lucchini, and Gianluca D'Errico. Coupling of in situ adaptive tabulation and dynamic adaptive chemistry: An effective method for solving combustion in engine simulations. *Proceedings of the Combustion Institute*, 33:3057–3064, 2011.

[2] J. P. H. Sanders and I. Gökalp. Scalar dissipation rate modelling in variable density turbulent axisymmetric jets and diffusion flames. *Physics of Fluids*, 10(938), 1998.

[3] I.K. Ye. *Investigation of the scalar variance and scalar dissipation rate in URANS and LES*. Phd thesis, University of Waterloo, Ontario, Canada, Waterloo, Ontario, Canada, 2011.

[4] J. A. Wünning and J. G. Wünning. Flameless oxidation to reduce thermal NO-formation. *Progress in Energy and Combustion Science*, 23:81–94, 1997.

[5] A. Cavaliere and M. de Joannon. MILD combustion. *Progress in Energy and Combustion Science*, 30:329–366, 2004.

[6] M. de Joannon, G. Sorrentino, and A. Cavaliere. MILD combustion in diffusion-controlled regimes of hot diluted fuel. *Combustion and Flame*, 159:1832–1839, 2012.

[7] Alessandro Parente, Mohammad Rafi Malik, Francesco Contino, Alberto Cuoci, and Bassam B. Dally. Extension of the Eddy Dissipation Concept for turbulence/chemistry interactions to MILD combustion. *Fuel*, 163:98–111, 2015.

[8] Yizhuo He, Chun Zou, Yu Song, Yang Liu, and Chuguang Zheng. Numerical study of characteristics on NO formation in methane MILD combustion with simultaneously hot and diluted oxidant and fuel (HDO/HDF). *Energy*, 112:1024–1035, 2016.

[9] Marco Ferrarotti, Chiara Galletti, Alessandro Parente, and Leonardo Tognotti. Development of reduced NOx models for flameless combustion. In *18th IFRF Members Conference*, 2015.

[10] G. G. Szegö, B. B. Dally, and G. J. Nathan. Scaling of NOx emissions from a laboratory-scale MILD combustion furnace. *Combustion and Flame*, 154:281–295, 2008.

[11] Amir Mardani, Sadegh Tabejamaat, and Shahla Hassanpour. Numerical study of CO and CO2 formation in CH4/H2 blended flame under MILD condition. *Combustion and Flame*, 160:1636–1649, 2013.

[12] Chiara Galletti, Alessandro Parente, and Leonardo Tognotti. Numerical and experimental investigation of a mild combustion burner. *Combustion and Flame*, 151:649–664, 2007.

[13] A. Parente, C. Galletti, and L. Tognotti. Effect of the combustion model and kinetic mechanism on the MILD combustion in an industrial burner fed with hydrogen enriched fuels. *International Journal of Hydrogen Energy*, 33:7553–7564, 2008.

[14] F. Xing, A. Kumar, Y. Huang, S. Chan, C. Ruan, S. Gu, and X. Fan. Flameless combustion with liquid fuel: A review focusing on fundamentals and gas turbine application. *Applied Energy*, 193:28–51, 2017.

[15] E.-S. Cho, B. Danon, W. de Jong, and D.J.E.M. Roekaerts. Behavior of a 300kwth regenerative multi-burner flameless oxidation furnace. *Applied Energy*, 88(12):4952–4959, 2011.

[16] E.-S. Cho, D. Shin, J. Lu, W. de Jong, and D.J.E.M. Roekaerts. Configuration effects of natural gas fired multi-pair regenerative burners in a flameless oxidation furnace on efficiency and emissions. *Applied Energy*, 107:25–32, 2013.

[17] Mario Sánchez, Francisco Cadavid, and Andrés Amell. Experimental evaluation of a 20kw oxygen enhanced self-regenerative burner operated in flameless combustion mode. *Applied Energy*, 111:240–246, 2013.

[18] Jingjing Ye, Paul R. Medwell, Emilien Varea, Stephan Kruse, Bassam B. Dally, and Heinz G. Pitsch. An experimental study on MILD combustion of prevaporised liquid fuels. *Applied Energy*, 151:93–101, 2015.

[19] Stephan Kruse, Bruno Kerschgens, Lukas Berger, Emilien Varea, and Heinz Pitsch. Experimental and numerical study of MILD combustion for gas turbine applications. *Applied Energy*, 148:456–465, 2015.

[20] W. P. Adamczyk, R. A. Bialecki, M. Ditaranto, P. Gladysz, N. E. L. Haugen, A. Katelbach-Wozniak, A. Klimanek, S. Sladek, A. Szlek, and G. Wecel. CFD modelling and thermodynamic analysis of a concept of a MILD-Oxy combustion large scale pulverized coal boiler. *Energy*, 140(1):1305–1315, 2017.

[21] Yaming Liu, Sheng Chen, Shi Liu, Yongxin Feng, Kai Xu, and Chuguang Zheng. Methane combustion in various regimes: First and second thermodynamic-law comparison between air-firing and oxyfuel condition. *Energy*, 115:26–37, 2016.

[22] A. Mardani and A. Fazlollahi Ghomshi. Numerical study of oxy-fuel MILD (Moderate or intense Low-oxygen Dilution combustion) combustion for CH4/H2 fueli. *Energy*, 99:136–151, 2016.

[23] A. Chinnici, Z. F. Tian, J. H. Lim, G. J. Nathan, and B. B. Dally. Comparison of system performance in a hybrid solar receiver combustor operating with MILD and conventional combustion. Part II: Effect of the combustion mode. *Solar Energy*, 147:478–488, 2017.

[24] E. Oldenhof, Mark J. Tummers, E.H. van Veen, and D.J.E.M. Roekaerts. Ignition kernel formation and lift-off behaviour of Jet-in-Hot-Coflow flames. *Combustion and Flame*, 157:1167–1178, 2010.

[25] B. B. Dally, A. N. Karpetis, and R. S. Barlow. Structure of turbulent non-premixed jet flames in a diluted hot coflow. *Proceedings of the Combustion Institute*, 29:1147–1154, 2002.

[26] P.A.M. Kalt and B.B. Dally. The effect of jet preheating on turbulence in a premixed jet in hot coflow. *Proceedings of the Australian Combustion Symposium*, 2013.

[27] Jingjing Ye, Paul R. Medwell, Michael J. Evans, and Bassam B. Dally. Characteristics of turbulent n-heptane jet flames in a hot and diluted coflow. *Combustion and Flame*, 183:330–342, 2017.

[28] R. Cabra, J.-Y.Chen, R.W. Dibble, A.N.Karpetis, and R.S. Barlow. Lifted methane-air jet flames in a vitiated coflow. *Combustion and Flame*, 143:491–506, 2005.

[29] R. Cabra, T. Myhrvold, J.Y. Chen, R.W. Dibble, A.N. Karpetis, and R.S. Barlow. Simultaneous laser raman-rayleigh-lif measurements and numerical modeling results of a lifted turbulent h2/n2 jet flame in a vitiated coflow. *Proceedings of the Combustion Institute*, 29(2):1881–1888, 2002.

[30] Paul R. Medwell and Bassam B. Dally. Effect of fuel composition on jet flames in a heated and diluted oxidant stream. *Combustion and Flame*, 159:3138–3145, 2012.

[31] Michael John Evans, Paul Ross Medwell, and Zhao Feng Tian. Modelling lifted jet flames in a heated coflow using an optimised eddy dissipation concept model. *Combustion Science and Technology*, 187(7):1093–1109, 2015.

[32] Ashoke De, Ernst Oldenhof, Pratap Sathiah, and Dirk Roekaerts. Numerical simulation of Delft-Jet-in-Hot-Coflow (DJHC) flames using the Eddy Dissipation Concept model for turbulence-chemistry interaction. *Flow Turbulence Combustion*, 87:537–567, 2011.

[33] Matthias Ihme and Yee Chee See. Prediction of autoignition in a lifted methane/air flame using an unsteady flamelet/progress variable mode. *Combustion and Flame*, 157:1850–1862, 2010.

[34] Zhiyi Li, Alberto Cuoci, Amsini Sadiki, and Alessandro Parente. Comprehensive numerical study of the Adelaide Jet in Hot-Coflow burner by means of RANS and detailed chemistry. *Energy*, 139:555–570, 2017.

[35] Paul R. Medwell, Peter A.M. Kalt, and Bassam B. Dally. Imaging of diluted turbulent ethylene flames stabilized on a Jet in Hot Coflow (JHC) burner. *Combustion and Flame*, 152:100–113, 2007.

[36] Jingjing Ye, Paul Medwell nd Michael J. Evans, and Bassam B. Dally. The impact of carrier gas on ethanol flame behaviour in a Jet in Hot Coflow (JHC) burner. In *The Australian Combustion Symposium 2015*, 2015.

[37] Jingjing Ye, Paul R. Medwell, Bassam B. Dally, and Michael J. Evans. The transition of ethanol flames from conventional to MILD combustion. *Combustion and Flame*, 171:173–184, 2016.

[38] Jingjing Ye, Paul R. Medwell, Konstantin Kleinheinz, Michael J. Evans, Bassam B. Dally, and Heinz G. Pitsch. Structural differences of ethanol and dme jet flames in a hot diluted coflow. *Combustion and Flame*, 192:473 – 494, 2018.

[39] Stephan Kruse, Jingjing Ye, Zhiwei Sun, Antonio Attili, Bassam Dally, Paul Medwell, and Heinz Pitsch. Experimental investigation of soot evolution in a turbulent non-premixed prevaporized toluene flame. *Proceedings of the Combustion Institute*, 2018.

[40] Paul R. Medwell and Bassam B. Dally. Effect of fuel composition on jet flames in a heated and diluted oxidant stream. *Combustion and Flame*, 159(10):3138–3145, 2012.

[41] Jingjing Ye, Paul R. Medwell, Emilien Varea, Stephan Kruse, Bassam B. Dally, and Heinz G. Pitsch. An experimental study on mild combustion of prevaporised liquid fuels. *Applied Energy*, 151:93–101, 2015.

[42] Roman Weber, John P. Smart, and Willem vd Kamp. On the (MILD) combustion of gaseous, liquid, and solid fuels in high temperature preheated air. *Proceedings of the Combustion Institute*, 30(2):2623–2629, 2005.

[43] V. Mahendra Reddy, Pratim Biswas, Prateek Garg, and Sudarshan Kumar. Combustion characteristics of biodiesel fuel in high recirculation conditions. *Fuel Processing Technology*, 118:310 –317, 2014.

[44] F. C. Christo and B. B. Dally. Modelling turbulent reacting jets issuing into a hot and diluted coflow. *Combustion and Flame*, 142:117–129, 2005.

[45] Robert L. Gordon, Assaad R. Masri, Stephen B. Pope, and Graham M. Goldin. Transport budgets in turbulent lifted flames of methane autoigniting in a vitiated co-flow. *Combustion and Flame*, 151:495–511, 2007.

[46] Alessio Frassoldati, Pratyush Sharma, Alberto Cuoci, Tiziano Faravelli, and Eliseo Ranzi. Kinetic and fluid dynamics modeling of methane/hydrogen jet flames in diluted coflow. *Applied Thermal Engineering*, 30:376–383, 2009.

[47] Amir Mardani, Sadegh Tabejamaat, and Mohsen Ghamari. Numerical study of influence of molecular diffusion in the MILD combustion regime. *Combustion Theory and Modelling*, 14(5):747–774, 2010.

[48] Seyed Reza Shabanian, Paul Ross Medwell, Masoud Rahimi, Alessio Frassoldati, and Alberto Cuoci. Kinetic and fluid dynamic modeling of ethylene jet flames in diluted and heated oxidant stream combustion conditions. *Applied Thermal Engineering*, 52:538–554, 2012.

[49] Javad Aminian, Chiara Galletti, and Leonardo Tognotti. Extended EDC local extinction model accounting finite-rate chemistry for MILD combustion. *Fuel*, 165:123–133, 2016.

[50] Amir Mardani. Optimization of the Eddy Dissipation Concept (EDC) model for turbulence-chemistry interactions under hot diluted combustion of ch4/h2. *Fuel*, 191:114–129, 2017.

[51] M.J. Evans, A. Chinnici, P.R. Medwell, and J. Ye. Ignition features of methane and ethylene fuel-blends in hot and diluted coflows. *Fuel*, 203:279–289, 2017.

[52] Z. Chen, V.M. Reddy, S. Ruan, N.A.K. Doan, W.L. Roberts, and N. Swaminathan. Simulation of MILD combustion using perfectly stirred reactor model. *Proceedings of the Combustion Institute*, 36(3):4279 –4286, 2017.

[53] Zhiyi Li, Marco Ferrarotti, Alberto Cuoci, and Alessandro Parente. Finite-rate chemistry modelling of non-conventional combustion regimes using a partially-stirred reactor closure: Combustion model formulation and implementation details. *Applied Energy*, 225:637–655, 2018.

[54] M. Ihme and Y. C. See. LES flamelet modeling of a three-stream MILD combustor: Analysis of flame sensitivity to scalar inflow conditions. *Proceeding of the Combustion Institute*, 33(1):1309–1317, 2011.

[55] Matthias Ihme, Jian Zhang, Guowei He, and Bassam Dally. Large Eddy Simulation of a Jet-in-Hot-Coflow burner operating in the oxygen-diluted combustion regime. *Flow, Turbulence and Combustion*, 89:449–464, 2012.

[56] P. Domingo, L. Vervisch, and D. Veynante. Large-eddy simulation of a lifted methane jet flame in a vitiated coflow. *Combustion and Flame*, 152(3):415–432, 2008.

[57] Chun Sang Yoo, Edward S. Richardson, Ramanan Sankaran, and Jacqueline H. Chen. A dns study on the stabilization mechanism of a turbulent lifted ethylene jet flame in highly-heated coflow. *Proceedings of the Combustion Institute*, 33(1):1619–1627, 2011.

[58] M. de Joannon, P. Sabia, G. Sorrentino, and A. Cavaliere. Numerical study of mild combustion in hot diluted diffusion ignition (hddi) regime. *Proceedings of the Combustion Institute*, 32(2):3147–3154, 2009.

[59] Manabendra Saha, Bassam B. Dally, Paul R. Medwell, and Emmet M. Cleary. Moderate or Intense Low oxygen Dilution (MILD) combustion characteristics of pulverized coal in a self-recuperative furnace. *Energy & Fuels*, 28(9):6046–6057, 2014.

[60] Y. Minamoto and N. Swaminathan. Subgrid scale modelling for MILD combustio. *Proceedings of the Combustion Institute*, 35(3):3529–3536, 2015.

[61] A. Parente, C. Galletti, and L. Tognotti. A simplified approach for predicting NO formatio in MILD combustion of CH4/H2 mixtures. *Proceeding of the Combustion Institute*, 33:3343–3350, 2011.

[62] Valentina Fortunato, Chiara Galletti, Leonardo Tognotti, and Alessandro Parente. Influence of modelling and scenario uncertainties on the numerical simulation of a semi-industrial flameless furnace. *Applied Thermal Engineering*, 76:324–334, 2014.

[63] Bjørn F. Magnussen. On the structure of turbulence and a generalized Eddy Dissipation Concept for chemical reaction in turbulent flow. In *19th AIAA Aerospace Science Meeting*, St. Louis, Missouri, USA, January 1981.

[64] I.R. Gran and B. F. Magnussen. A numerical study of a bluff-body stabilized diffusion flame, part 2: Influence of combustion modelling and finite-rate chemistry. *Combustion Science and Technology*, 119(1-6):191–217, 1996.

[65] Bj/orn F. Magnussen. The Eddy Dissipation Concept a bridge between science and technology. In *ECCOMAS Thematic Conference on Computational Combustion*, Lisbon, Portugal, 2005.

[66] *ANSYS® Academic Research, Release 17.0.*

[67] J. Chomiak. *Combustion: A Study in Theory, Fact and Application*. Abacus Press/Gorden and Breach Science Publishers, 1990.

[68] J. Chomiak and A. Karlsson. Flame liftoff in diesel sprays. In *Twenty-Sixth Symposium (International) on Combustion*, pages 2557–2564. The Combustion Institute, 1996.

[69] V. Golovitchev and J. Chomiak. Numerical modeling of high temperature air flameless combustion. In *The 4th international symposium on high temperature air combustion and gasification*, 2001.

[70] Fabian Peng Kärrholm. *Numerical Modelling of Diesel Spray Injection, Turbulence Interaction and Combustion*. Phd thesis, Chalmers University of Technology, Chalmers, Sweden, 2008.

[71] P. A. Niklas Nordin. *Comple Chemistry Modeling of Diesel Spray Combustio*. PhD thesis, Chalmers University of Technology, 2001.

[72] Marco Ferrarotti, Zhiyi Li, and Alessandro Parente. On the role of mixing models in the simulation of MILD combustion using finite-rate chemistry combustion models. *Proceeding of the Combustion Institute*, 000:1–8, 2018.

[73] Y. Afarin, S. Tabejamaat, and A. Mardani. Large eddy simulation study of H2/CH4 flame structure at MILD condition. In *Seventh Mediterranean Combustion Symposium*, Naples, Italy, 2011.

[74] Y. Minamoto, N. Swaminathan, R. S. Cant, and T. Leung. Reaction zones and their structure in mild combustion. *Combustion Science and Technology*, 186(8):1075–1096, 2014.

[75] C. Duwig and P. Iudiciani. Large eddy simulation of turbulent combustion in a stagnation point reverse flow combustor using detailed chemistry. *Fuel*, 123:256–273, 2014.

[76] Zhiyi Li, Alberto Cuoci, and Alessandro Parente. Large eddy simulation of mild combustion using finite rate chemistry: Effect of combustion sub-grid closure. *Proceedings of the Combustion Institute*, 2018.

[77] L. Tosatto, B. A. V. Bennett, and M. D. Smooke. A transport-flux-based directed relation graph method for the spatially inhomogeneous instantaneous reduction of chemical kinetic mechanisms. *Combustion and Flame*, 158:820–835, 2011.

[78] Shuliang Zhang, Linda J. Broadbelt, Ioannis P. Androulakis, and Marianthi G. Ierapetritou. Comparison of biodiesel performance based on hcci engine simulation using detailed mechanism with on-the-fly reduction. *Energy & Fuels*, 26:976–983, 2012.

[79] Kaiyuan He, Ioannis P. Androulakis, and Marianthi G. Ierapetritou. Numerical investigation of homogeneous charge compression ignition (hcci) combustion with detailed chemical kinetics using on-the-fly reduction. *Energy & Fuels*, 25:3369–3376, 2011.

[80] Qing Tang and Stephen B. Pope. Implementation of combustion chemistry by in situ adaptive tabulation of rate-controlled constrained equilibrium manifolds. *Proceedings of the Combustion Institute*, 29:1411–1417, 2002.

[81] Zhuyin Ren, Yufeng Liu, Tianfeng Lu, Liuyan Lu, Oluwayemisi O. Oluwole, and Graham M. Goldin. The use of dynamic adaptive chemistry and tabulation in reactive flow simulations. *Combustion and Flame*, 161:127–137, 2014.

[82] Mauro Valorani, Pietro Paolo Ciottoli, and Riccardo Malpica Galassi. Tangential stretching rate (TSR) analysis of non premixed reactive flows. *Proceedings of the Combustion Institute*, 36(1):1357–1367, 2017.

[83] Pinaki Pal, Mauro Valorani, Paul G. Arias, Hong G. Im, Margaret S. Wooldridge, Pietro Paolo Ciottoli, and Riccardo Malpica Galassi. Computational characterization of ignition regimes in a syngas/air mixture with temperature fluctuations. *Proceedings of the Combustion Institute*, 36(3):3705–3716, 2017.

[84] Dimitrios Manias, Alexandros-Efstathios Tingas, Francisco E Hernández Pérez, Hong G Im, Riccardo Malpica Galassi, Pietro Paolo Ciottoli, and Mauro Valorani. Analysis of hydrogen/air turbulent premixed flames at different karlovitz numbers using computational singular perturbation. In *2018 AIAA Aerospace Sciences Meeting*, page 0364, 2018.

[85] Dimitris M. Manias, Efstathios-Al. Tingas, Francisco E. Hernández Pérez, Riccardo Malpica Galassi, Pietro Paolo Ciottoli, Mauro Valorani, and Hong G. Im. Investigation of the turbulent flame structure and topology at different Karlovitz numbers using the tangential stretching rate index. *Combustion and Flame*, 200:155–167, 2019.

[86] H. G. Weller, G. Tabor, H. Jasak, and C. Fureby. A tensorial approach to computational continuum mechanics using object-oriented techniques. *COMPUTERS IN PHYSICS*, 12(6):620–631, 1998.

[87] Dmitry A. Lysenko, Ivar S. Ertesvåg, and Kjell Erik Rian. Numerical simulation of non-premixed turbulent combustion using the Eddy Dissipation Concept and comparing with the steady laminar flamelet model. *Flow, Turbulence and Combustion*, 53:577–605, 2014.

[88] I. Yimer, I. Campbell, and L. Y. Jiang. Estimation of the turbulent schmidt number from experimental profiles of axial velocity and concentration for high-reynolds-number jet flows. *Canadian Aeronautics and Space Journa*, 48(3):195–200, 2002.

[89] S. B. Pope. An explanation of the turbulent round-jet/plane-jet anomaly. Technical report, Imperial College London, 1978.

[90] Thierry Poinsot and Denis Veynante. *Theoretical and Numerical Combustion*. R. T. Edwards, 2000.

[91] A. Yoshizawa and K. Horiuti. A statistically-derived subgrid-scale kinetic energy model for the large-eddy simulation of turbulent flows. *Journal of the Physical Society of Japan*, 54:2834–2839, 1985.

[92] S. Huang and Q. S. Li. A new dynamic one-equation subgrid-scale model for large eddy simulations. *International Journal for Numerical Methods in Engineering*, 81:835–865, 2010.

[93] Benjamin J. Isaac, Alessandro Parente, Chiara Galletti, Jeremy N. Thornock, Philip J. Smith, and Leonardo Tognotti. A novel methodology for chemical time scale evaluation with detailed chemical reaction kinetic. *Energy Fuels*, 27(4):2255–2265, 2013.

[94] R. O. Fox. *Computational Models for Turbulent Reacting Flows*. Cambridge University Press, Cambridge, UK, 2003.

[95] L. Kjäldman, A. Brink, and M. Hupa. Micro mixing time in the Eddy Dissipation Concept. *Combustion Science and Technology*, 154:207–227, 2007.

[96] M. Gonzales and R. Borghi. *Turbulent Shear Flows*. Number 293-311 in 7. Springer Verlag, Berlin, 1991.

[97] V. Sabelnikov and C. Fureby. Extended les-pasr model for simulation of turbulent combustion. *Progress in Propulsion Physics*, 4:539–568, 2013.

[98] Venkatramanan Raman and Heinz Pitsch. A consistent LES/filtered-density function formulation for the simulation of turbulent flames with detailed chemistry. *Proceedings of the Combustion Institute*, 31(2):1711– 1719, 2007.

[99] J.-Y. Chen. Second-order conditional modeling of turbulent nonpremixed flames with a compositep pdf. *Combustion and Flame*, 69(1):1–36, 1987.

[100] W. P. Jones and P. Musonge. Closure of the reynolds stress and scalar flux equations. *The Physics of Fluids*, 31(3589), 1988.

[101] T.P. Sommer, R.M.C. So, and Y.G. Lai. A near-wall two-equation model for turbulent heat fluxes. *International Journal of Heat and Mass Transfer*, 35(12):3375 – 3387, 1992.

[102] E. Knudsen, E. S. Richardson, E. M. Doran, H. Pitsch, and J. H. Chen. Modeling scalar dissipation and scalar variance in large eddy simulation: Algebraic and transport equation closures. *Physics of Fluids*, 24(055103), 2012.

[103] C. Fureby. Comparison of flamelet and finite rate chemistry les for premixed turbulent combustion. In *45th AIAA Aerospace Sciences Meeting and Exhibit*. American Institute of Aeronautics and Astronautics, 2007.

[104] Christophe Duwig, Karl Johan Nogenmyr, Cheong Ki Chan, and Matthew J. Dunn. Large eddy simulations of a piloted lean premix jet flame using finite-rate chemistry. *Combustion Theory and Modelling*, 15(4):537–568, 2011.

[105] Zhenxun Gao, Chongwen Jiang, and Chun Hian Lee. On the laminar finite rate model and flamelet model for supersonic turbulent combustion flows. *International Journal of Hydrogen Energy*, 41(30):13238–13253, 2016.

[106] N. Peters. Laminar diffusion flamelet models in non-premixed turbulent combustion. *Progress in Energy and Combustion Science*, 10:319–339, 1984.

[107] C. D. Pierce and P. Moin. Progress-variable approach for large eddy simulation of non-premixed turbulent combustion. *Journal of Fluid Mechanics*, 504:73–97, 2004.

[108] S. B. Pope. Computationally efficient implementation of combustion chemistry using in situ adaptive tabulation. *Combustion Theory and Modelling*, 1:44–63, 1997.

[109] Francesco Contino. *Combustion in Homogeneous Charge Compression Ignition engines : experimental analysis using ethyl esters and development of a method to include detailed chemistry in numerical simulations.* PhD thesis, Université catholique de Louvain, 2011.

[110] F. Contino, T. Lucchini, G. D'Errico, C. Duynslaegher, V. Dias, and H. Jeanmart. Simulations of advanced combustion modes using detailed chemistry combined with tabulation and mechanism reduction techniques. *SAE International Journal of Engines*, 5(2):185–196, 2012.

[111] F. Contino, F. Foucher, P. Dagaut, T. Lucchini, G. D'Errico, and C. Mounaïm-Rousselle. Experimental and numerical analysis of nitric oxide effect on the ignition of iso-octane in a single cylinder hcci engine. *Combustion and Flame*, 160(8):1476–1483, 2013.

[112] F. Contino, J.-B. Masurier, F. Foucher, T. Lucchini, G. D'Errico, and P. Dagaut. Cfd simulations using the tdac method to model iso-octane combustion for a large range of ozone seeding and temperature conditions in a single cylinder hcci engine. *Fuel*, 137:179–184, 2014.

[113] N. Bourgeois, S. S. Goldsborough, G. Vanhove, M. Duponcheel, H. Jeanmart, and F. Contino. Cfd simulations of rapid compression machines using detailed chemistry: Impact of multi-dimensional effects on the auto-ignition of the iso-octane. *Proceedings of the Combustion Institute*, 36(1):383–391, 2017.

[114] T. Lu and C. K. Law. A directed relation graph method for mechanism reduction. *Proceedings of the Combustion Institute*, 30:1333–1341, 2005.

[115] P. Pepiot-Desjardins and H. Pitsch. An efficient error-propagation-based reduction method for large chemical kinetic mechanisms. *Combustion and Flame*, 154:67–81, 2008.

[116] L. Liang, J. G. Stevens, and J. T. Farrell. A dynamic adaptive chemistry scheme for reactive flow computations. *Proceedings of the Combustion Institute*, 32:527–534, 2009.

[117] Florian Karst, Matteo Maestri, Hannsjörg Freund, and Kai Sundmacher. Reduction of microkinetic reaction models for reactor optimization exemplified for hydrogen production from methane. *Chemical Engineering Journal*, 281:981–994, 2015.

[118] Wenting Sun, Zheng Chen, Xiaolong Gou, and Yiguang Ju. A path flux analysis method for the reduction of detailed chemical kinetic mechanisms. *Combustion and Flame*, 157:1298–1307, 2010.

[119] Nicolas Bourgeois. *Numerical study of multi-dimensional effects in Rapid Compression Machines*. PhD thesis, Université catholique de Louvain and Vrije Universiteit Brussel, 2017.

[120] Mauro Valorani, Habib N. Najm, and Dimitris A. Goussis. CSP analysis of a transient flame-vortex interaction: Time scales and manifolds. *Combustion and Flame*, 134(1-2):35–53, 2003.

[121] Mauro Valorani, Samuel Paolucci, Emanuele Martelli, Temistocle Grenga, and Pietro Paolo Ciottoli. Dynamical system analysis of ignition phenomena using the Tangential Stretching Rate concept. *Combustion and Flame*, 162(8):2963–2990, 2015.

[122] J. Prager, H.N. Najm, M. Valorani, and D. Goussis. Structure of n-Heptane/Air Triple Flames in Partially-Premixed Mixing Layers. *Combustion and Flame*, 158:2128–2144, 2011.

[123] Saurabh Gupta, Hong G Im, and Mauro Valorani. Analysis of n-heptane auto-ignition characteristics using computational singular perturbation. *Proceedings of the Combustion Institute*, 34(1):1125–1133, 2013.

Appendix A

Supplementary materials from Journal papers

A.1 Supplementary material from journal paper 1

Comprehensive numerical study of the Adelaide Jet in Hot-Coflow burner by means of RANS and detailed chemistry

Zhiyi Li[a,*], Alberto Cuoci[b], Amsini Sadiki[c], Alessandro Parente[a,**]

[a] *Université Libre de Bruxelles, Aero-Thermo-Mechanics Department, Belgium*
[b] *Politecnico di Milano, Department of Chemistry, Materials, and Chemical Engineering "G. Natta", Italy*
[c] *Technische Universität Darmstadt, Institute of Energy and Powerplant technology, Germany*

[*] Zhiyi.Li@ulb.ac.be
[**] Alessandro.Parente@ulb.ac.be

Supplemental Information

1. Introduction

In the current supplementary material, the impact of turbulent Schmidt number Sc_t and turbulent Prandtl number Pr_t on the simulation result is presented.

2. Theory Basis

In RANS simulations, the density-based Favre-averaged (denoted with ˜) governing equations of mass, momentum and energy are solved [1] :

$$\frac{\partial \bar{\rho}}{\partial t} + \frac{\partial}{\partial x_j}\left(\bar{\rho}\tilde{u}_j\right) = 0, \tag{1}$$

$$\frac{\partial}{\partial t}\left(\bar{\rho}\tilde{u}_i\right) + \frac{\partial}{\partial x_j}\left(\bar{\rho}\tilde{u}_i\tilde{u}_j\right) = -\frac{\partial \bar{p}}{\partial x_i} + \frac{\partial}{\partial x_j}\left(\bar{\tau}_{ij} - \bar{\rho}\widetilde{u_i'' u_j''}\right), \tag{2}$$

$$\frac{\partial}{\partial t}\left(\bar{\rho}\tilde{h}\right) + \frac{\partial}{\partial x_j}\left(\bar{\rho}\tilde{h}\tilde{u}_j\right) = \frac{\partial}{\partial x_j}\left(\bar{\rho}\alpha\frac{\partial \tilde{h}}{\partial x_j} - \bar{\rho}\widetilde{u_j'' h''}\right) - \frac{\partial}{\partial x_j}\left(\bar{q}_{rj}\right) + \bar{S}_{hc}. \tag{3}$$

In Eqn. 1 - 3, ρ, $\mathbf{u}$, p represent the density, velocity and pressure respectively; h is the enthalpy; α is the thermal diffusivity. The term $\mathbf{q}_r$ denotes the radiative heat loss and S_{hc} is the source term coming from combustion process. The turbulent Prandtl number Pr_t has an impact on the turbulent heat flux:

$$-\bar{\rho}\widetilde{u_j'' h''} \approx \frac{\mu_t}{Pr_t}\frac{\partial \tilde{h}}{x_j}. \tag{4}$$

In combustion processes, multiple species are involved. The Favre averaged transport equation of species Y_s reads:

$$\frac{\partial}{\partial t}\left(\bar{\rho}\widetilde{Y}_s\right) + \frac{\partial}{\partial x_j}\left(\bar{\rho}\widetilde{Y}_s\tilde{u}_j\right) = \frac{\partial}{\partial x_j}\left(\left(\bar{\rho}D_{m,s} + \frac{\mu_t}{Sc_t}\right)\frac{\partial \tilde{Y}_s}{\partial x_j}\right) + \bar{\dot{\omega}}_s, \tag{5}$$

where Sc_t is the turbulent Schmidt number and $D_{m,s}$ is the molecular diffusion coefficient for species s in the mixture. Because $Sc_t = \mu_t/(\rho D_t)$ (D_t is the turbulent diffusivity), the molecular diffusion can also be written as $Sc = \mu/(\rho D_m)$ (D_m is the molecular diffusivity) and therefore, $\rho D_m = \mu/Sc$. Assuming ideal gas conditions [2], $Sc = 1$; moreover, according to Yimer et al. [3], $Sc_t \approx 1$. Therefore, Eqn. 5 can be re-arranged as:

$$\frac{\partial}{\partial t}\left(\bar{\rho}\widetilde{Y}_s\right) + \frac{\partial}{\partial x_j}\left(\bar{\rho}\widetilde{Y}_s\tilde{u}_j\right) = \frac{\partial}{\partial x_j}\left(\left(\mu + \mu_t\right)\frac{\partial \widetilde{Y}_s}{\partial x_j}\right) + \bar{\dot{\omega}}_s. \tag{6}$$

In Eqn. 6, $\mu + \mu_t$ can be expressed as μ_{Eff} (the effective viscosity). The comparison between the formulations in Eqn. 5 and Eqn. 6 will be shown in Section 3.

3. Results and Discussion

The turbulent Schmidt number (Sc_t) in Eqn. 5 affects the turbulent mass diffusivity of the species. It is generally set to unity in the OpenFOAM® solvers as in Eqn. 6 to simplify the problem. According to Tominaga et al. [4], the values are widely spread from 0.2 to 1.3 depending on the geometry and flow properties. Tominaga et al. [4] also demonstrated that in axi-symmetric jets, $Sc_t = 0.7$ is recommend. Here, the results obtained with Sc_t numbers of 0.6, 0.7 and 1.0 are compared with experimental profiles. On the other hand, the turbulent Prandtl number (Pr_t) in Eqn. 4 impacts the turbulent heat flux in energy equation (see Eqn. 3). When the simplest Reynolds analogy [5] is used, it yields $Pr_t = 1.0$. But according to experimental data, Pr_t has an average value of 0.85 [6].

As far as the turbulent Schmidt number is concerned, the mean temperature profiles with varying Sc_t are presented in Fig. 1. It can be observed that with higher Sc_t, turbulent mass diffusivity is decreased, thus the over-prediction of the peak temperature at axial positions of 60 *mm* and 120 *mm* can be alleviated. On the centerline, for $Sc_t = 1.0$, there is an obvious under-prediction of the temperature profile, especially starting from 120 *mm* onward. With $Sc_t = 0.7$, the centerline temperature profile is well predicted. As a result, it is concluded that using $Sc_t = 0.7$ is the most appropriate choice for the current study.

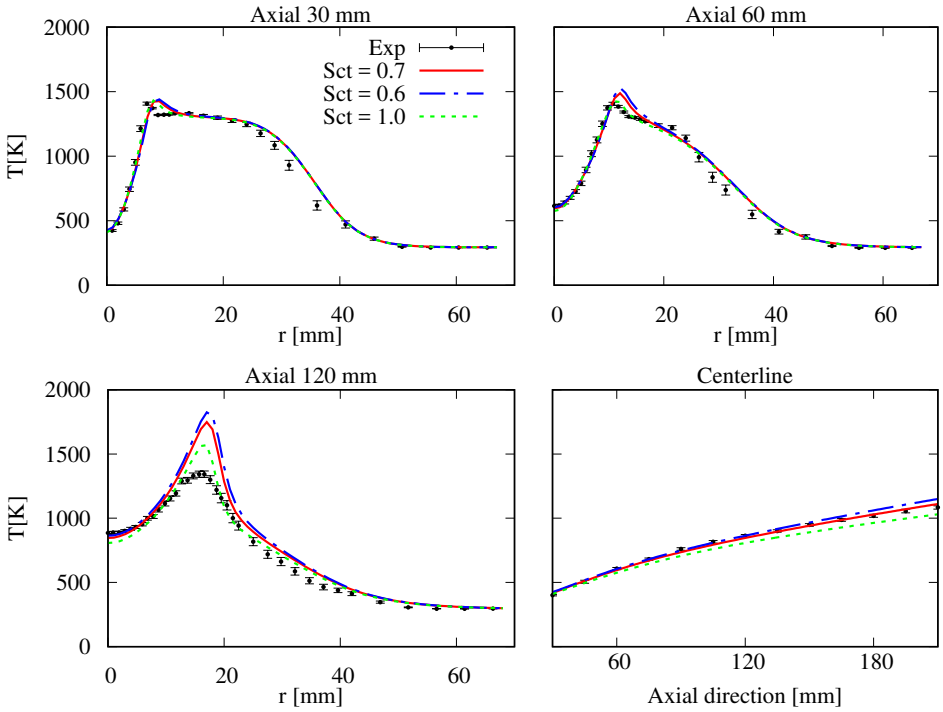

Figure 1: Effects of turbulent Schmidt number on predicted mean temperature profiles at several axial locations in radial direction and along the centerline.

Figure 2 shows the comparison between the temperature profiles obtained using $Pr_t = 1.0$ and $Pr_t = 0.85$, respectively. In general, small differences can be observed, although a value of $Pr_t = 0.85$ results in better agreement with the experimental data. Moreover, the temperature peak at 120 *mm* is slightly suppressed when $Pr_t = 0.85$.

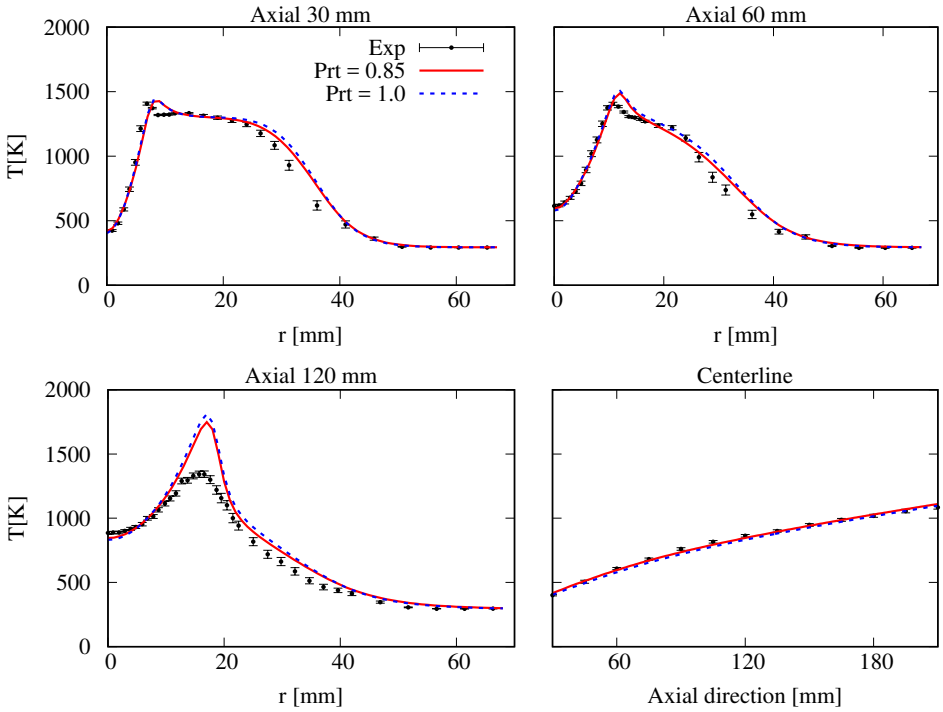

Figure 2: Effects of turbulent Prandtl number on predicted mean temperature profiles at several axial locations in radial direction and along the centerline.

In conclusion, the values of $Sc_t = 0.7$ and $Pr_t = 0.85$ are considered more suitable for the present case and helps increasing the prediction accuracy.

References

[1] D. A. Lysenko, I. S. Ertesvåg, K. E. Rian, Numerical simulation of non-premixed turbulent combustion using the eddy dissipation concept and comparing with the steady laminar flamelet model, Flow, Turbulence and Combustion 53 (2014) 577–605.

[2] M. Winterer, Nanocrystalline Ceramics: Synthesis and Structure, no. 43, Springer, 2002.

[3] I. Yimer, I. Campbell, L. Y. Jiang, Estimation of the turbulent schmidt number from experimental profiles of axial velocity and concentration for high-reynolds-number jet flows, Canadian Aeronautics and Space Journa 48 (3) (2002) 195–200.

[4] Y. Tominaga, T. Stathopoulos, Turbulent schmidt numbers for CFD analysis with various types of flowfield, Atmospheric Environment 41 (2007) 8091–8099.

[5] C. J. Geankoplis, Transport processes and separation process principles, 4th Edition, Prentice Hall, 2003.

[6] S. Vodret, D. Vitale, D. Maio, G. Caruso, Numerical simulation of turbulent forced convection in liquid metals, Journal of Physics: Conference Series 547.

A.2 Supplementary material from journal paper 2

Finite-rate chemistry modelling of non-conventional combustion regimes using a Partially-Stirred Reactor closure: combustion model formulation and implementation details ☆

Zhiyi Li[a,b], Marco Ferrarotti[a,b,c], Alberto Cuoci[d], Alessandro Parente[a,b,*]

[a] *Université Libre de Bruxelles, Ecole Polytechnique de Bruxelles, Aero-Thermo-Mechanics Laboratory, Bruxelles, Belgium*
[b] *Université Libre de Bruxelles and Vrije Universiteit Brussel, Combustion and Robust Optimization Group (BURN), Bruxelles, Belgium*
[c] *Service de Thermique et Combustion, Université de Mons, Mons, Belgium*
[d] *Department of Chemistry, Materials, and Chemical Engineering, Politecnico di Milano, Piazza Leonardo da Vinci, 20133 Milano, Italy*

☆ The short version of the paper was presented at ICAE2017, Aug 21-24, Cardiff, UK. This paper is a substantial extension of the short version of the conference paper.

* Corresponding author: Alessandro.Parente@ulb.ac.be

Supplemental Information

1. Supplementary material:The influence of radiation

The comparison with (red solid line) and without (green dashed line) radiation model (fv-DOM) and wsggm absorption/emission model for mean temperature and CO_2 species mass fraction with Fluent 17.0 are shown in Fig. 1 and Fig. 2. The second set of dynamic model parameters are used. The cases with Re = 10 k and varied co-flow oxygen levels (3%, 6% and 9%) are chosen for comparison. It can be observed that, there is no visual difference on the mean temperature profiles, for several co-flow oxygen levels. For the mean CO_2 species mass fraction profiles, minor differences can be observed for the 9% case. This confirms that at the locations where experimental data are available for comparison, the effect of the radiation models is negligible, thus they are not considered in the present study.

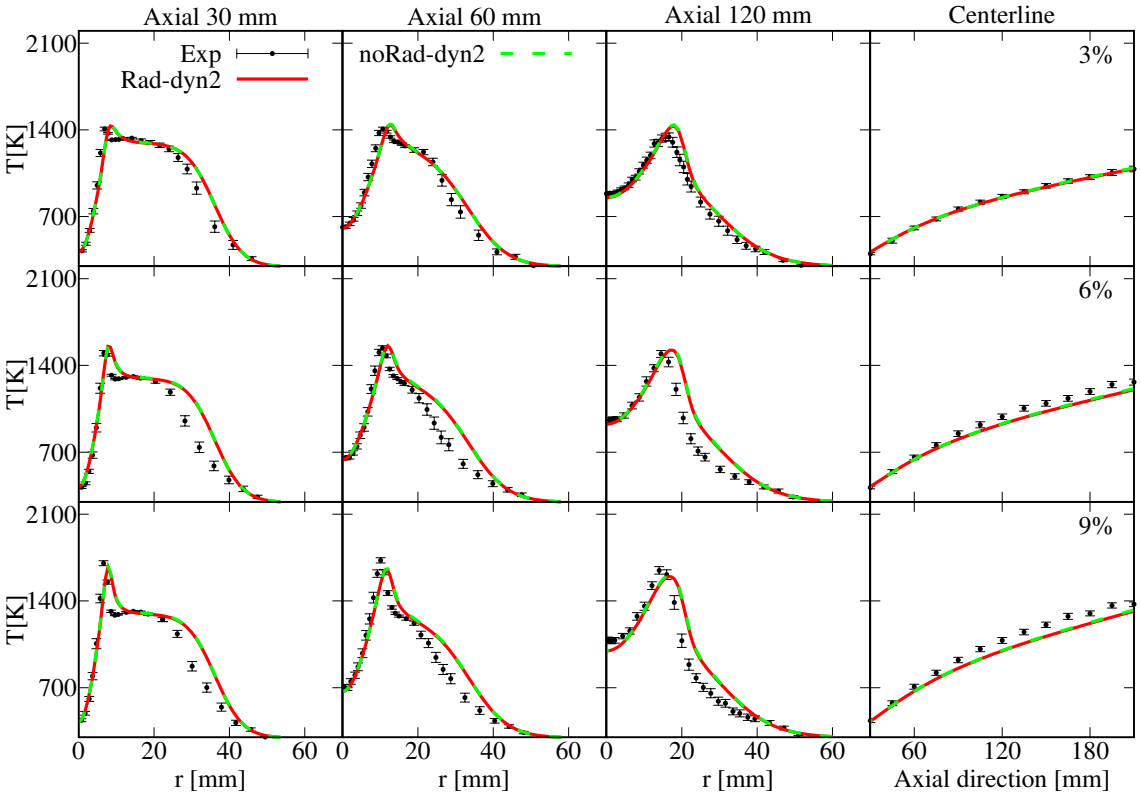

Figure 1: Comparison of the mean temperature profiles from the cases with and without radiation with different co-flow oxygen levels

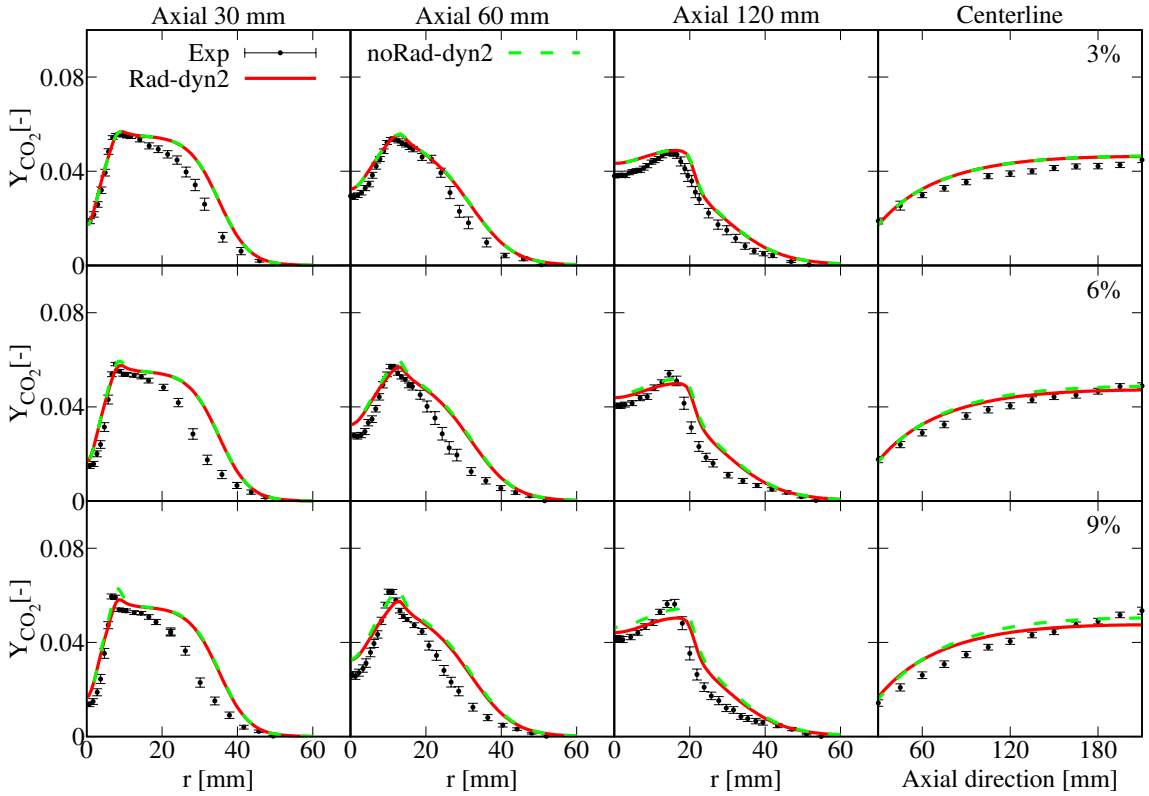

Figure 2: Comparison of the mean CO_2 species fraction profiles from the cases with and without radiation with different co-flow oxygen levels

A.3 Supplementary material from journal paper 3

Assessment of on-the-fly chemistry reduction and tabulation approaches for the simulation of MILD combustion

Zhiyi Li[a,b,*], Michał T. Lewandowski[c], Francesco Contino[d], Alessandro Parente[a,b,**]

[a] *Université Libre de Bruxelles, Ecole Polytechnique de Bruxelles, Aero-Thermo-Mechanics Laboratory, Bruxelles, Belgium*
[b] *Université Libre de Bruxelles and Vrije Universiteit Brussel, Combustion and Robust Optimization Group (BURN), Bruxelles, Belgium*
[c] *Institute of Fluid Flow Machinery, Polish Academy of Sciences, Gdańsk, Poland*
[d] *Vrije Universiteit Brussel, Department of Mechanical Engineering, Brussels, Belgium*

[*] Corresponding author: Zhiyi.Li@ulb.ac.be
[**] Corresponding author: Alessandro.Parente@ulb.ac.be

1. Supplementary material

The mean temperature and species mass fraction profiles from the five cases with different reduction methods (DRG, DRGEP, DAC, EFA and PFA) are compared with the case in which the reduction is turned off. ISAT is turned on for all the cases. Almost visually identical numerical results can be observed for mean temperature, mean species mass fractions of CO_2 and H_2O (see Figure 1, 2, 4). The errors of mean temperature prediction are below 2 % for most locations and below 5 % on all locations. For the major species of CO_2 and H_2O, the errors are controlled to 7 %. For the other species like CO and OH (see Figure 3, 5), higher error values can be captured, they are however mostly below 10-15 %.

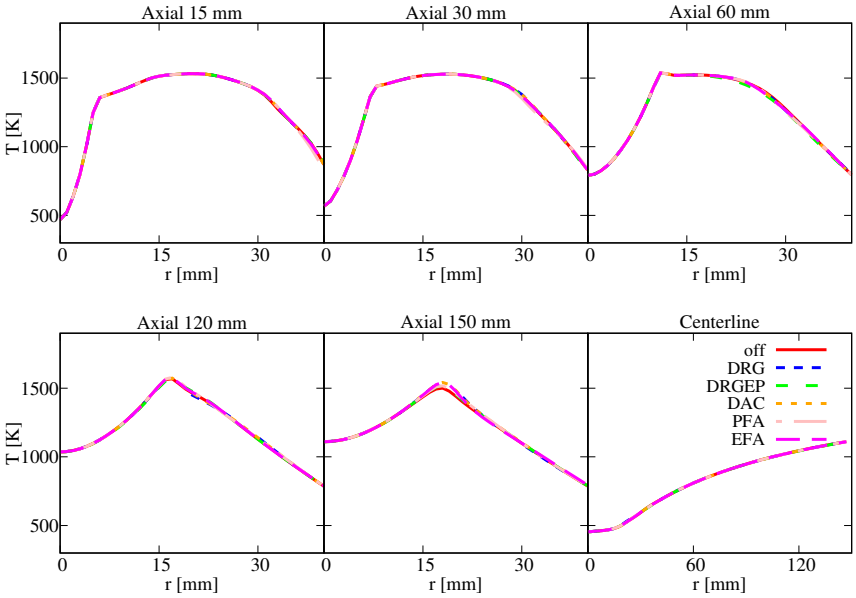

Figure 1: Mean temperature profiles obtained from the cases with five difference reduction methods (DRG, DRGEP, DAC, EFA and PFA) compared with the case without reduction. ISAT is turned on for all the cases.

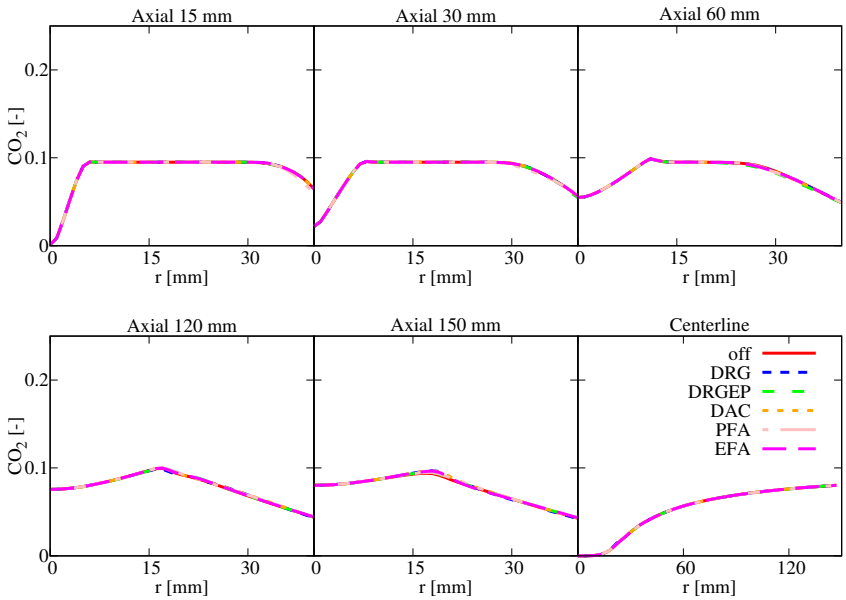

Figure 2: Mean CO_2 mass fraction profiles obtained from the cases with five difference reduction methods (DRG, DRGEP, DAC, EFA and PFA) compared with the case without reduction. ISAT is turned on for all the cases.

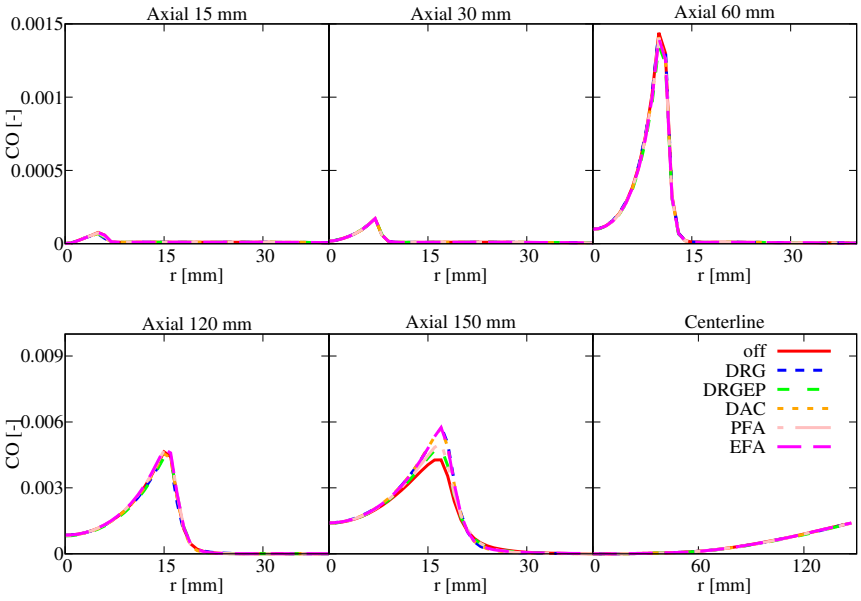

Figure 3: Mean CO mass fraction profiles obtained from the cases with five difference reduction methods (DRG, DRGEP, DAC, EFA and PFA) compared with the case without reduction. ISAT is turned on for all the cases.

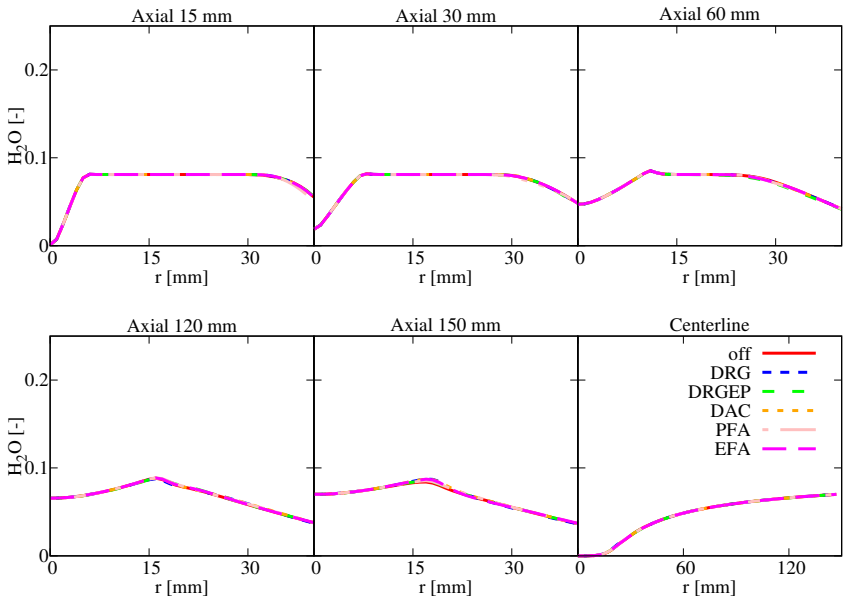

Figure 4: Mean H_2O mass fraction profiles obtained from the cases with five difference reduction methods (DRG, DRGEP, DAC, EFA and PFA) compared with the case without reduction. ISAT is turned on for all the cases.

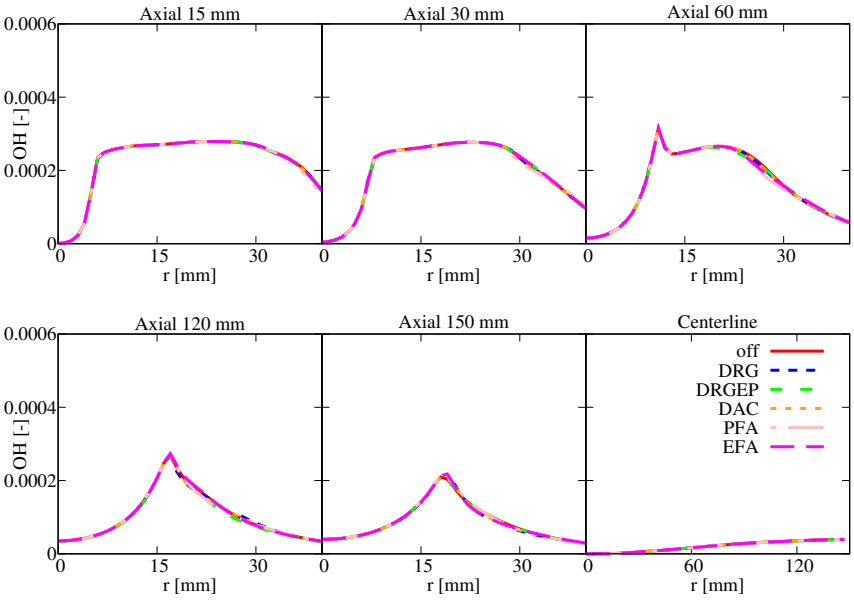

Figure 5: Mean OH mass fraction profiles obtained from the cases with five difference reduction methods (DRG, DRGEP, DAC, EFA and PFA) compared with the case without reduction. ISAT is turned on for all the cases.

A.4 Supplementary material from journal paper 4

Numerical investigation of turbulent n-heptane Jet in Hot Co-flow flames

Zhiyi Li[a,b,*], Michael Evans[c], Jingjing Ye[c], Paul Medwell[c], Alessandro Parente[a,b,**]

[a] *Université Libre de Bruxelles, Ecole polytechnique de Bruxelles, Aero-Thermo-Mechanics Laboratory, Brussels, Belgium*
[b] *Université Libre de Bruxelles and Vrije Universiteit Brussel, Combustion and Robust Optimization Group (BURN), Brussels, Belgium*
[c] *The University of Adelaide, School of Mechanical Engineering, Adelaide, Australia*

[*] Zhiyi.Li@ulb.ac.be
[**] Alessandro.Parente@ulb.ac.be

1. Discussion on the choice of chemical timescale

In combustion problems, a characteristic chemical timescale is often needed for the combustion model or to determine the system Damköhler number. In most cases a global chemical reaction rate is used to estimate the chemical timescale [1, 2]. However, finite rate chemistry is often required for systems with strong turbulence-chemistry interactions, such as MILD [3, 1, 4] combustion condition. Fox [5] provided a method which defines the chemical timescale considering the eigenvalues of the Jacobian matrix $\mathbf{J}$ of the chemical source terms. The inverse of eigenvalues is defined as the chemical timescale of each species. In this way, more complex kinetic schemes are included for the determination of chemical timescales. There are also simplified definition of using reaction rate [6], or chemical species formation rate [7, 8, 9], approximating the Jacobian diagonal terms. By using the definitions mentioned above, the chemical timescale for each species can be obtained. However, in finite rate chemistry mechanism, numerous number of species exist. Combustion model and Damköhler number calculation generally need only one characteristic chemical time.

According to Valorani et al. [10, 11, 12], in the eigen-system defined by the Jacobian matrix, the timescales which locally characterize the system evolution can be categorized in slow and fast timescales. The slow timescales or corresponding modes are leading the whole reaction system and the fast ones are following the slows ones. The fast modes reach equilibrium ("exhausted") very quickly. Therefore, the slow modes in the system is controlling the reaction and timescales describing such controlling modes should be used for the determination of chemical timescale in combustion models. As a result, after removing the dormant species, the maximum species chemical time is used as the characteristic chemical time in each cell in the current research.

Furthermore, Li et al. [9] tested the three ways of obtaining chemical timescale from Jacobian matrix, species formation rate and species reaction rate. Results show that the approach based on formation rate is more efficient and it approximates the Jacobian matrix method better than the one based on reaction rate.

2. Heat release rate profiles with radial strain rate

The radial strain rate plotted with contour lines and heat release rate with flood is shown in Figure 1. As it is with the axial strain rate, similar profiles of the radial strain rate distribution between the cases with various coflow oxygen levels can be observed. No direct correlation between the negative heat release location and axial strain rate value can be found.

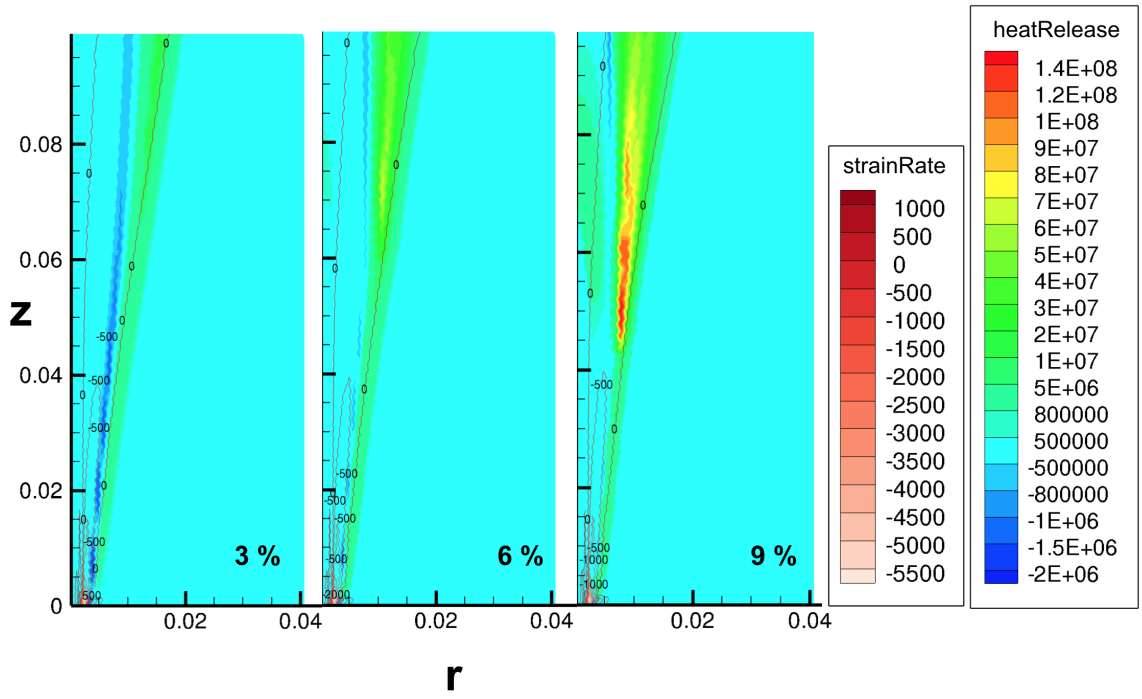

Figure 1: Heat release rate (HRR) for the cases with 3 %, 6 % and 9 % coflow oxygen levels with radial strain rate as contour line. The unit for strain rate is s^{-1} and for HRR is W/m^3.

3. Comparison with Livermore mechanism

The reduced n-heptane mechanism from Politecnico di Milano (polimi) with 106 species and 1738 reactions [13, 14, 15] is compared with the livermore detailed n-heptane mechanism [16, 17] with 654 species and 2827 reactions in Figure 2, 3 and 4. The temperature profiles from the reduced mechanism and detailed mechanism show no visual difference, while distinct features on OH number density distribution is captured on axial locations of 14.5, 22.5 and 29.5 mm. Even though the experimental OH number density data is half-quantified, the over-predicted OH peak value cannot be eliminated by multiplying with a scaling number, considering the fact that the modelled OH number density values for r≥20 mm are close to the experimental data for z = 14.5 mm and 29.5 mm. Regarding the normalized CH_2O number density distribution, similar shape of the profiles are obtained by using the livermore mechanism, compared to the polimi reduced mechanism. The livermore mechanism is showing slightly higher peak value of the normalized CH_2O number density.

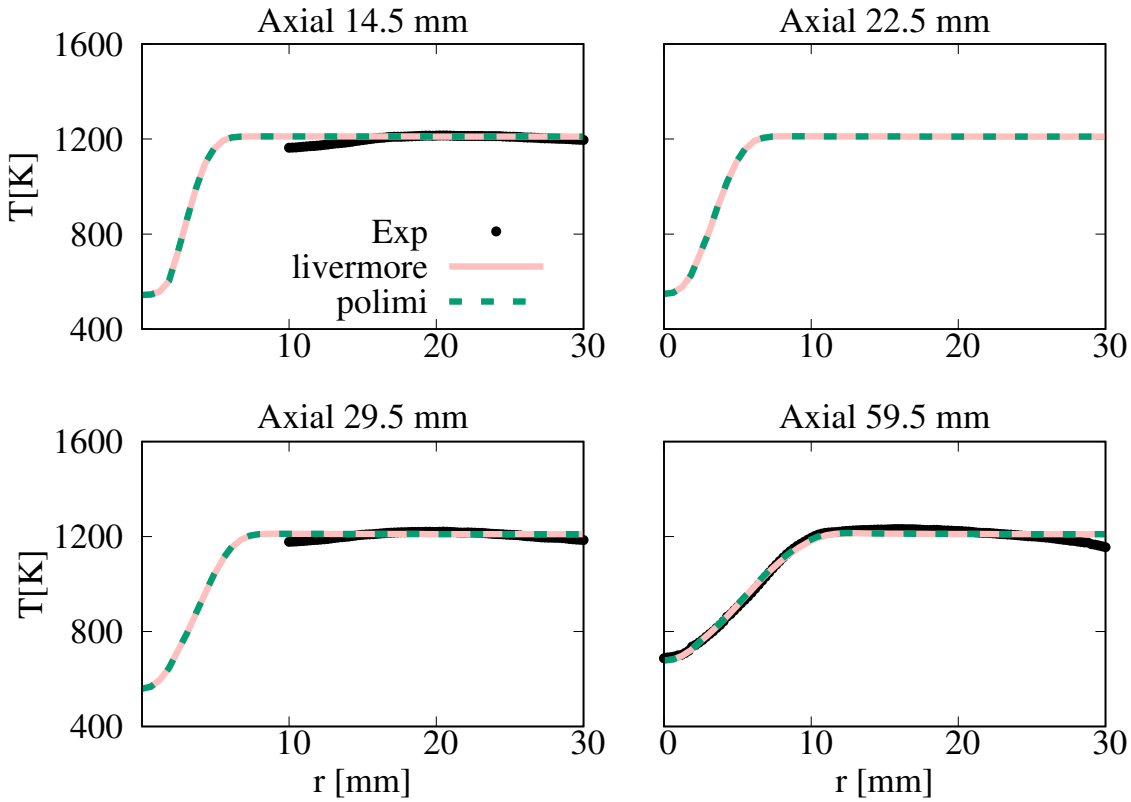

Figure 2: Mean temperature profiles obtained from the simulations with livermore and polimi n-heptane mechanism.

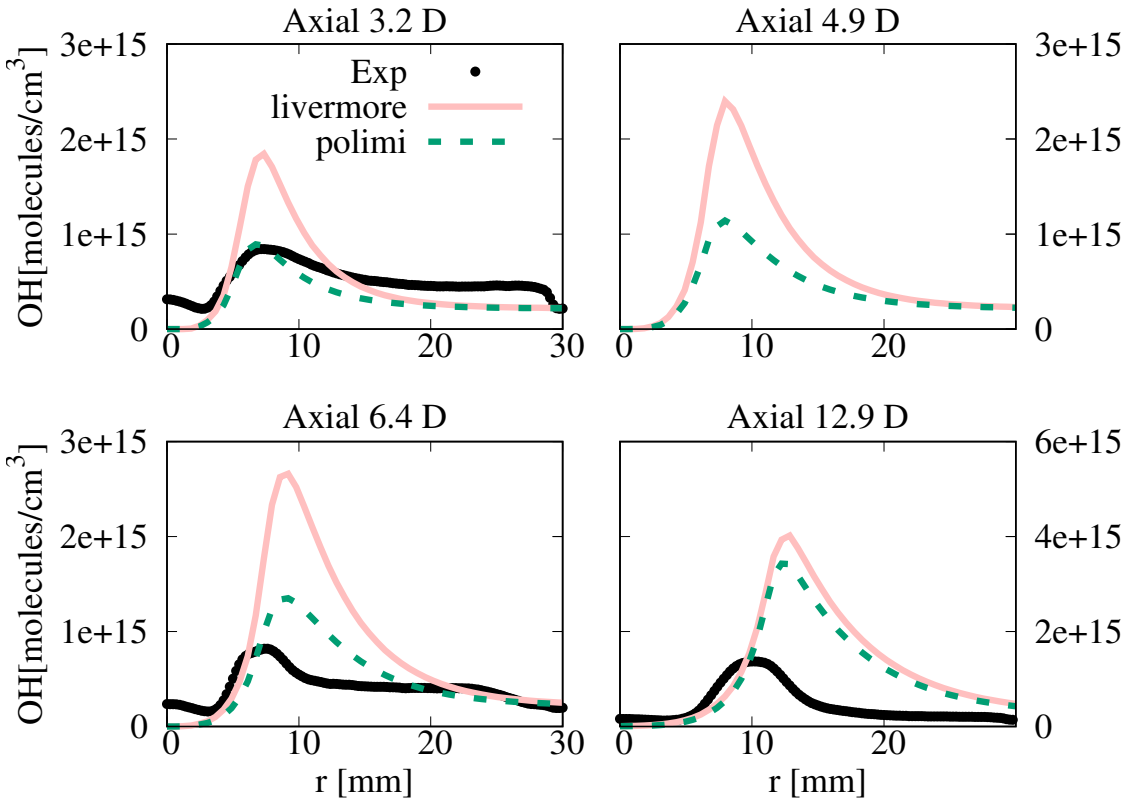

Figure 3: Mean OH number density profiles obtained from the simulations with livermore and polimi n-heptane mechanism.

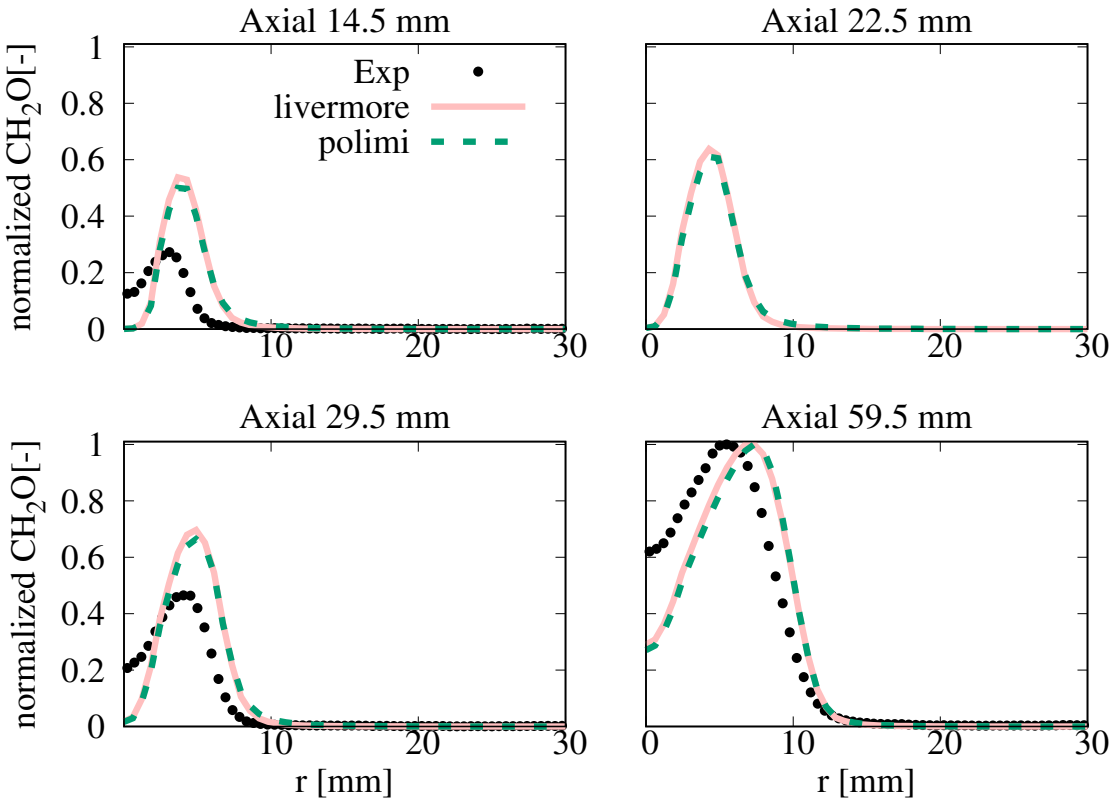

Figure 4: Normalized mean CH_2O number density profiles obtained from the simulations with livermore and polimi n-heptane mechanism.

The contour plots of heat release rate from the cases using livermore and polimi mechanisms are presented in Figure 5. The negative heat release area still exist and is expanded slightly by using the livermore mechanism, showing more pyrolysis reactions. When it comes to the positive heat release, the livermore mechanism predicts more heat generation close to the centerline and less on the radial position of around 0.02 m near the domain exit location (above z = 0.08 m).

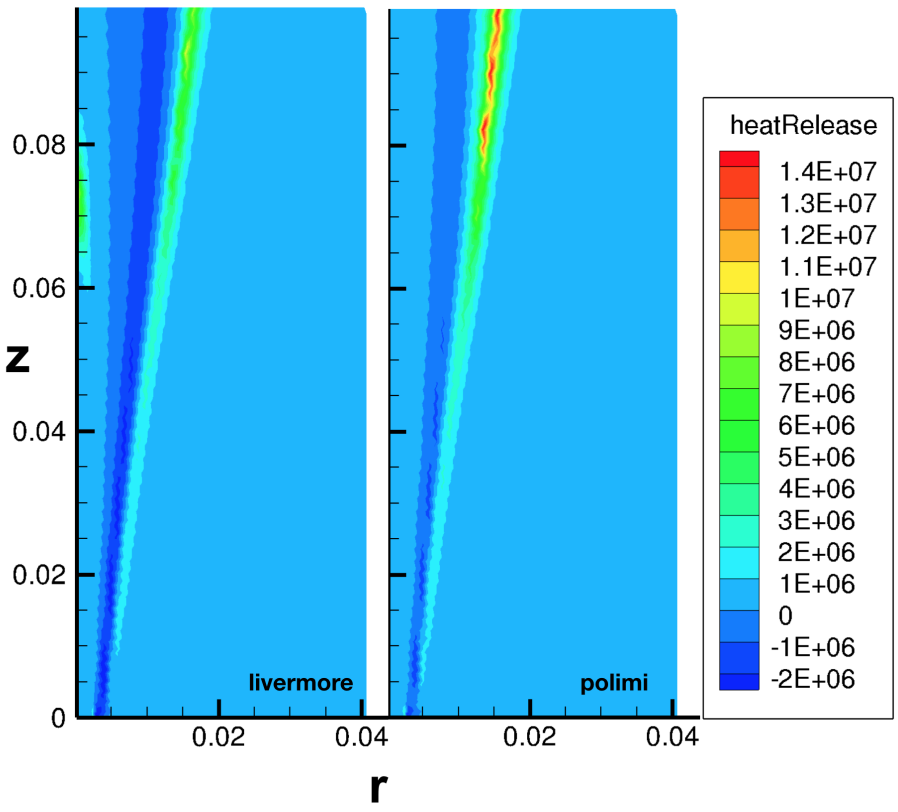

Figure 5: Heat release rate (HRR) for the cases with livermore and polimi mechanism. The unit for HRR is W/m^3.

In summary, the negative heat release area still exist by using a more detailed n-heptane mechanism and the over-prediction (more than that with polimi mechanism) of OH number density profiles are obtained by such mechanism.

4. Reducing coflow oxygen levels to 1% and 2%

If the coflow oxygen level is further decreased to 2%, even 1%, a steady solution can still be obtained with numerical simulation. Figure 6 demonstrates how the OH number density profiles change from 3% case (on the right) to 1% case (on the left). The number density threshold value is set to 5×10^{11} molecules/cm^3. Transitional area with gradually increasing OH signal is also observable for the 1% and 2% cases. The flame weak-to-strong heights with different OH number density values are summarized in Figure 7. The difference between the flame weak-to-strong heights for the 1% and 2% cases are more obvious for lower number density threshold value, such as 5×10^{11} molecules/cm^3.

In Figure 8, the heat release contour plots for the 1/2/3 % cases are shown. With decreased

coflow oxygen, the maximum positive heat release value is decreasing as well. At the same time, the absolute value for negative heat release is increasing. Therefore, the negative heat release region still exist with highly diluted case, 1% coflow oxygen content; the absolute value of negative heat release is even larger than the slight higher oxygen level cases: 2% and 3%.

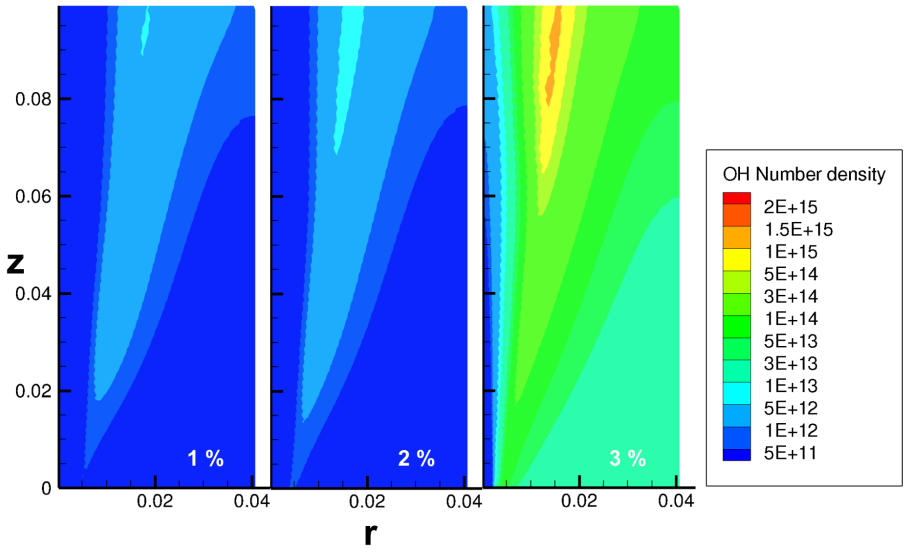

Figure 6: OH number density for the cases with 1% and 2% coflow oxygen levels. The unit for OH number density is molecules/cm^3.

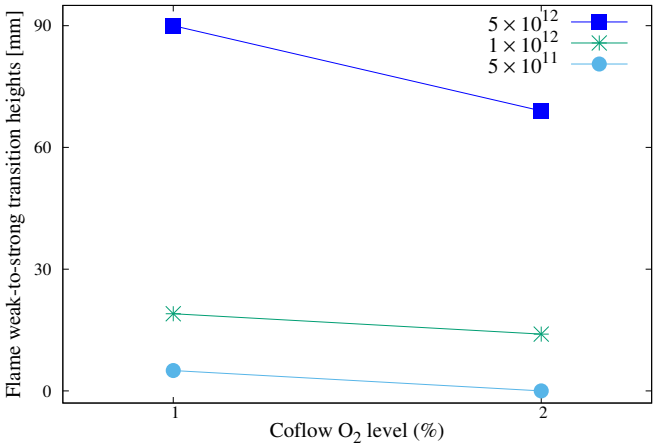

Figure 7: Flame weak-to-strong heights for the cases with 1% and 2% coflow oxygen levels.

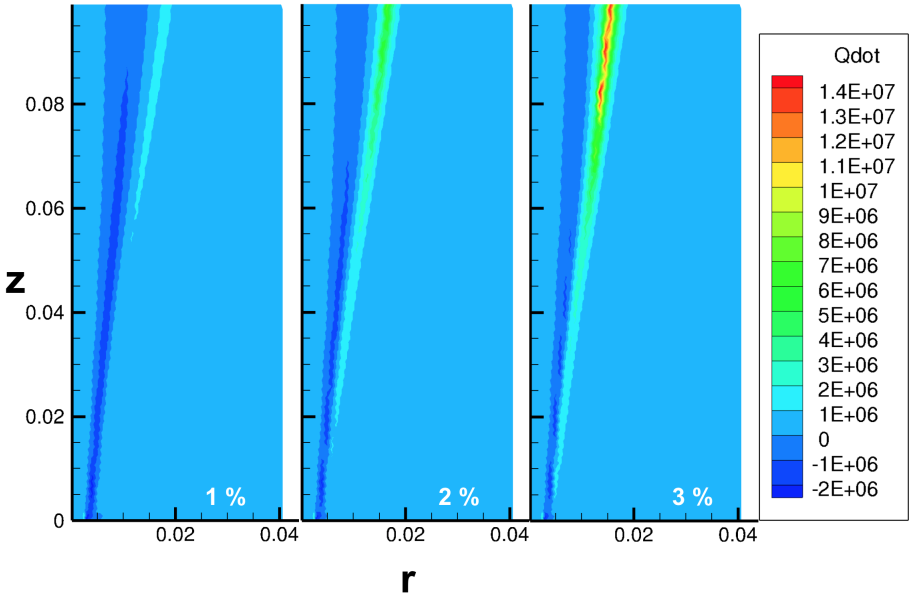

Figure 8: Heat release rate (HRR) for the cases with 1% and 2% coflow oxygen levels. The unit for HRR is W/m^3.

5. Mixing timescale distribution

The mixing timescale contour plot for the cases with 3 %, 6 % and 9 % coflow oxygen levels is shown in Figure 9. In general, all the cases show very similar distribution of the mixing timescale for most regions in the simulation domain. Close to the right boundary of the coflow stream, high value of mixing time is captured only for the 3 % and 6 % cases. This comes from the numerical issue.

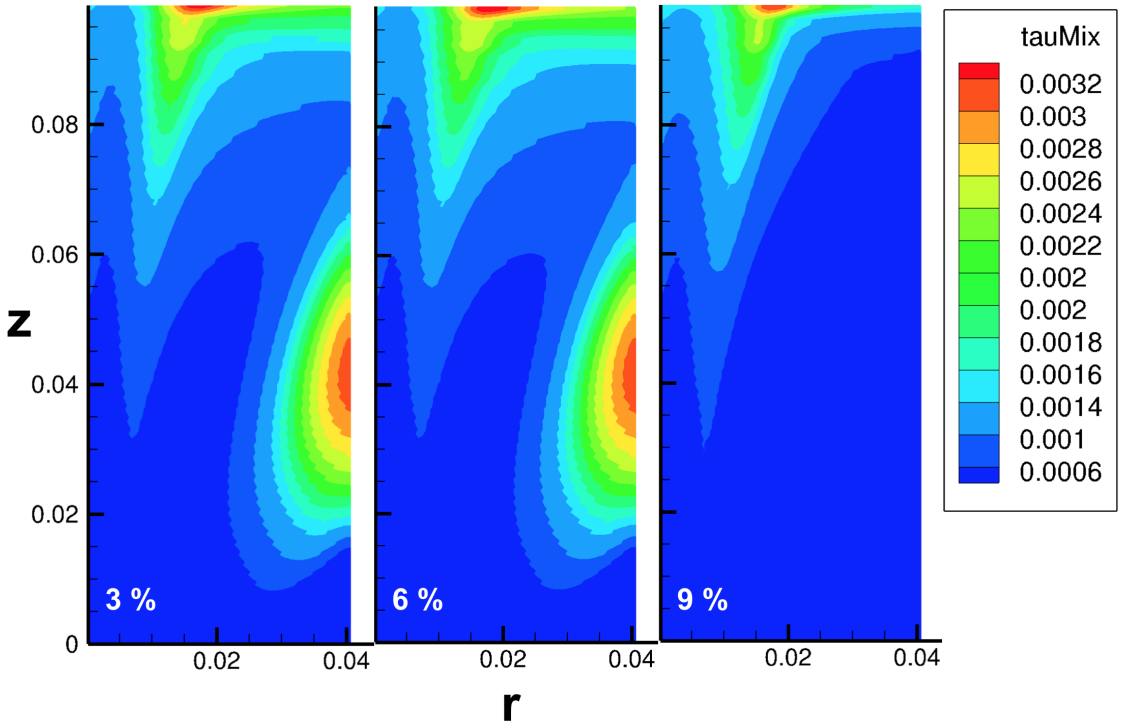

Figure 9: Mixing timescale (unit: s) contour plot for the cases with 3 %, 6 % and 9 % coflow oxygen levels.

References

[1] A. Cavaliere and M. de Joannon. MILD combustion. *Progress in Energy and Combustion Science*, 30:329–366, 2004.

[2] Kenneth Kuan yun Kuo. *Principles of Combustion*. Wiley-Interscience, New York, 1986.

[3] J. A. Wünning and J. G. Wünning. Flameless oxidation to reduce thermal NO-formation. *Progress in Energy and Combustion Science*, 23:81–94, 1997.

[4] M. de Joannon, G. Sorrentino, and A. Cavaliere. MILD combustion in diffusion-controlled regimes of hot diluted fuel. *Combustion and Flame*, 159:1832–1839, 2012.

[5] R. O. Fox. *Computational Models for Turbulent Reacting Flows*. Cambridge University Press, Cambridge, UK, 2003.

[6] V. Golovitchev and J. Chomiak. Numerical modeling of high temperature air flameless combustion. In *The 4th international symposium on high temperature air combustion and gasification*, 2001.

[7] J. Chomiak and A. Karlsson. Flame liftoff in diesel sprays. In *Twenty-Sixth Symposium (International) on Combustion*, pages 2557–2564. The Combustion Institute, 1996.

[8] Benjamin J. Isaac, Alessandro Parente, Chiara Galletti, Jeremy N. Thornock, Philip J. Smith, and Leonardo Tognotti. A novel methodology for chemical time scale evaluation with detailed chemical reaction kinetic. *Energy Fuels*, 27(4):2255–2265, 2013.

[9] Zhiyi Li, Alberto Cuoci, Amsini Sadiki, and Alessandro Parente. Comprehensive numerical study of the Adelaide Jet in Hot-Coflow burner by means of RANS and detailed chemistry. *Energy*, 139:555–570, 2017.

[10] Mauro Valorani, Habib N. Najm, and Dimitris A. Goussis. Csp analysis of a transient flame-vortex interaction: time scales and manifolds. *Combustion and Flame*, 134(1):35 – 53, 2003.

[11] Mauro Valorani, Samuel Paolucci, Emanuele Martelli, Temistocle Grenga, and Pietro P. Ciottoli. Dynamical system analysis of ignition phenomena using the tangential stretching rate concept. *Combustion and Flame*, 162(8):2963 – 2990, 2015.

[12] Mauro Valorani, Pietro Paolo Ciottoli, and Riccardo Malpica Galassi. Tangential stretching rate (tsr) analysis of non premixed reactive flows. *Proceedings of the Combustion Institute*, 36(1):1357–1367, 2017.

[13] E. Ranzi, A. Frassoldati, A. Stagni, M. Pelucchi, A. Cuoci, and T. Faravelli. Reduced kinetic schemes of complex reaction systems: Fossil and biomass-derived transportation fuels. *International Journal of Chemical Kinetics*, 46(9):512–542, 2014.

[14] A. Stagni, A. Cuoci, A. Frassoldati, T. Faravelli, and E. Ranzi. Lumping and reduction of detailed kinetic schemes: An effective coupling. *Industrial and Engineering Chemistry Research*, 53(22):9004–9016, 2014.

[15] A. Stagni, A. Frassoldati, A. Cuoci, T. Faravelli, and E. Ranzi. Skeletal mechanism reduction through species-targeted sensitivity analysis. *Combustion and Flame*, 163:382–393, 2016.

[16] Marco Mehl, William J. Pitz, Charles K. Westbrook, and Henry J. Curran. Kinetic modeling of gasoline surrogate components and mixtures under engine conditions. *Proceedings of the Combustion Institute*, 33(1):193–200, 2011.

[17] H.J. Curran, P. Gaffuri, W.J. Pitz, and C.K. Westbrook. A comprehensive modeling study of n-heptane oxidation. *Combustion and Flame*, 114(1):149–177, 1998.

A.5 Supplementary material from journal paper 5

Large Eddy Simulation of MILD combustion using finite rate chemistry: effect of combustion sub-grid closure

Zhiyi Li[a,*], Alberto Cuoci[b], Alessandro Parente[a,**]

[a]*Aero-Thermo-Mechanics Department, Université Libre de Bruxelles, Avenue Franklin Roosevelt 50, 1050 Brussels, Belgium*
[b]*Department of Chemistry, Materials, and Chemical Engineering, Politecnico di Milano, P.zza Leonardo da Vinci, 20133 Milano, Italy*

[*]Corresponding author: Zhiyi.Li@ulb.ac.be
[**]Corresponding author: Alessandro.Parente@ulb.ac.be

1. Introduction

In the current supplementary material from the research work of Li et al. [1], the Favre-filtered governing equations of continuity, momentum, species and energy are presented in detail [2].

2. Governing equations

Continuity:

$$\frac{\partial \overline{\rho}}{\partial t} + \frac{\partial \left(\overline{\rho}\widetilde{u_i}\right)}{\partial x_i} = 0, \tag{1}$$

Momentum:

$$\frac{\partial \overline{\rho}\widetilde{u_i}}{\partial t} + \frac{\partial \left(\overline{\rho}\widetilde{u_i}\widetilde{u_j}\right)}{\partial x_i} + \frac{\partial \overline{p}}{\partial x_j} = \frac{\partial}{\partial x_i}\Big[\overline{\tau}_{ij} - \overline{\rho}(\widetilde{u_i u_i} - \widetilde{u_i}\widetilde{u_j})\Big], \tag{2}$$

Species:

$$\frac{\partial \overline{\rho}\widetilde{Y_k}}{\partial t} + \frac{\partial \left(\overline{\rho}\widetilde{u_i}\widetilde{Y_k}\right)}{\partial x_i} = -\frac{\partial}{\partial x_i}\left[\overline{\rho}\overline{D_k}\frac{\partial \widetilde{Y_k}}{\partial x_i} + \overline{\rho}(\widetilde{u_i Y_k} - \widetilde{u_i}\widetilde{Y_k})\right] + \overline{\dot{\omega}_k} k = 1, N, \tag{3}$$

Energy:

$$\begin{aligned} &\frac{\partial \overline{\rho}\widetilde{h_s}}{\partial t} + \frac{\partial \left(\overline{\rho}\widetilde{u_i}\widetilde{h_s}\right)}{\partial x_i} = \\ &\frac{\overline{Dp}}{Dt} + \frac{\partial}{\partial x_i}\left[\overline{\lambda}\frac{\partial \widetilde{T}}{\partial x_i} - \overline{\rho}(\widetilde{u_i h_s} - \widetilde{u_i}\widetilde{h_s})\right] - \frac{\partial}{\partial x_i}\left(\overline{\rho \sum_{k=1}^{N} h_{s,k} D_k \frac{\partial Y_k}{\partial x_i}}\right) + \overline{\dot{\omega}}_T. \end{aligned} \tag{4}$$

From Equation 1 to Equation 4, k represents the number of species, h_s is the sensible enthalpy and λ is the thermal conductivity.

References

[1] Z. Li, A. Cuoci, A. Parente, Proc. Combust. Inst. 37 (2019).

[2] T. Poinsot, D. Veynante, Theoretical and Numerical Combustion, p164, R.T. Edwards, 2005.